THÈSE DE DOCTORAT

de l'Université de recherche Paris Sciences et Lettres
PSL Research University

Préparée à l'Observatoire de Paris

Resolved spectroscopy of debris disks with SPHERE/VLT

École doctorale n°127

ASTRONOMIE & ASTROPHYSIQUE D'ÎLE-DE-FRANCE

Spécialité HIGH CONTRAST IMAGING

COMPOSITION DU JURY :

Françoise ROQUES
LESIA, Observatoire de Paris, Président

Paul KALAS
University of California, Berkeley,
Rapporteur

François MÉNARD
IPAG/Grenoble, Rapporteur

Jean-Charles AUGEREAU
OSUG/Grenoble, Membre du jury

Maud LANGLOIS
CRAL/Lyon, Membre du jury

Anthony BOCCALETTI
LESIA, Observatoire de Paris,
Membre du jury

Soutenue par **Trisha Bhowmik**
le

Dirigée par **Anthony Boccaletti**

PSL UNIVERSITÉ PARIS

l'Observatoire de Paris | LESIA

Laboratoire d'Études Spatiales et d'Instrumentation en Astrophysique

THÈSE DE DOCTORAT
DE L'UNIVERSITÉ PARIS SCIENCES ET LETTRES

École Doctorale d'Astronomie & Astrophysique d'Île-de-France

LESIA, Observatoire de Paris

Resolved spectroscopy of debris disks with SPHERE/VLT

Présentée par

Trisha BHOWMIK

Et soutenue publiquement le 8 novembre 2019 devant un jury composé de :

Françoise ROQUES	Présidente du jury
Paul KALAS	Rapporteur
François MÉNARD	Rapporteur
Jean-Charles AUGEREAU	Examinateur
Maud LANGLOIS	Examinateur
Anthony BOCCALETTI	Directeur de thèse

Résumé

Les disques de débris sont présents autour de nombreuses jeunes étoiles de la séquence principale. Ils se caractérisent par un environnement poussiéreux, dépourvu de gaz, par opposition à des disques protoplanétaires riches en gaz. Les disques de débris sont également considérés comme des «disques secondaires» car ils sont constitués de grains de poussière non primordiaux générés par des collisions continues de planétésimaux. Des observations récentes dans le sub-millimètre ont apporté des preuves convaincantes qu'une quantité significative de gaz peut être présente dans certains de ces disques.

L'imagerie à haut contraste et à haute résolution s'est révélée très efficace pour observer les disques de débris et résoudre leurs structures morphologiques, en traçant la distribution des petits grains de poussière. L'imagerie en lumière diffusée dans le proche infrarouge permet de mesurer la distribution d'intensité dans le disque, qui est liée aux propriétés des grains. L'intensité du disque varie différemment en intensité totale et en intensité polarisée. Il est donc nécessaire d'utiliser les deux méthodes pour mieux contraindre les caractéristiques de la poussière.

Compte tenu des avantages de l'imagerie à haut contraste, j'ai cherché à étudier des images de disques de débris obtenues en lumière diffusée par l'instrument SPHERE (Spectro-Polarimetric High-contrast Exoplanet Research), installée au VLT au Chili. Pour obtenir une image en intensité total d'un disque à partir d'une observation coronographique en optique adaptative dans laquelle les résidus stellaires sont réduits, ont utilise généralement les techniques d'imagerie différentielle angulaire (ADI) et d'imagerie différentielle polarimétrique (PDI), mais celles-ci peuvent engendrer une auto-soustraction qui doit être corrigée pour retrouver la vraie photométrie. Afin de modéliser les disques de débris, j'ai utilisé un module de transfert radiatif, GRaTer. Ces images synthétiques sont traitées selon une technique de post-traitement identique aux données, ce qui permet de contraindre la morphologie du disque et la distribution des grains. Le but de ma thèse est d'interpréter les variations spectrales et temporelles des disques de débris, à la fois en termes de morphologie et de distribution des grains, pour mieux comprendre la formation de planètaire. Pour ce faire, j'ai étudié la morphologie du disque de débris HD32297 et j'ai développé un modèle reproduisant la distribution de densité et d'intensité du disque. Ce modèle a ensuite été utilisé pour mesurer la luminosité de surface et la réflectance moyenne du disque. La réflectance moyenne a ensuite été comparée à un spectre théorique obtenu pour une distribution de taille de grains et pour différentes compositions de grains. L'ajustement des spectres en réflectance moyenne a fourni un résultat important, indiquant que la taille de grain minimale est bien inférieure à la taille de « blow-out », indépendamment de la composition du grain. Plusieurs explications sont possibles pour expliquer la présence de grains submicrométriques: cascade collisionnelle en régime permanent, mécanisme d'avalanche de collisions et drainage par le gaz lié à la présence d'une grande quantité de gaz dans ce disque de débris.

Dans la suite de la thèse je reproduit ce travail pour l'étude des disques de débris HD106906 et HD141569 en intensité totale. Pour HD106906, l'asymétrie du flux visible entre les deux côtés du disque a été modélisée. Pour HD141569, en utilisant la photométrie d'ouverture, j'ai effectué une analyse spectrale d'une structure du disque que je compare à la partie sud du disque interne. En perspective, ce travail permettra une

analyse plus systématique des nombreuses observations multi-longueurs d'onde obtenues en imagerie haut contraste de disques de débris afin de comprendre l'évolution des grains vers les planètes.

Abstract

Debris disks are found around many young main-sequence stars. They are characterized by the dusty, gas-depleted environment as opposed to gas-rich protoplanetary disks. Debris disks are also considered as 'secondary disks' because they bear non-primordial dust grains which are constantly generated by continuous collisions of planetesimals. Recent observations in the sub-millimeter have shown compelling evidence that a significant amount of gas can be present in some of these disks.

High-contrast and high-resolution imaging have proven to be very effective to observe debris disks and to resolve their morphological structures, tracing the distribution of the small dust grains. Scattered light imaging in the near-infrared can measure the intensity distribution of the disk, which is related to the grain properties. The disk intensity varies differently in total intensity imaging and polarimetric imaging so it is necessary to use both to better constrain dust characteristics.

Considering the advantages of high-contrast imaging, I aimed to study the scattered light images of debris disks obtained by one such instrument, the Spectro-Polarimetric High-contrast Exoplanet Research (SPHERE) which is installed at the VLT in Chile. To obtain a post-processed intensity image with reduced stellar residuals in a post-adaptive optics coronographic observation, the angular differential imaging (ADI) and polarimetric differential imaging (PDI) techniques are usually performed but imply self-subtraction which must be corrected for to recover true photometry. In order to model debris disks, I used a radiative transfer module, GRaTer and processed disk synthetic images through equivalent post-processing technique as the data, from which the morphology of the disk and its grain-size distribution is constrained.

The goal of my thesis is to interpret spectral and temporal variations of debris disks, both in terms of their morphology and grain-size distribution to finally understand planet formation. To achieve this I studied the morphology of the debris disk HD32297 and developed a model mimicking the density and intensity distribution of the disk. This model then was used to retrieve the surface brightness and average reflectance of the disk. The average reflectance was then compared to a spectrum obtained from analyzing the particle size distribution within the disk for different grain compositions. Fitting the spectra to the average reflectance provided an important result, which indicated that the minimum grain size is well below blow-out size independent of the grain composition. The possible explanations which were looked into for the presence of sub-micron grains are a combination of a steady-state collisional cascade, collisional avalanche mechanism and gas drag due to the presence of a large quantity of gas in this debris disk. In second part of the thesis I applied similar work to debris disk HD106906 and HD141569 in total intensity. For HD106906 the visible flux asymmetry between the two sides of the disk was modeled and resolved and for HD141569 using aperture photometry a spectral analysis of the particular structure compared to the full southern part of the inner disk was performed. In perspective, this work will open a more systematic analysis of the many multi-wavelength observations obtained with high-contrast imaging of debris disks in order to understand the evolution of grains to planets.

Acknowledgements

There are about 2000 people whom I should thank for making me achieve my dream of pursuing a career in PhD. Today, I am most thankful to my father, *Tapash Bhowmik*, to have sowed the seed of astronomy in my 11 year old brain by introducing me to my inspiration Late Dr. Kalpana Chawla. I thank my mom, *Manika Bhowmik*, to have had the courage to send me so far away from home. Once I was mature enough to realise that Astronomy was my passion, my parents and my entire family stood by me and encouraged me to pursue it as a career. For this, I am forever thankful to my entire *Bhowmik family*. I would like to give a special thanks to my brother, *Tridib*, who is my rock and would fight the entire universe for me (Gui Gui Chotto Manush).

I joined PhD in 2016 in November for which I am grateful to ED127 to have selected me and funded me. I am extremely thankful to *Jacques Le Bourlot*, *Géraldine Gaillant* and *Jacqueline Plancy* to have helped me with the VISA issues to come to France and allowed me to start the thesis a month later. I would like to thank *Thierry Fouchet* and *Alain Doressoundiram* who helped me in completing all the administrative protocols regarding writing the manuscript and conducting the defense. I would like to give my regards to all the LESIA administrative staff *Vincent Coudé du Foresto*, *Sylvaine Destan* and *Cris Dupont* to have helped me with all the necessary paperworks in the duration of my entire thesis. I am grateful to *Pierre Dossart* and *Eric Gendron* to be the member of my comité de suivi. I greatly appreciate all the technical support provided by *Goran* and *Souda* whenever I went with my laptop to them.

Next, I would like to thank my supervisor, *Anthony*, to have guided and groomed me throughout my PhD. He has been more like Saint Anthony to me and have always found the time to dig me out from scientifically challenging situations. I would like to thank *Raphael* and *Pierre* to have helped me and cleared my scientific queries whenever I knocked at their doorsteps. I am very thankful to *Philippe* and *Quentin* to have contributed in modeling the grain properties and understanding the effects of gas in debris disks. I would like to thank *Johan* for finding time to have valuable discussion on the photometric extraction and error analysis for the paper on HD 32297. I will forever be thankful to each and every member of the SPHERE collaboration have given me my big break in High-Contrast Imaging.

Now entering office 11, I would first thank *Tobias* to have found the patience to sit with me for hours teaching me IDL and reduction techniques of High-Contrast Imaging. Also, thanks Tobias to have introduced me to Star Wars. Thank you *Fabien* to have motivated me to start writing my thesis and document my every day's work from the beginning of the thesis (eventhough I did not follow it routinely but I passed the same advise to the new PhD students). I would like to thank *Clement* and *Lucas* to have always helped me with French to English translation be it in social security office or with the apartment guardian (I hope I did not poison any of you with spicy Indian food). *Elsa* and *Lucie*, your motivation for science have helped me stay focused on my pursuit of being an astronomer, thank you for that. *Axel*, thank you for being my comic relief, thank you for tolerating my jokes and continuous leg pulling, you have been like a brother to me (Thanks *Emilin* to have taught me to make Crumble). I would next like to give my biggest thanks to *Garima* to have taken enormous amount of time to read my thesis, comment on it, correct it and

guide me through the entire process of writing it. Thank you Garima to pull me through the times when I broke down or panicked.

Reading till here you might be thinking I did not make any friends outside work, you are highly mistaken. Here, the biggest thanks should go to two people *Adarsh* and *Ajit* Bhaiya. Throughout, the final year of my thesis I never had to worry about what I am going to have for lunch or dinner because of Ajit. Thank you for making our apartment into home and never letting me miss home cooked delicious Indian food. Thank you Adarsh for being a great friend, for indulging with me into scientific/historical/political debates, for helping me out with my writing skills, for pulling me out of bed when I was too lazy to do anything and not trying too hard to hack into my work laptop for DOTA. I know I taught you a lottttt but still my parents insist that I thank you (I know that I would most probably have to share half of my inheritance with you). *Karan* bhaiya thank you for making amazing Chai and Roti for us. *Sarah*, I hope I can learn to be as brave and strong as you. Thank you for teaching me to relax and enjoy life sometimes. *Raj* di I am so thankful to you because of you even when I was living alone I had a part of family beside me, thank you for never pushing me away. I have never met a more respectable man in my life as you *Rahul* bhaiya, I always felt carefree and chill when you were around, thank you for taking care of all of us. *Vasu*, I have known you for a long time and I will always be thankful as you were there for me when I did not know anyone in the city. Despite of your own struggles you always made time for your friend, thank you for that. Thank you *Theu* and *Bin* for being so kind and helping me in my greatest need when no one else was able to stand with me. The two very important people whom I should thank and who have been in my life for more than 8 years now are *Kalyan* eta and *Lydia*. Kalyan eta you have helped me throughout the process of PhD applications and have been an inspiration for me to even think of stepping out of India for a PhD, thank you for all your valuable advices. Lydia you have been my strength since University, knowing that you are just a call away have always kept me away from my panic mode. Thanks Lydo for being my strength. I would like to thank the people who made my life more colourful without whom I wouldnt have enjoyed Paris as much as I did, so thanks a million *Evan, Shweta, Desh, Isadora, Ane Lise, Paula, Fiorella, Elena, Julien, Valeria, Brisa, Clement F and Anton.*

Last but not the least I would like to thank my faculties of Pondicherry University to have guided me and prepared me to pursue a PhD degree. Special thanks to *Alok Sharan* and *S. V. M. Stayanarayana* to have mentored me. Thank you *Manoj Puravankara* to have ignited the spark of circumstellar disk physics inside my mind.

कर्मण्येवाधिकारस्ते मा फलेषु कदाचन ।स्त्व कर्मणि ॥
मा कर्मफलहेतुर्भूर्मा ते सङ्गोऽस्त्वकर्मणि ।।

Translation: You have a right to "Karma" (actions) but never to any fruits thereof. You should never be motivated by the results of your actions, nor should there be any attachment of not performing your prescribed duties.

Bhagvat Gita
Chapter Two verse 47

"When you look at the stars and the galaxy,
you feel that you are not just from any particular piece of land,
but from the solar system."

–Late Dr Kalpana Chawla
NASA Astronaut
STS-87, STS-107

Table of Contents

Résumé i

Abstract iv

Acknowledgements vi

Table of contents xiii

List of figures xx

List of Symbols xxii

1 Introduction 1

1.1 From molecular clouds to stellar systems . . . 2

1.2 From planetesimals to planets . . . 3

1.3 Debris Disks . . . 5

1.3.1 Physics behind debris disk . . . 7

1.3.2 Debris disk architecture . . . 9

1.3.3 Detection of Debris disk with Infrared Spectroscopy and SED . . . 10

1.4 Observation of exoplanets . . . 11

1.4.1 Radial velocity method . . . 11

1.4.2 Transit method . . . 12

1.4.3 Microlensing . . . 13

1.4.4 Direct Imaging of exoplanets . . . 13

1.4.4.1 Adaptive optics . . . 14

1.4.4.2 Coronographs . . . 16
1.4.4.3 Speckle noise and suppression . . . 17
1.5 Imaging debris disk . . . 18
1.5.1 Thermal Imaging . . . 18
1.5.2 Scattered Light Imaging . . . 18
1.6 Motivation . . . 19
1.7 The course of this thesis . . . 21

2 Observation, data reduction and forward modelling 23

2.1 High-contrast observation with SPHERE . . . 23
2.1.1 Sub-system details . . . 24
2.1.1.1 IRDIS . . . 24
2.1.1.2 IFS . . . 25
2.1.1.3 ZIMPOL . . . 25
2.1.2 Consortium . . . 25
2.1.3 Procedure to obtain the sequence of a science observation . . . 26
2.2 Procedure of data reduction . . . 27
2.2.1 ADI imaging . . . 28
2.2.1.1 Classical ADI . . . 29
2.2.1.2 LOCI and TLOCI . . . 29
2.2.1.3 PCA-ADI . . . 30
2.2.2 DPI imaging . . . 32
2.3 Forward modeling of debris disk . . . 33
2.3.1 GRaTer . . . 35
2.3.1.1 Effect of α_{in} and α_{out} . . . 36
2.3.1.2 Effect of the scale height . . . 37
2.3.1.3 Effect of eccentricity . . . 38
2.3.1.4 Effect of anisotropic scattering factor and inclination . . . 39

3 The inclined bright debris disk HD 32297 **45**

3.1 Summary of the work . . . 46

3.1.1 Introduction . . . 46

3.1.2 Best Models and Photometry . . . 46

3.1.3 Grain Models . . . 47

3.1.4 Results . . . 49

3.2 Article on HD 32297 . . . 49

3.3 Supplements . . . 66

3.3.1 Histograms and selection of best-fit model . . . 66

3.3.2 Error measurement with fake disk . . . 66

3.3.3 Comparison with ALMA observation . . . 66

4 Test on other disks **71**

4.1 Debris disk around HD 141569 . . . 71

4.1.1 Observation and Data Reduction . . . 72

4.1.2 Morphology of the disk as observed in two epochs . . . 75

4.1.2.1 IRDIS images . . . 75

4.1.2.2 IFS images . . . 75

4.1.3 Modeling the ringlet R3 . . . 77

4.1.4 Photometry of the ringlet R3 . . . 81

4.1.5 Modeling the particle size distribution in the ringlet R3 . . . 87

4.1.6 Discussion and Conclusion . . . 88

4.1.7 Perspective and Outlook . . . 89

4.2 Preliminary study of HD 106906 . . . 90

4.2.1 Observation and Data Reduction . . . 90

4.2.2 Morphology of the debris disk and photometry of the planet . . . 93

4.2.3 Modeling the debris disk . . . 93

4.2.4 Photometry of the debris disk . . . 99

4.2.5 Modeling the particle size distribution in the debris disk . . . 99

4.2.6 Conclusion and Prospective . . . 104

5 Conclusion and Perspectives **107**

5.1 Conclusion . . . 107

5.2 Perspective . . . 109

5.2.1 Outlook on the characterization of morphological features . . . 109

5.2.2 Future Telescopes . . . 110

List of Figures

1.1 A schematic diagram of the different steps in the stellar and planetary system formation representing a) dense regions formation in molecular cloud, b) formation of a dense core, c) formation of protostellar environment, d) protoplanetary disk formation, e) debris disk formation and f) final planetary system. In f) the ellipses in black are representation of planetary orbits. This diagram is not to the scale. 4

1.2 A schematic SEDs profile depending on the object class is presented. The slope of the SEDs change from a positive to negative from Class I to Class III circumstellar disk stages, beyond 10 μm. This image is adapted from Perrot (2017). 4

1.3 A schematic diagram illustrating the "core accretion" (Left panel) and the "gravitational collapse" (Right panel) model, Credits: `https://www.nasa.gov/centers/goddard/images/content/96385main_i0319cw.jpg`. 6

1.4 On the left side, three possible types of orbits are shown. Depending on the value of beta experienced by the grain, either elliptical, hyperbolic or outward hyperbolic (anomalous hyperbolic) are followed. The image on the right hand side illustrates the elliptical orbits taken by the debris in the parent ring after the collision. Both the images are adapted from Krivov (2010). 8

1.5 This image shows a pictorial representation of five zones or belts of a debris disk detailed Su & Rieke (2014). The five zones are characterized by the temperature of the grains. This representation is based on the solar-system model. 9

1.6 The image shows SEDs modeled for different zones of debris disk by Hughes et al. (2018). The models are built around A0V stellar type and are adapted from SEDs of VEGA and β Pictoris. The dotted line represent the emission from the central star. The purple, blue, green, red, and black curves show the emission from the exozodis, the asteroid belts, the Kuiper belt, the halo and the total system (star+disk) respectively. 10

1.7 This image plot the mass (M_J) of exoplanets with respect to the semi major axis represented in AU. This data is collected from `http://exoplanet.eu` as of August, 2019. The solar system planets are over plotted for reference. 12

1.8 Top: A schematic diagram of an AO system as presented by Rigaut (2015). The correction of the distorted wavefront is performed in real time with the help of a wavefront sensor, a feedback loop and a deformable mirror. Bottom: An image created by distorted wavefront before AO correction (Left) and an image post AO correction (Right) showing the Airy pattern (Sauvage et al., 2016). 15

1.9 Top: The image is of the first coronagraph used by Lyot displayed in Observatoire de Meudon, France. Bottom: Schematic sketch of operation of Lyot coronagraph (Sivaramakrishnan et al., 2001). 16

1.10 Top:The image shows debris disk around Fomalhaut as observed by HST (a) Kalas et al., 2013), Herschel (b) Acke et al., 2012) and ALMA (c) MacGregor et al., 2017). The image in e) and f) show the debris disk around HR 4796 as observed in total intensity by Milli et al. (2017) and in polarimetry in Olofsson et al. (2016). North is up and East is left in all the images and the scale bar is 50 au for the top panel images. The disk is imaged in different wavelengths to see various structural features such as north-east south-west brightness asymmetry in (a), and brightness asymmetry between the two ansae in (b) and 1.3 mm thermal emission map in (c). 20

2.1 A top view of SPHERE bench with its sub-systems (IRDIS, IFS, ZIMPOL) and many opto-mechanical components labelled as seen in Beuzit et al. (2019) 24

2.2 A schematic representation of the ADI technique. Here the disk is in blue and diffraction from the telescopic optics and the stellar residual are seen in yellow. After subtraction of static speckle pattern (second column) from the science images (first column), each frames are re-rotated (fourth column) and averaged (last column) to obtain a speckle free image. 29

2.3 The section of interest (blue) and the section of optimisation (blue) representation for LOCI. The section of interest (blue) and the section of optimisation (red) representation for TLOCI as in Galicher et al. (2018) 30

2.4 a) and b) are the GRaTer images, using the geometrical parameters for $R_0 = 100$ au, h=0.04 and e=0. The FOV of these images are $3.675'' \times 3.675''$. The colorbar represent the brightness scale of both the images. c) and d) are the plots representing the density variation across the disk corresponding to images a) and b) and normalised to the maximum of the image intensities. 37

2.5 a) and b) are the GRaTer images, using the geometrical parameters $R_0 = 100$ au, $\alpha_{in} = 5$, $\alpha_{out} = -5$, $i = 89°$ and $e = 0$. The FOV of these images are $3.675'' \times 3.675''$. The colorbar represent the brightness scale of both the images. c) and d) are the plots representing the density variation across the disk corresponding to images a) and b) and normalised to the maximum of the image intensities. 38

2.6 a) and b) are the GRaTer images, using the geometrical parameters R_0=100 au, α_{in} = 5, α_{out} = −5. The FOV of these images are 3.675″ × 3.675″. The colorbars represent the brightness scale in the images. c) is the plot representing the density variation across the disk corresponding to images a) and normalised to the maximum of the image intensities. 40

2.7 GRaTer images including both geometrical and phase parameters to understand the affect of g in total intensity and polarimetry for an inclination i=40°. The FOV of these images is 3.675″ × 3.675″. The colorbar represent the brightness scale of all the images. 41

2.8 GRaTer images including both geometrical and phase parameters to understand the affect of g in total intensity and polarimetry for an inclination i=80°. The FOV of these images is 3.675″ × 3.675″. The colorbar represent the brightness scale of all the images. 42

2.9 Plot of phase functions for different values of g. The solid lines correspond to polarimetric phase function and the dashed line for the total intensity and the dotted sky blue line corresponds to the combination of 2 g parameters for total intensity. 43

3.1 The S/N map of the disk as observed in Asensio-Torres et al. (2016) in H band. c) is the S/N map of TLOCI reduced image and d) S/N map of the PCA reduced image. Both the images are in $[-5\sigma \times 5\sigma]$ linearly scale. The arrows point to potential gap at 0.75″ of north-east side and 0.65″ at south-west side of the disk. 46

3.2 The ALMA 1.3 mm continuum emission is overlaid as white contours as seen in MacGregor et al. (2018) over the HST STIS images as seen in Schneider et al. (2014) and on the bottom left corner of this image the beam size of ALMA is seen which is about 0.76″×0.41″. 47

3.3 Top to bottom: The TLOCI image with front and back side of the disk labelled, the KLIP image and the $Q_{\rm phi}$ polarimetric image. All the images are rotated to 90° - PA and cropped at 7″ × 1.3″. The TLOCI processed, KLIP processed and $Q_{\rm phi}$ images are scaled linearly between $[-1\times10^{-5}$,$1\times10^{-5}]$. 48

3.4 All the three images of Fig. 3.3 multiplied by the square of the radial scale. All the images are rotated to 90° - PA and cropped at 7″ × 1.3″. All the images are scaled linearly between [0.015,-0.025]. 48

3.5 Histograms of Total intensity models with 1 HG (Top) and 2 HG (Middle) parameter. Bottom: Polarimetric models with 1 HG parameter. Histograms are overlapped with Gaussian when significant 67

3.6 Top:KLIP image of fake-disk injected at 90 ° to the real disk. The model used for fake disk is i=88°, α_{out}=-6, α_{in}=2, R_0=140 au, g_1=0.70, g_2=-0.4, w_1=0.80, h=0.020, contrast = 0.0005. Bottom: Scaling factor retrieved for the fake-disk compared to its corresponding model 68

3.7 Total Intensity model with the parameters i=88°, α_{out}=-6, α_{in}=2, R_0=140 au, g_1=0.70, g_2=-0.4, w_1=0.80, h=0.020 convolved with a 2D Gaussian PSF of HWHM=0.37″. The dark stripes in the ADI processed model (Left) is an effect of ADI self-subtraction. Polarimetric model with parameters i=88.5°, $R_0 = 125au$, α_{in}= 10.0, α_{out}=-4.0, g=0.8, h=0.020 convolved with a 2D Gaussian PSF of HWHM=0.37″. 69

4.1 The two images correspond to the Fig. B.1 (Leftmost) and B.2 (Top-Left) from Perrot et al. (2016) respectively. The image on the left shows a bigger FOV with the outer ring, inner ring and associated features. The image on the right shows the IFS FOV with the ring R3 and the clump. 73

4.2 On the top row the median image of epoch 1 IRDIS-H2H3 reduced with KLIP-3 (Left) and TLOCI (Right) is shown. Similarly, on the bottom row the IRDIS-K1 image of epoch 1 reduced with KLIP-3 (Left) and TLOCI (Right) is shown. The features are labelled. The colorbar represents the intensity scale (in arbitrary units) for all images. All the three images are of the FOV 4.97″ × 5.85″ and smoothed to Gaussian kernel of radius of 5 pixels. 76

4.3 Contrast curves extracted with SpeCal for PCA 3 modes reduction of the epoch 1 (in blue) and epoch 2 (in red) images presented in Fig. 4.2. 77

4.4 Column 1 and Column 2 show the epoch 1 and epoch 2 median image of KLIP reduced IFS observation, duplicate image of the top panel overplotted with the two ringlets R2 (blue) and R3(green) and the epoch 1 (median image of H2H3 band) and epoch 2 (image of K1 band) of KLIP reduced IRDIS observation overplotted with R2 (blue) and R3 (green). The colorbar represents the intensity scale (in arbitrary units) in all the images. The IFS images are cropped to 1.71″ × 1.33″. The IRDIS image are cropped to 1.64″ × 1.25″. All the images are smoothed to a Gaussian kernel of radius of 3 pixels. 78

4.5 Histograms representing the 1% of reduced best-fit model for each parameter. Gaussians are overplotted for the histogram corresponding to the inclination and α_{in} parameters. The 80

4.6 From Left to right: The images show the epoch1 masked KLIP processed data, the KLIP processed data without the mask, the scaled best-fit model and the residuals map. The green ellipse drawn shows the innermost ringlet R3. The FOV is 0.7″ × 0.98″ for all the images and smoothed to Gaussian kernel of radius of 2 pixels. Colorbar represents the intensity scale (in arbitrary units) for all the images. 81

4.7 On left is the image representing the de-projected KLIP 3 modes reduced IRDIS H2 data. On right is the image representing the de-projected KLIP reduced best-fit model. The colorbar represent the intensity of both the images in arbitrary units. The image is cropped to 2″ × 1.36″ and smoothed to a Gaussian kernel of 2 pixels 82

4.8 Surface brightness profiles corresponding to northern part (red) of the disk and southern part (blue) of the disk in H2,H3, K1 and K2 band of IRDIS. 84

4.9 The figure represents spectral reflectance corresponding to the northern and southern part of the ringlet R3 in both epochs. 85

4.10 The figure represents spectral reflectance plot corresponding to the clump and the southern part of the ringlet R3 masking out the clump in both the epochs. 85

4.11 The figure (top) shows the three circular masks on the de-projected data where the red circular region is the clump and the pink dotted circular region encompasses the left and the right regions on each side of the clump.The figure (below) depicts the spectral reflectance at the clump and at circular masks adjacent to the clump (on each side) in both epochs. The dotted lines are the error-bars corresponding to the two other apertures other than that of the clump. 86

4.12 Fitted synthetic spectra to the reflectance spectrum of epoch2. The dotted line represents the best-fit spectra with s_{min} = 0.30 μm and κ = -3.00 and the dashed line represent the spectra for fiducial case where $s_{min} = s_{blow}$ and κ = -3.5. 88

4.13 Debris disk around HD 106906 AB from Kalas et al. (2015) (Left) and an arrow pointing to the planet HD 106906 AB b at 7″ as seen in Lagrange et al. (2016) (Right). In both the images, north is up and east is left. 90

4.14 The topmost image is the KLIP-5 science image of HD 106906 as observed by IRDIS BB_H. The image in the middle row is the IFS median image of the debris disk and the polarimetric Q_ϕ image of the disk smoothed to a Gaussian kernel of radius of 2 pixel is in the third row. 94

4.15 The disk and the thirteen point-sources encircled in green within the IRDIS FOV is presented in the top row. The white arrow indicates the already known planet. In the bottom row a plot of the contrast of the planet in IRDIS BB_H filter is presented. 95

4.16 The histograms of total intensity models and polarimetric models are presented in the bottom two and top two rows respectively. Histograms are overlapped with Gaussian functions unless the distribution is continuously increasing or decreasing. 100

4.17 Left image from top to bottom presents the KLIP 5 IRDIS BB_H image, the total intensity best-fit model convolved with the instrumental PSF, the corresponding reduced best-fit model and the residual. The science image, reduced best-fit model and the residual image are scaled linearly between $[-1 \times 10^{-5}, 1 \times 10^{-5}]$ and the best-fit model convolved with the instrumental PSF is scaled linearly between [0.0,0.5].image from top to bottom presents the Q_{phi} image, the polarimetric best-fit model convolved with the instrumental PSF and the residual. All the three images are scaled linearly between $[-4 \times 10^{-7}, 4 \times 10^{-7}]$. All the images are rotated to 90°-PA and cropped to 2.85″ × 0.5″. 101

4.18 The surface brightness profile in total intensity (Left) in BB_H filter and polarimetry (Right) in BB_J filter. 101

4.19 The spectral reflectance plot with a positive slope of 0.0012 contrast/arcsec^2 in NIR YJH bands 102

4.20 Best fits of the reflectance spectrum obtained for a fiducial case with $s_{min} = s_{blow}$ and $\kappa = -3.5$ (left), and for best-fit when s_{min} and κ are free parameters (right). 103

List of Symbols

F_λ	Flux distribution in SED
λ	Wavelength
D	Diameter of the focal plane of telescope
$\vec{F}_g$	Stellar gravitational force
$\vec{F}_{\rm rad}$	Radiation pressure
$\vec{F}_{\rm drag}$	Drag force
G	Gravitational constant
m	Mass of grains in debris disk
M_*	Mass of a central star
$M_\oplus$	Mass of the Earth
r	Radial distance in disk coordinates
$\vec{e_r}$	Radial unit vector
β	The ratio between the radiation pressure and the gravitational force
$\vec{F}_{\rm pg}$	Photogravitational force
e	Orbital eccentricity
ρ	Bulk density of grains
s	Grain size in debris disk
$s_{\rm blow}$	Blowout size of the grains in debris disk
dn	Particle size distribution of the grains in debris disk
κ	Power law index of particle size distribution
$f_{\rm IR}$	Fractional luminosity of the disk
L_*	Stellar luminosity
$L_{\rm IR}$	Disk's luminosity
$T_{\rm d}$	Disk temperature
$\mathcal{I}$	Master cube of science images observed with SPHERE
$\mathcal{A}$	Image of static speckle pattern
$\mathcal{I}_{\rm ADI}$	Image after speckle pattern is subtracted from science image
Θ	Parallactic angle
i, j	Spatial axis of the master cube
l	Index of temporal axis
$\mathcal{I}_{\rm f}$	Final image after speckle correction, re-rotation and averaged
$\mathcal{N}$	Total number of angular frames
n	Sections of image used for post-processing with LOCI technique
ϱ_l	Area of the sections n
lw	Index or temporal axis in the sections n
$\mathcal{I}'$	Speckle pattern calculated using LOCI or TLOCI techniques in different sections of the science image
c_{lw}	Coefficients computed by LOCI
b	combination of the spatial axis i, j
$\mathcal{I}_{\rm norm}$	Normalized science images

σ	Standard deviation of an image
v	Eigen vectors calculated during KLIP technique
PC	Principle components calculated during KLIP technique
T	Transpose of a vector
I, Q, U, V	Stokes vectors
Q^+, U^+, Q^-, U^-	Modulated set of images representing the Stokes vector
$I_L^0, I_L^{22.5}, I_L^{45}, I_L^{67.5}$	Images obtained in the left channel in four polarisation angle
$I_R^0, I_R^{22.5}, I_R^{45}, I_R^{67.5}$	Images obtained in the right channel in four polarisation angle
ϕ	Azimuthal angle with respect to center of the star
$Q_{\rm phi}, U_{\rm phi}$	Azimuthal stokes vector
ν	Degree of freedom in χ^2 calculation
$S_{i,j}$	Science image
$M_{i,j}$	Reduced model
$N_{\rm data}$	Total number of pixels in the region of interest where χ^2 is calculated
$N_{\rm params}$	Number of parameters used to create a GraTer model
a	Scaling factor between two arrays
$\mathcal{G}$	Distribution function in GRaTer
H	Scattering phase function
$\rho_{\mathcal{G}}$	Density distribution function in GRaTer
z	Distance to the midplane
g	Anisotropic scattering function
θ	Scattering angle
ρ_0	Density on the midplane
R_0	Distance where the density of the parent ring peaks
γ	Power law of the exponential function in the density distribution
β_f	Radial flaring index of a disk
ζ_0	Vertical thickness of the disk at different radial distance
h	Scale height of a disk
$\alpha_{\rm in}, \alpha_{\rm out}$	Positive and negative power law indices of the radial distribution
f_{TI}	Henyey Greenstein phase function
i	Inclination of the disk
x_d, y_d, z_d	The disk coordinates
θ_*	The angle between x_d and y_d axes
f_P	Polarised phase function
P	Porosity of grains in debris disk

CHAPTER 1

Introduction

1.1 From molecular clouds to stellar systems 2
1.2 From planetesimals to planets 3
1.3 Debris Disks 5
1.3.1 Physics behind debris disk 7
1.3.2 Debris disk architecture 9
1.3.3 Detection of Debris disk with Infrared Spectroscopy and SED . . 10
1.4 Observation of exoplanets 11
1.4.1 Radial velocity method 11
1.4.2 Transit method 12
1.4.3 Microlensing 13
1.4.4 Direct Imaging of exoplanets 13
1.5 Imaging debris disk 18
1.5.1 Thermal Imaging 18
1.5.2 Scattered Light Imaging 18
1.6 Motivation 19
1.7 The course of this thesis 21

Looking up at the night sky, we see millions of twinkling stars with naked eyes. In reality, there are billions of such stars in the universe. These are classified according to their properties such as stellar luminosity, surface temperature, age, mass, and size. Because of such diversity astronomers look for and study various types of stars to understand stellar evolution. In January 1983, the Infrared Astronomical Satellite (IRAS) was launched to survey the sky in far-infrared wavelengths. The first task of this satellite was to calibrate the detectors which had to be done by observing a few bright stars whose properties were thought to be well understood at that time. One such star observed was Vega, which is an A0 type star in the Lyra constellation. The blackbody spectrum of the star can be used to calculate the temperature of the star and Vega was often taken as a point of reference for astronomical objects to be scaled in magnitude. Therefore, Vega was one of the primary targets of IRAS. As soon as the spectrum of the star was generated, it was seen that there was an excess response at long wavelengths. This was a perplexing result and immediate

measurements of multiple such stars were obtained. It was soon realized that there was no instrumental issue with IRAS but this excess emission was from a cold dust-gas region at a distance of several astronomical units away from the stars. These emissions were from the circumstellar disks around their respective central stars.

The infrared excess emission of Vega opened a new class of study dedicated in the search of stellar systems or exosystems with a circumstellar disk around their central star. While on this quest, many stellar systems have been discovered which has helped our understanding of the formation and existence of our solar system. The solar system itself is an outcome of star and planet formation. To be precise, it is the final stage of the circumstellar disk to planet evolution. This thesis focuses on one of the intermediate steps between star to planet formation and that is the debris disk stage. This class of disk is the last stage of a circumstellar disk and a precursor of solar system. Observing such disks and possible planets within such systems can not only open gateways to finding life signatures but also tell more about the past of solar system. Thus, current and future telescopes are going leaps and bounds to detect debris disks where planet-forming signatures or an Earth-like exoplanet can be found.

1.1 From molecular clouds to stellar systems

Young stellar environments are formed within the cold and dense regions of the interstellar medium (ISM) known as molecular clouds. The schematic illustration of the stellar system evolution process is given in Fig. 1.1. Molecular clouds are made up of gas-dust mixture and are gravitationally unstable. The primary constituent (∼90%) of these clouds is molecular hydrogen (Krumholz, 2011). However, over 150 types of chemical constituents, including He and CO have been detected in their gaseous form in the molecular clouds. The dust present in these clouds is stellar remnants mostly consisting of silicates and carbonaceous sub-micron grains. At this stage, the cloud is optically thin with regions of density of 10^4-10^6 cm^{-3} (Fig. 1.1(a)) and temperature ∼10 K. In a few thousands of years, the density in these regions increases under the influence of gravitational collapse overpowering the gas pressure and the magnetic forces. This forms a "Class 0" stage with an optically thick core inside an envelope as seen in Fig. 1.1(b). The source of such dense cores is undetectable between the visible and mid-infrared (mid-IR) wavelengths because of the optical thickness and the low temperature (Hueso & Guillot, 2005; Yorke et al., 1993).

The accretion of the dense core starts to form the central protostar. The protostellar system is fed by the overlying envelope making this envelope thinner compared to that of its Class 0 counterpart. The high angular momentum of the dense core is vastly transported in forming a circumstellar disk surrounding the protostar. The transport of the angular momentum of the system is balanced by powerful out driven bipolar jets. The protostar, the surrounding disk, the remaining envelope, and the bipolar jets together form the "Class I" stage of the stellar system evolution (Fig. 1.1(c)).As gas and dust are transported inward through the disk onto the protostar, massive amounts of materials are ejected out of these lobes at a velocity of several hundreds of kilometers per second (Ollivier et al., 2009).The excess emission from the disk can be detected in the spectral energy distribution (SED)

over the black body curve followed by the protostar. SED describes the distribution of the energy in terms of λF_λ of a system as a function of wavelength. The power-law slope of the SED of Class I objects is positive (Armitage, 2019) compared to a pure star that follows Rayleigh-Jeans law as seen in Fig.1.2. The Class I stage remains for $\sim 10^5$ years.

The envelope around the protostar of Class I stage completely dissipates slowing down the accretion rate of the young stellar system. At this stage, the power-law slope of the SED becomes negative as seen in Fig.1.2. However, it still has a significant excess above the Rayleigh-Jeans curve followed by the central star and is classified as "Class II" (Fig. 1.1(d)). Class II lasts up to a few million years. The disk around the central star is known as the protoplanetary disk as seen in Fig. 1.1(d). The material within the protoplanetary disk continues to fuel the stellar accretion and the outflow. However, simultaneously, the dust grains and gas start processing to form planetesimals and protoplanets.

The process of protoplanet formation accretes the gas present in the protoplanetary disk and leaves behind the protoplanets and the debris of planetesimals. This leads to a "Class III" phase (Fig. 1.1(e)) where the power-law slope of the SED is steeper than the Class II phase but still has some amount of excess (Fig.1.2). The optically thin disk around the star is known as the debris disk. As planet cores and giant planets are expected to have already formed in this stage, they continuously collide and form smaller grains that survive in a debris disk. So this type of disk is not the leftover of a protoplanetary disk, rather they are the leftover of already formed planets (Hughes et al., 2018; Kral et al., 2016). With time, the disk loses its mass due to the formation and evolution of a planetary system as shown in Fig. 1.1(f). Evidence suggests that the Kuiper belt in our solar system is the remnant of a massive debris disk. Following this analogy, a stellar system with a debris disk can be considered as an immediate precursor of our star-planet system. This thesis concerns the study of debris disks formed around Class III objects. Details on the fundamentals of debris disk formation, their architectures and the physical processes involved are described in Sect. 1.3.

1.2 From planetesimals to planets

A sufficient amount of sub-micron dust and gas from the ISM is sustained during the evolution of circumstellar disks. Though there exist several theoretical models of explaining the evolution of planets, it is generally accepted that young planets are formed during the protoplanetary disk phase. Below, I briefly explain the two most established theories: core-accretion and gravitational instability.

- *Core-accretion* (Pollack et al., 1996; Rice et al., 2003): The sub-micron sized dust grains stick together to form centimeter-sized particles. Increasing size of grains force them in settling towards the disk mid-plane (Blum & Wurm, 2008; Dullemond & Dominik, 2008; Zsom et al., 2010). Goldreich & Ward (1973) proposed that the kilometer-sized planetesimals are formed when the clumps of meter-sized particles directly collide with each other. This stage can be of complex dynamics as there can be elastic collision (Booth et al., 2018), radial drifts of metric particles towards

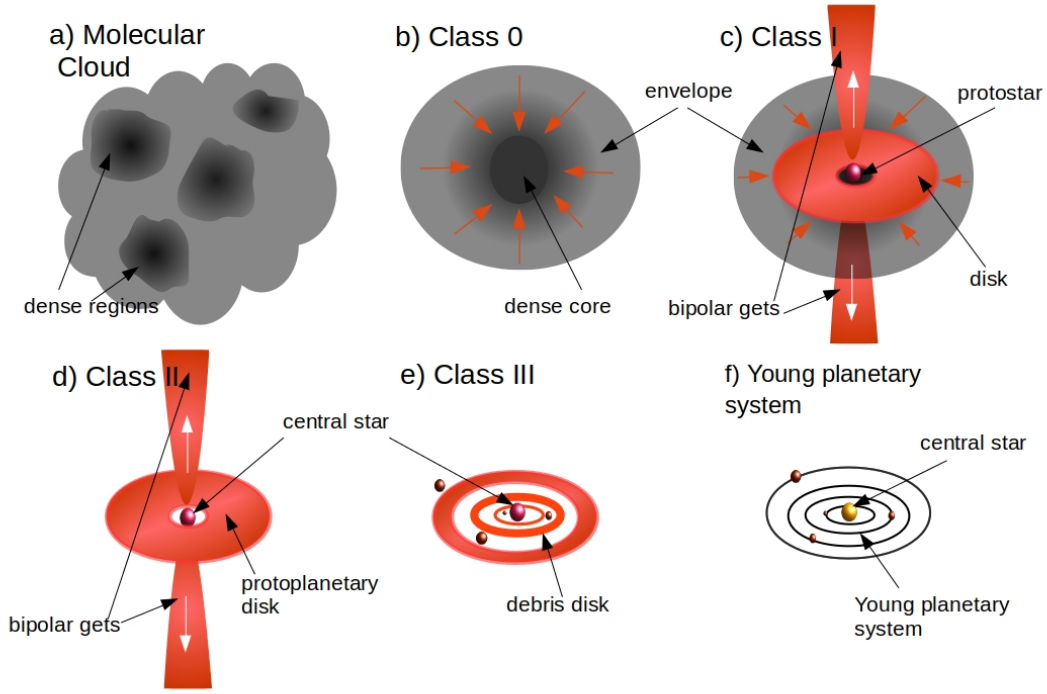

Figure 1.1 *– A schematic diagram of the different steps in the stellar and planetary system formation representing a) dense regions formation in molecular cloud, b) formation of a dense core, c) formation of protostellar environment, d) protoplanetary disk formation, e) debris disk formation and f) final planetary system. In f) the ellipses in black are representation of planetary orbits. This diagram is not to the scale.*

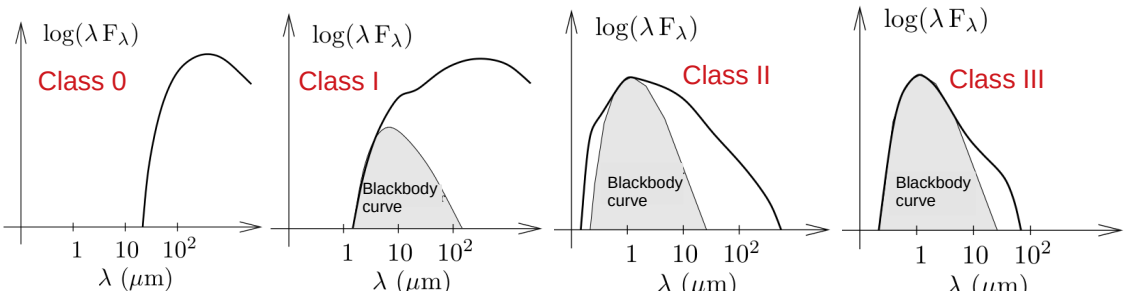

Figure 1.2 *– A schematic SEDs profile depending on the object class is presented. The slope of the SEDs change from a positive to negative from Class I to Class III circumstellar disk stages, beyond 10 μm. This image is adapted from Perrot (2017).*

the star (Laibe et al., 2012) and/or fragmentation of these particles during collisions instead of coagulation (Gonzalez et al., 2017). The planetesimals, under the gravitational influence, grow to form terrestrial planets or massive planetary cores for gaseous planets at outer orbits. Once these planetary cores have become sufficiently massive (10-20 $M_{\oplus}$), they accrete gas from the disk to form giant planets.

The limitation of this model is the timescale of the planet formation. Protoplanetary disks generally survive up to 5 Myr whereas, the core accretion process creating giant planets would require ∼10 Myr. The timescale of planet formation can be reduced by planetary migration. Evidence of planets younger than 10 Myr has already been found (e.g. PDS70b, Keppler et al., 2018). Under the influence of the negative torque produced by the gas, a planet would move inward. This process would lead to an accretion of a higher amount of gas and dust by the planet in much shorter timescale (Alibert et al., 2005).

- *Gravitational instability* (Boss, 2002; Cameron, 1978): This model is a "top down" route for planet formation in protoplanetary disks. According to *gravitational instability*, in massive and cold protoplanetary disks, dense gaseous regions are formed and they collapse under the influence of self-gravity. This collapse continues and forms a self-gravitating gas giant. The core of the planet is formed after the collapse, by the coagulation of dust from the disk carving out wide gaps. The planet formation in this process takes 1 Myr which is less than the core accretion model. Additionally, more distant planets can be formed by gravitational instability as compared to the core-accretion model where the planet formation is limited to 10-30 au. However, the limitation of this model is having a cold and massive protoplanetary disk as a prerequisite.

Figure 1.3 show a schematic diagram of the possible steps involved in core-accretion and gravitational instability models. These two models are widely accepted theories of planetary evolution in the scientific community. With more and more observational data, planet formation theories are evolving. Studying circumstellar environments is helping us constrain the stellar system evolution and planet formation theories. As debris disks are considered to be the evolved form of circumstellar disks where planet formation has already started, studying these disks can provide important clues about planet-disk-interactions in stellar environments. In the next section, details regarding the physical processes, architecture, and detection techniques using SED of such disks are provided.

1.3 Debris Disks

About 20 % of nearby main sequence stars have debris disk around them. As defined in Sect.1.1, these disks are the type of circumstellar disk which reaches "Class III" phase after planetesimals and giant planets have already been formed and believed to have accreated most of the gas in the system. The planetesimals continuously collide to form small grains and these small grains collide amongst each other to form sub-micron grain. This process of continuous grinding of grains in a thin belt is known as collisional cascade(Hughes et al., 2018). Debris disks are reservoirs of varied sized grains which depending on the size emit at different wavelengths (Sect. 1.3.2). Since these grains are mostly produced by secondary

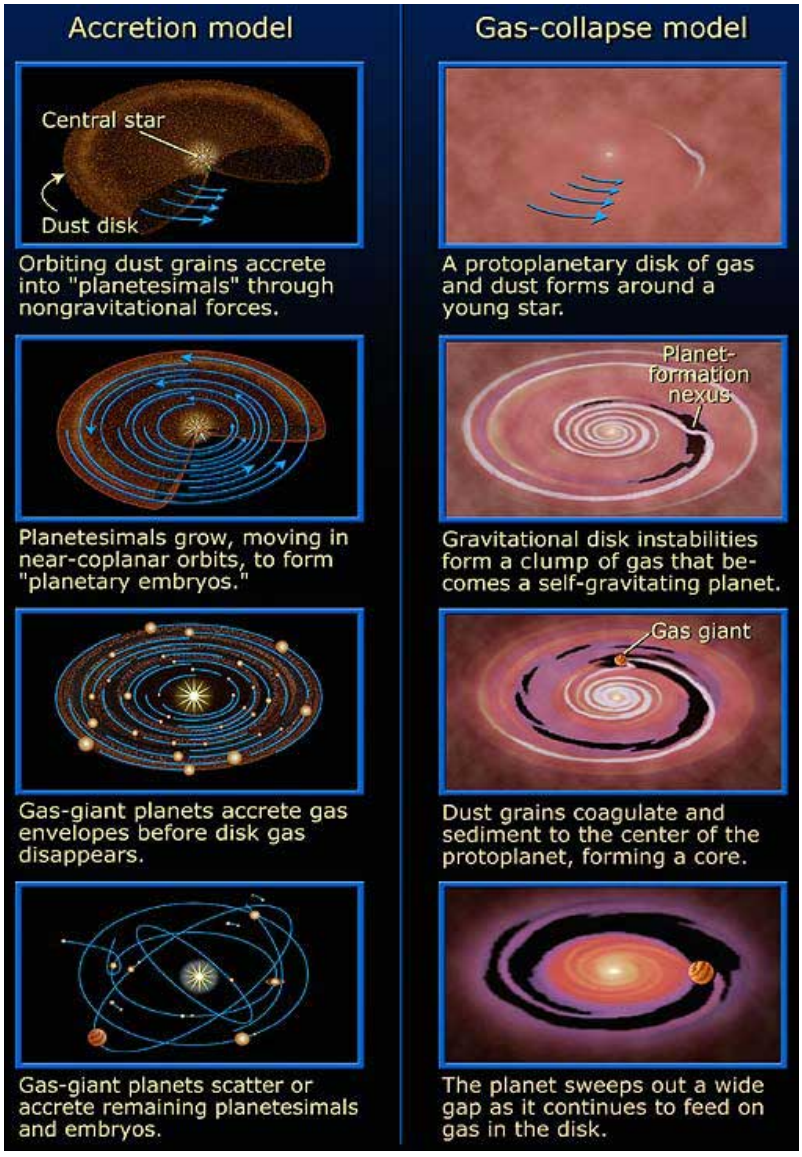

Figure 1.3 *– A schematic diagram illustrating the "core accretion" (Left panel) and the "gravitational collapse" (Right panel) model, Credits:* https://www.nasa.gov/centers/goddard/images/content/96385main_i0319cw.jpg.

processes the disk itself is called a secondary disk. The primary forces which act on such grains within a debris disk are the gravity of the central star $\vec{F}_{\rm g}$, the radiation pressure from the central star $\vec{F}_{\rm rad}$ and the drag forces $\vec{F}_{\rm drag}$. The effects of these forces are detailed in Sect. 1.3.1.

Apart from the presence of different types of dust grains in debris disks, recent observations by Atacama Large Millimeter Array (ALMA) have shown that a significant amount of gas is present in these disks (Kral et al., 2018; Moór et al., 2017). These observations contradict our previous understanding of debris disks that were known to have a much lower gas to dust ratio. This gas tends to affect the drag forces experienced by the grains which are discussed in Sect. 1.3.1.

1.3.1 Physics behind debris disk

The radiation pressure ($\vec{F}_{\rm rad}$) of the central star exerts an outward force that is responsible for blowing smaller grains out of the system (Burns et al., 1979). The net force of radiation pressure and stellar gravity ($\vec{F}_{\rm g}$) experienced by the grains is known as the "photogravitational" force. This is given by $\vec{F}_{pg}$ as detailed in Krivov (2010).

$$\vec{F}_{\rm pg} = \vec{F}_{\rm g} + \vec{F}_{\rm rad} = -\frac{GmM_*(1-\beta)}{r^2}\vec{e_r}, \tag{1.1}$$

where G is the gravitational constant, m is the mass of the grain located at distance r from a central star of mass $M_\star$, $\vec{e_r}$ is the radial unit vector and β is the ratio between the radiation pressure and gravitational force such that $\beta = \left|\vec{F}_{\rm rad}/\vec{F}_{\rm g}\right|$. β is inversely proportional to the grain size s and the grains bulk density ρ. This parameter classifies the orbits assumed by the dust grains. When $0 \leq \beta < 0.5$, the grains follow a circular ($\beta = 0$) or elliptical orbit ($0 < \beta < 0.5$) and are "bound" to the system. If $0 < \beta < 0.5$, the grains follow eccentricity orbit where the eccentricity is given by $e = \dfrac{\beta}{1-\beta}$. When $\beta = 0.5$, the "blowout size" $s_{\rm blow}$ limit is set, which is the minimum size needed for a grain to be able to stay bound to the system. If $0.5 < \beta < 1$, the grains become "unbound" and are blown out of the system following either a parabolic ($\beta = 0.5$) or a hyperbolic ($\beta > 0.5$) orbit. Finally, for $\beta > 1.0$ the gravitational force is overwhelmed by the radiation pressure. As a result, such grains follow a non-Keplerian trajectory defined by "anomalous hyperbola" which moves the grains outward from the release point. Figure 1.4 (Left) illustrates the cases of β with different values and the corresponding orbital trajectory followed by the grains. When β is within the range of 0.0-0.5, the grains are segregated according to their sizes in different orbits. Since β is inversely proportional to the grain size s, a higher value of β corresponds to smaller grains and because the effect of radiation pressure is stronger on smaller grains, such grains tend to move to a larger orbit. Figure 1.4 (Right) shows that the size of the orbit increases with an increasing value of β within the range of 0.0-0.5.

The particle size distribution is often described $dn(s) \propto s^{\kappa} ds$ where κ is the power-law index. For the debris disk to be stable, there exist a balance between the grain loss due to radiation pressure and an increase in the production of such grains by a collisional

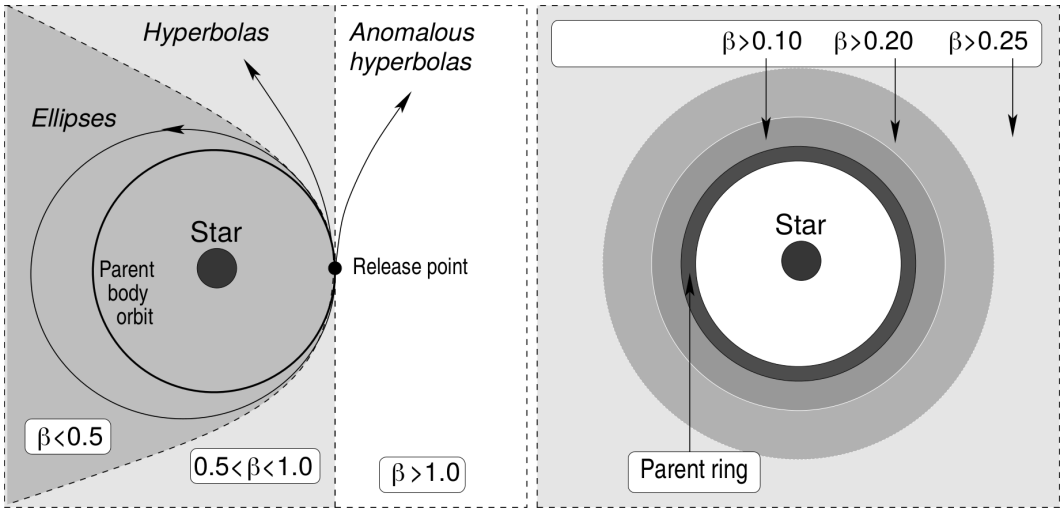

Figure 1.4 *– On the left side, three possible types of orbits are shown. Depending on the value of beta experienced by the grain, either elliptical, hyperbolic or outward hyperbolic (anomalous hyperbolic) are followed. The image on the right hand side illustrates the elliptical orbits taken by the debris in the parent ring after the collision. Both the images are adapted from Krivov (2010).*

cascade. This state is known as the "quasi-steady state" where the power-law index is -3.5 Dohnanyi (1969) for the particle size distribution within the debris disk. Most current models identify κ to be in between -3.0 to -4.0.

The drag forces, in general, tend to affect the grains in a way such that they move inward within the system. In the context of a debris disk, these forces include Poynting-Robertson (PR) effect and gas drag. The PR effect is caused due to an orthoradial component of the stellar radiation pressure (Kral et al., 2016). As a result, this force acts opposite to the radiation pressure and millimeter-sized grains spiral towards the central star. Wyatt (2005b) described that under the effect of grain-grain collision in case of massive debris disks, millimeter-sized grains would break into much smaller pieces before migrating further in towards the star. Consequently, the effect of PR drag is very small for most observed debris disks. Another drag force that plays an important role is the Epstein force (Takeuchi & Artymowicz, 2001). This effect is due to the presence of gas in the disk. Some theories predict that the gas present in these systems can interact with the grains and affect the morphology of the disk when the gas-to-dust ratio is close to unity. For example, Lyra & Kuchner (2013) discussed the formation of gaps in the presence of gas when the gas-to-dust ratio is close to unity without taking into account the formation of planets. The presence of gas can also explain the presence of small grains below the blowout size in the disk (Bhowmik et al., 2019).

Other forces, such as the magnetic fields creating clumps (Rieke et al., 2016; Su et al., 2016), sublimation of larger grains while undergoing PR drag (e.g. Kobayashi et al., 2009), eccentric planet perturbing the disk's eccentricity (Wyatt et al., 1999), etc can influence the disk's chemistry and geometry.

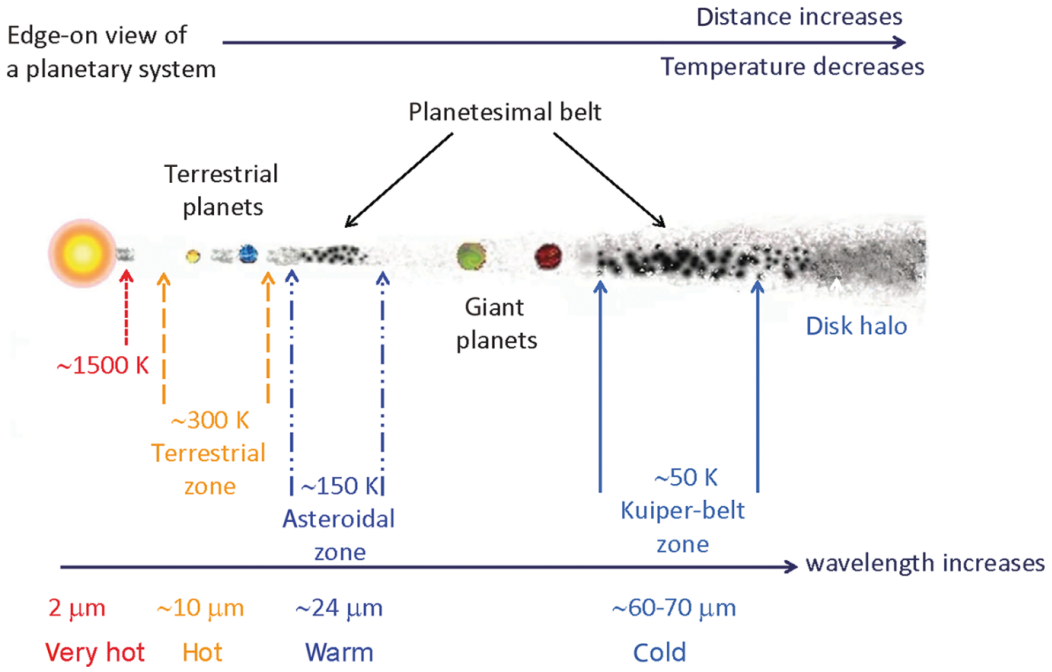

Figure 1.5 *– This image shows a pictorial representation of five zones or belts of a debris disk detailed Su & Rieke (2014). The five zones are characterized by the temperature of the grains. This representation is based on the solar-system model.*

1.3.2 Debris disk architecture

New development in the field of debris disk theory and observation has led to constrain the architecture of such disks. Debris disks are often comprised of multiple belts (Kennedy & Wyatt, 2014). Based on the solar system model, five zones of debris disk has been proposed by Su & Rieke (2014) as seen in Fig. 1.5. The classification of different zones is based on the temperature of the grains present in that particular zone. The most easily observable part of the disk is the outer part which has dense cold grains with $\sim$ 50 K temperature. The dust grains mostly emit in the far-IR wavelengths. This is analogous to a massive form of "Kuiper belt" of our solar system (Carpenter et al., 2009). The dust mass is expected to be between $10^0 - 10^3$ $M_\oplus$. Many disks consist of a warm component (100-200 K Ballering et al., 2013; Moór et al., 2009; Morales et al., 2012) comparable to the present asteroid belt of our solar system. The dust grains in the warm belt emit at mid-IR wavelengths. The mass of such disk is estimated by Krivov (2010) to be in between $10^{-8} - 10^{-6}$ $M_\oplus$. Broadly, it can be said that multiple parent belts can be present in a debris disk which consists of the warm and cold component. Beyond the Kuiper-belt zone there is expected to be a disk halo of smaller dust grains (e.g. Schneider et al., 2014).

The terrestrial zone which is populated with larger grains is at a closer separation from the central star. This zone on closer inspection can probe certain features associated with rocky planet formation, such as grain crystallization and/or Moon-forming impact (Lisse

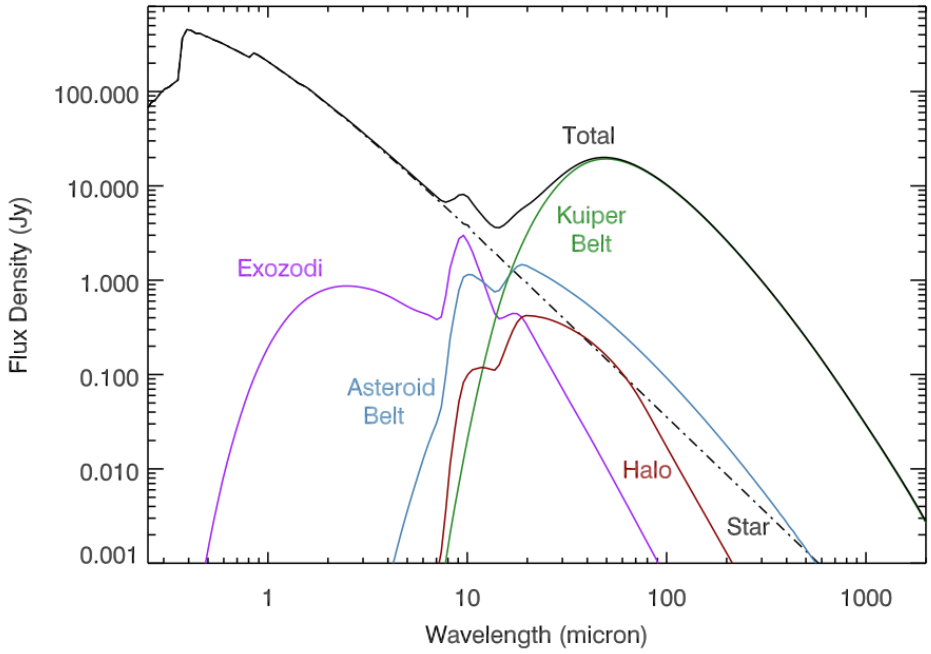

Figure 1.6 *– The image shows SEDs modeled for different zones of debris disk by Hughes et al. (2018). The models are built around A0V stellar type and are adapted from SEDs of VEGA and β Pictoris. The dotted line represent the emission from the central star. The purple, blue, green, red, and black curves show the emission from the exozodis, the asteroid belts, the Kuiper belt, the halo and the total system (star+disk) respectively.*

et al., 2009; Mittal et al., 2015). At a very close distance of 1 au, exozodiacal dust or sometimes referred to as "exozodis" of temperature ∼1500K have been detected.

This scheme is largely inspired by the solar system model. However, observations of exoplanets have taught us that the solar system model might not be an ideal paradigm to describe all debris disks. Therefore, further observations of different types of debris disks would constrain our understanding of the grain distribution within debris disks and their architectures.

1.3.3 Detection of Debris disk with Infrared Spectroscopy and SED

Historically, the most immediate way of detecting a debris disk is to obtain its SED. The dust grains in the disks are heated by the stellar radiation, which emit to show an IR excess mostly in 10-170 μm. The debris disk around Vega was the first disk detected by the IR excess using IRAS (Infrared Astronomical Satellite, Aumann et al., 1984). Over 500 nearby debris disks are observed by Spitzer Space Telescope, ISO (Infrared Space Observatory) and Herschel (Chen et al., 2019). The most important physical parameter obtained from these observations is the fractional luminosity of the disk given by $f_{\rm IR} = L_{\rm IR}/L_*$, where, $L_{\rm IR}$ and L_* are the disk and stellar luminosity respectively. Here, the disk luminosity can

either be calculated by integrating the disk flux from the SED or the maximum of the flux and the corresponding wavelength in the SED (Wyatt, 2008). The temperature of the grains in the disk can also be calculated using Wien's displacement law.

Some SEDs studied by Morales et al. (2011) showed a bimodal distribution of temperature (a cold $T_d \sim 50$ K and warm dust component $T_d \sim 200$ K) which can be explained by multiple zones or belts in the debris disk. In Vega (Absil et al., 2006) and τ Ceti (even warmer, di Folco et al., 2007) exozodiacal dust has been inferred from the SED. SEDs modeled by Hughes et al. (2018) for multiple belts in a debris disk is illustrated in Fig. 1.6. The illustrated SED is adapted from the models of Vega and β Pictoris debris disk. The model is built for an A0V star, 7.7 pc away with a total integrated luminosity of 1.4×10^{-3}.

Apart from the calculation of fractional luminosity and disk temperature, features associated with terrestrial events can also be inferred. Silicate features at 10μm can be extracted which can be indicative of grain growth and crystallization (e.g. Bouwman et al., 2001). In a few other cases, spectral features such as Fe-rich sulfides feature, water ice feature, etc, are also detected (e.g. Lisse et al., 2007).

Current observations of debris disks are continuously changing and challenging the known theories of debris disks. For example, the presence of massive amounts of gas led us to integrate a gas drag in the influential forces experienced by grains within a debris disk. Also, the detection of giant planets at a very close distance from the star made us realize that the solar system model for debris disk architecture might be a special case and not a general representation. The most recent developments in theories of debris disks have come from the detection and resolving of exoplanets. As a result, exoplanet and debris disk studies have become complementary to each other. Hence, in the upcoming sections, I am briefly explaining a few techniques to observe exoplanets and debris disks.

1.4 Observation of exoplanets

An exoplanet is a planet that orbits a star other than our Sun. Over the past two decades, several thousands of exoplanets were detected by different techniques. The most commonly known methods are radial velocity, transits, microlensing, and direct imaging. As of 30^{th} of August 2019, we have confirmed the detection of 4,110 exoplanets by the existing techniques described below. Apart from these confirmed discoveries, about 2,500 planet candidates are yet to be confirmed. The plotted data in Fig. 1.7 shows the distribution of exoplanets detected by various indirect and direct methods in terms of mass and semi-major axis, which are briefly explained below.

1.4.1 Radial velocity method

One of the oldest methods to detect exoplanets is by identifying a Doppler shift in the stellar spectrum due to the gravitational pull of the planet. When a planet with significant mass orbits its star, the star acquires a periodic motion and rotates about the center of

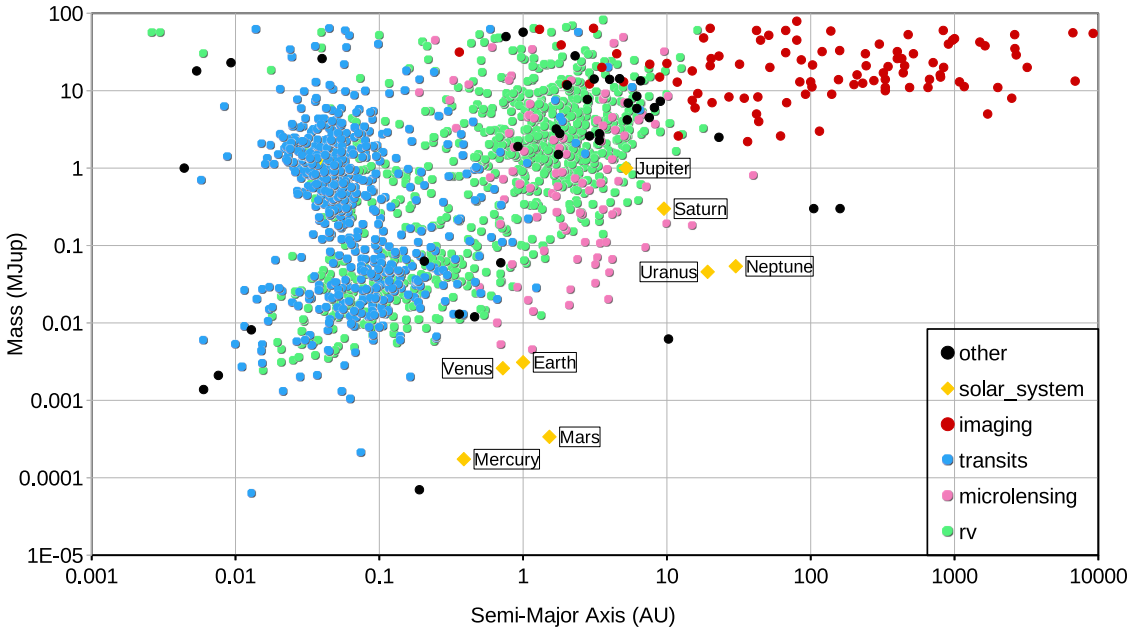

Figure 1.7 – *This image plot the mass (M_J) of exoplanets with respect to the semi major axis represented in AU. This data is collected from* `http://exoplanet.eu` *as of August, 2019. The solar system planets are over plotted for reference.*

mass of the system. By monitoring the perturbation in the radial velocity of the star, the minimum mass, eccentricity and the orbital period of the planet can be calculated. This calculation is possible only when Keplerian orbits are assumed. However, this technique is most sensitive to planets with a small orbital period in between 0-5 au (peaking at 1 au) and, like "Hot Jupiters" (masses greater than 100 $M_\oplus$) and "super-Earths" (3-30 $M_\oplus$), as seen in Fig. 1.7. A limitation of this technique is the underestimation of the planetary mass when the orbital plane of the planet is not aligned to the line of sight of the observer.

1.4.2 Transit method

In this technique, the dimming of starlight is observed when a planet passes in front of its star. To successfully find a planet using transit, the orbital plane of a planet should be aligned with the line of sight of an observer. The periodic dimming of starlight determines the planet's mass and radius (Ollivier et al., 2009). Moreover, the spectrum of a planetary atmosphere can be studied using this technique. Apart from the alignment requirement, the detection of transiting planets is sensitive to short-period planets. However, owing to space missions such as KEPLER/K2 and TESS (Ricker et al., 2015) the number of exoplanets discovered and validated by this technique has largely increased as seen in Fig. 1.7. With 2,954 planets detected until August 2019, the transit method has been the most successful technique among all the other methods.

1.4.3 Microlensing

The microlensing technique detects planets based on the phenomenon of a gravitational lens that creates an effect of magnification (Einstein, 1936). When a massive object is present between the observer and the source, the image of the source is deformed and magnified. In the case of microlensing, distortion of starlight of a background star due to a source star with an exoplanet in the foreground is detected and associated with the planet detection. This technique has an advantage as it can detect less massive planets and/or planets with an orbital period of more than a few hundred days. This trend can be seen in Fig 1.7 where super Earth-type planets are detected. The biggest drawback to this technique is that the microlensing events are extremely rare and never repeat for the same target.

1.4.4 Direct Imaging of exoplanets

Direct imaging, in contrast to the above-explained indirect methods, obtains the image of the planets. The goal of obtaining the image of an exoplanet is to measure its flux, obtain a spectrum and determine its orbit. The exoplanet candidates which are point sources can either be detected in reflecting light (at visible wavelengths) or in its thermal emission (at IR wavelengths). While indirect observations have proven quite effective in exoplanet detection, direct imaging technique offers complimentary advantages.

This technique gives access to the spectro-photometric and possibly polarimetric measurements of planet atmospheres. Spectral information can determine certain key parameters, such as the temperature, surface gravity, the presence of certain molecules such as methane or water, cloud fraction, the mass of the planet, etc.. However, atmospheric and planet formation models are mandatory to interpret such data. Also, in just a few epoch observations, orbital characterization of the exoplanet can be done by direct imaging. Also, images of young stellar systems can be obtained. These observations can detect planets at a very young age before migration takes place. This way the technique can potentially put a constraint on planet formation. Another major advantage of this technique is the possibility to capture an entire stellar system at once. Therefore, in principle a system with multiple planets, exo-moons and a circumstellar disk can all be detected. These observations have led to a better understanding of circumstellar disk evolution. Direct imaging, however, is quite challenging because of two requirements.

1. *The star-planet contrast*: The flux ratio, F_p/F_*, of an Earth-Sun system with an angular separation of $0.5''$ at 10 pc is 10^{-10} in the visible range. For a Jupiter-Sun system, it is 10^{-9} (Traub & Oppenheimer, 2010). As flux is wavelength-dependent the flux ratio for an Earth-like planet will lie in between 10^{-8} to 10^{-7} at $0.1''$ in the IR, which is still non-achievable with current ground-based high-contrast imagers.

2. *The star-planet angular resolution*: The second challenge is to observe an exoplanet at small separations. A planet of interest (exo-earth or super-Earth) would lie between 0.1-$0.5''$. However, 30 plus meter class telescopes are expected to observe terrestrial planets. From space, imaging terrestrial planets around Sun-like star

would still need greater than 4 meter class telescopes. Using such monolithic telescope can induce launching limitations. However, segmented mirrors in telescopes as used in JWST (James Webb Space Telescope) is the next advancement to this technology.

Because of the two challenges, until now there are only a handful of exoplanets that are directly imaged, as seen in Fig. 1.7. The most observed planets are giant planets at large separations known as EGP (Extrasolar Giant Planets) which is because of the current challenge faced by imaging from both space (Hubble Space Telescope) and ground.

The requirement to achieve high contrast is challenging, firstly wavefront errors are always present and secondly, the stellar glare infiltrates the image which incapacitates observation of faint exoplanets. Wavefront aberrations can occur in space-based observation due to optomechanical vibrations. And for ground-based observations, the Earth's atmosphere introduces turbulence. This turbulence adds to the wavefront aberrations, degrading the image quality. To solve this issue an AO (Adaptive Optics, Babcock, 1953) system is used to correct for the aberrations induced by the turbulence. Similar techniques are required for space-based observations. Secondly, to suppress the starlight or the diffraction effect of a telescope an optics called coronagraph is used. In this thesis, such a ground-based instrument including these techniques are used. Thus, these techniques are explained in the forthcoming subsections.

1.4.4.1 Adaptive optics

The light from a stellar object is emitted in the form of a spherical wave. Traveling a quasi-infinite distance to the Earth these spherical waves are treated as plane waves and ideally should form an "Airy Disk" diffraction pattern (Point Spread Function or PSF) at the telescope's focal plane. When limited by diffraction, the angular resolution of a telescope is given by λ/D where D is the diameter of the entrance pupil of the telescope. However, atmospheric turbulence distorts the wavefront at the entrance pupil and degrades the angular resolution. The distortions are dominated by phase fluctuations and have comparatively small amplitude fluctuations. These fluctuations produce residuals known as speckles in the images. These speckles can be misidentified as planet signals in the science images. Therefore it is necessary to correct for such distortions. The distorted wavefront can be corrected in real-time with AO, to approach the theoretical diffraction limit.

The atmospheric turbulence-control requires three steps: measurement of the wavefront distortion, calculation of the necessary correction and application of the correction to the incident wavefront. The diagram of a conventional AO system is presented in Fig. 1.8 (Top). The incident light from the source is divided into two paths using a beam-splitter, one of them sends the light towards a wavefront sensor and the other towards the camera. The distorted wavefront is then measured by a wavefront sensor and a real-time calculator determines the shape to be applied on the deformable mirror to compensate for wavefront phase errors (Madec, 2012). The AO system works in a closed-loop.

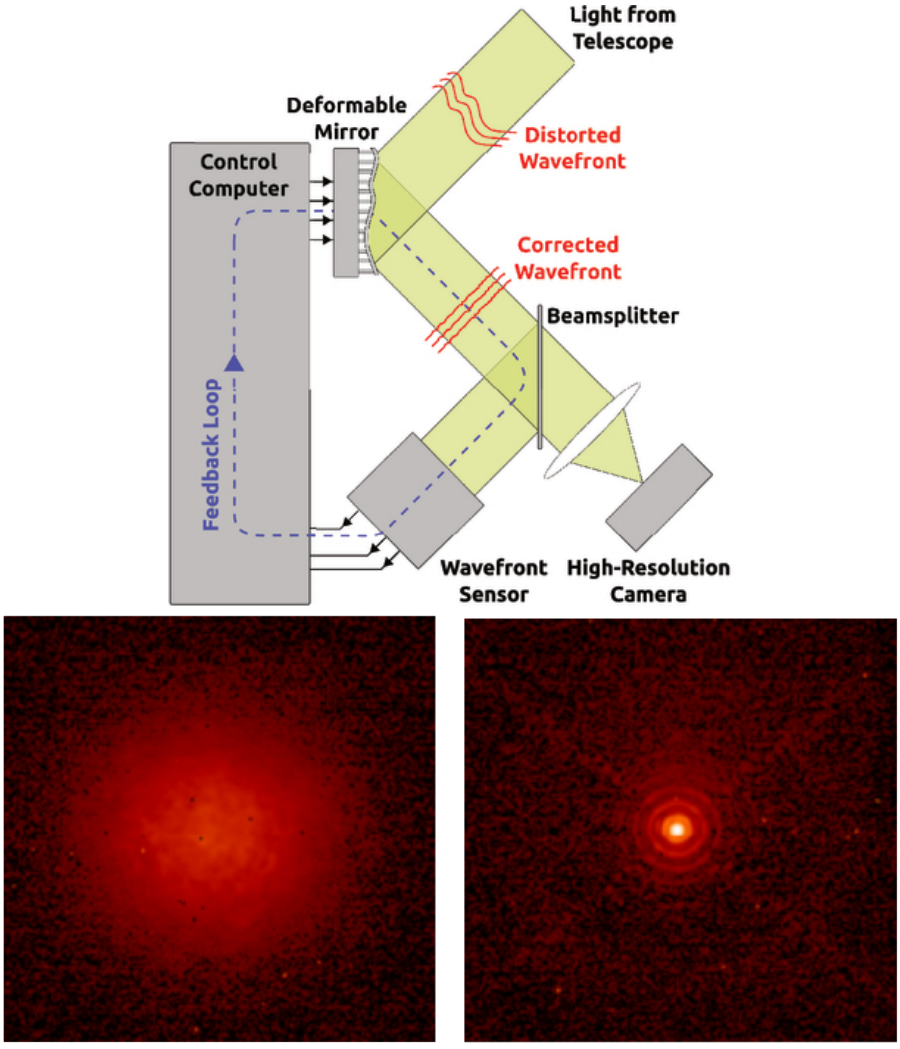

Figure 1.8 – *Top: A schematic diagram of an AO system as presented by Rigaut (2015). The correction of the distorted wavefront is performed in real time with the help of a wavefront sensor, a feedback loop and a deformable mirror. Bottom: An image created by distorted wavefront before AO correction (Left) and an image post AO correction (Right) showing the Airy pattern (Sauvage et al., 2016).*

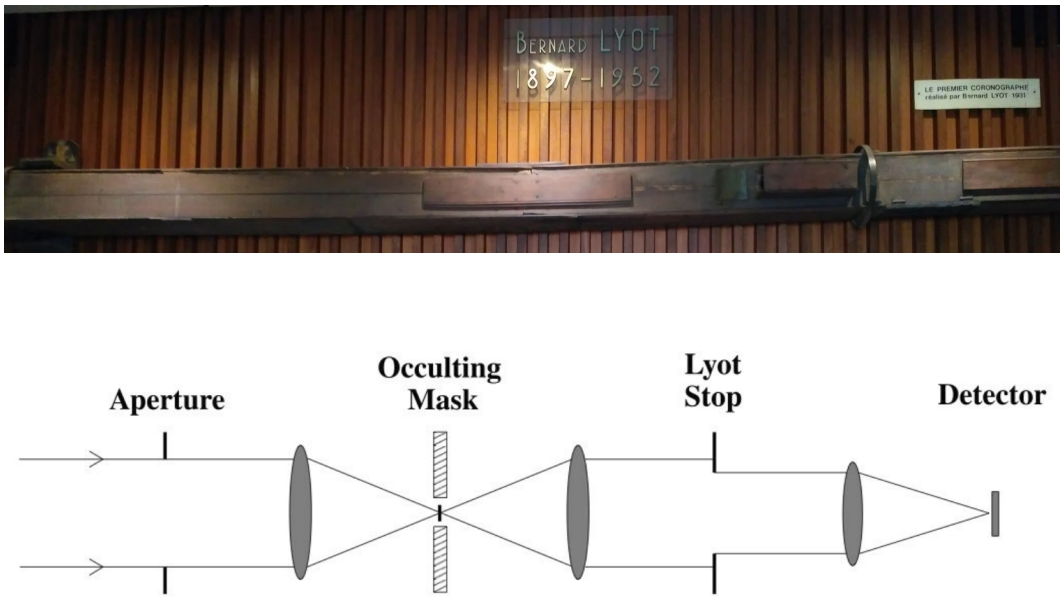

Figure 1.9 *– Top: The image is of the first coronagraph used by Lyot displayed in Observatoire de Meudon, France. Bottom: Schematic sketch of operation of Lyot coronagraph (Sivaramakrishnan et al., 2001).*

The path taken to correct for the distorted wavefront does not account for any optical aberrations in the science path i.e. between the beamsplitter and science camera, hence generating non-common path aberrations (NCPA). These aberrations are present mostly in the form of quasi-static speckles in the final long exposure images but can be compensated with calibrations.

Further developments in the field of exoplanet led to the development of Extreme AO (XAO) which is used in current ground-based instruments such as VLT-SPHERE (Spectro-Polarimetric High-contrast Exoplanet Research, Beuzit et al., 2019) and GPI (Gemini Planet Imager, Macintosh et al., 2008). In these XAO systems, the Strehl ratio (SR) is greater than 90%. SR is defined as the ratio of maximum diffraction intensities of an aberrated wavefront to a perfect wavefront. An image before and after AO correction is shown in Fig.1.8 (Bottom) where the expected "Airy disk" is seen in AO corrected image.

1.4.4.2 Coronographs

Coronagraphs are needed to block the stellar light to increase contrast and observe faint off-axis point sources. This concept was proposed and first used by Lyot (1930) for observing the solar corona.

The principle is to place an opaque mask at the focal plane to mask the core of the Airy disk from the star. Due to the presence of this mask, diffraction occurs which sends the light to the periphery of the pupil plane where a Lyot stop is used to block this

contribution. In the next focal plane, the stellar contribution is reduced. A detailed description of the Lyot coronograph is present in Sivaramakrishnan et al. (2001).

The Lyot coronagraph was used in Gemini-South NICI (Chun et al., 2008) and Subaru-CIAO (Tamura et al., 2000) which are the most recent imagers. However, Lyot coronagraph can be improved using an apodized amplitude mask such as the APLC (Apodized Pupil Lyot Coronagraph, Soummer, 2005). A major disadvantage of the Lyot coronograph is the minimum angular separation which can not be smaller than the size of the mask used to block the star-light, usually of the order of a few λ/D. This can be overcome using a phase mask such as the FQPM (Four Quadrant Phase Mask, Rouan et al., 2000), or the OVCM (Optical Vortex Coronagraph, Mawet et al., 2005). The APLC is used in SPHERE (Carbillet et al., 2010) and the FQPM is also implemented in SPHERE and JWSTs MIRI (Baudoz et al., 2006). OVCM is installed in Keck/NIRC2 (Serabyn et al., 2017)and NACO (Nasmyth Adaptive Optics System CONICA, Lenzen et al., 2003).

The raw contrast in the focal plane delivered by XAO and coronagraphs is of the order of 10^{-3}-10^{-4} as measured in SPHERE and GPI. Further reduction of starlight is required, which is discussed in the next section.

1.4.4.3 Speckle noise and suppression

Ideally, the coronagraphic output image after AO correction should provide a smooth diffraction halo. However, this is not observed because the images are contaminated by speckles. Speckles as mentioned in Sect. 1.4.4.1 are formed by random interference of wavefront appearing due to the uncorrected atmospheric turbulence and/or due to instrumental imperfections. Fast evolving speckles originate due to the atmospheric turbulence and are mostly attenuated by the AO system. The quasi-static and static speckles originate from optical defects. They have a lifetime longer than the exposure time, therefore, they tend to remain in the science exposure images.

This residual starlight can be derived and removed from the science images via several post-processing techniques developed by Marois et al. (2006a); Quanz et al. (2011); Racine et al. (1999); Schneider et al. (2003). Some of these techniques are detailed in Sect. 2.2. With the current post-processing techniques, the contrast achieved is between 10^{-5}-10^{-6} for GPI and SPHERE.

Active suppression of the quasi-static speckles can be done with techniques such as focal plane wavefront sensor (FPWS, Baudoz et al., 2012; Bordé & Traub, 2006; Give'on et al., 2007; Sauvage et al., 2012) and other similar techniques which are being developed and tested both on laboratory (some results in Potier et al, in prep, Singh et al. accepted, Mazoyer et al. (2014a); Trauger et al. (2012)) and on sky (some results in Vigan et al., 2019; Wilby et al., 2017). These techniques are still in the testing phase and yet to be used to obtain science images free of quasi-static speckles. They can be implemented as an upgrade to the present high contrast imagers such as SPHERE and in the future can be applicable to ELT (Extremely Large Telescope), TMT (Thirty Meter Telescope) and other future space telescopes as well.

1.5 Imaging debris disk

The development in the field of imaging complements the SED observations of debris disks. Some degeneracies in terms of the temperature of the grains present in these systems and their size are broken by high contrast observations. In SED analysis, it is generally assumed that small grains emit like blackbodies, which may not be necessarily true because small dust grains are less effective emitters (Draine, 2004). This assumption can lead to an inaccurate measurement of the grain size and propagates to a miscalculation of the radius of the "parent belt" of the disk. This discrepancy can be broken by imaging, which can resolve the parent belt and its physical parameters, such as radial distance, size, etc..

Also, a collective study of SED and imaging can determine the presence of a warm and cold component of the disk with better efficiency. For instance, after imaging the disk around HR 8799, its SED was re-analysed by Chen et al. (2009). This study concluded the possibility of the presence of both warm and cold components in the disk of HR 8799 system.

1.5.1 Thermal Imaging

Thermal imaging resolved many debris disks in IR and millimeter wavelengths. At longer wavelengths, the observations are sensitive to bigger grains and therefore are expected to be least influenced by radiation pressure. Few space telescopes providing this facility are Spitzer (e.g. Ballering et al., 2016; Su et al., 2005, 2009, 2008) and Herschel (e.g. Acke et al., 2012; Booth et al., 2013; Matthews et al., 2014; Pawellek et al., 2014). Ground-based thermal imaging has been successfully done by KECKII and Gemini South. These observations from space and ground were able to resolve stellocentric offsets, brightness asymmetry (e.g. Fitzgerald et al., 2007; Moerchen et al., 2011; Telesco et al., 2005) and observation of extended halo (e.g. Matthews et al., 2015). Future space- and ground-based telescopes include JWST/MIRI, ELT (Extremely Large Telescope)/METIS which would continue observing in mid-IR wavelengths.

With the technological advances, high-resolution imaging with sub-mm/radio interferometry has proven to be successful in imaging various detailed structures of circumstellar disks. Apart from varied grain sizes, millimeter observations are also sensitive in detecting molecular transition primarily CO. Ground-based interferometers such as SMA (Submillimeter Array, e.g. MacGregor et al., 2015; Wilner et al., 2018) and especially ALMA (Atacama Large Millimeter/Submillimeter Array, e.g. Boley et al., 2012; Dent et al., 2014) have provided good angular and spectral resolutions to detect secondary gas in debris disks.

1.5.2 Scattered Light Imaging

Scattered light imaging probes smaller dust grains which are influenced by radiation pressure, therefore, the blowout halo can be seen as an effect of radiation pressure. This imaging technique provides several ways to parameterize the physical properties, photometry,

spectroscopy, and polarimetry of debris disks. For example, the geometry of the debris disk and grain properties can be constrained by using radiative transfer models (Augereau et al., 1999b; Lebreton et al., 2013) and grain properties can also be constrained by measuring the scattering phase function as performed in Milli et al. (2017). A disk's intensity varies differently in total intensity imaging and polarimetric imaging so a comparative study between them can be used to measure the polarisation fraction and relevant parameters for phase functions. These comparative studies often provide stronger constraints on the spatial dust distribution within the disk (Olofsson et al., 2019) compared to a that of just studying either the total intensity or the polarimetric images. The polarimetric image of the disk around HR 4796 along its total intensity counterpart is presented in Fig. 1.10 d) and e) as seen by Olofsson et al. (2019) and Milli et al. (2017).

Scattered light coronagraphic imaging with HST (Hubble Space Telescope, e.g., Apai et al., 2015; Golimowski et al., 2006; Schneider et al., 2014) and ground based telescopes such as NACO (e.g., Boccaletti et al., 2012; Mazoyer et al., 2014b), MagAO (Magellan Adaptive Optics, e.g., Rodigas et al., 2015), LBT (Large Binocular Telescope, e.g., Rodigas et al., 2014), GPI (e.g. HR 4796 Perrin et al., 2015), SPHERE (e.g., Boccaletti et al., 2018; Lagrange et al., 2012; Milli et al., 2017) and Suburu/HiCIAO (Thalmann et al., 2011) has been acheived.

Multi-wavelength imaging can study different morphological features and sub-structures (as in, Fomalhaut Acke et al., 2012; Boley et al., 2012; Kalas, 2005). Figure 1.10 shows the HR 4796 debris disk as observed by HST, Herschel, and ALMA. Spectro-photometry retrieved from multi-wavelength imaging with thermal emission or scattering light also expands the SED characterization of disks, leading us to better study the dust-grain evolution and transport properties.

1.6 Motivation

By now it is understood that scattered light imaging has been quite successful in imaging and characterizing debris disks. The field of debris disk study is continuously evolving with new observations and filling the canvas of planet formation and evolution theories. Studying specific disk features can provide clues on the presence of faint planets that are undetectable by current instruments such as SPHERE and GPI. However, SPHERE and GPI are the only available instruments to have integral field spectrographs operational in the NIR wavelengths, which are used for spectro-photometry of debris disks. Additionally, an extracted spectrum can be analyzed to identify the color of the disk and grain properties. Therefore, the comprehensive motivation of this thesis was to take advantage of the morphological and spectroscopic information while observing debris disks with SPHERE.

Incidentally, the innermost ringlet of HD 141569 at ∼40 au was discovered with SPHERE observations by Perrot et al. (2016). A possible clump was seen at the southern ansa of the ringlet. A motivation of doing aperture photometry to isolate this clump feature and analyze it to understand whether it was a planet-forming dense region or an instrumental/post-processing artifact was drawn. This work required the development of spectral extraction tools and extensive usage of forward modeling techniques which was done in the due course of this thesis.

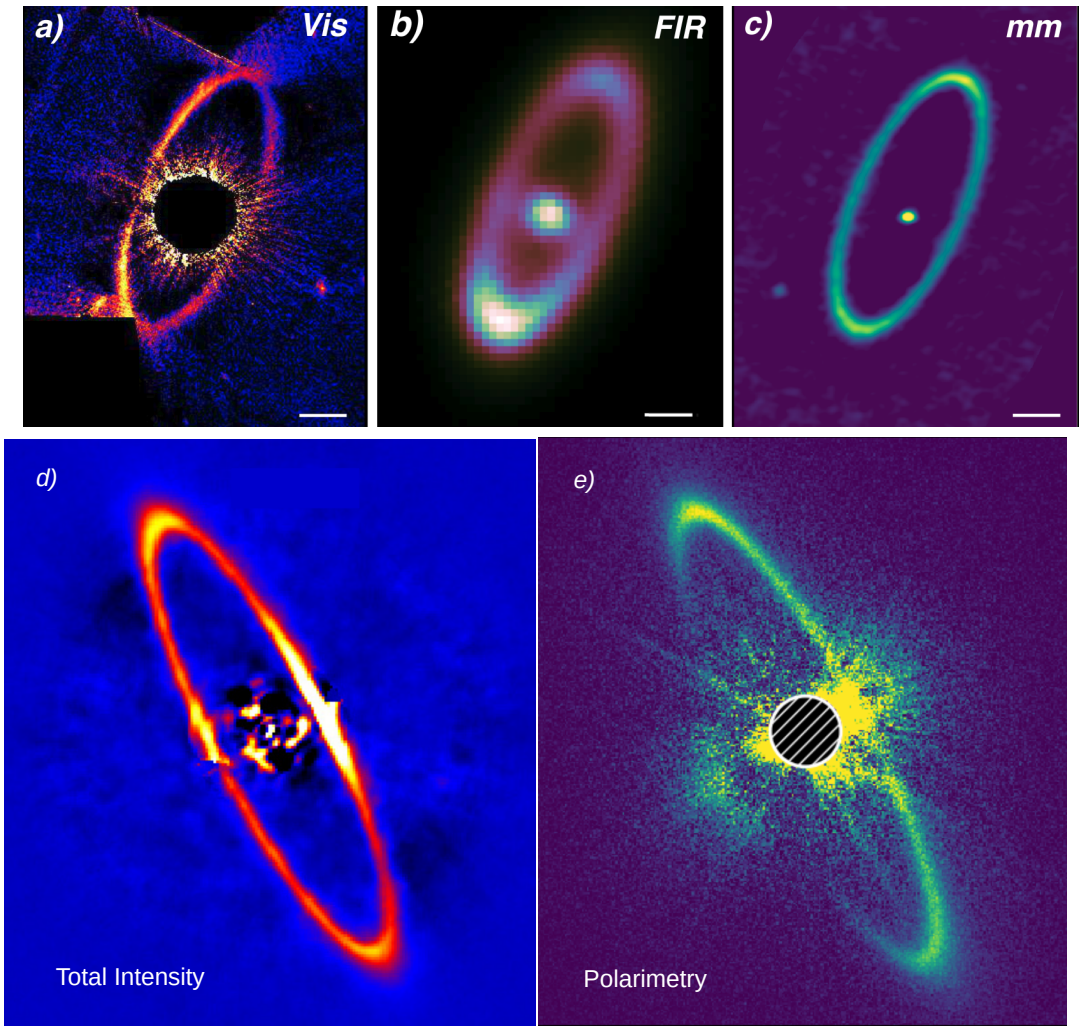

Figure 1.10 *– Top:The image shows debris disk around Fomalhaut as observed by HST (a) Kalas et al., 2013), Herschel (b) Acke et al., 2012) and ALMA (c) MacGregor et al., 2017). The image in e) and f) show the debris disk around HR 4796 as observed in total intensity by Milli et al. (2017) and in polarimetry in Olofsson et al. (2016). North is up and East is left in all the images and the scale bar is 50 au for the top panel images. The disk is imaged in different wavelengths to see various structural features such as north-east south-west brightness asymmetry in (a), and brightness asymmetry between the two ansae in (b) and 1.3 mm thermal emission map in (c).*

1.7 The course of this thesis

To extract an unbiased spectro-photometry of the debris disk HD 141569 the first step was to perform forward modeling accompanied with ADI post-processing techniques. The details of forward modeling along with SPHERE's observation and data post-processing techniques are detailed in Chapter 2. However, as the debris disk HD 141569 is comparatively faint and quite complex in geometry, HD 32297 was taken as a test-case study.

A spectro-photometric study of an inclined debris disk around HD 32297 led to the determination of the color of the disk and the grain properties. The details can be found in Chapter 3 and this study resulted in a publication in a peer-reviewed journal Bhowmik et al. (2019).

After the analysis of debris disk HD 32297, HD 141569 was revisited with the initial intention of isolating the clump from the disk and analyzing them, So, a spectrum of the whole ringlet was extracted and compared to the spectrum of the clump to identify if they can be disentangled. To have a better perspective of debris disk geometry, color, and grain properties, another inclined disk around HD 106906 system was analysed with a similar approach as used for the disk of HD 32297. The specialty of HD 106906 system is that it is a close spectroscopic binary system that harbors a massive planet, outside the debris disk, at a large distance. Hence, the study of this disk was also motivated by understanding planet-disk interaction from the disk's photometry. The details and results of the two disks can be found in Chapter 4.

All three disks studied in this thesis have different characteristics in terms of geometry, presence of planets and multiple belts. Also, their spectra are globally different but their grain properties show a very similar trend. Therefore, the implication of this study and a perspective in terms of future observation is presented in Chapter 5.

CHAPTER 2

Observation, data reduction and forward modelling

2.1 High-contrast observation with SPHERE 23
2.1.1 Sub-system details 24
2.1.2 Consortium 25
2.1.3 Procedure to obtain the sequence of a science observation 26
2.2 Procedure of data reduction 27
2.2.1 ADI imaging 28
2.2.2 DPI imaging 32
2.3 Forward modeling of debris disk 33
2.3.1 GRaTer 35

This chapter provides an introduction to the SPHERE instrument since the work done in this thesis have relied upon observations from SPHERE. First, architectural details about the sub-systems of SPHERE are provided and then I explain the observation sequence followed by the disk and exoplanet surveys within the consortium. In Sect. 2.2 different data reduction and post-processing methods used to obtain coronagraphic imaging with high contrast is presented. Finally, in Sect. 2.3 a detailed explanation of the forward modelling technique along with the GRaTer code is given, which has been used extensively during the course thesis.

2.1 High-contrast observation with SPHERE

The SPHERE instrument is an example of a second generation high contrast imager installed on the 8m class telescope. SPHERE was envisioned as a planet finder. The main goal of this instrument is to image and discover giant exoplanets and circumstellar disks around young nearby stars. This instrument is installed at UT3 Nasmyth focus of the VLT in Chile. SPHERE has successfully imaged several circumstellar disks (Boccaletti et al., 2015; Engler et al., 2018a; Lagrange et al., 2018, 2016; Olofsson et al., 2016) and young giant planets (Keppler et al., 2018; Müller et al., 2018; Vigan et al., 2016; Wagner et al.,

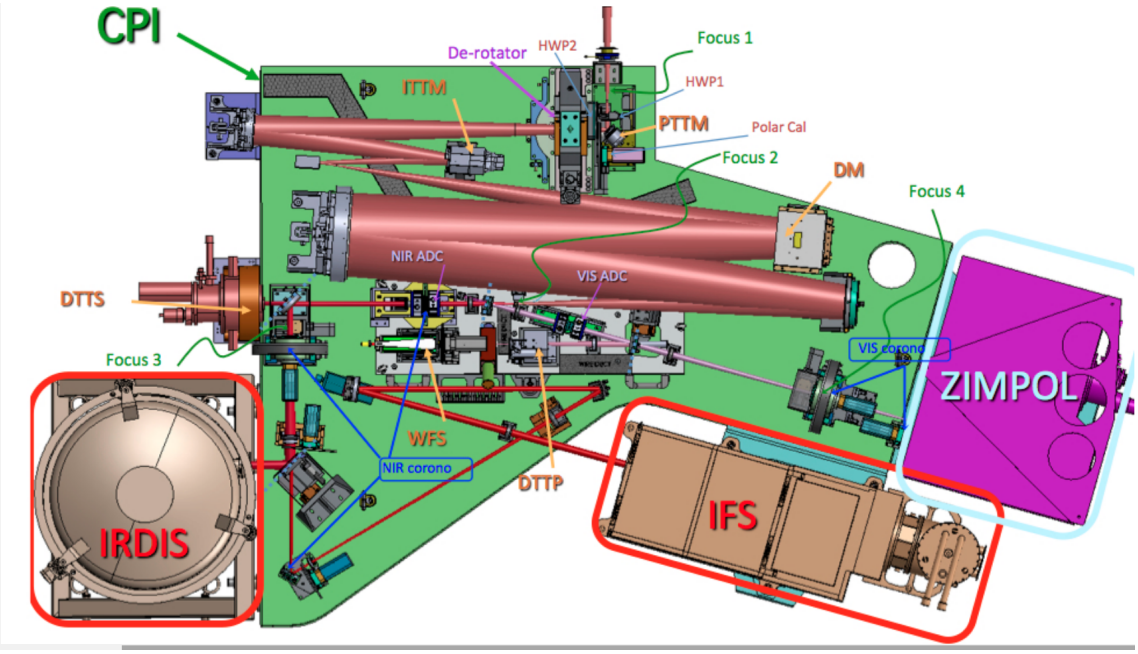

Figure 2.1 *– A top view of SPHERE bench with its sub-systems (IRDIS, IFS, ZIMPOL) and many opto-mechanical components labelled as seen in Beuzit et al. (2019)*

2016) from the beginning of 2015. This instrument has three sub-systems namely the Infra-Red Dual-beam Imager and Spectrograph (IRDIS, Dohlen et al., 2008), the Integral Field Spectrograph (IFS, Claudi et al., 2008), and the Zurich IMaging POLarimeter (ZIMPOL, Thalmann et al., 2008) as shown in Fig. 2.1. The Common Path and Infrastructure (CPI) as seen in Fig. 2.1 is a system consisting of the high-order extreme adaptive optics system SAXO (Fusco et al., 2014) and the coronagraphs (Boccaletti et al., 2008) feeding the three sub-systems. The coronagraphs used here are classical Lyot coronagraph, four quadrant phase mask (FQPM) and apodized pupil Lyot coronagraph (APLC). The details of the sub-systems and enabled science observations are provided in the next following subsections.

2.1.1 Sub-system details

2.1.1.1 IRDIS

IRDIS (Dohlen et al., 2008) is an imager with several observing modes, such as Dual-Band Imaging (DBI), Dual Polarimetric Imaging (DPI), Classical Imaging (CI) and Long-Slit Spectroscopy (LSS, Vigan et al., 2008). The field of view (FOV) is $11''\times12.5''$ with a pixel scale of 12.25 mas per pixel, provided by a detector of 2048×2048 pixels. The instrument can be operated in *Y, J, H* and *K* band of the near-infrared wavelengths spanning the range from 0.95 μm to 2.30 μm. Several combinations of filters can be used for different observing modes. The central wavelength and the width of the filters are provided in `https://www.eso.org/sci/facilities/paranal/instruments/sphere/inst/filters.html`

The dual-band and the classical imaging observations are performed in the pupil tracking mode to take advantage of Angular Differential Imaging (ADI, Marois et al., 2006a). In DBI the observation is simultaneously taken in two narrow band filters to also have a spectral information useful for the Spectral Differential Imaging (SDI, Racine et al., 1999). In CI, the two narrow band filters are replaced with the two identical broadband filters.

The DPI observing mode is by default used in field-stabilised mode. However, pupil-stabilised mode has been recently implemented. The dual-band filters are replaced by two orthogonal linear polarisers which are simultaneously used to obtain images in two linear polarisation directions. Multiple polarisation cycles are obtained by inserting a rotatable half-wave plate in the CPI (Langlois et al., 2010).

2.1.1.2 IFS

IFS (Claudi et al., 2008) is SPHERE's integral field unit spectrograph with 39 spectral channels. The IFS detector also has a size of 2048×2048 pixels providing a FOV of $1.73'' \times 1.73''$ with a pixel size of 7.46 mas. The raw data of 23,140 spectra are collected and each spectrum is projected on a rectangular area of 41×5.093 pixels on the detector and aligned in columns to cover the full FOV (Beuzit et al., 2019). IFS is mostly used in the pupil stabilized mode to utilize the benefits of ADI.

IFS and IRDIS are most commonly used simultaneously in IRDIFS mode or IRDIFS-EXT mode. In IRDIFS mode, IRDIS operates in either broadband H filter ($\lambda \pm \delta\lambda = 1.625 \pm 0.29\,\mu$m) or dual narrow band H2H3 filter ($\lambda \pm \delta\lambda = 1.593 \pm 0.052\,\mu\text{m}, 1.667 \pm 0.054\,\mu$m) along with IFS operating in YJ (0.95-1.35μm) band filters with a spectral resolution ($\lambda/\delta\lambda$) of 50. In IRDIFS-EXT mode, IRDIS operates in either broadband Ks filter ($\lambda \pm \delta\lambda = 2.182 \pm 0.30\,\mu$m) or dual narrow band K1K2 filter ($\lambda \pm \delta\lambda = 2.110 \pm 0.102\,\mu\text{m}, 2.251 \pm 0.109\,\mu$m) along with the IFS operating in YJH (0.95-1.65μm) band filters with a spectral resolution of 35.

2.1.1.3 ZIMPOL

ZIMPOL (Thalmann et al., 2008) is an imaging polarimeter for SPHERE. There are two detectors of 2k×2k pixels translating to a FOV of $3.5'' \times 3.5''$ with a pixel size of 3.5 mas per pixel. This instrument works in the visible wavelengths ranging between 500 to 900 nm both in broad and narrow band filters. This instruments can also be used in both the field and pupil tracking modes. There are two possible observing modes classical and dual polarimetric imaging in ZIMPOL. This sub-system is extensively used for circumstellar disk observation. This thesis does not involve the processing of data obtained with ZIMPOL.

2.1.2 Consortium

The SPHERE consortium includes 11 major European institutes and laboratories, such as IPAG (PI. J.L. Beuzit), ASTRON, ETH Zurich, INAF, LAGRANGE, LAM, LESIA,

MPIA, Observatoire de Genève, ONERA and ESO with more than 150 active researchers. 260 nights of guaranteed time observation (GTO) was provided to this consortium for a period of 5 years. Two hundred nights were attributed to the SpHere INfrared survey for Exoplanets (SHINE, PI: G. Chauvin, S. Desidera, Chauvin et al., 2017) with a primary science objective oriented to the discovery and characterisation of exoplanets. Twenty nights were reserved for the DISK (PI: C. Dominik) survey. As the name suggest the DISK survey is dedicated to the discovery and characterisation of circumsteller disks ranging from the protoplanetary to debris disks around young stars. REFPLANETS (PI: H.-M. Schmid) is a program which has twenty nights reserved for the observation and discovery of exoplanets in the visible wavelengths. The other programs include OTHERSCIENCE (PI. E. Lagadec) with 12 nights to observe the evolved systems (such as, Betelgeuse, Kervella et al., 2016), solar system objects (small bodies and satellites), Active Galactic Nuclei (AGN), etc. Apart from the GTO observations, there has been several open time (OT) observations with SPHERE especially targeted towards the study of circumstellar disks.

During my thesis, I took part in the *data reduction team* (DRT) for several GTO SHINE programs. My contribution has been the reduction of raw data from the telescope.

2.1.3 Procedure to obtain the sequence of a science observation

The conventional observation sequence followed in SHINE is as follows:

- First, a non-coronagraphic image, the point spread function (PSF) is acquired for the photometric purpose. This observation is done for few minutes to average out the atmosphere-induced wavefront variations.
- Then, a coronagraphic image is obtained together with a waffle mode applied on the deformable mirror (Langlois et al., 2013). This step is done to locate the position of the hidden star (in post-processing) in all the science images which are acquired during an observing sequence. Four wavelength dependent satellite spots are created at a given separation, which create a cross pattern to center the star in each science image. This observation takes a few minutes.
- A series of coronographic science observations start after the PSF acquisition and centering of the star. The duration of the process is about 1 to 1.3 hours to accumulate a large field rotation. Each frame is obtained for an individual exposure time ranging from 0.8s to 96s depending on the magnitude of the target.
- A second waffle sequence is obtained to re-check for centering of the star.
- A second off-axis PSF is obtained to ensure consistency in the photometry and to monitor variations.
- Finally, a sequence of sky backgrounds are obtained by observing various areas around the star avoiding any background stellar objects in the field. This step can either be done in the beginning or at the end of the observing sequence.

The observing sequence differs very slightly between the total intensity and the polarimetric observations. In DPI observations, the light is split into two orthogonal directions using a beam-splitter and a set of orthogonal polarizers. The two images are taken simultaneously. One polarimetric cycle consists of observations taken with the half wave plates (HWPs) rotated at four orientations (0°, 22.5°, 45° and 67.5°). One can construct the Stokes parameters by combining several such polarimetric cycles. The details are provided in Sect. 2.2.2.

2.2 Procedure of data reduction

After the observations, a first step of data reduction is done with the SPHERE Data reduction and handling (DRH, Pavlov et al., 2008) pipeline. This pipeline is installed at the SPHERE Data Center (DC, Delorme et al., 2017) at IPAG where all the observations and reductions are recorded. A DRT is formed during every observation run. The DRT uses the DRH pipeline and the DC to run preliminary data reduction the next day of the observation date. An immediate data reduction of the targets during the ongoing observing run gives an idea of the data quality and if any rescheduling of an observation is needed. The steps of preliminary data reduction are listed below which are referred from `http://www.eso.org/sci/facilities/paranal/instruments/sphere/doc/VLT-MAN-SPH-14690-0430_P104_jun30_2019_zwa.pdf`.

- The first step involves the background subtraction and bad-pixel correction by subtracting the dark frame and the sky frame on each raw frame. The sky frames may be taken at the time of observation. The dark frames are obtained everyday for each instrument by closing the shutter and all other internal light sources.
- Next, a flat-field correction is performed to remove the pixel-to-pixel variations on the detector or any other types of in-homogeneity. At-least three flat frames are taken everyday with different filters in the beam.
- The calibration of wavelength is performed only for IFS observation. In this step, a map is obtained where each pixel on the detector is assigned an index. These indices correspond to specific wavelengths which is obtained from several laser light sources (Desidera et al., 2008).
- In the next step, an IFS flat field allows to correct lenslet to lenslet variations.
- For IFS reductions, the pixels corresponding to the same wavelength are grouped together to form an image. A cross-talk correction (Desidera et al., 2008) is also performed for IFS observations.
- The previous three steps are omitted for IRDIS observations. A 4-dimensional cube (2 spatial, 1 spectral, 1 angular/temporal axes) is recovered by combining several science images.
- Next, the cube of all the coronagraphic science images is centered frame by frame using the waffle image. This step is essential in the pupil-tracking mode for applying differential imaging techniques.

- Along with the cube there are three other fits files produced with the information on the PSF, the parallactic angle and wavelength values of the filters used for each image. These files are used for further reduction and analysis.

The DC is equipped with a tool SpeCal (Galicher et al., 2018) which handles all the further ADI, RDI and SDI post-processing. Some of the ADI-based algorithms which I have used in my thesis are explained in the sections below.

2.2.1 ADI imaging

ADI (Marois et al., 2006a) is a powerful tool for suppressing speckles in post-observation and improving detection contrast of the observations obtained in the pupil tracking mode of the ground-based altitude/azimuth telescopes. In this technique the telescope pupil is fixed and tracks the star throughout an observing sequence. The FOV is slowly rotating in each frame which remains centered around the star. The first column of Fig. 2.2 shows this process where multiple images $\mathcal{I}_\mathrm{l}$ are acquired at various parallactic angles. Therefore, a static speckle pattern $\mathcal{A}$ can be reconstructed by carefully studying the starlight left unattenuated by coronagraph in each image. A high contrast image $\mathcal{I}_\mathrm{f}$ of the object of interest is recovered by subtracting the reconstructed speckle pattern from each frame, re-rotating and stacking them as seen in Fig. 2.2. A diagrammatic representation is given in Fig. 2.2

In case of observation obtained with SPHERE lets consider $\mathcal{I}(i,\ j,\ \Theta_l,\ \lambda)$ as a 4 dimensional master cube where the star is centered in each image. Here i and j are the spatial axes, Θ corresponds to parallactic angle, l is the index of the temporal axis and λ being the spectral axis. In ADI, one builds an image $\mathcal{I}_\mathrm{ADI}(i,\ j,\ \Theta_\mathrm{l},\ \lambda)$ by subtracting a reconstructed static speckle pattern $\mathcal{A}$ using the equation below:

$$\mathcal{I}_{ADI}(i,j,\Theta_l,\lambda) = \mathcal{I}(i,j,\Theta_l,\lambda) - \mathcal{A}(i,j,\Theta_l,\lambda), \tag{2.1}$$

here I follow the same mathematical convention as used in Galicher et al. (2018). To construct $\mathcal{A}(i,j,\Theta,\lambda)$ accurately, various ADI-based algorithms can be used such as Locally Optimised Classical Imaging (LOCI, Lafrenière et al., 2007), template LOCI (TLOCI, Marois, 2015) and Principle Component Analysis (PCA, Soummer et al., 2012). The final step includes rotating and aligning all the images in the cube $\mathcal{I}_\mathrm{ADI}(i,\ j,\ \Theta,\ \lambda)$ to the north. These images are then either averaged or median combined over all the angular frames to obtain $\mathcal{I}_\mathrm{f}(i,j,\lambda)$

In this thesis the algorithm PCA has been extensively used and the algorithm TLOCI has also occasionally been used. Therefore, an explanation on these two techniques is provided in the upcoming subsections.

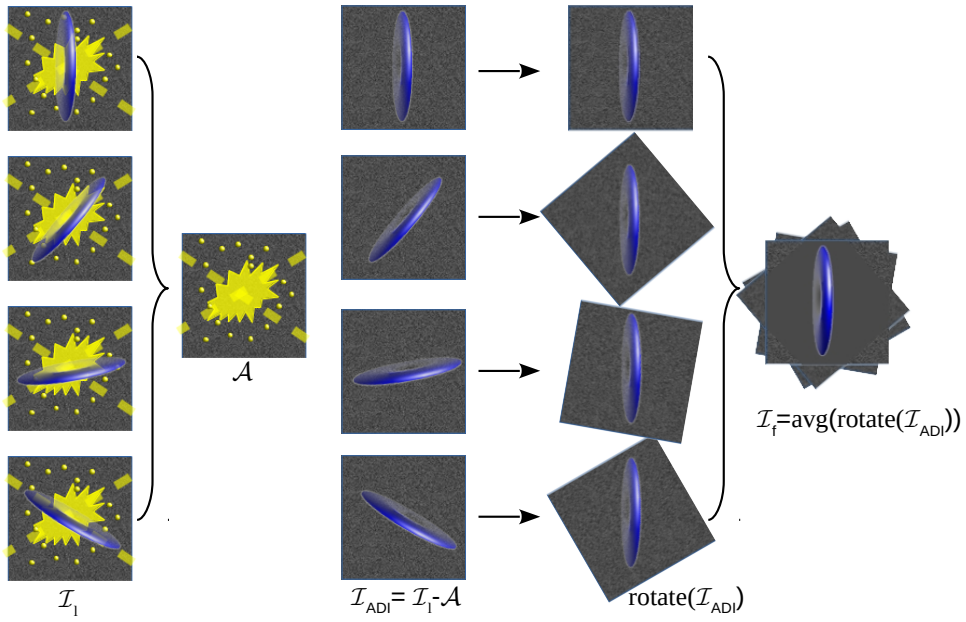

Figure 2.2 *– A schematic representation of the ADI technique. Here the disk is in blue and diffraction from the telescopic optics and the stellar residual are seen in yellow. After subtraction of static speckle pattern (second column) from the science images (first column), each frames are re-rotated (fourth column) and averaged (last column) to obtain a speckle free image.*

2.2.1.1 Classical ADI

In classical ADI (Marois et al., 2006a) the parameter $\mathcal{A}(i,j,\Theta,\lambda)$ is simply either an angular average or an angular median of all the frames in $\mathcal{I}(j,\ j,\ \Theta,\ \lambda)$.

$$\mathcal{A}(i,j,\lambda) = \frac{1}{\mathcal{N}} \sum_{l=1}^{\mathcal{N}} \mathcal{I}(i,j,\Theta_l,\lambda), \tag{2.2}$$

here, $\mathcal{N}$ represents the total number of angular frames. After this image $\mathcal{A}(i,j,\lambda)$ is obtained, the procedure is followed as described above to retrieve an ADI induced image.

2.2.1.2 LOCI and TLOCI

To use LOCI (Lafrenière et al., 2007), the speckle intensity is minimized in each science image corresponding to a particular Θ_l. The image is divided into n sections with an area ϱ_l as shown in Fig 2.3 (Left). The sections are of a geometry as shown in Fig 2.3 (Left) in greyscale, the image is divided into different annuli and then each annulus is divided into the smaller sectors as seen in 2.3 (Right) in blue. The subtraction of the speckle pattern is done section by section for each frame corresponding to Θ_l. The speckle pattern in each of these sections is obtained by taking a linear combination of all the other images within the defined section and corresponding to Θ_{lw} where $lw = 1, ..., \mathcal{N}$ excluding some frames

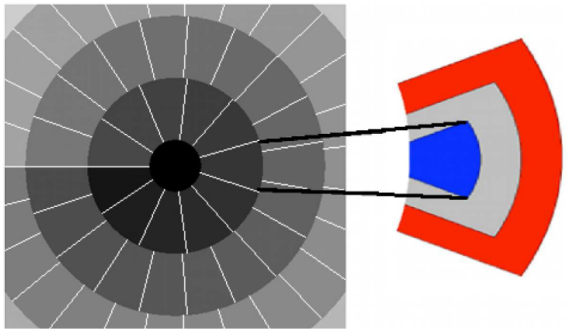

Figure 2.3 *– The section of interest (blue) and the section of optimisation (blue) representation for LOCI. The section of interest (blue) and the section of optimisation (red) representation for TLOCI as in Galicher et al. (2018)*

corresponding to $l \pm \delta l$. The δl restriction is taken to incorporate enough field rotation $\left(>0.5\frac{\lambda}{D}\right)$ between the l^{th} science image and the other frames from which the speckle pattern is obtained to avoid significant overlap of the object of interest. This can simply be represented as in Eq (2.3)

$$\begin{aligned} \mathcal{I}_{\mathrm{l}} &= \int_{\varrho_n} \Big(\mathcal{I}(\varrho_n) - \mathcal{I}'(\varrho_n)\Big), \\ \mathcal{I}'(\varrho) &= \Big\{\Big(\sum_{lw} c_{lw}\mathcal{I}(\Theta_{lw})\Big)\Big\}, \end{aligned} \tag{2.3}$$

where c_{lw} are the coefficients computed by LOCI (Lafrenière et al., 2007). It was observed that this method induced bias in the subtraction when there was an off-axis source in the section of area ϱ and could subtract science signal from a planet candidate within the section. To overcome this limitation TLOCI (Marois et al., 2014) was developed where the section of interest (represented in blue in Fig. 2.3) in the science image and the section to be optimised (represented in red in Fig. 2.3) from which the speckle pattern is constructed are non-overlapping. The section of optimisation is greater than the section of interest as represented in Fig 2.3. The area between the section of interest and the section of optimisation is set to 0.5 FWHM in SpeCal such that it is close enough to obtain an optimal $\mathcal{I}'$ but not too close to overlap and cause biases (Galicher et al., 2018). This method induces less *self-subtraction* compared to LOCI but it is also less aggressive. Finally, after subtracting the speckle pattern from all the frames, these are rotated to the North and averaged or median combined to complete the ADI post-processing.

TLOCI can also be used with SDI (Marois et al., 2006b) and a combination of ADI and SDI known as ASDI (Maire et al., 2014).

2.2.1.3 PCA-ADI

PCA or Karhunen-Loève Image Projection (KLIP, Soummer et al., 2012) is an algorithm very commonly used for image reconstruction. In SpeCal, the PCA algorithm follows similar steps as explained in Soummer et al. (2012).

Along with SpeCal, a KLIP-based algorithm was developed by Boccaletti et al. (2015) which I have used for processing several data sets all along my thesis. Both pipelines use the following steps while computing the PCA or KLIP post processed image.

1. First, for each wavelength, the two spatial axis in the array $\mathcal{I}(i,j,\Theta_l)$ are converted into a single spatial axis making it a two dimensional array $\mathcal{I}(\Theta_l,b)$ of which b represents the spatial axis.

2. After that the array is subtracted from an average value of the same array and normalised to obtain a new array $\mathcal{I}_{norm}(\Theta_l, b) = \frac{\mathcal{I}(\Theta_l,b)-\langle\mathcal{I}(\Theta_l,b)\rangle}{\sigma(\mathcal{I}(\Theta_l,b))}$. The $\sigma(\mathcal{I}(\Theta_l, b))$ used here is the standard deviation of $\mathcal{I}(\Theta_l, b)$.

3. In the next step, eigen vectors v_i are computed from the covarience matrix given as $\mathcal{I}_{\rm norm}(\Theta_l, b) \otimes \mathcal{I}^T{}_{\rm norm}(\Theta_l, b)$. T here, represents the transpose of the vector.

4. After that, the principle component is calculated, which is given by $PC = \mathbb{v}^T{}_l \otimes \mathcal{I}_{norm}(\Theta_l, b)$.

5. After calculating the principle components, the KL basis is obtained by truncating these principle components to a user defined "number of modes" along with truncating the eigen vectors.

6. Next, the reference image $\mathcal{A}(i,j,\Theta_l,\lambda)$ is built in two steps. First, by taking the inner product of KL basis and the truncated eigen vectors. Then, by multiplying the $\sigma(\mathcal{I}(\Theta_l, b))$ to the inner product calculated in the previous step, adding the averages $\langle\mathcal{I}(\Theta_l, b)\rangle$ and converting the two dimensional array back to a three dimensional array of (i, j, Θ_l).

7. The above steps are repeated for all the wavelengths to obtain a cube of $\mathcal{A}(i,j,\Theta_l,\lambda)$, which is subtracted from the target image cube as in defined Eq. 2.1.

Note that I could have used PCA with the SpeCal pipeline in ASDI. However, it is computationally extensive because of which I chose ADI technique to post-process total intensity data.

While using KLIP for extended objects such as disks, *self-subtraction* becomes unavoidable. Unlike in TLOCI where the self-subtraction arises due to a linear process of the possible section by section subtraction, in PCA this subtraction may be non-linear. The KL basis in PCA is itself dependent on the science image and therefore on the astrophysical signal (disk or planet). To be precise, the principle components obtained from the covariance matrix is in the form of quadrature of the speckles and the astrophysical signal in the image $\mathcal{I}_{norm}$. This behaviour propagates to produce KL basis which also depends quadratically on the astrophysical signal (Pueyo, 2016). It is to note that more aggressive the ADI post-processing, stronger is the self-subtraction. Also, at smaller separations this effect becomes even stronger.

The advantage of PCA over TLOCI while both producing some version of self-subtraction is that PCA is computationally less expensive, thus giving a drastic convenience to use it for detailed modelling purpose. This is because the formation of a speckle pattern is done

on the whole image in PCA unlike a region-to-region optimisation in TLOCI. The self-subtraction can be estimated using forward models, which will be discussed in Sect. 2.3. Independent of total intensity observation, another possibility is to observe the target in the polarimetric mode, which provides complementary observation to the total intensity observation.

2.2.2 DPI imaging

The polarised light can be represented by Stokes parameters $[I, Q, U, V]$. In dual band imaging with polarimetry, the images are split into two orthogonal polarisation states, for example I_0 and I_{90}: the difference between the two images would give another image corresponding to the Q parameter. This difference eliminates the unpolarised speckle halo (Langlois et al., 2014). To be more effective, a second set of images is obtained I_{45} and I_{135}, whose difference results in the U image.

To allow reducing instrumental polarisation, a rotating HWP is used which modulates the polarisation at 0°, 22.5°, 45° and 67.5°. A 22.5° rotation of HWP is chosen as it rotates the polarization of to twice of the rotation of the incident light and the HWP that is by 45°. From this new set, images corresponding to Q^+, U^+, Q^-, U^- parameters can be extracted. Each of the images is obtained in two channels *left* and *right* denoted as $I_L^0, I_L^{22.5}, I_L^{45}, I_L^{67.5}$ at the left channels and $I_R^0, I_R^{22.5}, I_R^{45}, I_R^{67.5}$ at the right channels.

With the double difference method (Kuhn et al., 2001; Tinbergen, 1996), to obtain Q and U parameters the difference between the two orthogonal states are done twice such that the final Q and U parameters are written as follows:

$$\begin{aligned} Q^+ = I_L^0 - a_1.I_R^0, \quad Q^- = I_L^{45} - a_2.I_R^{45}, \\ U^+ = I_L^{22.5} - a_3.I_R^{22.5}, \quad U^- = I_L^{67.5} - a_4.I_R^{67.5}, \\ Q = \frac{(Q^+ - Q^-)}{2}, \\ U = \frac{(U^+ - U^-)}{2}. \end{aligned} \tag{2.4}$$

Here, a_1, a_2, a_3 and a_4 are the scaling factors determined by minimizing the instrumental transmission effect causing the difference in intensity between the images in the left and right channels. The double subtraction method is used to better subtract the instrumental polarisation (Avenhaus et al., 2014; de Boer et al., 2019)

Q_ϕ and U_ϕ are the azimuthal Stokes vector expressed in polar coordinates as explained in Schmid et al. (2006). The Q_ϕ and the U_ϕ parameters can be written as:

$$\begin{aligned} Q_\phi &= -Q\cos 2\phi + U\sin 2\phi, \\ U_\phi &= -Q\sin 2\phi - U\cos 2\phi, \\ \phi &= 0.5\arctan\frac{U}{Q}. \end{aligned} \tag{2.5}$$

ϕ is the azimuthal angle with respect to the star's center.

The key advantage of polarised imaging is that due to the absence of ADI self-subtraction, an astrophysical signal is well resolved at smaller separations in case the object light is polarized. This is valid for light which is scattered by dust grains. A combined study of total intensity and polarimetric images is more powerful to constrain the properties of grains in disks.

2.3 Forward modeling of debris disk

The ADI technique as explained in previous sections is a powerful tool to enhance the detection contrast by distinguishing an astrophysical signal from the persisting speckle noise. However, while performing ADI the astrophysical signal is not completely suppressed in the reference frames $\mathcal{A}$ which when subtracted from the observed frames $\mathcal{I}$ induces a self-subtraction effect on the final image of the astrophysical signal $\mathcal{I}_{\rm f}$. The presence of self-subtraction biases the geometry and photometry especially of extended sources, such as disks as compared to point sources. To overcome the self-subtraction and perform accurate photometry, I have used the technique of forward modeling.

The technique of forward modeling can broadly be defined as a means of generating a model similar to the data and comparing them to extract accurate information of the astrophysical signal. Historically, forward modeling in the context of directly imaged exoplanets is defined as injecting a point-like source into the science image cube (containing a real planet signal) and post-processing the image cube with ADI-based algorithm. Minimizing the position and flux of the fake planet to the real planet gives the unbiased photometry of the planet (Galicher et al., 2018; Marois et al., 2010; Pueyo, 2016).

In case of extended objects, such as disks, injecting a fake disk into the image cube is more complicated because the disk image has a higher degree of freedom (in terms of geometry) compared to a point source. When using forward modeling to extract the photometry of a particular disk, a synthetic model of the disk could be injected into an empty data cube. This data cube should have the same dimension as the science image cube and can be free of speckle noise. The model is then processed with the same ADI algorithm that was used to process the science image cube. Minimizing the intensity between the post-processed disk data and the model provides the photometry of the disk.

Because of the varied morphologies of the circumstellar disks, the forward modeling is different for each system under study unlike the cases of point sources. For point sources, the only variable parameters are its position and flux which ease their characterization compared to that of the circumstellar disks'.

Throughout this thesis, I have used ADI-based KLIP algorithm to process the SPHERE data of different debris disks. Therefore, the forward modeling involves using the same algorithm on the science image and corresponding synthetic images. In order to use KLIP for forward modeling (KLIP-FM), first the synthetic image of the disk is convolved with the observed PSF and then normalised to obtain $\mathcal{I}_{\rm norm}$ similar to step 2 in Sect. 2.2.1.3.

Second, applying step 4 to 6 of Sect. 2.2.1.3, a KLIP reduced model is obtained using the same eigen vectors calculated for the data. Numerous synthetic images with varied geometrical properties can be processed using KLIP-FM to create a grid of reduced models.

The reduced χ^2 is calculated between the science image ($S_{i,j}$) and the reduced models ($M_{i,j}$) at i, j^{th} pixel and summed over the total number of pixels in the region of interest ($N_{\rm data}$). It is described as follows:

$$\chi^2_\nu = \frac{1}{\nu} \sum_{i,j=1}^{N_{\rm data}} \left(\frac{S_{i,j} - a.M_{i,j}(p)}{\sigma_{i,j}} \right)^2, \tag{2.6}$$

where ν is the degree of freedom $\nu = N_{\rm data} - N_{\rm params}$, $N_{\rm params}$ denote the number of free parameters and p the parameter space explored in these reduced models. The parameter a is the scaling factor between the science image and the reduced models. The noise term ($\sigma_{i,j}$) is derived from the azimuthal standard deviation in the science imaging removing the disk.

To identify a reduced model comparable to the science image, a χ^2 threshold is defined $\chi^2 \pm \sqrt{2\nu}$ and reduced models within this threshold are considered the best models. In case of an insufficient number of best models I consider 1% of the reduced models corresponding to the lowest χ^2 values to be the best models. It is important to have a significant number of best models falling within the threshold to plot the histograms corresponding to each parameter for the set of best models, although this criterion is somewhat arbitrary. From these histograms, the parameters for the best-fit model and corresponding errors can be derived. Throughout the thesis the correlation between the parameters creating the models has not been analysed as the primary aim is to find a model to perform spectroscopy. The synthetic image corresponding to the best-fit model is first convolved with the PSF and then scaled to a factor which is obtained by minimizing the reduced best-fit model to the science image. This scaled best-fit model is then used for extraction of photometry. The details of retrieving the scaling factor for each disk and its photometry are discussed in the subsequent chapters.

Using χ^2 analysis a comparable model to the data is obtained (hereafter best model). This method is fairly straight forward. Certainly, there are popular Bayesian techniques, such as the Markov chain Monte Carlo (MCMC, Foreman-Mackey et al., 2013) method which is extensively used for forward modelling of point sources, such as in Chauvin et al. (2015); Pueyo et al. (2015) and so on. For disk studies this technique has been used for polarimetric observations for example Engler et al. (2018b); Olofsson et al. (2016). However, in the presence of self subtraction in the ADI observations, there can be stronger degeneracies between models complicating the use of MCMC. Nevertheless, the χ^2 analysis through MCMC has been successfully done in Feldt et al. (2017); Milli et al. (2017). The prospects of MCMC has not been explored in this thesis. With a less aggressive ADI reduction algorithm, such as the masked classical ADI, the MCMC for forward modelling becomes more accessible as presented for debris disk HR4796 (Milli et al., 2017).

The core of this thesis is modeling the synthetic images of the disk which is done using a radiative transfer code originally developed by Augereau et al. (1999b) to model the debris

disk around HR 4796. Modeling a disk is essential not only for the purpose of overcoming the self-subtraction but also to set constrains on the morphological parameters of the disk under study. For total intensity images, such a method provides a pathway to extract the photometry and understand the morphology of the disk. With polarimetric images, the modeling process can further confirm the morphological constraints with additional accuracy.

2.3.1 GRaTer

GRaTer (Grenoble Radiative Transfer, Augereau et al., 1999b) code produces scattered light images of debris disk assuming it has a thin ring of planetesimal, the *parent ring*, where dust and grains are released by *collisional cascade*. GRaTer can be used as only a parametric model and also a model which involves Mie scattering where the grain parameters such as minimum size, porosity, composition of the grains etc can be controlled. Below I explain the process of using GRaTer to form 2d images of geometric parameters.

It uses a density distribution function $\rho_{\mathcal{G}}(r, z)$ and a scattering phase function $H(g, \theta)$ to develop the synthetic images of a disk under study as follows.

$$\mathcal{G} = \rho_{\mathcal{G}}(r, z) H(g, \theta), \tag{2.7}$$

$$\rho_{\mathcal{G}}(r, z) = \rho_0 \sqrt{2} \left[\left(\frac{r}{R_0} \right)^{-2\alpha_{in}} + \left(\frac{r}{R_0} \right)^{-2\alpha_{out}} \right]^{-1/2} \exp\left(- \frac{|z|}{\zeta_0 (r/R_0)^{\beta_f}} \right)^{\gamma}, \tag{2.8}$$

where r is the radial distance in AU in disk coordinate and at a distance of R_0 the dust density peaks. α_{in} and α_{out} are radial slopes. At $r = R_0$, $\alpha_{in} > 0$, $\alpha_{out} < 0$ and ρ_0 is the density on the midplane. β_f is the radial flaring index and z is the distance to the midplane in AU. The exponential part of Eq. (2.8) defines the vertical density distribution of the disk where the scale height is $h = \zeta_0 / R_0$. The radial distribution can also include an eccentricity e in the disk, inducing an offset from the star.

For the case of total intensity, the Henyey Greenstein (HG) phase function is used as the scattering phase function taking the form as given below.

$$H(g, \theta) = f_{TI}(\theta) = \frac{1 - g^2}{4\pi (1 + g^2 - 2g \cos\theta)^{3/2}} \text{ such that } \int_0^{\pi} f_{TI}(\theta) \sin\theta d\theta = \frac{1}{2\pi}, \tag{2.9}$$

where, TI stands for total intensity.

The θ is the scattering angle in the HG phase function which is defined in cylindrical coordinates as:

$$\theta = \arccos\left(\frac{\left(\sqrt{x_d^2 + y_d^2} \right) \sin(i) \sin(\theta_*) + z_d \cos(\mathrm{i})}{\sqrt{x_d^2 + y_d^2 + z_d^2}} \right), \tag{2.10}$$

where, x_d, y_d and z_d are the coordinates of the disk elements in the disk plane and $\theta_* = \arctan(y_d/x_d)$. i is the inclination of the disk.

The parameter g corresponds to the anisotropic scattering factor or asymmetry parameter. This factor is normalised such that it takes values between [-1,1], here, $g = 0$ indicates isotropic scattering of all the grains where forward scattering is when $0 < g \leq 1$ and back scattering is $-1 \leq g < 0$.

It has been commonly found that a single HG phase function can show discrepancies in fitting a debris disk image as seen in HR 4796 (Milli et al., 2017) and HD 32297 (Currie et al., 2012). Considering one of the phase function assumes a positive asymmetry parameter and the other assumes a negative value, a combination of phase function will account for both forward and back scattering. As a result, to obtain a phase function with a linear combination of two HG functions the following equation can be used

$$H(g, \theta) = w.f_{TI}(g_1, \theta) + (1 - w).f_{TI}.(g_2, \theta). \tag{2.11}$$

Here, w is the percentage of weight to be put for each of the phase function.

Even though, the DPI observations do not suffer from *self-subtraction*, modeling such data can put constrains on the physical parameters of a debris disk. A Rayleigh approximation to the HG phase function f_{TI} can mimic the first order angular dependency of linear polarisation. Therefore, models for DPI observations can be obtained using a phase function given in Eq.(2.12).

$$H(g, \theta) = f_P(\theta) = f_{TI}(\theta)\frac{1 - \cos^2\theta}{1 + \cos^2\theta}. \tag{2.12}$$

It should be noted that using a HG function or a combination of HG function and a Rayleigh function to depict the phase function in the debris disk is an approximation. This choice of using the functions is based on the experimentally measured phase functions for the scattering by the zodiacal dust grains (e.g. Lienert et al. 1976) or cometary dust (e.g. Bertini et al., 2017; Frattin et al., 2019).

2.3.1.1 Effect of α_{in} and α_{out}

The radial dependence from R_0 which is the location of ring is given by $\alpha_{\rm in}$ and $\alpha_{\rm out}$. In Fig. 2.4 I present the output of a GRaTer for an array of a few parameters. The parameters which are constant for this panel are $R_0 = 100$ au, $h = 0.04$ and $e = 0$. Comparing the images a) and b) a clear distinction in the width of the planetesimal belts can be seen. This means that with stronger radial slopes, a higher peaked radial distribution can be obtained. The variation in the width can also be seen in the plots in panel Fig. 2.4 c) and d). The radial slopes shape the geometry of the disk providing clues of the dust dynamics, for example whether the disk is shaped by the radiation pressure, planetary perturbation or by other external perturbation.

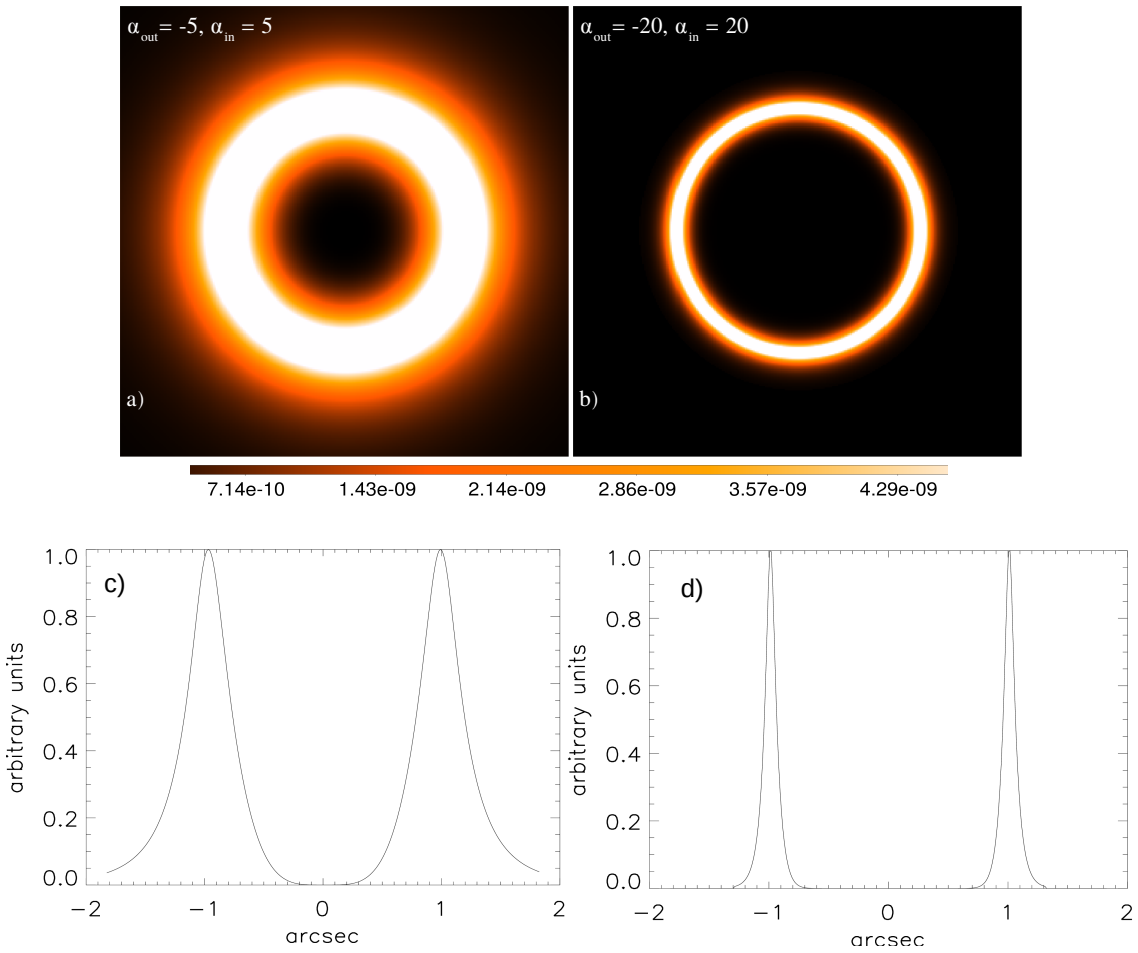

Figure 2.4 *– a) and b) are the GRaTer images, using the geometrical parameters for $R_0 = 100$ au, h=0.04 and e=0. The FOV of these images are $3.675'' \times 3.675''$. The colorbar represent the brightness scale of both the images. c) and d) are the plots representing the density variation across the disk corresponding to images a) and b) and normalised to the maximum of the image intensities.*

2.3.1.2 Effect of the scale height

The scale height h is the ratio of the vertical width of the disk at the location of R_0 to the horizontal location of R_0. As shown in Fig. 2.5 the value assumed for h is significantly lower in image a) and that is why the disk is visibly thinner in a) than in image b). The variation in the vertical height can be constrained accurately for an edge on disk compared to a face on disk. This variation in the vertical density can be seen in Fig. 2.5 c) and d) indicating that the planetesimal belt in image a) is thinner than in image b). In these simulated images, I assumed the values of constant parameters as $R_0 = 100$ au, $\alpha_{in} = 5$, $\alpha_{out} = -5$, $i = 89°$ and $e = 0$.

A combination of physical phenomena, such as the effect of radiation pressure and grains collisions would lead to debris disks having a natural vertical thickness. Thébault (2009) suggested to consider $h_{min} = 0.04 \pm 0.02$ and should remain fairly constant for debris disk in general.

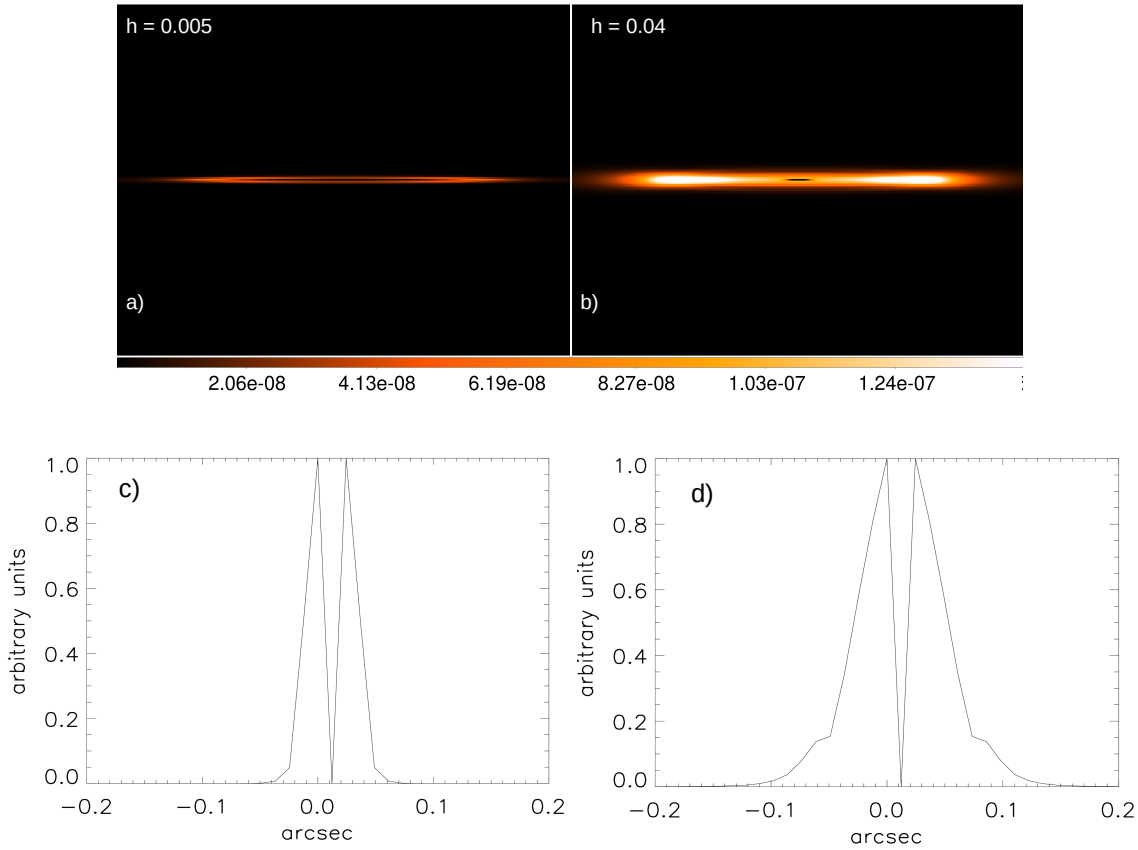

Figure 2.5 *– a) and b) are the GRaTer images, using the geometrical parameters* $R_0 = 100$ *au,* $\alpha_{in} = 5$, $\alpha_{out} = -5$, $i = 89°$ *and* $e = 0$. *The FOV of these images are* $3.675'' \times 3.675''$. *The colorbar represent the brightness scale of both the images. c) and d) are the plots representing the density variation across the disk corresponding to images a) and b) and normalised to the maximum of the image intensities.*

2.3.1.3 Effect of eccentricity

In Fig. 2.6 the effect of eccentricity e is shown. For face-on disks as represented in the simulated Fig. 2.6 a) the impact of eccentricity is visible as an asymmetry in the brightness. It is even more prominent for an inclined disk where a "needle" like feature can emerge as seen in Fig. 2.6 b). The variation in the intensity across the horizontal axis of the disk can be seen in Fig 2.6 c) where the intensity is plotted for a face-on disk as shown in the GRaTer image in Fig 2.6 a).

A shift from the centro-symmetric nature of the disk can be adjusted with this parameter which would provide a different aphelion '*ah*' and perihelion '*ph*' distance from the center of a star. The eccentricity can be defined by $\mathrm{e} = \dfrac{ah - ph}{2R_0}$, here R_0 is the average radii as defined for GRaTer in Eq (2.8). For $R_0 = 100$ au and $e = 0.25$ a shift of 50 au between the aphelion and perihelion is seen. The brightness asymmetry observed in several debris disks can be related to eccentricity.

2.3.1.4 Effect of anisotropic scattering factor and inclination

The anisotropic scattering factor g gives the measure of forward or back scattering effect in the debris disk. The effect of inclination angle on the disk can be seen comparing the Fig. 2.7 and Fig. 2.8. The effect of a combination of the anisotropic scattering factor g and the inclination angle can be seen in Fig. 2.8. All the images in Fig. 2.8 have the same density parameters with inclination = 80°, α_{in} = 5, α_{out} = -5, h = 0.04 and e = 0.0 for a position angle of 90°. The scattering angles probed differ for different inclinations of the disk. The intensity of forward scattering peak increases with increasing value of g for case of total intensity as seen in Fig. 2.9. This effect is especially visible for highly inclined disks and therefore a strong forward scattering peak is seen in Fig. 2.8. With a combination of two g values, an additional back scattering peak can be noticed in Fig. 2.8 f).

The intensity of phase function is also dependent on the scattering angle of the disk. To visualize the effect scattering phase function as a function of scattering angle, the phase function is plotted for different values of g parameters in Fig. 2.9. The solid lines corresponding to the polarimetric phase function have a different shape than the dashed profiles corresponding to phase function for the models of total intensity observations. It is to note that the function considered for polarimetric phase function is a combination of Rayleigh's and Henyey-Greenstein function as seen in Eq. (2.12). For g=0, the maximum scattering of polarised intensity would occur at 90°. For anisotropic scattering with g>0 it is observed that the polarimetric scattering peak shifts towards smaller scattering angle. The effect of forward scattering peak at smaller scattering angle for polarimetric observations is commonly observed for example in HD 32297, HR 4796, HD 61005, etc.

The HG parameter gives a sense of the type of grains. Being able to extract the scattering phase function is an important step because it can enhance the understanding of the grain type and its composition in a disk. This has been successfully shown by (Milli et al., 2017) for the bright debris disk around HR4796.

A grid of models, keeping R_0, α_{in}, α_{out}, h, e, g as free parameters, is processed through KLIP-FM. It should be noted that combination of certain parameters can have a degenerate models. Therefore, I perform a reduced χ^2 analysis as well as visual inspection to find an optimum best model which will be discussed in upcoming chapters.

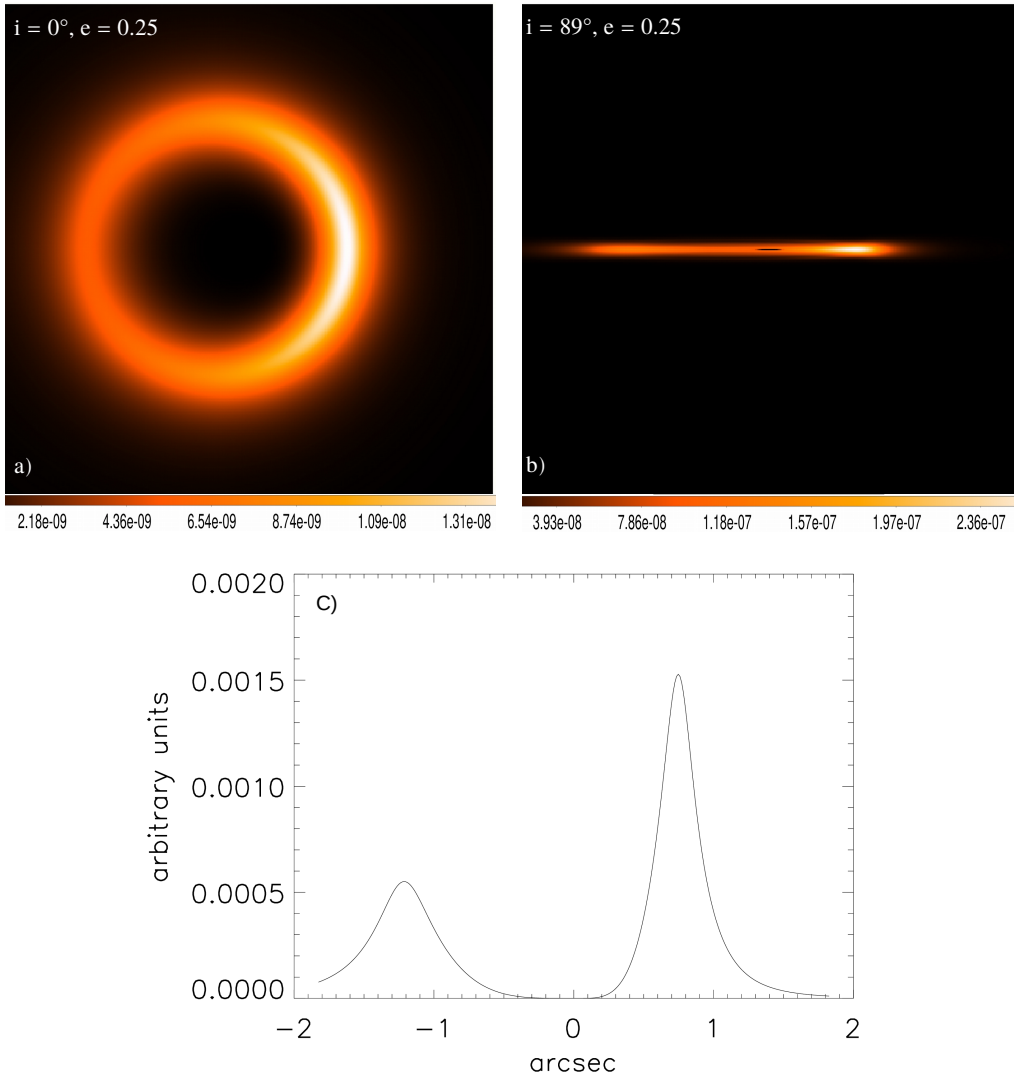

Figure 2.6 *– a) and b) are the GRaTer images, using the geometrical parameters* R_0*=100 au,* $\alpha_{in} = 5$*,* $\alpha_{out} = -5$*. The FOV of these images are* $3.675'' \times 3.675''$*. The colorbars represent the brightness scale in the images. c) is the plot representing the density variation across the disk corresponding to images a) and normalised to the maximum of the image intensities.*

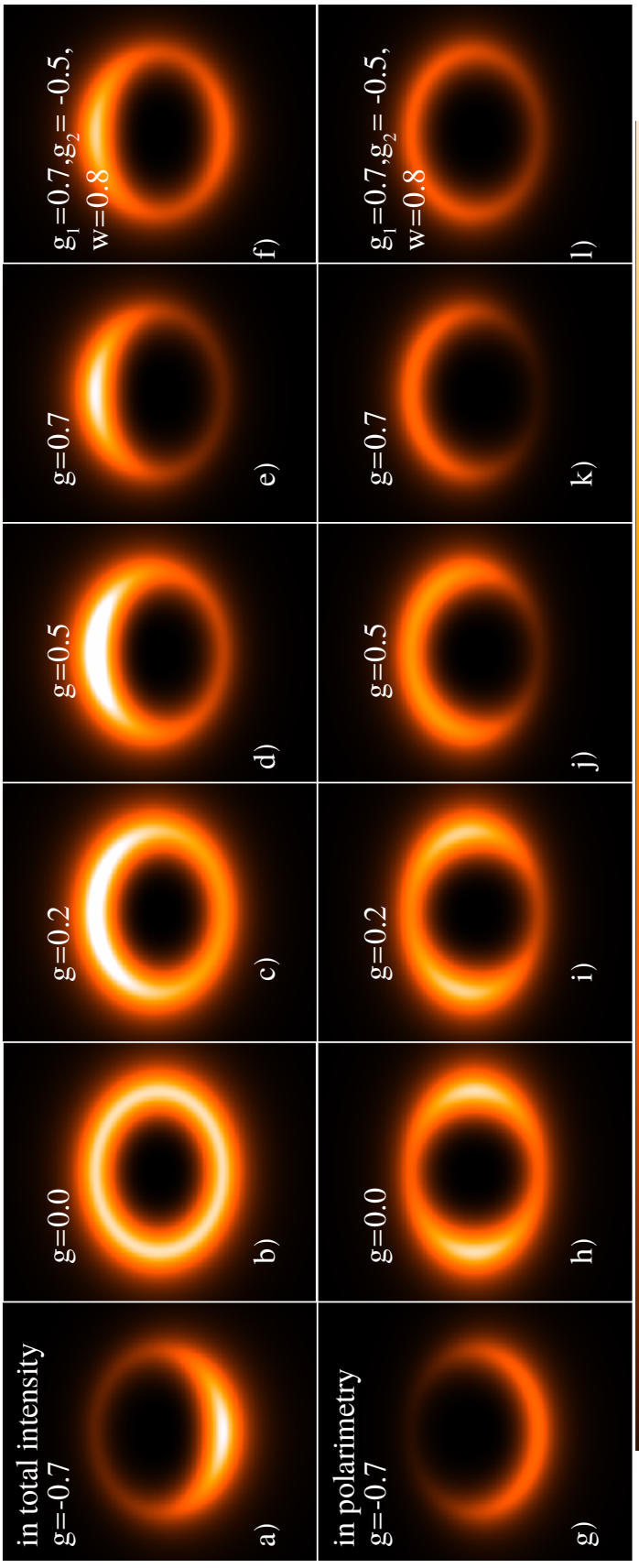

Figure 2.7 *– GRaTer images including both geometrical and phase parameters to understand the affect of g in total intensity and polarimetry for an inclination i=40°. The FOV of these images is* $3.675'' \times 3.675''$*. The colorbar represent the brightness scale of all the images.*

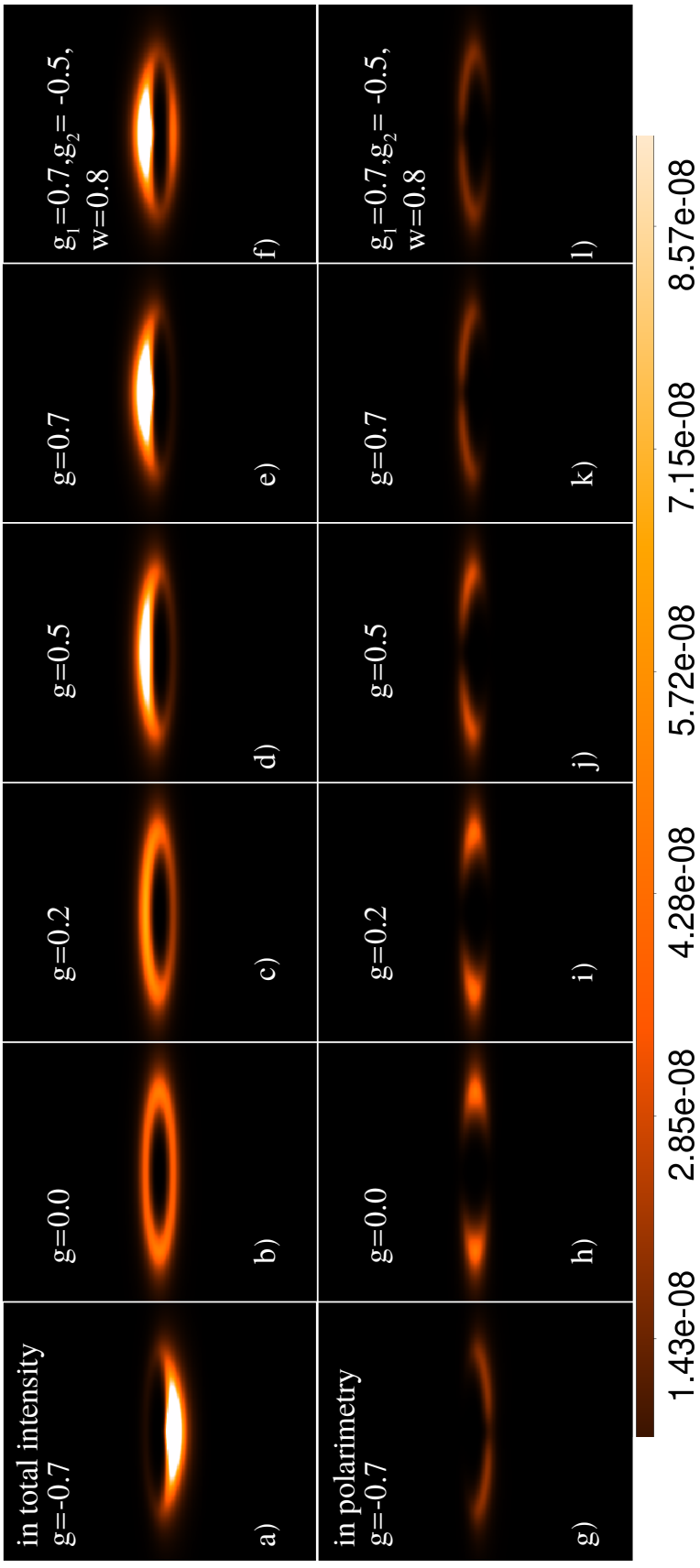

Figure 2.8 *– GRaTer images including both geometrical and phase parameters to understand the affect of g in total intensity and polarimetry for an inclination i=80°. The FOV of these images is* $3.675'' \times 3.675''$*. The colorbar represent the brightness scale of all the images.*

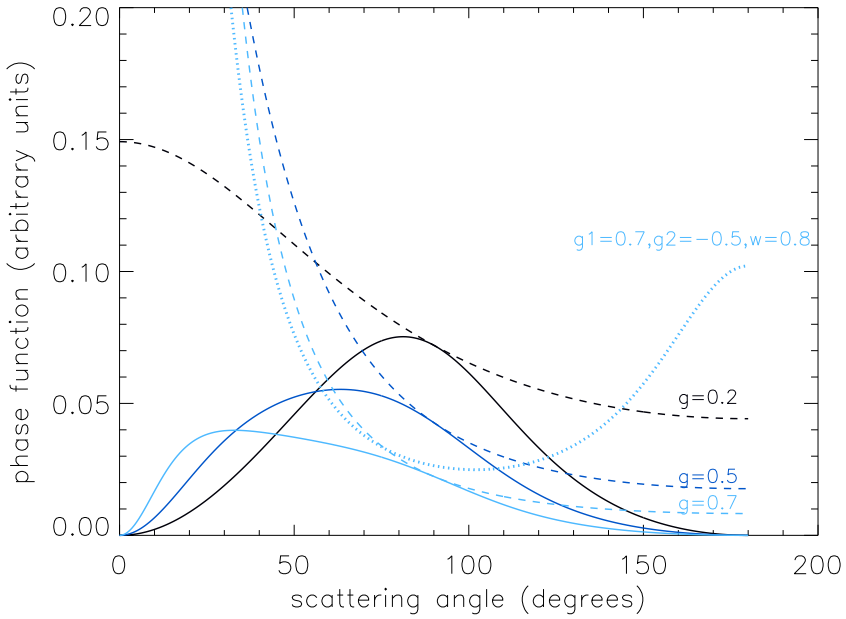

Figure 2.9 *– Plot of phase functions for different values of g. The solid lines correspond to polarimetric phase function and the dashed line for the total intensity and the dotted sky blue line corresponds to the combination of 2 g parameters for total intensity.*

CHAPTER 3

The inclined bright debris disk HD 32297

3.1 Summary of the work 46
3.1.1 Introduction 46
3.1.2 Best Models and Photometry 46
3.1.3 Grain Models 47
3.1.4 Results 49
3.2 Article on HD 32297 49
3.3 Supplements 66
3.3.1 Histograms and selection of best-fit model 66
3.3.2 Error measurement with fake disk 66
3.3.3 Comparison with ALMA observation 66

This chapter provides a detailed analysis of the debris disk HD 32297. Section 3.1 presents a summary of the study that has resulted in an article accepted in Astronomy & Astrophysics. The article can be found in Sect. 3.2. Further details of the analysis is discussed in Sect. 3.3.

HD 32297 has a debris disk extending up to 1680 au (Schneider et al., 2014) around an A6V star (Moór et al., 2017), which is 133 pc (Gaia Collaboration, 2018) away. This disk was first observed with HST by Schneider et al. (2005) and then with several ground-based telescopes (e.g. Kalas, 2005). Because of the disk's extension, symmetry and brightness, it was meant as a test-bed for modeling and spectral analysis of SPHERE data. Another motivation to study this disk was to investigate the likelihood of a gap within the disk as observed by Asensio-Torres et al. (2016) seen in Fig 3.1. Finally, with ALMA, millimeter observations put some constraints on the disk's structure (MacGregor et al., 2018) making it interesting to be compared with SPHERE's NIR observations. The Fig. 3.2 shows the concavity towards the north-east side of the disk, at large separation and the ALMA observation is overlaid on the HST observation. Also, ALMA observed an abundance of CO within the disk as hypothesized in Kral et al. (2013), can make smaller grains within the disk to survive for a longer period of time. Therefore, the motivation to retrieve a spectrum and then study the grain type present in the disk was drawn.

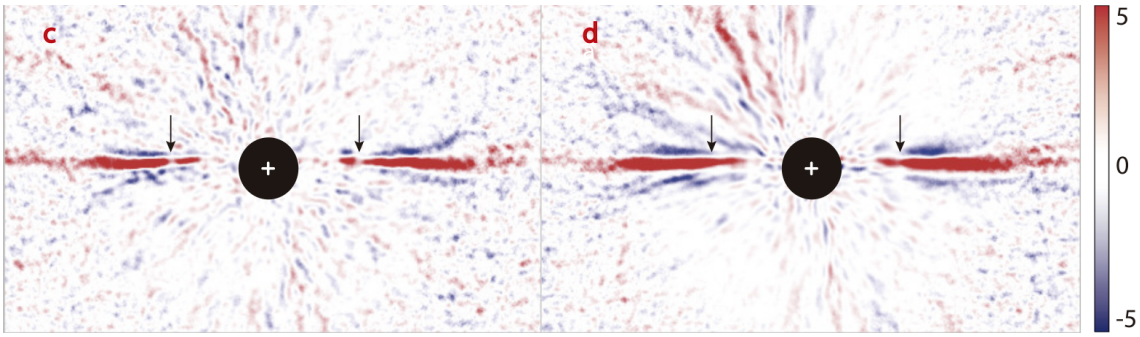

Figure 3.1 *– The S/N map of the disk as observed in Asensio-Torres et al. (2016) in H band. c) is the S/N map of TLOCI reduced image and d) S/N map of the PCA reduced image. Both the images are in $[-5\sigma \times 5\sigma]$ linearly scale. The arrows point to potential gap at 0.75″ of north-east side and 0.65″ at south-west side of the disk.*

3.1 Summary of the work

3.1.1 Introduction

This work involves the reduction and analysis of the debris disk HD 32297 as observed in YJH bands of NIR wavelengths. The processed data show: 1) the disk is resolved as close as a stellocentric distance of 20 au, and 2) the back side of the disk is resolved for the first time as seen in the top two panel of Fig. 3.3. The disk seems continuous without any gap as seen in all the images of Fig. 3.3 unlike observed in Asensio-Torres et al. (2016). The concavity of the disk beyond 2″ as earlier seen in the HST images (Schneider et al., 2014) is also seen in the images in Fig. 3.4 which is multiplied by the square of the radial scale. Additionally, the polarimetric $Q_{\rm phi}$ image showed intensity peaks corresponding to the disk's ansae. The lowermost panel in Fig. 3.3 represents the $Q_{\rm phi}$ polarimetric image.

3.1.2 Best Models and Photometry

Using GRaTer a grid of synthetic models are created and then processed through the KLIP algorithm. Then a best-fit model is retrieved and the geometrical parameters is constrained from a χ^2 analysis. This analysis favoured a positive/negative combination of two-parameter HG phase function, the positive g supporting the forward scattering for the front side of the disk and the negative g supporting the back-scattering in the back side of the disk. However, while modeling the polarimetric Q_{phi} image, a single g value larger than the value found for total intensity images was favoured (details in Sect. 4.3 of the article Bhowmik et al. (2019)), suggesting an intensity peak at scattering angle smaller than 20°.

The best-fit model was used to retrieve the surface brightness (measured at a separation between 20-266 au) and average reflectance in contrast/arcsec^2 (measured at a separation between 26-106 au) of the disk. From the surface brightness profiles of the disk, a symmetric nature between the north-east and south-west side of the disk is confirmed and a 15%

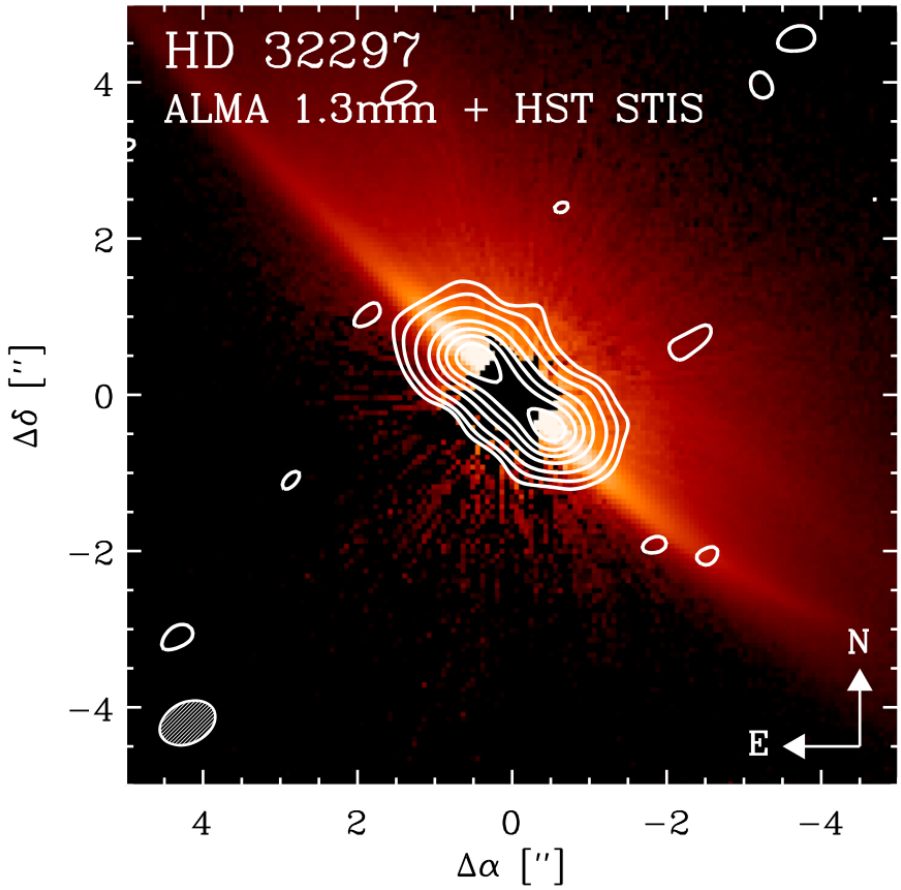

Figure 3.2 *– The ALMA 1.3 mm continuum emission is overlaid as white contours as seen in MacGregor et al. (2018) over the HST STIS images as seen in Schneider et al. (2014) and on the bottom left corner of this image the beam size of ALMA is seen which is about 0.76″×0.41″.*

fraction of polarisation is also seen comparing the profiles of total intensity and polarimetric science images in J band. The disk's blue color at NIR wavelengths is established from the slope in the reflectance plot.

3.1.3 Grain Models

The average reflectance was then compared to a synthetic spectrum obtained from analysing the particle size distribution within the disk for different grain compositions: astro-silicates, porous astro-silicate (P=0.25) and one to one mixture of astro-silicate and icy grains. This analysis was done with the help of a simpler form of GRaTer by parameterising the minimum grain size and the power-law index of the particle size distribution. The morphological parameters were kept constant to the optimal values derived from the modeled synthetic images as explained above.

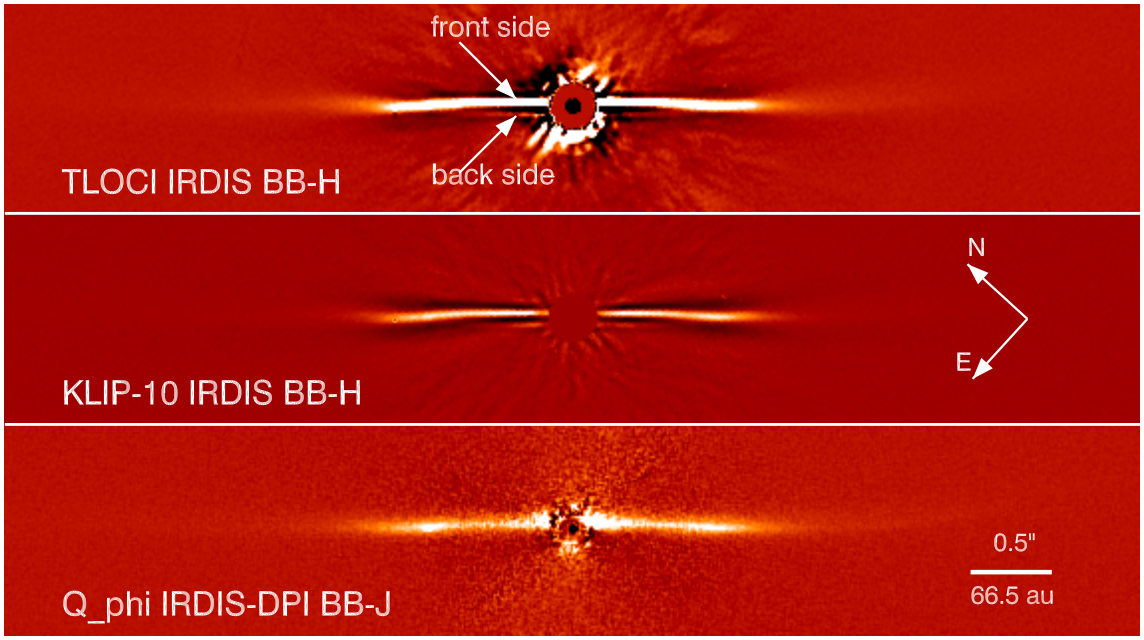

Figure 3.3 *– Top to bottom: The TLOCI image with front and back side of the disk labelled, the KLIP image and the $Q_{\rm phi}$ polarimetric image. All the images are rotated to 90° - PA and cropped at $7'' \times 1.3''$. The TLOCI processed, KLIP processed and $Q_{\rm phi}$ images are scaled linearly between $[-1 \times 10^{-5}, 1 \times 10^{-5}]$.*

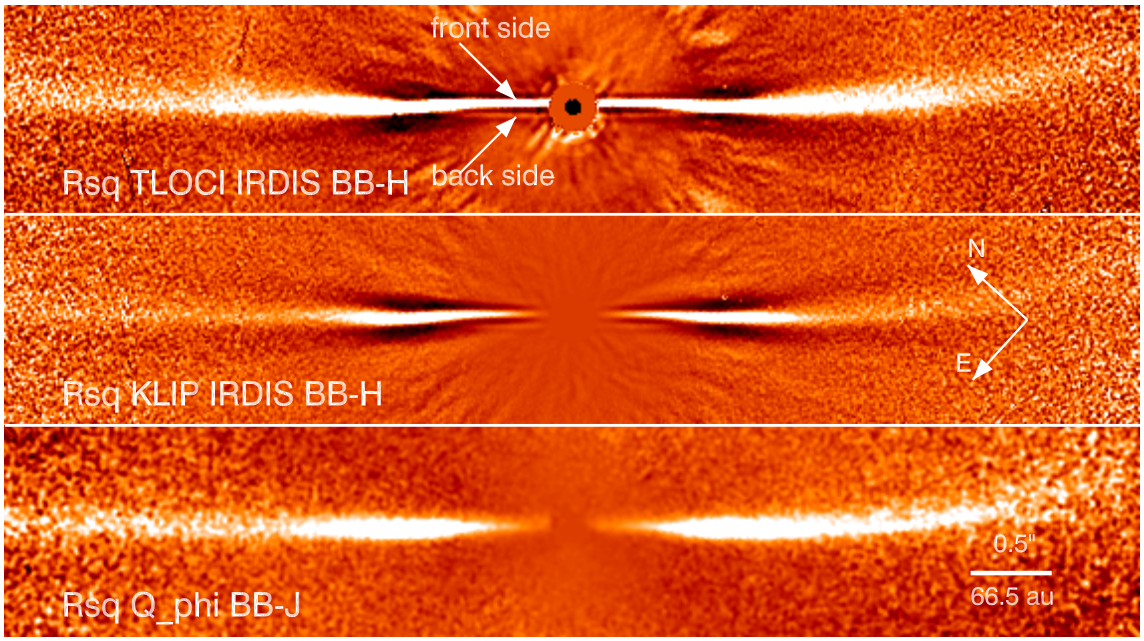

Figure 3.4 *– All the three images of Fig. 3.3 multiplied by the square of the radial scale. All the images are rotated to 90° - PA and cropped at $7'' \times 1.3''$. All the images are scaled linearly between [0.015,-0.025].*

3.1.4 Results

Fitting the spectra obtained by modeling the particle size distribution to the average reflectance provided an important result, which indicated that the minimum grain size was well below the blow-out size for every composition. This result is in contradiction to the traditional belief that grains smaller than the *blowout size* are transported out of the system due to radiation pressure (Kral et al., 2013; Krivov et al., 2006). The possible explanations which I had looked into for the presence of sub-micron grains are a combination of a steady-state collisional cascade, collisional avalanche mechanism (Grigorieva et al., 2007; Thebault & Kral, 2018) and gas drag (because CO has been observed in MacGregor et al., 2018; Takeuchi & Artymowicz, 2001) as detailed in Sect. 7.2 and 7.3 of the article Bhowmik et al. (2019). A double belt scenario suggested in previous studies (Donaldson et al., 2013; Rodigas et al., 2014) offers more potential for avalanche mechanism to generate (and sustain) a significant amount of smaller grains in a debris disk (Thebault & Kral, 2018), but with our observation, the large quantity of gas seemed the most likely explanation. The significant amount of gas can retain the unbound grains within the system longer than the radiation pressure blow-out time as predicted in Takeuchi & Artymowicz (2001). This work has resulted in an article accepted by Astronomy & Astrophysics on August 2019.

3.2 Article on HD 32297

A&A 630, A85 (2019)
https://doi.org/10.1051/0004-6361/201936076

Astronomy & Astrophysics

Spatially resolved spectroscopy of the debris disk HD 32297

Further evidence of small dust grains⋆,⋆⋆

T. Bhowmik[1], A. Boccaletti[1], P. Thébault[1], Q. Kral[1], J. Mazoyer[2,⋆⋆⋆], J. Milli[3,8], A. L. Maire[4,7], R. G. van Holstein[10], J.-C. Augereau[3], P. Baudoz[1], M. Feldt[4], R. Galicher[1], T. Henning[4], A.-M. Lagrange[3], J. Olofsson[4,5,6], E. Pantin[9], and C. Perrot[1,5,6]

[1] LESIA, Observatoire de Paris, Université PSL, CNRS, Sorbonne Université, Université de Paris, 5 place Jules Janssen, 92195 Meudon, France
e-mail: Trisha.Bhowmik@obspm.fr
[2] Jet Propulsion Laboratory, California Institute of Technology, 4800 Oak Grove Drive, Pasadena, CA 91109, USA
[3] CNRS, IPAG, Université Grenoble Alpes, 38000 Grenoble, France
[4] Max-Planck-Institut für Astronomie, Königstuhl 17, 69117 Heidelberg, Germany
[5] Instituto de Física y Astronomía, Facultad de Ciencias, Universidad de Valparaíso, Avenue Gran Bretaña 1111, Valparaíso, Chile
[6] Núcleo Milenio Formación Planetaria â NPF, Universidad de Valparaíso, Avenue Gran Bretaña 1111, Valparaíso, Chile
[7] STAR Institute, Université de Liège, Allée du Six Août 19c, 4000 Liège, Belgium
[8] European Southern Observatory, Alonso de Córdova 3107, Casilla 19001 Vitacura, Santiago 19, Chile
[9] Laboratoire AIM, CEA/DRF – CNRS – Université Paris Diderot, IRFU/SAp, UMR 7158, 91191 Gif-sur-Yvette, France
[10] Leiden Observatory, Leiden University, PO Box 9513, 2300 RA Leiden, The Netherlands

Received 12 June 2019 / Accepted 13 August 2019

ABSTRACT

Context. Spectro-photometry of debris disks in total intensity and polarimetry can provide new insight into the properties of the dust grains therein (size distribution and optical properties).
Aims. We aim to constrain the morphology of the highly inclined debris disk HD 32297. We also intend to obtain spectroscopic and polarimetric measurements to retrieve information on the particle size distribution within the disk for certain grain compositions.
Methods. We observed HD 32297 with SPHERE in Y, J, and H bands in total intensity and in J band in polarimetry. The observations are compared to synthetic models of debris disks and we developed methods to extract the photometry in total intensity overcoming the data-reduction artifacts, namely the self-subtraction. The spectro-photometric measurements averaged along the disk mid-plane are then compared to model spectra of various grain compositions.
Results. These new images reveal the very inner part of the system as close as 0.15″. The disk image is mostly dominated by the forward scattering making one side (half-ellipse) of the disk more visible, but observations in total intensity are deep enough to also detect the back side for the very first time. The images as well as the surface brightness profiles of the disk rule out the presence of a gap as previously proposed. We do not detect any significant asymmetry between the northeast and southwest sides of the disk. The spectral reflectance features a "gray to blue" color which is interpreted as the presence of grains far below the blowout size.
Conclusions. The presence of sub-micron grains in the disk is suspected to be the result of gas drag and/or "avalanche mechanisms". The blue color of the disk could be further investigated with additional total intensity and polarimetric observations in K and H bands respectively to confirm the spectral slope and the fraction of polarization.

Key words. techniques: image processing – stars: individual: HD 32297 – techniques: high angular resolution – methods: data analysis – infrared: planetary systems

1. Introduction

Debris disks are a class of circumstellar disks in which the dust content is thought to be continuously replenished by collisions of planetesimals, usually distributed in a single belt or in multiple belts. The dust present in these disks can be observed by scattered light imaging and/or thermal emission. Morphological and photo-spectroscopic analysis provide constraints on the spatial distribution and physical properties of grains present in a planetary system. Even though debris disks are believed to be depleted in gas, a number of them are significantly gas rich, very likely because of second-generation production of gas released when planetesimals collide and produce the observed dust (Kral et al. 2017). In addition, debris disks frequently show identifiable structures like blobs (AU Mic, Boccaletti et al. 2018), warps (β Pic, Mouillet et al. 1997), multiple belts (Bonnefoy et al. 2017; Boccaletti et al. 2019, HIP 67497 and NZ Lup), asymmetries (Mazoyer et al. 2014, HD 15115), and other irregularities in the disk. These structures might be sculpted by transient breakups of massive bodies (Jackson et al. 2014; Kral et al. 2015), stellar flybys (Lestrade et al. 2011), stellar companions (Thébault 2012), or interactions with the inter-stellar medium (ISM;

⋆ Reduced images are also available at the CDS via anonymous ftp to cdsarc.u-strasbg.fr (130.79.128.5) or via http://cdsarc.u-strasbg.fr/viz-bin/cat/J/A+A/630/A85
⋆⋆ Based on data collected at the European Southern Observatory, Chile under the programs 098.C-0686(A) and 098.C-0686(B).
⋆⋆⋆ Sagan NHFP Fellow.

Hines et al. 2007; Kalas 2005), or be owing to the presence of gas (Lyra & Kuchner 2013) within the disk. One of the most frequently invoked explanations for the presence of most of these structures is, however, the perturbing effect of a planet (Thebault et al. 2012). In this scenario, structures can be the telltale signature of undetected planets, such as in the case of β Pictoris b, which was first inferred indirectly from a warp in the disk and later imaged directly confirming the prediction (Mouillet et al. 1997; Lagrange et al. 2009).

HD 32297 is an A-type star (Silverstone 2000) ($V = 8.14 \pm 0.01$, $J = 7.687 \pm 0.024$, $H = 7.624 \pm 0.051$, $K = 7.594 \pm 0.018$) located at 133 pc (*Gaia* DR2, Gaia Collaboration 2018). The age of the star is estimated to be $\gtrsim$15 Myr (Rodigas et al. 2014) and <30 Myr (Kalas 2005). A fractional luminosity of $L_{\rm IR}/L_\star \geq 2.7 \times 10^{-3}$ found with the Infrared Astronomical Satellite (IRAS, Silverstone 2000) provides evidence for the presence of cold dust arranged in a belt. This high fractional luminosity makes it one of the brightest debris disks known to date (e.g., Thebault & Kral 2019). The disk was first resolved in scattered light by the *Hubble* Space Telescope (HST) NICMOS as an edge-on system and detected up to radial distances of 400 au (Schneider et al. 2005). A significant surface brightness asymmetry (southwest ansae brighter than northeast ansae) was reported and attributed tentatively to the presence of an unseen planet. Kalas (2005) detected the disk at larger separations (400 to 1680 au) from the ground with Keck in the R band and measured a blue color when comparing to the HST near-infrared (NIR) data.

In apparent contradiction to the scattered light observations of Kalas (2005) and Schneider et al. (2005), mid-infrared (MIR) observations show that the northeast side appears brighter than the southwest side at 0.6″ (Fitzgerald et al. 2007a) and beyond 0.75″ (Moerchen et al. 2007), although the impact of the angular resolution and signal to noise ratio (S/N) in these images could be questionable. Maness et al. (2008) and Mawet et al. (2009) observed a similar brightness asymmetry to Schneider et al. (2005) and Kalas (2005) in millimeter emission and K band respectively, but still with low angular resolution.

At large distances, as observed with Keck and confirmed with HST/NICMOS, the disk appears bowed, which has been interpreted as the possible interaction of small dust grains residing at large distances with the ISM (Debes et al. 2009). Rodigas et al. (2014) confirmed the bow shape of the disk at the L' band. Recently, Lee & Chiang (2016) showed that similar structures could also be the result of an interaction between a planet in an eccentric orbit and planetesimals perturbed by radiation pressure. The presence of small dust grains in a large halo has been confirmed with very deep HST/STIS observations (Schneider et al. 2014).

With the advance of high-contrast imaging, Boccaletti et al. (2012), Currie et al. (2012) and Esposito et al. (2014) were able to resolve the disk in the NIR as an inclined belt (~88°) located at ~130 au (after correcting for the new *Gaia* distance). According to Boccaletti et al. (2012), there is no significant brightness asymmetry between the two sides of the disk in H and K bands as observed with NACO, while Currie et al. (2012) suggest the southwest side to be brighter than the northeast side at r = 35–80 au.

High-contrast polarimetry combined with total intensity in the NIR was first achieved by Asensio-Torres et al. (2016) with Subaru/HiCIAO observations, and with the aim to break degeneracies on the geometrical parameters and grain properties. They reported a gap in the total intensity H band data, which was not visible in their polarimetric data.

Finally, the most recent observations were carried out with ALMA by MacGregor et al. (2018, hereafter MG18) who concluded that at millimeter wavelengths the disk is composed of a planetesimal belt with an inner edge at 78 au and a outer edge at 122 au, and an extended halo up to 440 au. The presence of millimeter grains in the halo complicates the understanding of the large bow, which is expected to be populated with loosely bound grains placed on very eccentric orbits by stellar radiation pressure (Strubbe & Chiang 2006; Thébault & Wu 2008) that should be sensitive to interactions with the ISM. We note however that there are some other alternatives and the ALMA halo may be explained as the presence of a scattered disk (Geiler et al. 2019).

Furthermore, CO gas emission (Greaves et al. 2016, MG18) was detected with ALMA corresponding to a total mass of $\sim 7 \times 10^{-2}\, M_\oplus$ derived from an optically thin CO isotopolog (Moór et al. 2019). This large quantity of gas could interact and drag the dust in this system (Takeuchi & Artymowicz 2001). The smallest bound grains would be pushed backwards and the unbound grains would be slowed down and may accumulate in greater quantity than in gas-depleted systems.

Modeling of the spectral energy distribution (SED) suggests that the main belt is populated with sub-micron grains (Fitzgerald et al. 2007a; Currie et al. 2012), which is in agreement with the color index measured between visible and NIR by Kalas (2005). The presence of such sub-micron grains is unexpected, because they should be smaller than the blowout size due to radiation pressure, and should therefore be ejected on very short timescales (Kral et al. 2013). Moreover, taking into account the size of the belt inferred by Boccaletti et al. (2012) and using photometry from *Herschel*, Donaldson et al. (2013) were able to draw constraints on the grain composition. These latter authors concluded that the system is made of an inner warm belt at $\geq$1.1 au, and an outer ring at 110 au populated with $\geq 2.2\,\mu$m, high-porosity grains consistent with cometary-like composition. However, this result was questioned by Rodigas et al. (2014) who favored pure icy grains instead.

In this paper we present new high-contrast imaging observations of HD 32297 with Spectro-Polarimetric High-contrast Exoplanet Research (SPHERE, Beuzit et al. 2019) at VLT in Chile, in the NIR from Y to H band complemented with polarimetric observations in the J band. With the new observations at NIR wavelengths, we resolve the disk at separations as close as 0.15″ and perform a spectral analysis. We briefly discuss the observational technique and the data reduction for total intensity and polarimetric data in Sect. 2. The disk features seen in the images are described in Sect. 3. The procedure of the modeling and parametric study is presented in Sect. 4. In Sect. 5, we describe how the photometry is retrieved from the images in the various spectral channels, for both total intensity and polarimetry. The resulting spectrum is compared to various grain models in Sect. 6. Finally, we discuss the implication of the colors in terms of grain sizes in Sect. 7.

2. Observation and data reduction

2.1. SPHERE

SPHERE is an instrument installed at the VLT for high-contrast direct imaging of giant planets around young nearby stars (Beuzit et al. 2019). Its combination of extreme adaptive optics (AO, Fusco et al. 2014) and advanced coronagraphy has allowed observation of circumstellar disks from the ground. SPHERE consists of three instruments: the Infra-Red Dual-beam Imager

Table 1. SPHERE observation log.

Data UT	Prog. ID	Filter	PC	Field rotation (°)	DIT (s)	T_{exp} (s)	Seeing (″)	τ_0 (ms)	TN (°)
2016-12-19	098.C-0686(A)	IRDIS-BB_H		25.16	64	7168	0.72	8.8	−1.75
2016-12-19	098.C-0686(A)	IFS-YJ		25.42	64	7168	0.72	8.7	−1.75
2016-12-16	098.C-0686(B)	IRDIS-DPI-BB_J	10	Stabilized	64	5120	0.47	8.0	−1.7

Notes. From left to right: the observation data, program ID, filter combination, the number of polarimetric cycle (PC), the total field rotation in degrees, the individual integration time of each frame (DIT) in seconds, the true time in seconds (T_{exp}), the DIMM seeing in arcseconds, τ_0 the correlation time in milleseconds and the true north correction angle in degrees (TN).

and Spectrograph (IRDIS, Dohlen et al. 2008), the Integral Field Spectrograph (IFS, Claudi et al. 2008), and the Zurich IMaging POLarimeter (ZIMPOL, Thalmann et al. 2008). IRDIS is a dual band imager using two narrowband or broadband filters in the Y, J, H, or K bands (Vigan et al. 2010). The IFS is a spectro-imager which delivers 39 simultaneous images across the YJ (IRDIFS mode) or YJH (IRDIFS-ext mode) bands. These two instruments can be used for parallel observations with the IRDIFS mode.

2.2. Observations

HD 32297 was observed with SPHERE on December 19, 2016, in the IRDIFS mode using pupil stabilization in order to take advantage of angular differential imaging (ADI, Marois et al. 2006) for calibration of stellar residuals during post processing. An apodized Lyot coronagraph N_ALC_YJH_S (Carbillet et al. 2011) with a diameter of 185 mas allows attenuation of the starlight in the AO corrected radius (0.84″ at 1.65 μm).

For IRDIS the observations were performed in the broadband H filter (1.625 μm central wavelength, 0.29 μm filter width). IRDIS has a field of view (FOV) of 11″ × 11″ and pixel size of 12.25 ± 0.02 mas. For IFS we used the YJ mode (0.95–1.35 μm), which provides a spectral resolution $R \simeq 54$. The IFS has a FOV of 1.73″ × 1.73″ and a pixel size of 7.46 ± 0.02 mas (Maire et al. 2016). The atmospheric conditions were good with seeing below 0.8″ and correlation time of about 8–9 ms. The observing sequence is as follows: point-spread function (PSF; with the star outside the coronagraphic mask with a neutral density ND2), star center (coronagraphic image with four cross-wise replicas of the star created with the deformable mirror to monitor, Langlois et al. 2013), long science coronagraphic exposures, second PSF and sky background. Further details on the observation log are provided in Table 1.

Furthermore, HD 32297 was observed with IRDIS dual polarimetric imaging (DPI) mode a few days apart in field stabilized mode to measure the polarized flux of the disk. Several polarization cycles were taken in the J band (1.25 μm), each consisting of exposures at four orientations of the half wave plate (0°, 22.5°, 45°, 67.5°) to measure the full Stokes parameters. The observing sequence is similar to that of the IRDIFS mode for IRDIS; the two filters of IRDIS are replaced with polarizers to split the polarization into two orthogonal directions (Langlois et al. 2014).

2.3. IRDIFS data reduction

The preliminary data reduction, including flat-field corrections, sky and dark subtractions, star-centering using waffle pattern, bad-pixel removal, distortion correction (Maire et al. 2016), and wavelength calibration, is done at the SPHERE Data Centre[1] (Delorme et al. 2017) using the data reduction and handling (DRH) pipeline (Pavlov et al. 2008; Mesa et al. 2015) for the total intensity data obtained in IRDIFS mode. This step provides a data cube which is further processed with ADI techniques based on several algorithms, such as Karhunen-Loève Image Projection (KLIP, Soummer et al. 2012), classical angular differential imaging (cADI, Marois et al. 2006), and template locally optimized combination of images (TLOCI, Marois 2015), using two pipelines, namely the SpeCal pipeline (Galicher et al. 2018) and another one developed by Boccaletti et al. (2015).

Karhunen-Loève Image Projection is an algorithm based on the principle component analysis (PCA). The algorithm involves reformatting the science data into a covariance matrix to remove redundancy. Eigenvalues and eigenvectors are calculated for the covariance matrix which is used to form the KL (Karhunen Loève) basis, which itself is truncated to a given number of modes (Soummer et al. 2012). The reference image is built by projecting the science data onto the truncated KL basis and then subtracting them out frame by frame. The result is derotated according to the parallactic angle variation as in any other ADI techniques allowing reduction of the stellar halo. The final image is normalized to the maximum of the measured PSF.

In this paper, we work with the KLIP reduced data truncated to ten modes using the pipeline developed by Boccaletti et al. (2015) as it provides the optimal S/N.

2.4. Dual polarimetric imaging data reduction

The stokes vectors Q and U are calculated from the polarization cycle observed through each half-wave plate position. To mitigate the instrumental polarization we use the double subtraction method (Tinbergen 1996). The final Q and U vectors can be written as follows:

$$Q = \frac{Q^+ - Q^-}{2}, \qquad U = \frac{U^+ - U^-}{2}, \tag{1}$$

where Q^+, U^+, Q^-, U^- are obtained from observations through the half wave plate positions at 0°, 22.5°, 45°, 67.5°.

We retrieve the Q_ϕ and U_ϕ azimuthal Stokes vectors which are expressed in polar coordinates as explained in Schmid et al. (2006). The Q_ϕ and the U_ϕ vectors can be written as:

$$Q_\phi = -Q\cos 2\phi + U\sin 2\phi, \qquad U_\phi = -Q\sin 2\phi - U\cos 2\phi, \tag{2}$$

where ϕ is the azimuthal angle with respect to the center of the star. We recover the disk signal in the Q_ϕ vector and the noise in the U_ϕ vector under the assumption that the disk is optically thin and undergoes only single scattering. Further correction to

[1] http://sphere.osug.fr

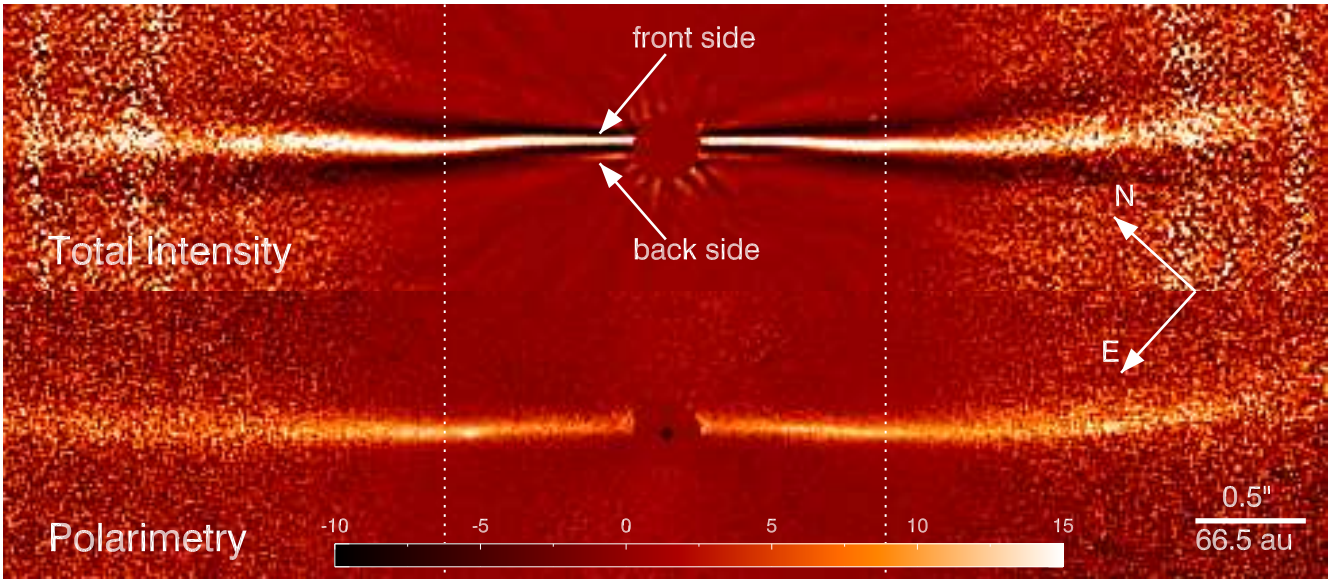

Fig. 1. *Top:* S/N map of total intensity with IRDIS in BB_H filter. *Bottom:* S/N map of polarimetric image observed with IRDIS in BB_J filter. The dashed line indicates approximate position of the ansa in both images and the arrows indicate front and back sides of the disk. Both images are rotated to 90° – PA and cropped at 6″ × 1.3″. The color bar shows the intensity in both the images.

instrumental offset is not done as the U_ϕ image is dominated by noise and has very low true disk signal.

3. Morphology of the disk

3.1. General description

The full extension of the disk in total intensity (H band) and polarimetry (J band) is shown in the S/N map in Fig. 1, while a smaller FOV is displayed in Fig. 2 for IRDIS (H band), IRDIS-DPI (J band), and IFS (YJ band, collapsed image). The S/N map is the ratio between the reduced image and the azimuthal standard deviation of the same image.

The disk of HD 32297 is relatively bright compared to the stellar residuals. We detect the disk extending to the same distance as observed by HST-NICMOS (Schneider et al. 2005, up to 3.3″ from the star). The disk is almost edge-on and the shape appears globally symmetrical in both the northeast (NE) and southwest (SW) sides as seen in both the total intensity and polarimetric images. Some local asymmetries between the NE and SW sides of the disk are discussed in detail in the photometric analysis in Sect. 5.

The IRDIS images feature a concavity at large separations towards the northwest, which becomes significant at a stellocentric distance of about 2″. This pattern is observed in both the IRDIS BB_H image and the DPI BB_J image (as well observed in Fig. 1). This concavity or bow shape was also observed with HST/NICMOS as mentioned in Schneider et al. (2014), and attributed to the interaction with the ISM of small particles on very eccentric orbits.

On closer inspection at a smaller scale, inside 1″ the disk takes a half-elliptical shape indicative of an inclined ring (likely the planetesimal belt), as suggested first by Boccaletti et al. (2012) and Currie et al. (2012). The high quality of SPHERE images now allows us to resolve this ellipse, with the innermost part of the disk observed at a stellocentric radial distance as close as 0.15″ (compared to 0.5–0.6″ in Boccaletti et al. 2012). We measure the position of the ring ansa at 0.8–0.9″. The asymmetry with respect to the major axis is reminiscent of

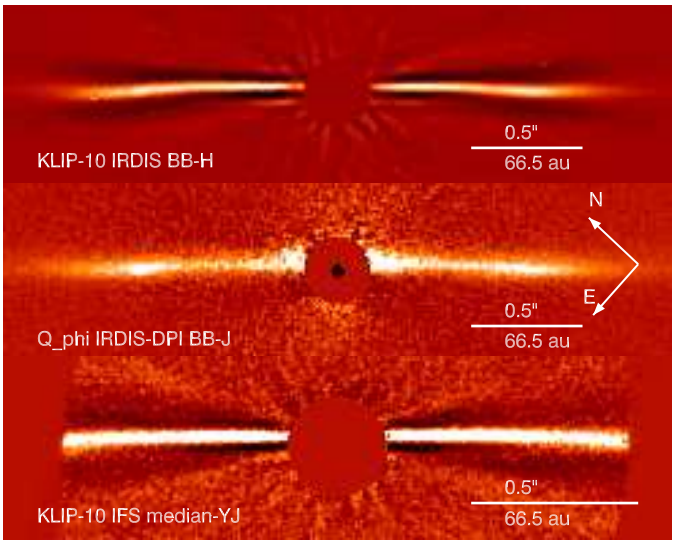

Fig. 2. Inner part of the disk with IRDIS in BB_H (KLIP, *top*), IRDIS in DPI (Q_ϕ, *middle*), and IFS (YJ combined, *bottom*). The top two images are cropped at 3″ × 0.8″ and the IFS image is cropped at 2″ × 0.5″. All images are rotated to 90° – PA. All images are scaled linearly in the range $[-1 \times 10^{-5}, 1 \times 10^{-5}]$.

forward scattering suggesting that the bright part is the front side of the disk. Interestingly, the S/N map (Fig. 1) built from the IRDIS BB_H image suggests that the back side of the disk is also detected which is also visible in the IRDIS BB_H intensity image (Fig. 2). This is discussed in Sect. 4.

Even though the photometry of the disk is impacted by the so-called ADI self-subtraction (Milli et al. 2012), the intensity along the disk varies monotonically, and so does not feature any sign of a gap contrary to the observation reported in Asensio-Torres et al. (2016). Additionally, the stellar residual halo in the SPHERE images is much lower than in HiCIAO observations, confidently ruling out such a gap. This is confirmed with our photometric analysis discussed further in Sect. 5.

The IFS image features a highly symmetrical ring on each side of the minor axis, inside the achievable FOV corresponding to stellocentric distances of <0.9″.

In polarimetry, the intensity along the disk varies differently than in total intensity because the scattering phase function is vastly different. As a result, we observe a peak of intensity located at ~0.8″ and associated to the location of the disk ansa. Due to the absence of self-subtraction in DPI, strong signal is observed at small angles <0.15″ (Fig. 2). At this stage, it is not yet clear whether this signal is produced by stellar residual or by the disk itself, although it is moderately visible in the S/N map (Fig. 1). There are two possible explanations for this signal to be a true disk signal, one being a strong forward scattering peak at small angular separation, and another being a detection of a potential inner belt.

3.2. Position angle of the disk

The position angle (PA) is determined by a method developed for edge-on disks as presented in Lagrange et al. (2012). The science data are first rotated to an initial guess of the PA, and a Gaussian profile is fitted perpendicular to the disk mid-plane in a range of angular separations from which the spine of the disk and the local slope, globally or separately for the NE and SW sides, are derived. This process is repeated until the slope reaches a minimum corresponding to a horizontal disk and providing a measurement of the actual disk PA. The average PA retrieved for both total intensity and polarimetric data is 47.60° ± 0.2° and 47.50° ± 0.15°, respectively. The errors consist of measurement error for the applied method and the additional TN uncertainty of 0.1°.

The local minima in the spine of the disk can determine the position of the ansae (Mazoyer et al. 2014). For higher accuracy, a simple ellipse fit to the spine of the disk can give the position of the ansae corresponding to the semi-major axes of the ellipse. Additionally, the inclination can be derived from the semi-major and semi-minor axes of the fitted ellipse. The ellipse fitting the total intensity data is centered at (−0.06″,−0.008″) and (−0.02″,−0.015″) for the polarimetric data. The plots are presented in Fig. 3. We do this ellipse fit to the spine measured on all the images reduced by the methods, TLOCI (Marois 2015), KLIP 3,5,10 modes (Soummer et al. 2012), classical ADI (Marois et al. 2006), No ADI (Galicher et al. 2018), and DPI Q_ϕ (Schmid et al. 2006), and the dispersion between these measurements is used as error. The position of the ansae measured from the spine is 126.4 ± 12.8 au and the inclination is 88.4° ± 0.6°.

4. Geometrical modeling

4.1. Modeling total intensity with a single phase function

Angular differential imaging techniques induce biases to the disk photometry due to self-subtraction. To overcome this problem and recover the unbiased photometry of the disk we proceed with forward modeling, which involves the generation of synthetic images from a model, given some parameters, undergoing a similar post processing to that used on the original data. We used the GRaTer model to generate synthetic images of debris disks (Augereau et al. 1999). The model assumes a ring of planetesimals releasing dust from a collisional cascade and located at a distance r from the star. The position R_0 is where the dust density peaks corresponding to the position of the ansae and we then impose that the dust density distribution scales radially as $r^{\alpha_{\rm in}}$ inwards and $r^{\alpha_{\rm out}}$ outwards. The vertical distribution is fixed to be a Gaussian function, the height of which is controlled by the parameter H_0 obtained at a radius R_0.

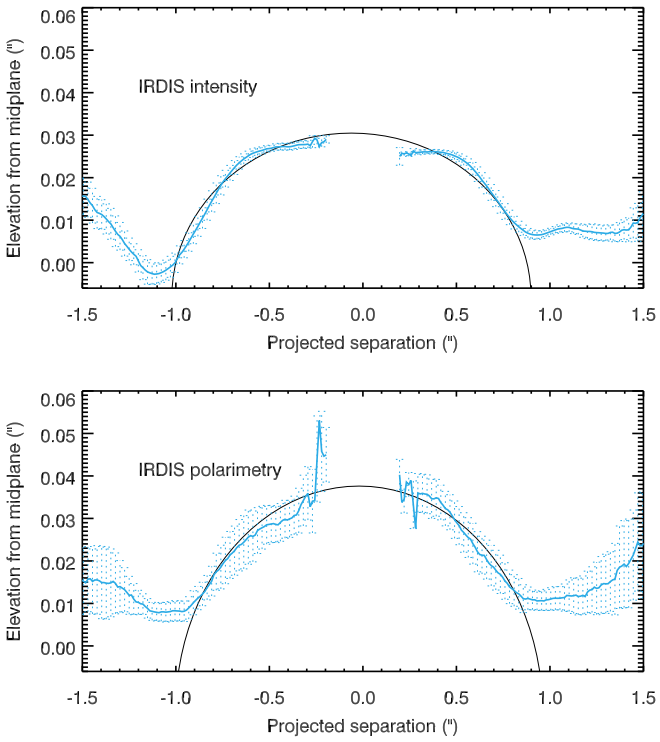

Fig. 3. Spine of the disk measured in total intensity image in BB_H (*top*) and in polarimetric image in BB_J (*bottom*). The spines are fitted with an ellipse.

From this geometrical prescription, GRaTer calculates, for a given model, the resulting scattered light image taking into account the scattering angle θ, which depends on the inclination and PA. The phase function is given by the Henyey Greenstein (HG) function (Henyey & Greenstein 1941) for total intensity

$$f_I(\theta) = \frac{1 - g^2}{4\pi(1 + g^2 - 2g\cos\theta)^{3/2}}, \quad (3)$$

where g is an anisotropic scattering factor that we leave as a free parameter. For $0 < g < 1$, the scattering by dust particles is predominantly forward (isotropic if $g = 0$), and conversely backward for $-1 < g < 0$.

The free parameters of our model are listed below. The initial guesses are obtained from previous work on this system (Currie et al. 2012; Boccaletti et al. 2012) and first-order estimations from the SPHERE images, totalling 23 040 models.

- inclination i (°): 87.5, 88.0, 88.5, 89.0;
- position of the ansae R_0 (au): 115, 120, 125, 130, 135, 140, 145, 150;
- power-law index $\alpha_{\rm in}$: 2, 5, 8, 10;
- power-law index $\alpha_{\rm out}$: −4, −5, −6, −7, −8 ;
- HG parameter g: 0.4, 0.5, 0.6, 0.7, 0.8, 0.9;
- disk aspect ratio $h = H_0/R_0$: 0.01, 0.015, 0.02, 0.025, 0.03, 0.035.

The PA is kept constant at 47.6° as a result of the analysis presented in Sect. 3.2. Each GRaTer model is first injected into an empty data cube void of noise and convolved with the measured PSF. To account for the ADI photometric bias in the forward modeling, a given GRaTer model defined by a set of parameters is projected onto the KL basis which was formed and used for the data. Each model is then normalized to the maximum

PSF intensity as formerly done for the data (Sect. 2). Looking for the best-fit model implies that we compare the science image with a series of model images in an appropriate region encompassing the pixels containing disk signal. A numerical mask $\sim 0.15'' \times 3''$, aligned with the disk mid-plane, is applied, which is compared to observations in a χ^2 fashion. The central part with a stellocentric distance lower than $\sim 0.15''$ is removed from the mask. The northeast and the southwest parts are analyzed separately. A comparison between the science image and the noiseless model masked with an effective aperture is credible as the disk has high S/N assuming that there is no over-subtraction due to the combination of noise and disk. Also, in Boccaletti et al. (2019) a comparison between forward modeling with noiseless models and the injected model into the science image at a different PA with a certain flux resulted in similar χ^2 values. Therefore, we refrain from doing the latter due to reduced computational momentum.

The reduced χ^2 is calculated between the science image ($S_{i,j}$) and the models ($M_{i,j}$) at i, jth pixel and summed over the number of pixels in the mask ($N_{\rm data}$). The calculation is described as follows:

$$\chi^2_\nu = \frac{1}{\nu} \sum_{i,j=1}^{N_{\rm data}} \left(\frac{S_{i,j} - a.M_{i,j}(p)}{\sigma_{i,j}} \right)^2, \quad (4)$$

where ν is the degree of freedom equal to $N_{\rm data} - N_{\rm param}$, where $N_{\rm param}$ is the number of free parameters and p the parameter space explored in these models. The noise term ($\sigma_{i,j}$) is derived from the azimuthal standard deviation in the image masking the disk. In high-contrast imaging, the noise has a spatial structure related to the stellar residuals, varying with wavelengths, while χ^2 minimization applies to Gaussian errors and linear models. These two conditions are not rigorously met in our forward modeling technique, which imposes some limitations to this approach. The parameter a is the scaling factor between the data and the model.

To identify the best models, we select 1% of those with the lowest reduced χ^2 values. This approach is considered instead of taking models corresponding to the 1σ deviation of the reduced χ^2 distribution using the theoretical threshold of $\sqrt{2\nu}$. This is because there are very few models falling into this latter category, which puts overly strong restrictions on the measurements of error bars. Also, this threshold is theoretically applicable for Gaussian errors and linear models which, as discussed earlier, our models do not follow. As a final output we derive the histogram for each parameter, for the given set of best models. A Gaussian profile is fitted to the histograms and Table 2 provides the peak of the Gaussian and the 1σ deviation from the measured peak as errors. Albiet, in two scenarios a Gaussian cannot be fitted. The first is when the distribution of the histogram is flat. The second is when the number of values explored for the parameter are less than four. The best-fit model taken for creating the residual image as shown in Fig. 4 is the model which has the minimum value of the reduced χ^2 ($\chi^2 = 5.26$).

The inclination we find, $88.3° \pm 0.3°$, is compatible with previous measurements (Boccaletti et al. 2012; Currie et al. 2012) but achieves a higher accuracy. The position of the ansae R_0 is 134.7 ± 9.3 au. The variation of the dust density inwards from the belt ($\alpha_{\rm in}$) is relatively difficult to constrain for inclined disks; only limited values are explored for this parameter and evidently the retrieved value of 6.0 ± 4.0 is not constrained. On the other hand, the values for $\alpha_{\rm out}$, g, and h are relatively well constrained with values of -6.17 ± 1.17, 0.55 ± 0.13, and 0.020 ± 0.006, respectively.

Table 2. Parameters that provide the best GRaTer model fitting of the IRDIS BB_H science image with the one HG phase function.

	NE side	SW side	Full disk
i (°)	88.2 ± 0.4	88.3 ± 0.3	88.3 ± 0.3 (88.5)
R_0 (au)	136.8 ± 10.0	129.4 ± 8.4	134.7 ± 9.3 (130)
$\alpha_{\rm in}$	6.00 ± 4.00	6.00 ± 4.00	6.00 ± 4.00 (10)
$\alpha_{\rm out}$	-6.0 ± 0.9	-5.7 ± 0.8	-6.17 ± 1.17 (-6)
g	0.55 ± 0.14	0.49 ± 0.14	0.55 ± 0.13 (0.6)
h	0.026 ± 0.005	0.024 ± 0.006	0.020 ± 0.006 (0.020)

Notes. The model parameters corresponding to the smallest χ^2 value are provided in brackets in the fourth column. The mean value of the distribution and the dispersion is used for $\alpha_{\rm in}$ as its histogram has a flat distribution.

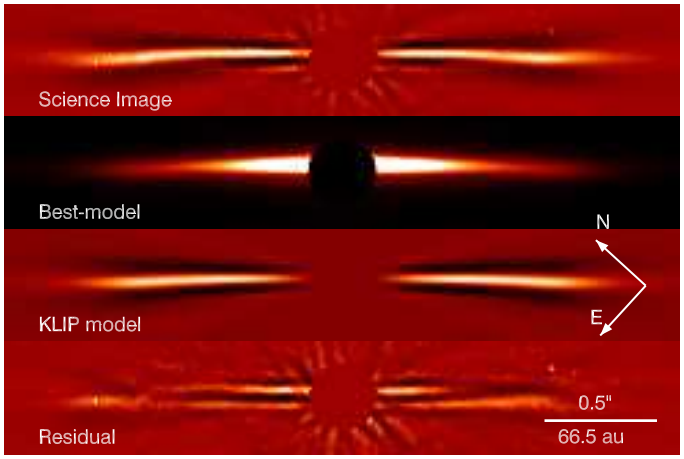

Fig. 4. *From top to bottom*: IRDIS science image in BB_H, best GRaTer model with the parameters $i = 88.5°$, $\alpha_{\rm out} = -6$, $\alpha_{\rm in} = 10$, $R_0 = 130$ au, $g = 0.60$, $h = 0.020$, KLIP processed image for the corresponding GRaTer model, and the residual image. The images are cropped at $3'' \times 0.5''$ and rotated at $90° - {\rm PA}$. The science image, KLIP processed image, and the residual image are scaled linearly in the range $[-1 \times 10^{-5}, 1 \times 10^{-5}]$ and the GRaTer model is scaled linearly in the range [0.0, 0.5].

From Fig. 4, one can see that the residuals are still relatively large, which indicates that the adopted model does not perfectly explain the data. Using two HG phase functions instead of one has been proved effective to better fit inclined disks (Currie et al. 2012; Milli et al. 2017). Similarly, we also try to improve our model by using two HG phase functions to model the disk.

4.2. Modeling total intensity with two HG phase functions

The previous section uses a single HG function to model the scattering phase function but allowed to explore a large range if parameters. In the total intensity IRDIS image, a faint signature of the back side is visible (Fig. 1). In trying to better model the back scattered grains in the disk, we adopt a new phase function based on two HG functions as shown below.

$$f_T(\theta) = w_1.f_I(g_1, \theta) + (1 - w_1).f_I(g_2, \theta), \quad (5)$$

where g_2 is assumed to be negative as it models the backward scattering component of the disk.

We reduced the parameter space guided by our results from the previous section and thus the explored parameters for this case are:

Table 3. Parameters that provide the best GRaTer models fitting the IRDIS BB_H KLIP science image with two HG phase functions.

	NE side	SW side	Full disk
i (°)	88.0	88.2 ± 0.2	88.2 ± 0.2 (88.0)
R_0 (au)	132.4 ± 8.3	128.5 ± 8.6	134.4 ± 8.5 (140)
α_{in}	5.2 ± 2.8	6.0 ± 4.0	6.0 ± 4.0 (2)
α_{out}	-6.0 ± 1.0	-6.0 ± 1.0	-6.0 ± 1.0 (-6)
g_1	0.68 ± 0.05	0.69 ± 0.06	0.69 ± 0.06 (0.7)
g_2	-0.3 ± 0.2	-0.3 ± 0.2	-0.3 ± 0.2 (-0.4)
w_1	0.82 ± 0.04	0.80 ± 0.06	0.81 ± 0.05 (0.80)
h	0.025 ± 0.005	0.022 ± 0.003	0.022 ± 0.002 (0.020)

Notes. The model parameters corresponding to least χ^2 are provided in bracket in the fourth coloumn.The mean value of the distribution and the dispersion is used for i, α_{in}, α_{out}, g_2 and h as they have either flat distribution or small parameter space.

- inclination i (°): 88.0, 88.5;
- position of the ansae R_0 (au): 120, 125, 130, 135, 140, 145;
- power-law index α_{in}: 2, 5, 8, 10;
- power-law index α_{out}: −5, −6, −7;
- first HG parameter g_1: 0.4, 0.5, 0.6, 0.7;
- second HG parameter g_2: −0.5, −0.4, −0.3, −0.2, −0.1;
- disk aspect ratio h: 0.02, 0.025, 0.03;
- weight w_1: 0.80, 0.83, 0.87, 0.90, 0.93.

The range of weights w_1 is chosen to encompass the values derived for (HD 32297 with KECK by Currie et al. 2012, w_1 = 0.90) and another inclined debris disk (HR 4796 Milli et al. 2017, $w_1 = 0.83$).

With the combination of the above listed parameters, 43 200 models are created, for which the reduced χ^2 is measured and the best models are identified following the same approach as described in Sect. 4.1. The parameters giving the best-fit model for this case are provided in Table 3.

The inclination is very well constrained to $88.2 \pm 0.2°$, but we highlight the fact that we considered only two values to explore the parameter space as this is relatively well-constrained from previous studies as well as in the previous section (Sect. 4.1). The position of the ansae and the inner power-law index are found to be $R_0 = 134.4 \pm 8.5$ au and $\alpha_{in} = 6.0 \pm 4.0$, and α_{out} is -6.0 ± 1.0 which are within the error bars retrieved in the previous section. The value of $h = 0.022 \pm 0.002$ is also consistent with results from the previous section.

We find $g_1 = 0.69 \pm 0.06$, $g_2 = -0.3 \pm 0.2$, and $w_1 = 0.81 \pm 0.05$. These values do not agree with the best fits in K band in Currie et al. (2012), where a similar HG function to Eq. (5) was used to model the phase component with $g_1 = 0.96$, $g_2 = -0.1$, and $w_1 = 0.9$. It should however be considered that our data have better S/N compared to the observations of Currie et al. (2012) and we observe the back side of the disk in our data.

In Fig. 5, we plot our best-fit model together with the data and the residuals found after subtracting them both. The reduced χ^2 value for the best-fit model is 3.29. We find that our model provides a 31% better match to the data compared to models with single HG phase function. Irrespective of the improvement, some residuals remain, which may be due to limitations that are combination of several factors. The simplicity of our model with only eight parameters cannot reproduce the complexity of the disk; the variation of the PSF during observation, the possibility of over-subtraction and indirect self-subtraction in the forward modeling (Pueyo 2016), along with nonlinear terms ignored in this study can all add to limitation of our best-fit model.

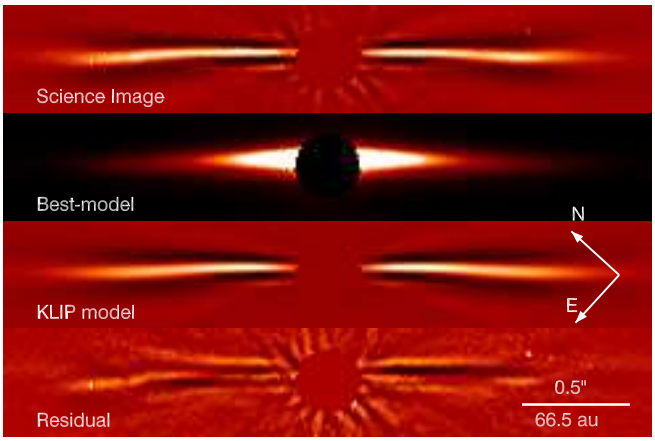

Fig. 5. (a) *From top to bottom*: IRDIS science image in BB_H, best GRaTer model with the parameters $i = 88°$, $\alpha_{out} = -6$, $\alpha_{in} = 2$, $R_0 = 140$ au, $g_1 = 0.70$, $g_2 = -0.4$, $w_1 = 0.80$, $h = 0.020$, KLIP processed image for the corresponding GRaTer model, and the residual image. All the images are cropped at $3'' \times 0.5''$ and rotated to 90° − PA. The science image, KLIP processed image, and the residual image are scaled linearly in the range $[-1 \times 10^{-5}, 1 \times 10^{-5}]$ and the GRaTer model is scaled linearly in the range [0.0, 0.25].

Independently fitting the disk observed in each spectral channel of IFS with the same set of parameters (R_0, α_{in}, α_{out}, h) but g_1, g_2, and w_1 being free parameters, we found that the variation of the anisotropic scattering factors is no larger than 8%. This gives confidence in selecting the same value for all spectral channels. We note that the disk is observed only partly in the IFS FOV, and therefore any degeneracy between morphological and phase parameters is not considered in this test.

4.3. Modeling polarimetric images

Polarimetric observations complement total intensity data and depend differently on the morphological parameters. For instance, as shown in Engler et al. (2017), the phase function in polarimetry peaks close to ~90° phase angle as opposed to the total intensity phase function, which reaches a maximum at small phase angles. As a result, the ansae has stronger signatures in polarimetry than in total intensity. Modeling the polarimetric image is therefore crucial to derive the geometry of the debris disk (Olofsson et al. 2016).

We use GRaTer to create a grid of 32 256 geometrical models with a polarised phase function $f_P(\theta)$, given below:

$$f_P(\theta) = f_I(\theta)\frac{1 - \cos^2\theta}{1 + \cos^2\theta}, \quad (6)$$

where θ is the scattering angle. The phase function used is the combination of the HG function (Eq. (5)) and Rayleigh scattering, to account for the angular dependence of linear polarization due to single scattering of an optically thin disk.

The back side of the disk is not visible in the polarimetric image, and therefore we used a single HG function to construct the phase function in the GRaTer models. The free parameters are as follows:

- inclination i (°): 87.5, 88.0, 88.5, 89.0;
- position of the ansae R_0 (au): 115, 120, 125, 130, 135, 140, 145, 150;
- power-law index α_{in}: 2, 5, 8, 10;

Table 4. Parameters that provide the best GRaTer model fitting of the IRDIS BB_J science image.

	NE side	SW side	Full disk
i (°)	88.7 ± 0.3	88.5 ± 0.3	88.6 ± 0.3 (88.5)
R_0 (au)	135.8 ± 9.8	127.3 ± 9.1	127.9 ± 8.0 (125)
α_{in}	7.4 ± 3.2	8.1 ± 3.1	8.1 ± 3.2 (10)
α_{out}	−4.1 ± 1.0	−3.7 ± 0.7	−3.9 ± 0.8 (−4)
g	0.85 ± 0.09	0.88 ± 0.05	0.84 ± 0.08 (0.8)
h	0.023 ± 0.006	0.022 ± 0.006	0.022 ± 0.006 (0.020)

Notes. The model parameters corresponding to the smallest χ^2 are provided in bracket in the fourth column.

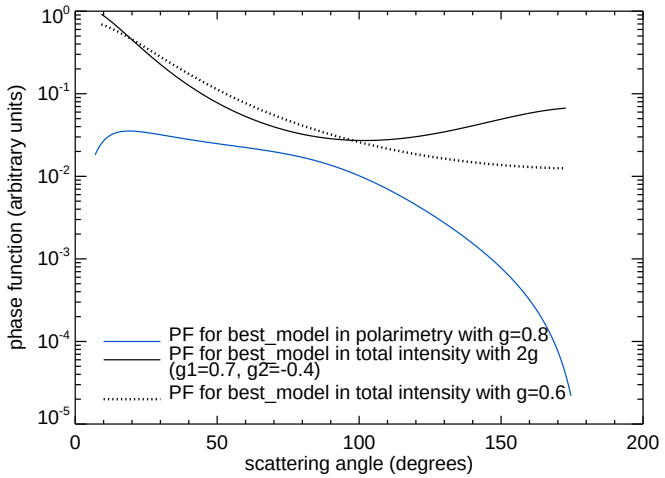

Fig. 6. Scattering phase function adopted for the total intensity and polarimetric best-fit models.

– power-law index α_{out}: −3, −4, −5, −6, −7, −8;
– HG parameter g: 0.4, 0.5, 0.6, 0.7, 0.8, 0.9, 0.99;
– disk aspect ratio h: 0.01, 0.015, 0.02, 0.025, 0.03, 0.035.

We applied the same procedure as in Sect. 4.1 to measure the reduced χ^2 and derive the range of best models. The value of the reduced χ^2 is 3.52 for the best-fit model.

The parameters for the best-fit model of the polarimetric image are given in Table 4. We find that the inclination of the disk is 88.6° ± 0.3°and the position of the ansae (127.9 ± 8.0 au) is consistent with the one obtained in total intensity within error bars. Regarding the slopes of the surface density profile, polarimetry favors a steep inner edge (α_{in} = 8.1 ± 3.2) while this parameter was essentially unconstrained in total intensity. On the contrary, the outer slope α_{out} = −3.9 ± 0.8 is flatter.

The anisotropic scattering factor is significantly larger in polarimetry (0.84 ± 0.08) as compared to intensity irrespective of the number of g parameters we considered. Therefore, the dust grains which are probed in these data are more prone to forward scattering in polarimetry. It should be noted that in the case of strong forward scattering, the polarised phase function peaks at a smaller scattering angle as well as at the ansae (Milli et al. 2019), which is visible in our best-fit model as seen in Fig. 7. Figure 6 plots the scattering phase functions for total intensity and polarimetric best-fit models. The scattering angles probed for HD 32297 are between 6° and 175°. The phase function in polarimetry peaks at scattering angles smaller than ∼90° as seen in Fig. 6 while in total intensity we observe an increase beyond 110° due to the back-scattering for a double HG function.

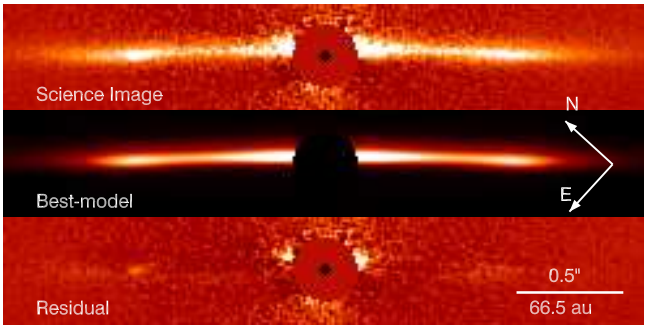

Fig. 7. *From top to bottom*: DPI Q_ϕ science image, best GRaTer model with parameters i = 88.5°, R_0 = 125 au, α_{in} = 10.0, α_{out} = −4.0, g = 0.8, h = 0.020, and the residual image. The images are cropped at 3″ × 0.5″ and rotated at 90° - PA. All images are scaled linearly in the range $[-1 \times 10^{-5}, 1 \times 10^{-5}]$.

Finally, although the residuals displayed in Fig. 7 are much lower than for the modeling of total intensity, there is still some intensity left near the ansae, indicating that the model does not perfectly reproduce the disk. The residuals could also be an indication of our preference of larger g values over a possibility of an inner component at a separation of <40 AU. Modeling the polarimetric observation with consecutive inner and outer belts is beyond the scope of this paper.

5. Photometry and analysis

5.1. Self-subtraction profile and photometry for the total intensity

There are several possible approaches to retrieving the spectrophotometry of the disk. We compare two methods which we use to retrieve the surface brightness of the disk and discuss the limitations associated with each of them.

Method 1. The first method is similar to the one used to measure the photometry of the HD 32297 disk in Boccaletti et al. (2012) and HD 15115 in Mazoyer et al. (2014). It was developed for highly inclined debris disks and relies on estimating the self-subtraction caused by the ADI process. The edge-on geometry allows simplification of this calculation to a 1D problem. Given the best fit model fitting the data identified in Sect. 4.2, we first extracted the radial profile of the GRaTer model (convolved with the PSF) and its associated KLIP image. The profiles for both the model and the KLIP image are measured in the same numerical mask as for the χ^2 minimization, and we average the flux in nonoverlapping concentric arcs of 0.15″ vertical width, and four-pixel (∼0.05″) length.

The self-subtraction is derived from the ratio of these two profiles (Fig. 8, left) and can be significant at short separations when using KLIP (about 60 at 0.2″ in the H band). The unbiased surface brightness (in counts) of the disk is then obtained by multiplying the self-subtraction profile with the science (KLIP) image profile to compensate for the ADI effect, in each spectral channel of the IFS and each filter of IRDIS.

Self-subtraction could also be deduced directly from the ratio of the images of the GRaTer model (PSF convolved) and its KLIP version instead of using profiles. Milli et al. (2017) used this method in the case of a less inclined disk and using a specific ADI process (masked classical ADI), which minimizes the self-subtraction beforehand. Here, in the case of a highly inclined disk together with KLIP processing, this method would lead to the self-subtraction profile presented in the right panel of Fig. 8,

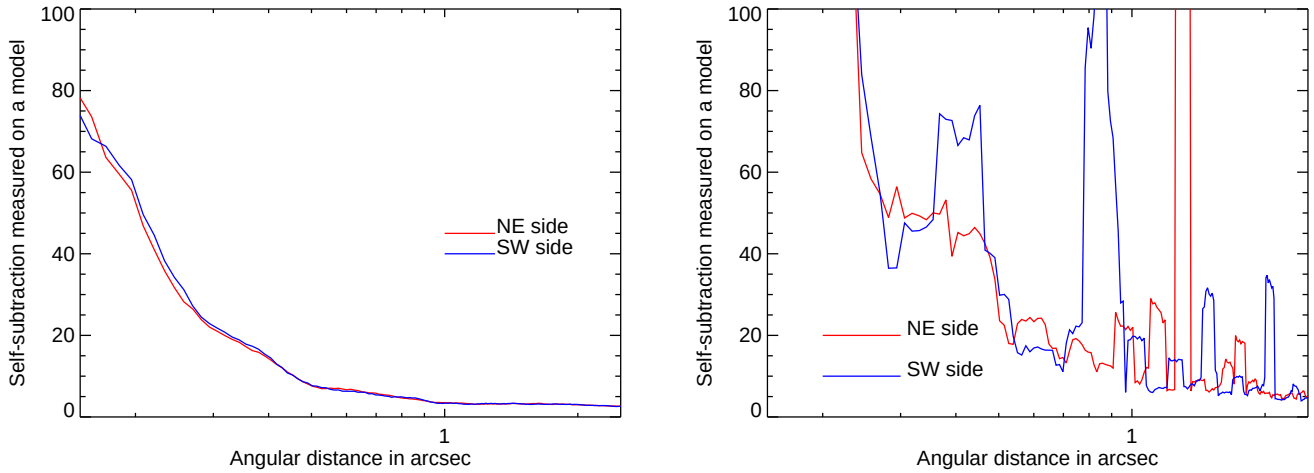

Fig. 8. Self-subtraction measured for IRDIS in the BB_H filter for the method 1 (see text for details) using the ratio of radial profiles (*left*) and the ratio of images (*right*).

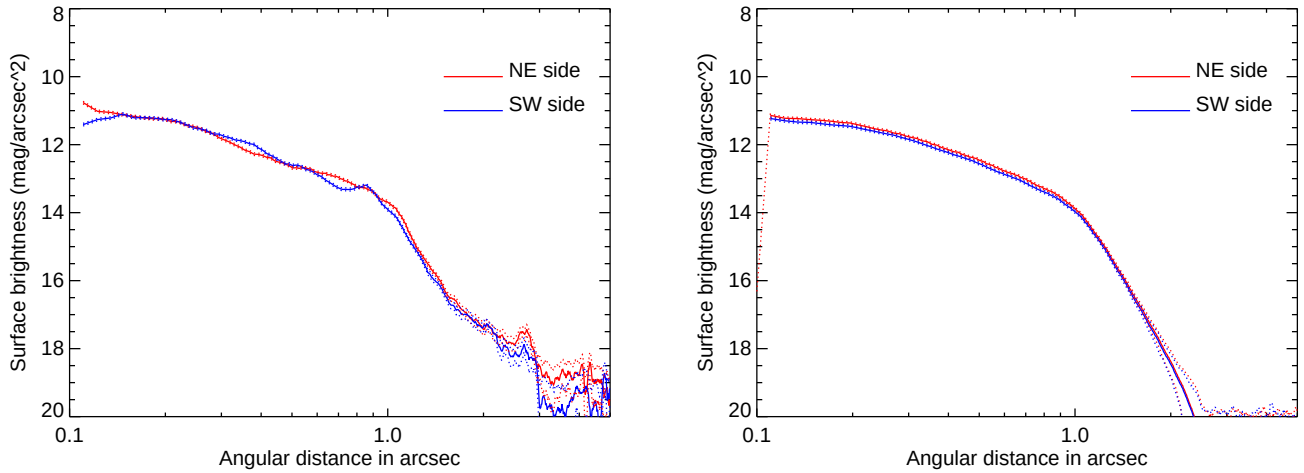

Fig. 9. Surface brightness of the disk measured for IRDIS in the BB_H filter for method 1 (*left*) and method 2 (*right*). The blue (resp. red) solid line represents the SW (resp. NE) side of the disk. The dotted lines show the errors in the measurements.

which clearly cannot be used for photometric correction. The large variations are attributed to the strong positive to negative fluctuations resulting from the KLIP processing. Therefore, we conclude that this method of self-subtraction measurement should be avoided for KLIP-processed data.

Method 2. The second solution does not require evaluation of the self-subtraction, but instead uses one step of the modeling when the reduced χ^2 is calculated. For the minimum value of reduced χ^2, the scaling parameter a in Eq. (4) directly provides the scaling factor between the KLIP image of the best-fit model and the data. Therefore, contrary to method 1, the surface brightness profile is evaluated in the scaled GRaTer model (PSF convolved) image instead of the real disk image.

For further calculation we first obtain the stellar flux by integrating over a masked PSF which contains 99.99% of its total flux. The radius obtained for the mask is 0.4″ for the PSF obtained by IRDIS and 0.3″ for IFS. Surface brightness profiles are then converted to magnitude arcsec^{-2} taking into account the pixel size and normalizing with respect to the stellar flux. The error bars linearly combine two terms, the dispersion of the stellar+background residual intensity as measured in the mask rotated by 90° relative to the real disk for each radial bin, and the accuracy of the photometric extraction. The latter is estimated with a fake disk (same parameters as the best-fit model) injected into the raw data at 90° from the real disk at a contrast level of 5×10^{-4} and processed in the same way. The photometric extraction is found to be consistent with this initial contrast within ~3.3%.

The two methods provide very similar results as seen in Fig. 9. Hence, we derived surface brightness profiles for all spectral channels of IFS and IRDIS. Flowcharts representing the calculations using either method are shown in Fig 10.

At this stage, and contrary to Asensio-Torres et al. (2016), we do not confirm the presence of a dip or break in the surface brightness profiles near 0.75″ on the NE side or 0.65″ in the SW, and therefore we rule out the presence of a gap (Fig. 9).

5.2. Photometry for polarimetric images

In polarimetry, the disk photometry is not affected by self-subtraction and therefore can be directly measured from the image. Contrast is calculated directly from the science DPI BB_J image, instead of a model, using the same process as explained in method 2 of Sect. 5.1.

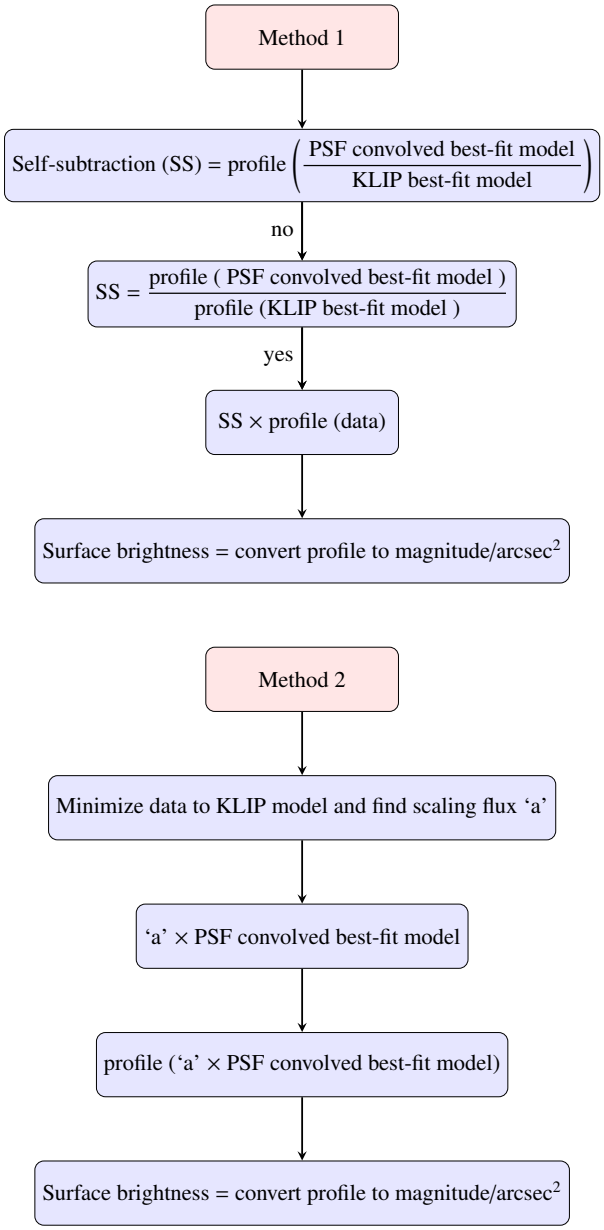

Fig. 10. Flowchart representing surface brightness calculations using method 1 or method 2. In Method 1 the arrow anchored with "no" depicts that the calculation of SS with the previous process does not work, resulting in Fig. 8 (right). Next, we proceed with another process providing Fig. 8 (left) which is used further and therefore the arrow is anchored with a "yes".

As a result of the scattering angle dependence (Sect. 4.3), the slope of the surface brightness profile is clearly different in polarimetry compared to total intensity, with a less steep decrease from 0.1″ to about 0.7″ (Fig. 11). At the location of the ansae (~0.9″), the surface brightness shows a peak instead of a break. As advocated in Engler et al. (2019) for the case of the inclined debris disk around HD 15115, this dependence of the phase function provides a better sensitivity for polarimetric data to pinpoint the inner edge or the ansae of a dust belt, or to reveal multiple structures. In the case of HD 32297, the polarimetric surface brightness does not show any particular signs of such multiple belts. The polarimetric surface brightness is about two magnitudes fainter than in total intensity for a stellocentric

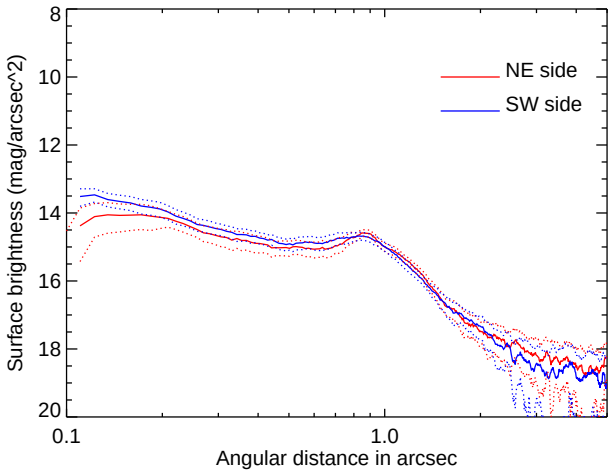

Fig. 11. Surface brightness profile of the disk measured in the IRDIS BB_J DPI Q_ϕ science image. The blue line represents the SW side of the disk and the red line represents its counterpart on the NE side. The dotted lines represent the error bars.

distance of 0.5″, which translates to a polarized fraction of about 15%.

5.3. Average spectral reflectance

To derive the reflectance of the grains as a function of wavelength, we converted the surface brightness profiles into contrast with respect to the star and averaged the values between 0.2″ and 0.8″, for all spectral channels of IFS and IRDIS, as well as for polarimetric data. Even though, the intensity decreases by ~1 mag arcsec^{-2} between 0.2 and 0.8″ for all spectral channels, this separation range is chosen as it corresponds to the minimal and maximal distances where the disk signal starts to dominate over the stellar halo (>0.2″) while encompassing the IFS field of view. The reflectance spectra obtained with the two methods of Sect. 5.1 are plotted in Fig. 12, in which the error bars are obtained from the averaged errors of the surface brightness between 0.2″ and 0.8″ for each wavelength. The main characteristic of the reflectance, irrespective of the method used, is a slow decreasing trend with wavelength which gives the disk a gray to blue color in the *YJH* spectral range (Fig. 12). Independently of any assumptions on the grain properties, by fitting a straight line to the spectra, we measured a contrast arcsec^{-2} variation of -0.013 ± 0.002 per μm.

Method 1 (Fig. 12, left) clearly produces more dispersion in the *YJ* band as a result of biases introduced by the self-subtraction estimation. Since method 2 (Fig. 12, right) is based on photometry extracted from models, it provides a smoother spectrum, but a slightly lower reflectance (~12–20%) than method 1. For further assurance, we checked the consistency of the two methods by injecting a fake disk 90° to the real disk PA and performing consecutive photometry for the real disk and the fake disk with both methods. We find that the uncertainty on the measurement between the real disk and the fake disk in Method 1 is twice that found when using Method 2. We therefore chose to use Method 2 for subsequent analyses.

Using previous measurements from the literature to confirm the trend of the reflectance on a larger spectral range would be valuable, but photometric measurements are usually derived from various methods, and at various locations on the disk

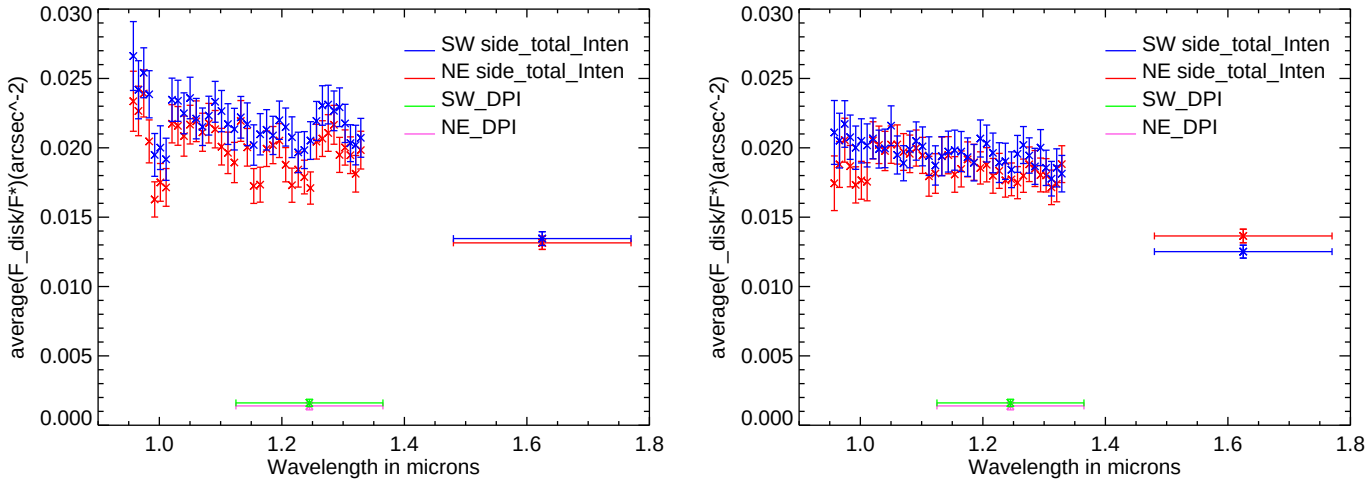

Fig. 12. Average spectral reflectance of HD 32297 as measured with method 1 (*left*) and method 2 (*right*), for total intensity data in IFS *YJ* and IRDIS BB_H, as well as polarimetric data in IRDIS BB_J.

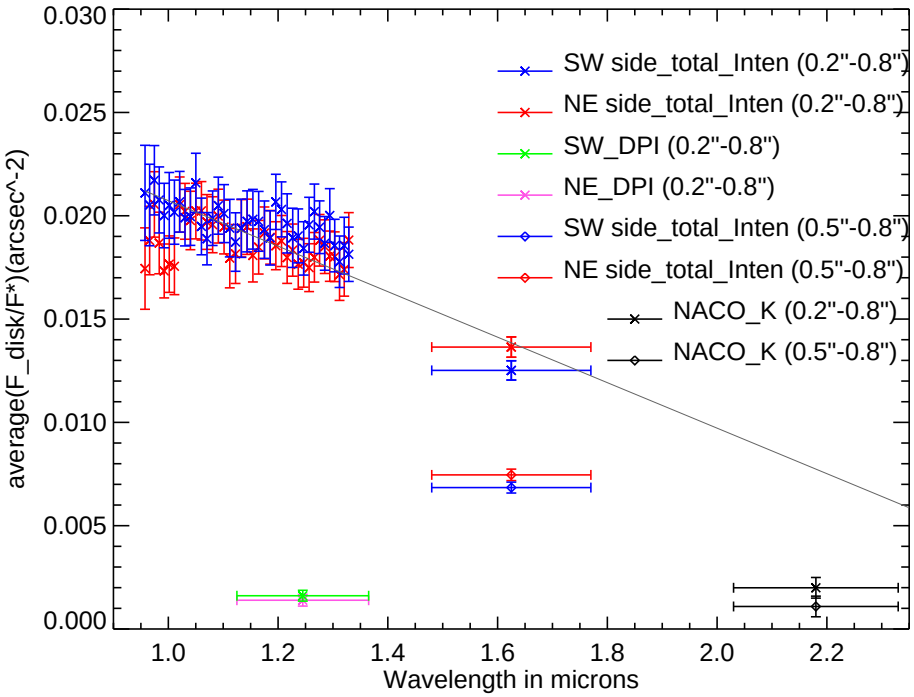

Fig. 13. Average spectral reflectance of HD 32297 as measured with method 2, for total intensity data in IFS *YJ* (in the 0.2–0.8″ range) and IRDIS BB_H (0.2–0.8″ and 0.5–0.8″), as well as polarimetric data in IRDIS BB_J (0.2–0.8″). The NACO *K* band measurements in the range 0.5–0.8″ (Boccaletti et al. 2012), and an extrapolated value in the range 0.2–0.8″ are over-plotted. The SPHERE *YJH* band data are fitted with a straight line (in gray) to estimate a global slope which is (-0.013 ± 0.002) arcsec^{-2} per μm.

image, which makes the comparison difficult. However, in the case of HD 32297, *Ks* band data were obtained by some of us using similar (but not quite identical) methods (Boccaletti et al. 2012). In these data, the disk is only detected at stellocentric distances of 0.5–0.8″ for both the NE and SW sides and the surface brightness is $\sim 15 \pm 0.5$ mag arcsec^{-2} which translates to a contrast of $(1.09 \pm 0.5) \times 10^{-3}$ arcsec^{-2}.

Considering the variation of the disk intensity in SPHERE images between the two ranges of separations 0.2″–0.8″ and 0.5″–0.8″ at *H* band, we can extrapolate this *Ks* band contrast to $(1.99 \pm 0.5) \times 10^{-3}$. Therefore, at first order, the photometry in the *Ks* band confirms the spectral slope of the reflectance (Fig. 13). Observing the disk at the *Ks* band with SPHERE would further validate the current value of the slope found.

The globally blue behavior of the spectrum is a key element that can help to constrain the size distribution of the grains composing the HD 32297 disk.

6. Grain modeling

Now that we have constrained the geometry and morphology of the disk, we return to the GRaTer radiative transfer code to constrain the particle size distribution (PSD) of the dust grains. We take as a reference morphology ($R_0 \pm dr$) the best fit obtained for the "full disk" fit displayed in Table 3 and produce synthetic spectra of the disk as a function of grain-related parameters, which we then compare to the observed spectrum in the NIR.

We consider three different grain compositions: astro-silicates, porous astro-silicates with 80% porosity, and a mixture with 50% water ice and 50% astro-silicates. The two crucial free parameters are the minimum grain size $s_{\rm min}$ and the index κ of the power-law that the PSD is assumed to follow ($dn(s) \propto s^{\kappa} ds$). We explore values of $s_{\rm min}$ between 0.1 and 10 μm with an increment of 0.1 μm and values of κ ranging from −5.0 to −3.0 with an increment of 0.1.

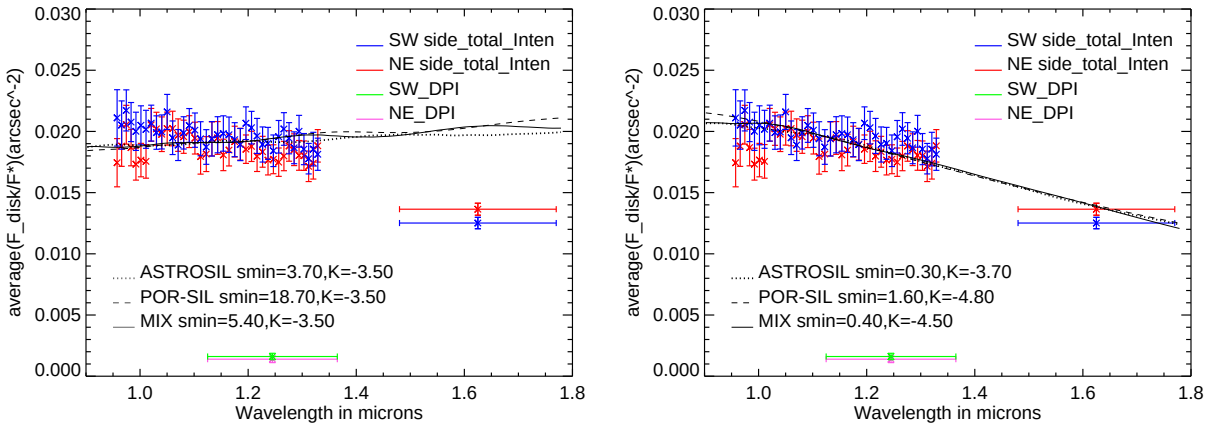

Fig. 14. Best fits of the reflectance spectrum (method 2) obtained for three different grain compositions, for a fiducial case where we force $s_{\rm min} = s_{\rm blow}$ and $\kappa = -3.5$ (*left*), and when $s_{\rm min}$ and κ are free parameters (*right*).

Table 5. Parameters of the grains and their size distribution that generate the best fit to the spectrum.

Grain type	Volume ratio	Density g cm^{-3}	κ	$s_{\rm min}$	$s_{\rm blow}$	$s_{\rm min}/s_{\rm blow}$	χ^2
Astro-silicate	–	2.7	-3.79 ± 0.34	0.30 ± 0.02	3.7	0.081	0.471 ± 0.084
Vacuum+astro-silicate	4:1	0.54	-4.24 ± 0.60	1.59 ± 0.11	18.7	0.085	0.628 ± 0.114
Astro-silicate+water ice	1:1	1.85	-4.65 ± 0.35	0.44 ± 0.03	5.4	0.081	0.502 ± 0.091

Each model spectrum is interpolated on the forty wavelength channels (39 for IFS and 1 for IRDIS) and globally scaled to the data using the same χ^2 minimization framework as in Sect. 4.1.

For all wavelength channels (i), the reduced χ^2 is measured between the average spectral reflectance D_i and each grain model spectrum M_i as given below

$$\chi^2_\nu = \frac{1}{\nu} \sum_{i=1}^{40} \left(\frac{D_i - M_i(p)}{\sigma_i} \right)^2, \tag{7}$$

where σ_i is given by the error bars for each data point in Fig. 9 and p is the parameter space. There are 40 wavelength channels ($n_{\rm data}$) and two parameters ($n_{\rm param}$; minimum grain size and distribution index), and therefore there are 38 degrees of freedom; $\nu = 38$. The best models are selected as per 1σ deviation of the reduced χ^2 distribution, which is given by $\chi^2_{\nu,\rm th} = \chi^2_{\nu,\rm min} + \Delta\chi^2_\nu$, with $\Delta\chi^2_\nu = \sqrt{2\nu}$.

The reflectance spectrum corresponding to the best fits obtained for the three considered compositions is displayed in Fig. 14 (right) and the best-fit parameters are provided in Table 5. An important result is that, for all considered compositions, $s_{\rm min}$ is well below the blow-out limit size $s_{\rm blow}$. We indeed always have $s_{\rm min}/s_{\rm blow} \leq 0.085$, where we derive $s_{\rm blow}$ in gm cm^{-3} using the prescription by Wyatt (2008):

$$s_{\rm blow} = 0.8 \frac{L_*}{M_*} \frac{2.7}{\rho}, \tag{8}$$

where L_* and M_* are the stellar luminosity and mass expressed in solar values, and ρ is the bulk density of the material (given in Table 5). We take $L_* = (8.4 \pm 0.2)\ L_\odot$ (Moór et al. 2017) and $M_* = 1.8\ M_\odot$ (Kalas 2005).

As for the best fit of the slope (Fig. 14, right) of the size distribution, we find $\kappa = -3.79 \pm 0.34$ for astro-silicates, which is relatively close to the slope expected for collisional steady states (between -3.6 and -3.7; see Gáspár et al. 2012, and references therein). For the other two compositions, we find slightly steeper PSDs, with $\kappa \sim -4.5$. For all three slopes, it is important to stress that the geometrical cross section, and thus the flux, is dominated by the smallest grains in the PSDs, that is, those close to $s_{\rm min}$ (Thebault & Kral 2019). Also, $s_{\rm min} = 2.2\,\mu$m, the minimum size found by Donaldson et al. (2013), also corresponds to $s < s_{\rm blow}$ grains given the very high 90% porosity they assumed. To further stress the crucial role of unbound $s \leq s_{\rm blow}$ grains, we display in Fig. 14 (left) the best fits that would be obtained when considering a PSD stopping at $s_{\rm min} = s_{\rm blow}$ and a canonical slope with $\kappa = -3.5$. As can be clearly seen, in the absence of the unbound grains no satisfying match can be obtained, in particular regarding the blue slope of the reflectance spectrum.

These results, especially those regarding the minimum grain size, only weakly depend on the morphology assumed for the disk. Taking a size for the planetesimal belt other than that of Table 3 indeed leads to relatively similar results. This is expected, as the slope of the reflectance spectrum is essentially imposed by the size-dependence of the scattering coefficient $Q_{\rm sca}$, which does not depend on the location of the grains with respect to the star. The scattering anisotropy parameters g do depend on this location, but under the assumption made in Sect. 4 that there is no size dependence for g, this would not translate into a different slope of the reflectance spectra for a given PSD. Therefore, we note that at this stage it is safe to derive synthetic spectra without a dependence of anisotropic scattering parameter.

7. Discussion

7.1. Comparison of geometrical parameters to millimeter observations by ALMA

From the analysis presented in Sect. 4.3 we find that the disk is best described as a relatively narrow belt peaking at

132.3 ± 6.2 au (according to polarimetric data), which agrees with previous scattered light observations (Currie et al. 2012; Boccaletti et al. 2012, after the correction of the distance from the new *Gaia* measurements). HD 32297 was also observed recently with ALMA in the dust continuum at 1.3 mm by MG18. However, the beam size was about $0.76'' \times 0.51''$ which is more than ten times larger than the SPHERE angular resolution, meaning that the ALMA resolution is significantly poorer.

While considering a geometrical model that is similar to GRaTer, MG18 concluded that the disk is rather broad, extending from 78 ± 8 to 122 ± 3 au, with a surface density rising as r^2. The peak in density occurs slightly closer-in than in the SPHERE images, but this discrepancy could be the result of the angular resolution. In any case, the radial dependency of the surface density, even if relatively poorly constrained in our case, is considerably steeper with SPHERE.

Beyond the planetesimal ring at 122 au, MG18 observed a halo extending out to 440 ± 32 au, where the surface density decreases as r^{-6}. This is consistent with the SPHERE image in which we observe dust scattering as far as $3.3''$ (equivalent to 440 au), with a comparable radial decrease in density. MG18 do not report any asymmetry in this outer part while the aforementioned concavity is obvious at shorter wavelengths. This could again be a resolution effect or because of the sensitivity of ALMA to bigger grains. Nevertheless, subtracting an axi-symmetrical disk model from the ALMA image leaves residuals co-located with the region where the concavity is detected by SPHERE and HST. The presence of millimeter grains at such stellocentric distances would, however, be at odds with the expected mechanism creating such concavity. For the same reason, our value for the disk inclination is significantly more precise ($88.2 \pm 0.3°$) than the one derived by MG18 ($83.6° \, ^{+4.6}_{-0.4}$).

In order to check the compatibility of the ALMA and SPHERE models, we used the MG18 parameters $\alpha_{\rm in}$, $\alpha_{\rm out}$, $R_{\rm in}$, $R_{\rm out}$, and took the other parameters (g_1, g_2, w_1, h) from our best-fit values (Table 6). As a result, we obtained a much larger χ^2 value of 8.5 for total intensity compared to our best fit. For polarimetry, $\chi^2 = 3.6$, which is not far from the value we find for our best-fit model. This is because $R_0 = 122$ au, as used in MG18, is close to that of our polarimetric best-fit model $R_0 = 125$ au. We also explored models with g_1, g_2, w_1 as free parameters corresponding to the parameter space of Sect. 4.2 for total intensity and Sect. 4.3 for polarimetry in order to restrict possible degeneracies between dust density distribution corresponding to the ALMA values and phase function. The attempt resulted in larger χ^2 (8.3 for total intensity and 3.6 for polarimetry) values compared to our best fit indicating that the ALMA model does not match the SPHERE image. The disagreement between the models derived from these two instruments could stem from one of two factors, or both. The first is the angular resolution as mentioned above. The second is that ALMA and SPHERE probe different grain size of which the dynamics can be governed by different processes resulting in two distinct spatial distributions.

Table 6. Parameters used to create models comparable to millimeter observations by ALMA.

Parameters	Total intensity	Polarimetry
Inclination i (°)	88.0	88.5
R_0	122	122
$\alpha_{\rm in}$	2	10
$\alpha_{\rm out}$	−6	−4
$R_{\rm in}$	78	78
$R_{\rm out}$	440	440
g_1	0.7	0.8
g_2	−0.4	0.0
w_1	0.80	1.00
$h = H_0/R$	0.020	0.020
χ^2	8.53	3.64

Notes. Here, $R_{\rm in}$ and $R_{\rm out}$ are the inner and outer edges of the disk.

7.2. Disk color and sub-micron grains

7.2.1. Quantity of sub-micron grains produced naturally in debris discs

Our new observations and analysis confirm two striking characteristics of the HD 32297 disk: the blue color of the spectrum in the NIR and the significant presence of tiny grains much smaller than $s_{\rm blow}$. Moreover, we confirm that there is an intrinsic coupling between these two characteristics, as was also inferred for the HD 15115 (Debes et al. 2008) or AU Mic systems (Augereau & Beust 2006; Fitzgerald et al. 2007b).

This link between a blue NIR spectrum and sub-micron grains has been quantitatively investigated in the recent study by Thebault & Kral (2019). This numerical exploration shows that for bright debris disks with high fractional luminosity $f_{\rm d}$, a collisional cascade at steady-state can "naturally" produce a level of unbound sub-micron grains that is high enough to lead to a blue slope of the spectrum in the NIR. This is because for bright and dense disks, the drop in grain number density at the $s = s_{\rm blow}$ frontier, which is to a first order $\propto 1/f_{\rm d}$, is much less pronounced than for fainter systems. For a very bright disk with $f_{\rm d} = 5 \times 10^{-3}$ comparable to that of HD 32297, Thebault & Kral (2019) found a profile of the relative NIR $L_{\rm d}/L*$ spectrum that is qualitatively similar to the one obtained here (see Fig. 13 of that paper). However, the blue slope they obtained is not as steep as in the present case, with a flux ratio between the $\lambda = 1\,\mu$m and $\lambda = 1.6\,\mu$m fluxes that is ∼1.1, as compared to ∼1.6 here.

This could indicate an additional source of sub-micron grains, which cannot be explained by the steady-state collisional evolution of the system. One possible cause could be the so-called collisional "avalanche" mechanism (Grigorieva et al. 2007; Thebault & Kral 2018), initiated by the break-up of a large planetesimal closer to the star, which releases large amounts of unbound dust grains that then trigger a collisional chain-reaction as they sandblast at very high velocity through a dense outer disk. The ideal case for an avalanche-producing system is a double-belt configuration, with an inner belt (where the large planetesimal breaks up) at ∼1–10 au with $f_{\rm d} \gtrsim 10^{-4}$, and a bright outer belt with $f_{\rm d} \gtrsim 10^{-3}$ (Thebault & Kral 2018). This could match the structure of HD 32297, for which an inner belt of brightness $f_{\rm d} \sim 6 \times 10^{-4}$ has been inferred by Donaldson et al. (2013), even though the reality of this inner belt is still debated (e.g., Kennedy & Wyatt 2014). Observational confirmation of an inner belt would need to achieve contrasts significantly higher (a factor of 10) than those currently feasible with SPHERE. In this case, the level of $s \leq s_{\rm blow}$ grains would vary stochastically, on a timescale $t_{\rm av}$ that is roughly a third of the typical dynamical timescale in the disk (Thebault & Kral 2018). This would, however, correspond here to $t_{\rm av} \sim$ 300–400 yrs, much too long to be observationally monitored. Moreover, it is not guaranteed that the rate at which large planetesimals break up in the inner regions

is high enough for such an event to be likely to be witnessed (see discussion in Thebault & Kral 2018).

7.2.2. Effect due to gas on the presence of sub-micron grains

Another possibility is that the system is able to retain $s \leq s_{\rm blow}$ grains significantly longer than the radiation pressure blow-out time. If there is enough gas in the system, gas drag could act to significantly increase the time for an unbound grain to leave the system. To check that, we first compute the stopping time for the case where grains are bound to their host star, equal to (Takeuchi & Artymowicz 2001)

$$T_{\rm sb} \sim 2\left(\frac{\rho}{1.5\,{\rm g\,cm^{-3}}}\right)\left(\frac{s}{1\,\mu{\rm m}}\right)\left(\frac{M_{\rm gas}}{0.1\,M_{\oplus}}\right)^{-1}, \quad (9)$$

where we assume $M_{\star} = 1.8\,M_{\odot}$, $R = 130$ au, $\Delta R = 50$ au to be consistent with results from Sect. 4. We also fix the gas temperature to 30 K and its mean molecular weight to 28 based on Cataldi et al. (2019), where they show that the gas mass is dominated by CO rather than carbon in HD 32297. Accounting for the observed neutral and ionized carbon (in addition to CO, Moór et al. 2019), the total gas mass barely goes above $0.1\,M_{\oplus}$. If accounting for potential CO_2 or water being released from planetesimals at the same time as CO (and thus producing extra oxygen not coming from CO and some extra hydrogen), and assuming a solar-system comet-like composition (e.g., Kral et al. 2016), the total gas mass could go up to $0.5\,M_{\oplus}$[2].

Therefore, small bound grains close to the blow-out limit (i.e., 1–10 μm, see Table 5) will have a stopping time close to 1 and will be affected by gas drag over a few orbital periods before they have time to collisionally deplete. The smallest bound grains will likely (depending on the gas-pressure gradient) move outwards before being collisionally destroyed (Takeuchi & Artymowicz 2001) and will therefore be present for longer than usually assumed in a standard size distribution (e.g., Kral et al. 2013).

For unbound grains, Eq. (9) needs to be adjusted. The velocity of unbound grains can reach $\sqrt{2(\beta-1)}$ of the Keplerian velocity at which they are released initially, which would increase the velocity difference between gas and dust, hence entering the Stokes regime of drag (rather than the Epstein regime, Takeuchi & Artymowicz 2001). On top of that, the stopping time of Eq. (9) is calculated over an orbital period and unbound grains travel almost radially over ΔR, the width of the disk. Therefore, we calculate a new dimensionless Stokes stopping time for unbound grains $T_{\rm su}$ (based on Takeuchi & Artymowicz 2001), scaled by the crossing time over ΔR and therefore equal to $T_{\rm sb}[2c_{\rm s}/v_{\rm K}][R/\Delta R]$, where $v_{\rm K}$ is the Keplerian velocity and $c_{\rm s}$ the sound speed:

$$T_{\rm su} \sim 0.03\left(\frac{\rho}{1.5\,{\rm g\,cm^{-3}}}\right)\left(\frac{s}{0.1\,\mu{\rm m}}\right)\left(\frac{M_{\rm gas}}{0.1\,M_{\oplus}}\right)^{-1}, \quad (10)$$

meaning that 0.1 μm grains will be slowed down significantly before they have time to leave the disk[3]. The exact orbit of unbound grains interacting with gas is time dependent and is not derived here as it goes beyond the scope of this paper, but generally speaking, an unbound grain would start on a very hyperbolic orbit and eventually be circularized around the star. These grains will then accumulate before being destroyed collisionally. Therefore, we find tantalizing evidence that gas observed in this system may be able to explain the blue color of the disk by allowing small unbound grains to be present for longer.

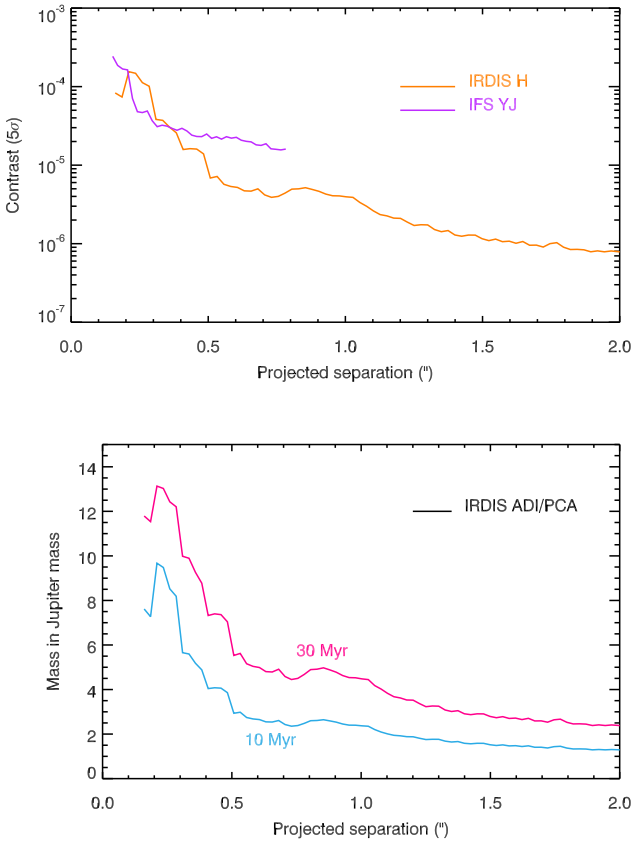

Fig. 15. Limits of detection in contrast (*top*) for IRDIS (solid line) and IFS (dashed line), and converted into Jovian masses (*bottom*, IRDIS only) for two age assumptions (10 and 30 Myr), using the COND evolutionary model.

7.3. Point-source detection limit

We do not detect any point source in the entire IRDIS field of view. The contrast curves at 5σ are measured with the SpeCal pipeline (Galicher et al. 2018) for KLIP-reduced data (Fig. 15). IRDIS provides contrasts of about 10^{-5} at 0.5″ and 10^{-6} at 1″. The IFS contrasts are similar or slightly better at <0.4″ and then degrade for larger separations. For this reason, we considered the IRDIS contrast curve only to derive the limit of detection in terms of mass. Figure 15 displays the limit of detection using the COND model (Allard et al. 2001), and assuming two possible ages of the system: 10 and 30 Myr. We note that if the system were 10 Myr old we should be able to detect a planet of 3 Jupiter masses at a separation of 0.5″ (and respectively 1.3″ for 30 Myr). The values below 1 $M_{\rm J}$ are unreliable in the framework

[2] We note that if the gas were primordial, the total gas mass (accounting for extra H_2) could go up to $10^2\,M_{\oplus}$, but this is probably not the case as shown in Kral et al. (2017, 2018).

[3] If grains become slow enough because of gas drag and come back to the Epstein regime, we calculate that for β values between 1 and 5 (realistic for an A6V star, see Thebault & Kral 2019), the unbound stopping times (over the crossing time) are roughly one to two orders of magnitude larger than derived in Eq. (9), meaning that even in the Epstein regime, grains of 0.1 μm will also have stopping times close to 1–10, i.e., gas will have time to substantially brake unbound grains before they leave the disk.

of the COND model. Since the noise is estimated azimuthally in SpeCal, the disk itself contributes 40% to the contrast curve in the range 0.2″–1.2″.

8. Conclusions

The findings of this paper can be summarized as follows:

- We observed the debris disk of HD 32297 in the NIR in the *Y*, *J*, and *H* bands out to stellocentric distances of 3.3″, and for the first time as close as 0.15″. We obtained both total intensity and polarimetric images as well.
- At large separations, the disk is characterized by a concavity as reported by Schneider et al. (2014). At shorter separations (<1″), a bow-like shape is reminiscent of a very inclined belt of which we see mostly one side (northwest) due to the forward scattering by the grains. Noticeably, we were able to detect the back side of the disk which we modeled using two HG phase functions. This feature is not observed in polarimetric data possibly due to low S/N.
- Upon first inspection, the disk appears to be symmetrical in NE and SW sides and has no gapped structure in contrast to the claims of Asensio-Torres et al. (2016). This is confirmed unambiguously with our photometric study in which the surface brightness profiles do not show any significant brightness asymmetry between the two sides, or any gap.
- We present two methods for extracting the photometry of inclined disks observed in total intensity. The first method includes the estimation of the ADI self-subtraction in model images and accounting for this bias into the data. We find that this method can induce some irregularities depending on the accuracy of measurement of the ADI self-subtraction. In the second method we calculate a scaling factor between the ADI processed data and its corresponding model. The scaled model is used to measure the photometry instead of the data. As a drawback any departure from the model is not represented in the measurements.
- Comparing total intensity and polarimetry in the *J* band we derived a polarisation fraction of about 15% which is in accordance with other debris disks.
- From photometric measurements obtained in 40 spectral channels we obtained an average spectral reflectance and conclude that the disk is "gray to blue" color in the *YJH* spectral range. Using a radiative transfer module in GRaTer we were able to compare this measured reflectance with those expected for a variety of grain sizes and compositions. We found that irrespective of the composition, grains should be significantly smaller than the corresponding blowout size (sub-micron size for astrosilicates).
- Finally, we discussed that the presence of the small grains and the associated blue color of the disk can originate from a combination of several physical processes, including steady-state collisional evolution and the avalanche process. Given the amount of gas in this system (Greaves et al. 2016; Cataldi et al. 2019), we also found that the gas drag can retain smaller unbound grains over a longer timescale.

HD 32297 is amongst the very few known bright and extended debris disks with gas. The SPHERE observations are of unprecedented quality allowing the detection of this disk at high S/N in all spectral channels, and strong constraints to be derived on the grain properties. Confirming the trend of the spectral reflectance would require additional SPHERE observations in the *K* band in total intensity as well as polarimetric data in the *H* and *K* bands. It would be interesting to perform the very same type of observations and data analysis for other gas-rich debris disks and investigate if they share similarities with HD 32297 as an attempt to understand whether the presence of gas can fully explain the dust size distribution.

Acknowledgements. French co-authors acknowledge financial support from the Programme National de Planétologie (PNP) of CNRS-INSU in France. The project is supported by CNRS, by the Agence Nationale de la Recherche (ANR-14-CE33-0018). Finally, this work has made use of the SPHERE Data Centre, jointly operated by OSUG/IPAG (Grenoble), PYTHEAS/LAM/CESAM (Marseille), OCA/Lagrange (Nice) and Observatoire de Paris/LESIA (Paris). J.Ma. acknowledges support for this work was provided by NASA through the NASA *Hubble* Fellowship grant HST-HF2-51414.001 awarded by the Space Telescope Science Institute, which is operated by the Association of Universities for Research in Astronomy, Inc., for NASA, under contract NAS5-26555. J.O. and C.P. acknowledge financial support from the ICM (Iniciativa Científica Milenio) via the Núcleo Milenio de Formación Planetaria grant. J.O. acknowledges financial support from the Universidad de Valparaíso, and from Fondecyt (grant 1180395). C.P. acknowledges financial support fron Fondecyt (grant 3190691).

References

Allard, F., Hauschildt, P. H., Alexander, D. R., Tamanai, A., & Schweitzer, A. 2001, ApJ, 556, 357
Asensio-Torres, R., Janson, M., Hashimoto, J., et al. 2016, A&A, 593, A73
Augereau, J.-C., & Beust, H. 2006, A&A, 455, 987
Augereau, J. C., Lagrange, A. M., Mouillet, D., Papaloizou, J. C. B., & Grorod, P. A. 1999, A&A, 348, 557
Beuzit, J.-L., Vigan, A., Mouillet, D., et al. 2019, A&A, submitted [arXiv:1902.04080]
Boccaletti, A., Augereau, J.-C., Lagrange, A.-M., et al. 2012, A&A, 544, A85
Boccaletti, A., Thalmann, C., Lagrange, A.-M., et al. 2015, Nature, 526, 230
Boccaletti, A., Sezestre, E., Lagrange, A.-M., et al. 2018, A&A, 614, A52
Boccaletti, A., Thébault, P., Pawellek, N., et al. 2019, A&A, 625, A21
Bonnefoy, M., Milli, J., Ménard, F., et al. 2017, A&A, 597, L7
Carbillet, M., Bendjoya, P., Abe, L., et al. 2011, Exp. Astron., 30, 39
Cataldi, G., Wu, Y., Ohashi, N., et al. 2019, ApJ, submitted [arXiv:1904.07215]
Claudi, R. U., Turatto, M., Gratton, R. G., et al. 2008, Proc. SPIE, 7014, 70143E
Currie, T., Rodigas, T. J., Debes, J., et al. 2012, ApJ, 757, 28
Debes, J. H., Weinberger, A. J., & Song, I. 2008, ApJ, 684, L41
Debes, J. H., Weinberger, A. J., & Kuchner, M. J. 2009, ApJ, 702, 318
Delorme, P., Meunier, N., Albert, D., et al. 2017, in SF2A-2017: Proceedings of the Annual meeting of the French Society of Astronomy and Astrophysics, eds. C. Reylé, P. Di Matteo, F. Herpin, et al., 347
Dohlen, K., Langlois, M., Saisse, M., et al. 2008, Proc. SPIE, 7014, 70143L
Donaldson, J. K., Lebreton, J., Roberge, A., Augereau, J.-C., & Krivov, A. V. 2013, ApJ, 772, 17
Engler, N., Schmid, H. M., Thalmann, C., et al. 2017, A&A, 607, A90
Engler, N., Boccaletti, A., Schmid, H. M., et al. 2019, A&A, 622, A192
Esposito, T. M., Fitzgerald, M. P., Graham, J. R., & Kalas, P. 2014, ApJ, 780, 25
Fitzgerald, M. P., Kalas, P. G., & Graham, J. R. 2007a, ApJ, 670, 557
Fitzgerald, M. P., Kalas, P. G., Duchêne, G., Pinte, C., & Graham, J. R. 2007b, ApJ, 670, 536
Fusco, T., Sauvage, J.-F., Petit, C., et al. 2014, Proc. SPIE, 9148, 91481U
Gaia Collaboration 2018, VizieR Online Data Catalog: I/345
Galicher, R., Boccaletti, A., Mesa, D., et al. 2018, A&A, 615, A92
Gáspár, A., Psaltis, D., Rieke, G. H., & Özel, F. 2012, ApJ, 754, 74
Geiler, F., Krivov, A. V., Booth, M., & Löhne, T. 2019, MNRAS, 483, 332
Greaves, J. S., Holland, W. S., Matthews, B. C., et al. 2016, MNRAS, 461, 3910
Grigorieva, A., Artymowicz, P., & Thébault, P. 2007, A&A, 461, 537
Henyey, L. G., & Greenstein, J. L. 1941, ApJ, 93, 70
Hines, D. C., Schneider, G., Hollenbach, D., et al. 2007, ApJ, 671, L165
Jackson, A. P., Wyatt, M. C., Bonsor, A., & Veras, D. 2014, MNRAS, 440, 3757
Kalas, P. 2005, ApJ, 635, L169
Kennedy, G. M., & Wyatt, M. C. 2014, MNRAS, 444, 3164
Kral, Q., Thébault, P., & Charnoz, S. 2013, A&A, 558, A121
Kral, Q., Thébault, P., Augereau, J.-C., Boccaletti, A., & Charnoz, S. 2015, A&A, 573, A39
Kral, Q., Wyatt, M., Carswell, R. F., et al. 2016, MNRAS, 461, 845
Kral, Q., Matrà, L., Wyatt, M. C., & Kennedy, G. M. 2017, MNRAS, 469, 521

Kral, Q., Marino, S., Wyatt, M. C., Kama, M., & Matra, L. 2018, MNRAS, submitted [arXiv:1811.08439]
Lagrange, A.-M., Kasper, M., Boccaletti, A., et al. 2009, A&A, 506, 927
Lagrange, A.-M., Boccaletti, A., Milli, J., et al. 2012, A&A, 542, A40
Langlois, M., Vigan, A., Moutou, C., et al. 2013, in Proceedings of the Third AO4ELT Conference, eds. S. Esposito, & L. Fini, 63
Langlois, M., Dohlen, K., Vigan, A., et al. 2014, Proc. SPIE, 9147, 91471R
Lee, E. J., & Chiang, E. 2016, ApJ, 827, 125
Lestrade, J.-F., Morey, E., Lassus, A., & Phou, N. 2011, A&A, 532, A120
Lyra, W., & Kuchner, M. 2013, Nature, 499, 184
MacGregor, M. A., Weinberger, A. J., Hughes, A. M., et al. 2018, ApJ, 869, 75
Maire, A.-L., Langlois, M., Dohlen, K., et al. 2016, in Proc. SPIE, 9908, 990834
Maness, H. L., Fitzgerald, M. P., Paladini, R., et al. 2008, ApJ, 686, L25
Marois, C. 2015, IAU Gen. Assem., 22, 2254053
Marois, C., Lafrenière, D., Doyon, R., Macintosh, B., & Nadeau, D. 2006, ApJ, 641, 556
Mawet, D., Serabyn, E., Stapelfeldt, K., & Crepp, J. 2009, ApJ, 702, L47
Mazoyer, J., Boccaletti, A., Augereau, J.-C., et al. 2014, A&A, 569, A29
Mesa, D., Gratton, R., Zurlo, A., et al. 2015, A&A, 576, A121
Milli, J., Mouillet, D., Lagrange, A.-M., et al. 2012, A&A, 545, A111
Milli, J., Vigan, A., Mouillet, D., et al. 2017, A&A, 599, A108
Milli, J., Engler, N., Schmid, H. M., et al. 2019, A&A, 626, A54
Moerchen, M. M., Telesco, C. M., De Buizer, J. M., Packham, C., & Radomski, J. T. 2007, ApJ, 666, L109
Moór, A., Curé, M., Kóspál, Á., et al. 2017, ApJ, 849, 123
Moór, A., Kral, Q., Ábrahám, P., et al. 2019, ArXiv e-prints [arXiv:1908.09685]
Mouillet, D., Larwood, J. D., Papaloizou, J. C. B., & Lagrange, A. M. 1997, MNRAS, 292, 896
Olofsson, J., Samland, M., Avenhaus, H., et al. 2016, A&A, 591, A108
Pavlov, A., Möller-Nilsson, O., Feldt, M., et al. 2008, Proc. SPIE, 7019, 701939
Pueyo, L. 2016, ApJ, 824, 117
Rodigas, T. J., Debes, J. H., Hinz, P. M., et al. 2014, ApJ, 783, 21
Schmid, H. M., Joos, F., & Tschan, D. 2006, A&A, 452, 657
Schneider, G., Silverstone, M. D., & Hines, D. C. 2005, ApJ, 629, L117
Schneider, G., Grady, C. A., Hines, D. C., et al. 2014, AJ, 148, 59
Silverstone, M. D. 2000, PhD Thesis, University of California, Los Angeles
Soummer, R., Pueyo, L., & Larkin, J. 2012, ApJ, 755, L28
Strubbe, L. E., & Chiang, E. I. 2006, ApJ, 648, 652
Takeuchi, T., & Artymowicz, P. 2001, ApJ, 557, 990
Thalmann, C., Schmid, H. M., Boccaletti, A., et al. 2008, Proc. SPIE, 7014, 70143F
Thébault, P. 2012, A&A, 537, A65
Thebault, P., & Kral, Q. 2018, A&A, 609, A98
Thebault, P., & Kral, Q. 2019, A&A, 626, A24
Thébault, P., & Wu, Y. 2008, A&A, 481, 713
Thebault, P., Kral, Q., & Ertel, S. 2012, A&A, 547, A92
Tinbergen, J. 1996, Astronomical Polarimetry (Cambridge, UK: Cambridge University Press), 174
Vigan, A., Moutou, C., Langlois, M., et al. 2010, MNRAS, 407, 71
Wyatt, M. C. 2008, ARA&A, 46, 339

3.3 Supplements

While the article gives specifications of the modeling and the photometry performed for the disk, here I am presenting further details and providing corresponding plots.

3.3.1 Histograms and selection of best-fit model

As explained in Chapter 2.3 the selection of best models is done by taking the 1% of the reduced models having least χ^2 values. The parameters of the best models are represented in histograms (Fig 3.5) for the total intensity models (both single HG phase functions and two HG phase function) and the polarimetric models. Gaussians are fitted to the histograms except when the histograms have a flat distribution or if there are less than four values for a given parameter space. The flat distribution is seen for α_{in} and g_2 in panels corresponding to total intensity. In case a Gaussian can not be fitted an average value of the distribution is taken as the best value and the dispersion from the average to the highest and lowest values as the limits.

3.3.2 Error measurement with fake disk

To measure an extraction error as mentioned in Sect. 5.1 of the article a fake disk corresponding to the best-fit model parameter is scaled to a flux of 5×10^{-4} and injected into each science frame at an angle 90° to the position angle. These data are processed with KLIP and the final IRDIS image is shown in Fig 3.6 (Top). The scaled GraTer model corresponding to the fake disk is also processed with KLIP using the same basis used in previous step.

A channel by channel minimization of the science image and the KLIP image of the fake disk is done and plotted in Fig. 3.6 (Bottom). This factor is expected to be ~ 1 as both the data and the reduced model are scaled to the same contrast of 5×10^{-4}. Any deviation from 1 is the contribution from the noise in the science image. The standard deviation of this minimisation factor at all spectral channel is 0.033. Therefore, this 3.3% is considered as an extraction error and this error is propagated in the photometric measurements.

Photometric extraction using both Method 1 and 2 are done for the fake disk to determine the accuracy of the process as explained in Sect. 5.3 of the article.

3.3.3 Comparison with ALMA observation

Study of the millimeter ALMA observation of the disk provided a different geometry compared to our modeling. This disagreement between the models is argued in the article to have occurred due to poor resolution of ALMA compared to SPHERE and/or because the two instruments probe different grain size. The ALMA beam size was $0.76'' \times 0.51''$

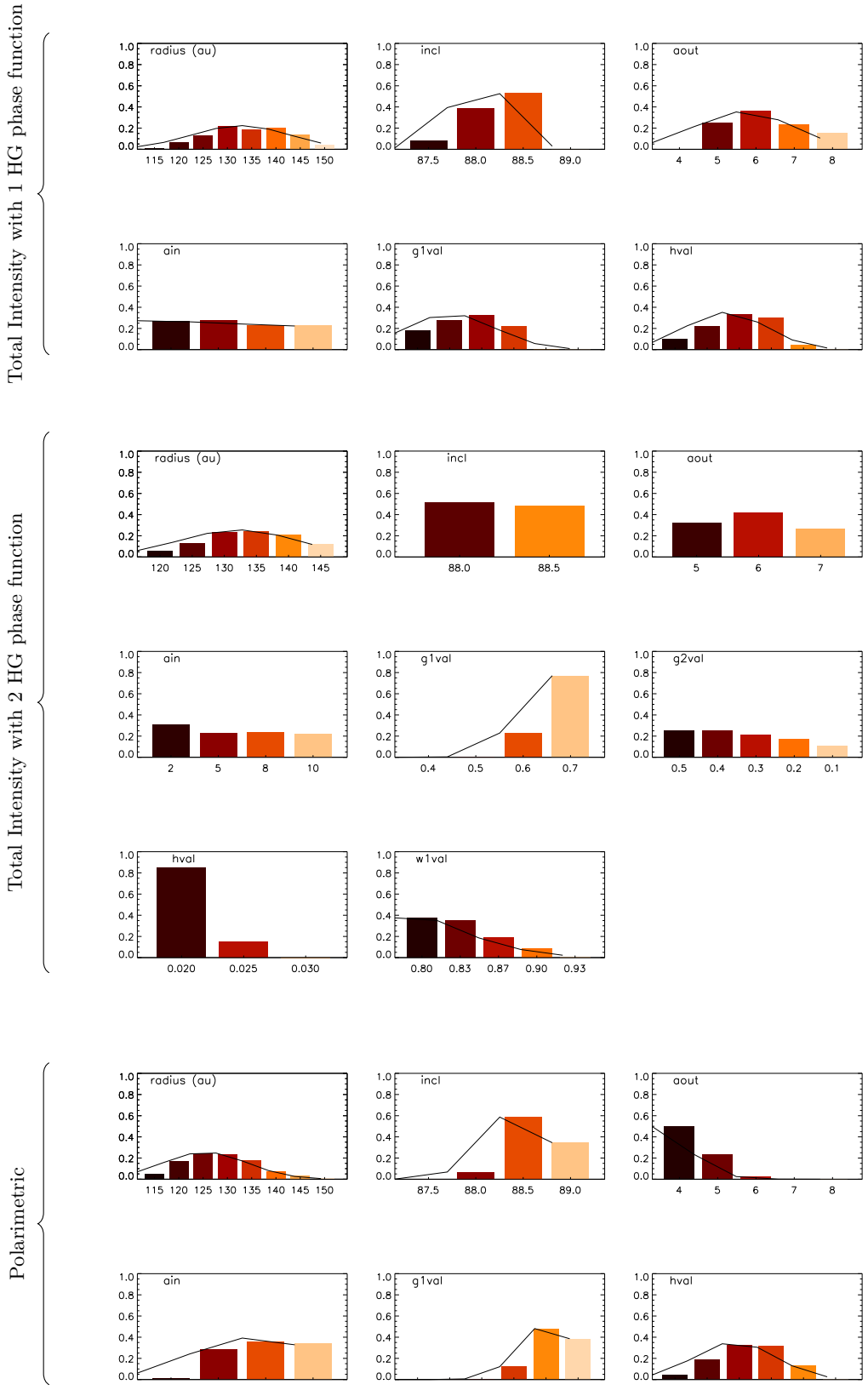

Figure 3.5 *– Histograms of Total intensity models with 1 HG (Top) and 2 HG (Middle) parameter. Bottom: Polarimetric models with 1 HG parameter. Histograms are overlapped with Gaussian when significant*

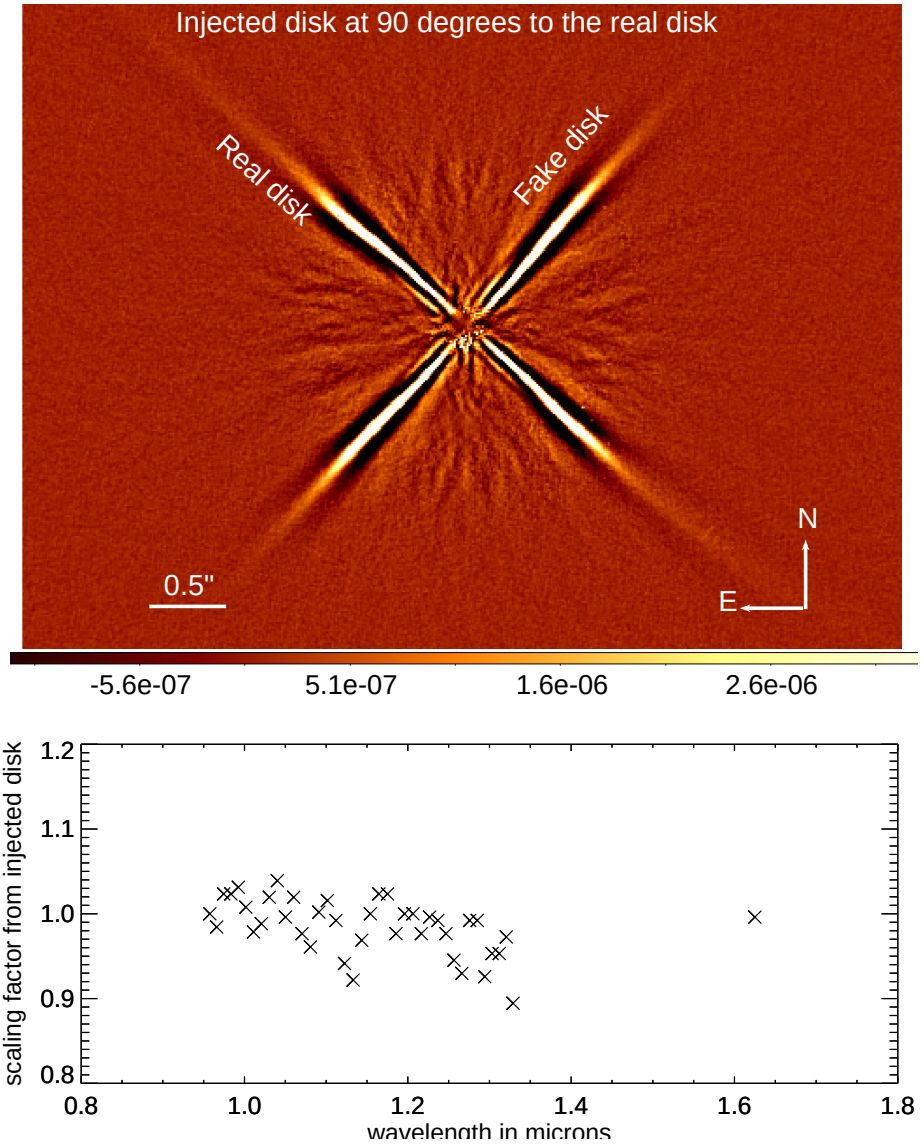

Figure 3.6 – *Top:KLIP image of fake-disk injected at 90 ° to the real disk. The model used for fake disk is i=88°, α_{out}=-6, α_{in}=2, R_0=140 au, g_1=0.70, g_2=-0.4, w_1=0.80, h=0.020, contrast = 0.0005. Bottom: Scaling factor retrieved for the fake-disk compared to its corresponding model*

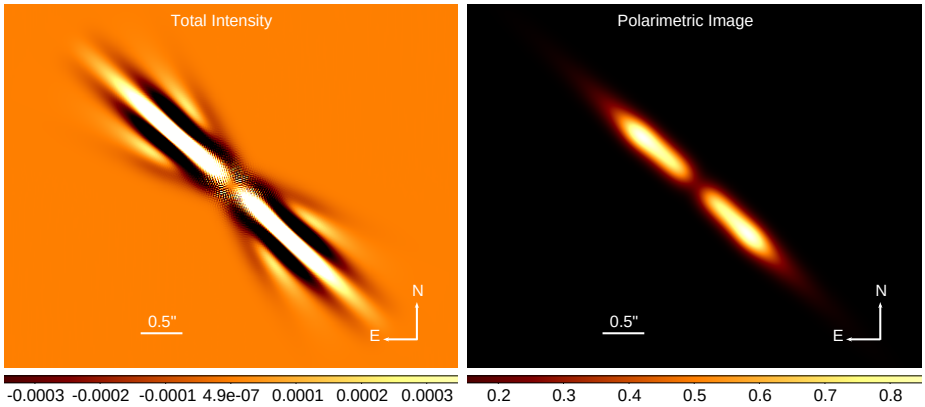

Figure 3.7 *– Total Intensity model with the parameters i=88°, α_{out}=-6, α_{in}=2, R_0=140 au, g_1=0.70, g_2=-0.4, w_1=0.80, h=0.020 convolved with a 2D Gaussian PSF of HWHM=0.37″. The dark stripes in the ADI processed model (Left) is an effect of ADI self-subtraction. Polarimetric model with parameters i=88.5°, R_0 = 125au, α_{in}= 10.0, α_{out}=-4.0, g=0.8, h=0.020 convolved with a 2D Gaussian PSF of HWHM=0.37″.*

To verify the first argument and have a visible comparison the best-fit model retrieved for our total intensity and polarimetric observation is convolved with a 2D Gaussian PSF of HWHM = 0.37″ instead of the instrumental PSF. The PSF used in SPHERE measurements have a HWHM of less than 0.1″. The resulting models as seen in Fig. 3.7 appear to be thicker and less resolved (the back side of the disk is not visible) than the reduced best-fit models retrieved in Fig. 5 and 7 of the article, eventhough the geometrical parameters are kept the same. Irrespective of the point that ALMA and SPHERE probe different wavelength regime, hence different grain sizes, the difference of resolution of the two instruments is sufficient to explain the discrepancy found in the values of their respective best-models. Therefore, it is obvious to conclude a different geometry (probably more accurate) of the disk with SPHERE's observation.

CHAPTER 4

Test on other disks

4.1 Debris disk around HD 141569 71
4.1.1 Observation and Data Reduction 72
4.1.2 Morphology of the disk as observed in two epochs 75
4.1.3 Modeling the ringlet R3 77
4.1.4 Photometry of the ringlet R3 81
4.1.5 Modeling the particle size distribution in the ringlet R3 87
4.1.6 Discussion and Conclusion 88
4.1.7 Perspective and Outlook 89
4.2 Preliminary study of HD 106906 90
4.2.1 Observation and Data Reduction 90
4.2.2 Morphology of the debris disk and photometry of the planet . . . 93
4.2.3 Modeling the debris disk 93
4.2.4 Photometry of the debris disk 99
4.2.5 Modeling the particle size distribution in the debris disk 99
4.2.6 Conclusion and Prospective 104

This chapter is divided into two parts dedicated to the disks HD 141569 and HD 106906. In each part, an introduction to the respective disks, the sequence of their observation and forward modeling performed on the subsequent data is provided. Both subsections dedicated to these two disks focus on photometric extraction of the disks and obtaining constraints on particle size distribution. Two different studies are performed given the different geometry of disks under analysis.

4.1 Debris disk around HD 141569

The disk HD 141569 is a young (5 Myr, Dent et al., 2005) gas-rich debris disk around a star which is of B9.5V/A0V stellar type and 110 pc (Gaia DR2, Gaia Collaboration, 2018) away. When imaged by HST, this disk was classified as a two-ring system with an

inner and outer disk positioned roughly at 237 au and 389 au from the star respectively (Augereau et al., 1999a; Weinberger et al., 1999). A detailed study on the HST observation was performed that suggested the presence of multiple structures (Mouillet et al., 2001) within the inner and the outer belts, including a multiple spiral systems (Clampin et al., 2003). The possibility of spirals was revisited and its origin triggered by associated two M type stellar companions HD 141569 B and C or at least one of them perturbing at an orbit of periastron distance of 930 AU and eccentricity of 0.7 to 0.9 (Augereau & Papaloizou, 2004) or by outer planets (Wyatt, 2005a) or both (Beust et al., 2009) were discussed.

The observation of this disk by the ground-based Palomar telescope was first performed in the K band where an east-west asymmetry in the disk was discussed Boccaletti et al. (2003). The follow-up observation of the disk with a high-contrast imager NICI in NIR resolved the inner ring in its entirety at 237 au by Biller et al. (2015) and Mazoyer et al. (2016). Mazoyer et al. (2014b) also suggested the inner edge of the cavity to be symmetric. Apart from the dust component, a large amount of hot and cold CO was observed at different wavelengths (Brittain et al., 2007; Dent et al., 2005; Péricaud et al., 2017; Thi et al., 2014).

The first photometry evidence provided in Augereau et al. (1999a) suggested the presence of inner material closer than 100 au from the star. CO detection was also confirmed at $\sim$ 50 au by Goto et al. (2006). The presence of polycyclic aromatic hydrocarbon (PAH) emission by Thi et al. (2014) was found at the same distance. In scattered light observation, Konishi et al. (2016) detected a uniform pattern at 45-100 au. However, this pattern was reported to be detected at a closer distance of 30 au in L' band observation by Currie et al. (2016). With the SPHERE instrument in 2015, the innermost region of the disk at less than 40 au was imaged. The inner region of the disk is of particular interest because it features several broken concentric ringlets. Perrot et al. (2016) presented resolved images of several features, such as the inner and outer rings, a split structure, an arm to the inner ring, a finger and the third innermost ringlet R3 with a semi-major axis of $0.4''$ (46 au) from the star as shown in Fig 4.1. At the ansae of the inner ring, the presence of a clump similar to a point source was discussed in the same study. The clump is seen in Fig. 4.1 (Right) which is a zoomed view of the disk of the left side of Fig. 4.1.

Similar to other debris disks, previous studies were concentrated on resolving the structural features and postponing a detailed study of the photometry of this disk. Therefore, the motivation of this study is to obtain and investigate the photometric measurements of the innermost ringlet R3 and a possible clump in this ringlet.

4.1.1 Observation and Data Reduction

The disk was observed with SPHERE several times. In this study, I am focusing on two epochs of observations under the GTO, first taken on May 2015 and the second in March 2016. Both observations were performed with an Apodized Lyot Coronagraph (N_ALC_YJH_S, Carbillet et al., 2011) with a diameter of 185 mas. The first epoch observation was done in pupil-stabilized IRDIFS mode. In IRDIS, the target was observed in H2 ($\lambda = 1.593\mu$m, $\delta\lambda = 0.52\mu$m) and H3 ($\lambda = 1.667\mu$m, $\delta\lambda = 0.52\mu$m) filters and with IFS it was observed in YJ band ($0.95 - 1.35\mu$m). The atmospheric conditions were good

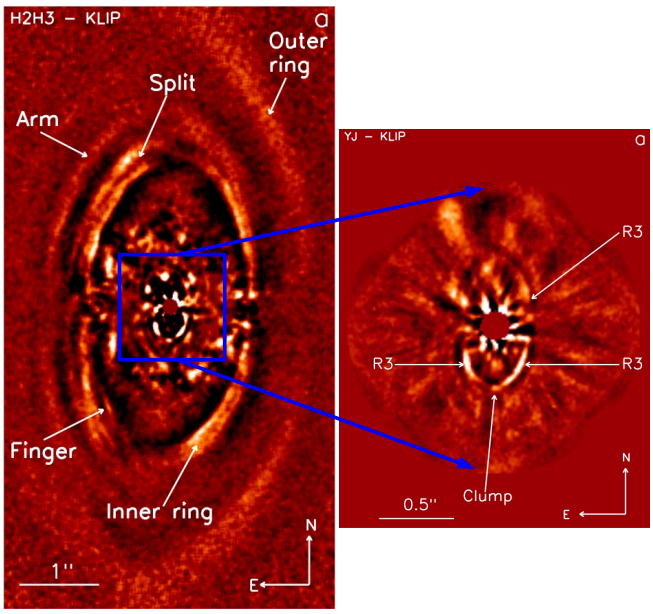

Figure 4.1 *– The two images correspond to the Fig. B.1 (Leftmost) and B.2 (Top-Left) from Perrot et al. (2016) respectively. The image on the left shows a bigger FOV with the outer ring, inner ring and associated features. The image on the right shows the IFS FOV with the ring R3 and the clump.*

with coherence time $\tau_0 = 3.5$ ms and seeing $= 0.83''$ for H2H3-YJ. The observations in the second epoch were done in pupil-stabilized IRDIFS-EXT mode. IRDIS observation was done with K1 filter ($\lambda = 2.11\mu$m, $\delta\lambda = 1.02\mu$m) and K2 ($\lambda = 2.251\mu m, \delta\lambda = 1.09\mu$m). In IFS, the observations were done with the YJH band ($0.95 - 1.65\mu$m). The atmospheric conditions and the seeing were similar to the first epoch. The details of the observation log are provided in Sect. 4.1. The subsequent observations have poor data quality and therefore not used in this thesis.

The preliminary data reduction was done at the data center (Delorme et al., 2017) with the DRH pipeline (Mesa et al., 2015; Pavlov et al., 2008). It included the sky and dark subtractions, flat field corrections, correction for bad-pixel, distortion correction (Maire et al., 2016) and wavelength calibration. Then, the data cubes were processed with TLOCI and PCA (3, 5 modes), which are ADI based algorithms, using the SpeCal code (Galicher et al., 2018).

The two epochs are reduced with KLIP 3 and 5 modes using an algorithm developed by Boccaletti et al. (2012). All the images are normalized to the maximum of the instrumental point spread function (PSF).

***Table 4.1** – SPHERE observation log of HD 141569*

Data UT	prog. ID	Filter	Field rotation (°)	DIT (s)	T_{exp} (s)	Seeing (″)	τ_0 (ms)	TN (°)
2015-05-16	095.C-0298(A)	IRDIS-H23	42.70	64	4096	0.83	3.5	-1.712
2015-05-16	095.C-0298(A))	IFS-YJ	42.70	64	4096	0.83	3.5	-1.712
2016-03-30	096.C-0241(E)	IRDIS-K12	42.64	64	4090	0.86	3.1	-1.756
2016-03-30	096.C-0241(E)	IFS-YH	43.14	64	4096	0.86	3.1	-1.81

The following information is provided from left to right: the observation data, program ID, filter combination, the total field rotation in degrees, the individual integration time of each frame (DIT) in seconds, the true time in seconds (T_{exp}), the DIMM seeing in arcseconds, τ_0 the correlation time in milleseconds and the true north correction angle in degrees (TN).

4.1.2 Morphology of the disk as observed in two epochs

4.1.2.1 IRDIS images

The top row of Fig. 4.2 shows the science image of the IRDIS H2H3 band epoch 1 observation. The images on the left and right are reduced by KLIP (truncated at 3 modes) and TLOCI respectively. Similarly, the bottom row of Fig. 4.2 represents the epoch 2 IRDIS K1 band observations reduced by KLIP 3 mode on the left and TLOCI on the right respectively. The observations in the second epoch taken in the K1 band (Fig. 4.2 Middle and Right) are noisier than in the H2H3 band of first epoch (Fig. 4.2 Left) because of data polluted by the thermal background of the instrument. The effect of thermal background on the contrast of the images are significantly visible in the contrast curves, which are plotted in Fig. 4.3 using the SpeCal (Galicher et al., 2018) for PCA 3 modes. As seen in Fig. 4.3, IRDIS H2H3 observation of epoch 1 reaches deeper contrasts than K1K2 of epoch 2, especially beyond the separation of 1″. The K band images are often affected by the thermal gradient in the instrument. This effect is stronger in the K2 than in the K1 filter which makes the image quality degrade.

A part of the outer ring as labeled in Fig. 4.1 and in Fig. B.1 of Perrot et al. (2016) with semi-major axis of ∼3.3″ is seen in epoch 1 Fig. 4.2 observation however is faintly visible in epoch 2. The inner ring with a semi-major axis of ∼2.1 ″ and a split structure in the north-eastern part of this ring at an angular separation of ∼1.77″, as labeled in (Fig. 4.2 (Bottom)), are well observed in both the epochs. The arms just outside the inner ring in the eastern part, a finger-like structure at a separation of ∼1.5″ and a possible spiral S2 at a separation of ∼0.9″ in the south-eastern part are faintly observed in the second epoch compared to the first epoch image.

At a separation below 0.8″ the parts of inner ringlets labeled R1, R2, and R3 in Fig. 4.2 (Right) are observed. Parts of R1 are observed in the south-eastern and north-western regions in the first epoch image tracing an ellipse with a semi-major axis of 0.6″. A part of R1 is visible only in the south-eastern region in the second epoch images (Fig. 4.2 Right). North-western and southern parts of R2 are visible in both the epochs in H2H3 and K1 bands. The southern ringlet R3 bearing a possible clump at ∼0.4 ″ is also visible in both the epochs.

4.1.2.2 IFS images

Figure 4.4 (top and middle) show the median images of IFS YJ (in epoch 1) and YJH (in epoch 2) band reduced with KLIP 3. In Fig 4.4 in the top row, the northern part of R2 is much more prominently distinguishable than in epoch 1 and fragments of R2 are seen in the southern part in both epochs. R3 is comparatively better observed than R2 in both epochs however comparing the northern and the southern parts, the southern part of R3 is well detected. In the middle row of Fig. 4.4, ellipses are drawn to denote the position of the rings, where the green ellipse denotes R3 (semi-major axis = 0.43″) and the blue denotes R2 (semi-major axis = 0.56″). In the bottom row of Fig 4.4, the IRDIS images

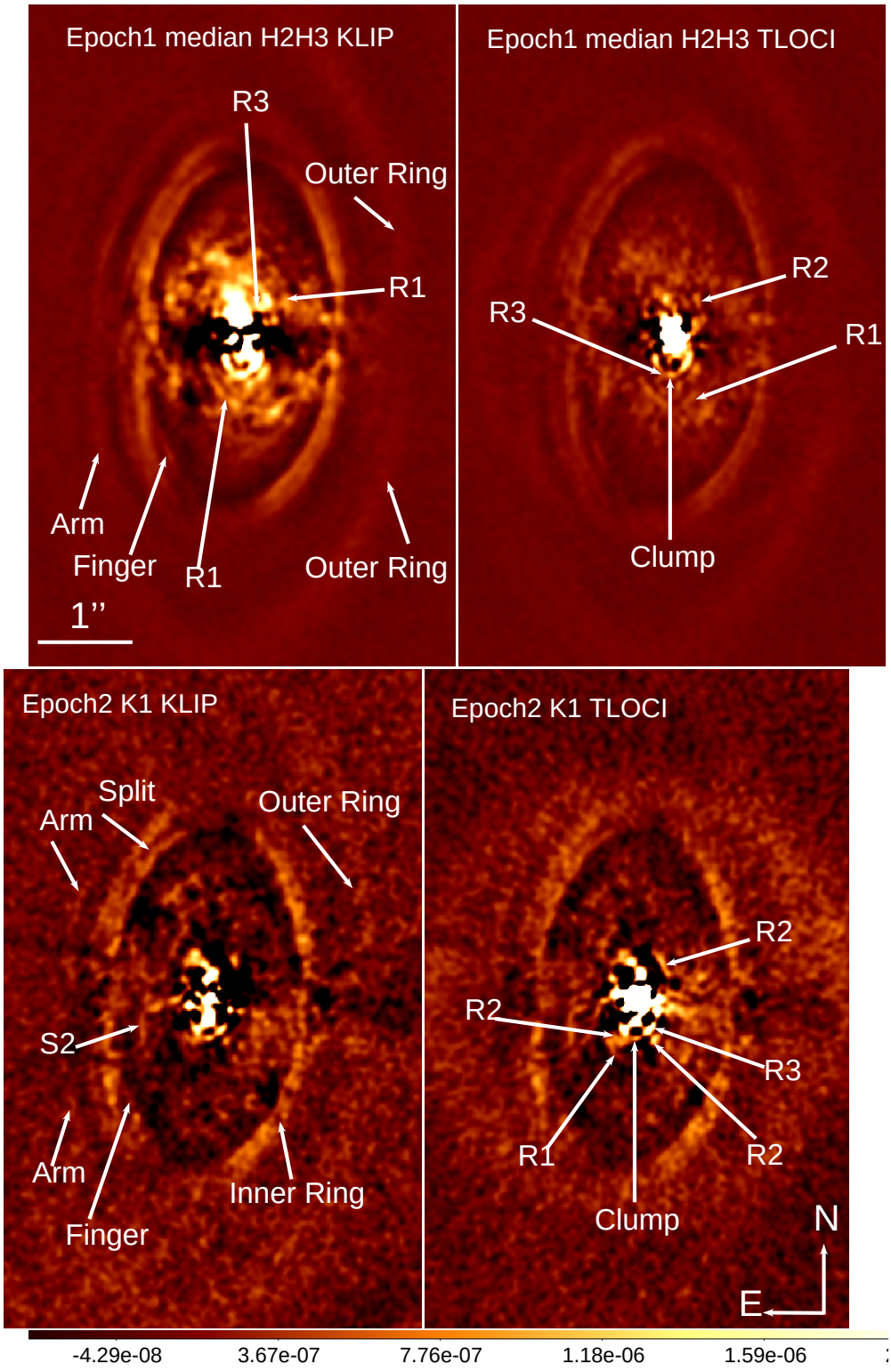

Figure 4.2 *– On the top row the median image of epoch 1 IRDIS-H2H3 reduced with KLIP-3 (Left) and TLOCI (Right) is shown. Similarly, on the bottom row the IRDIS-K1 image of epoch 1 reduced with KLIP-3 (Left) and TLOCI (Right) is shown. The features are labelled. The colorbar represents the intensity scale (in arbitrary units) for all images. All the three images are of the FOV* $4.97'' \times 5.85''$ *and smoothed to Gaussian kernel of radius of 5 pixels.*

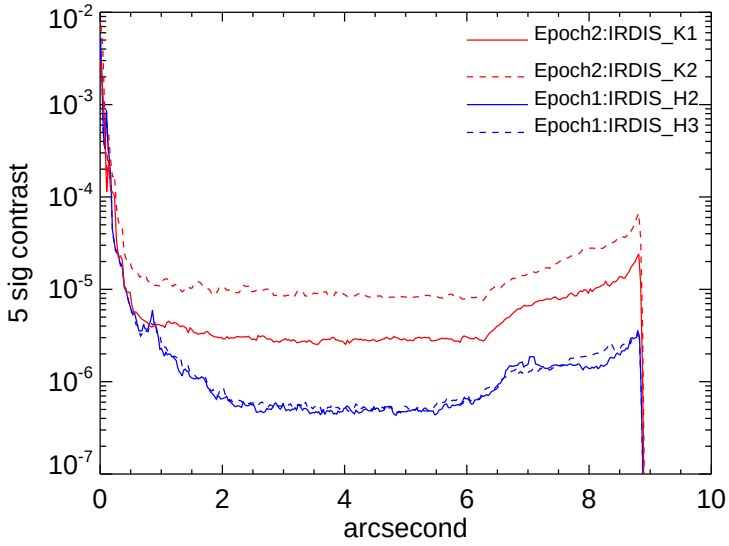

Figure 4.3 *– Contrast curves extracted with SpeCal for PCA 3 modes reduction of the epoch 1 (in blue) and epoch 2 (in red) images presented in Fig. 4.2.*

are zoomed to a comparable scale of IFS images. In the IRDIS image, it can be seen that R2 is not well observed compared to its IFS counterpart.

The clump is consistently visible in both epochs and both IFS and IRDIS observations as seen in Fig. 4.4. To understand whether this clump is an ADI artifact or a physical structure similar to a point source I have performed forward modeling to extract spectrometry of the clump and of the whole ringlet R3 which is discussed in the upcoming subsections.

4.1.3 Modeling the ringlet R3

To account for the self-subtraction from ADI reduction, I create a synthetic image of the innermost ringlet using GraTer code (Augereau et al., 1999b) and then process them with the same KLIP 3 mode algorithm with the same eigenvalues as the data was processed. This technique is described in Sect. 2.3 and 3.2.

The search of best-fit model is done only using the southern part of the ringlet R3 of epoch 1 IRDIS H2 band science image. This is because the data quality of epoch 1 is better compared to epoch 2 as well the southern part of the ringlet is better visible than the northern part. Including the full ringlet in extracting the parameters would induce biases and the model itself does not handle such north-south asymmetries.

The list of free-parameters are listed below where the initial guesses are assumed from Perrot et al. (2016):

- ansae of the disk r_0 (au): 44, 45, 46, 47, 48

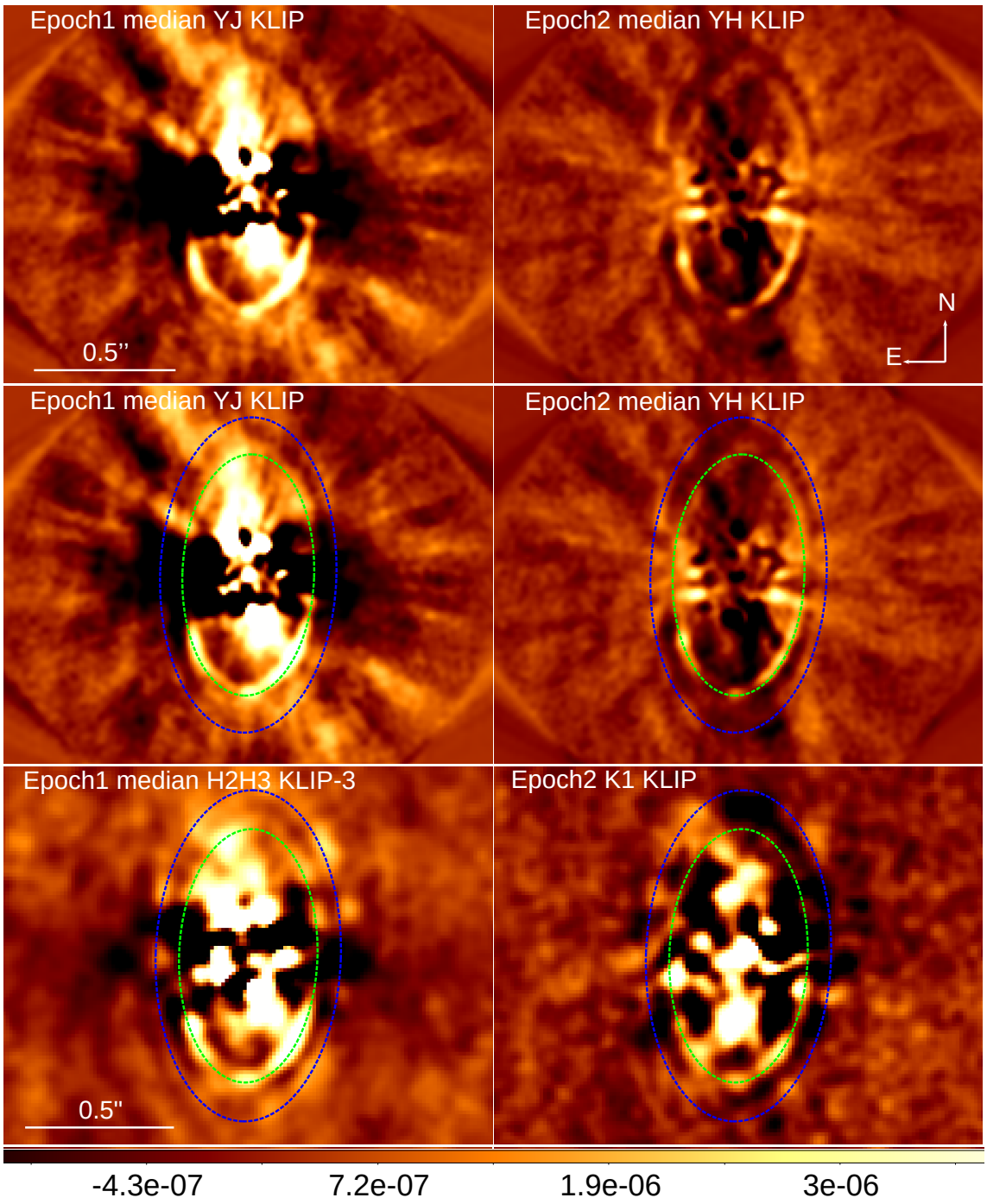

Figure 4.4 *– Column 1 and Column 2 show the epoch 1 and epoch 2 median image of KLIP reduced IFS observation, duplicate image of the top panel overplotted with the two ringlets R2 (blue) and R3(green) and the epoch 1 (median image of H2H3 band) and epoch 2 (image of K1 band) of KLIP reduced IRDIS observation overplotted with R2 (blue) and R3 (green). The colorbar represents the intensity scale (in arbitrary units) in all the images. The IFS images are cropped to* $1.71'' \times 1.33''$*. The IRDIS image are cropped to* $1.64'' \times 1.25''$*. All the images are smoothed to a Gaussian kernel of radius of 3 pixels.*

- α_{in}: 5, 10, 15, 20, 25, 30, 35, 40
- α_{out}: - α_{in}
- scale height h: 0.01, 0.02, 0.03, 0.04
- inclination i (°): 50, 51, 52, 53, 54, 55, 56, 57, 58, 59, 60
- HG parameter g: 0.0, 0.1, 0.2

The α_{in} = -α_{out} is used for an assumption of symmetrical ring. This assumption is made for the simplicity of modeling. The parameter space for g is restricted to values close to 0.0 because the the south-eastern and south-western part of the ringlet R3 is equally bright exhibiting signs of isotropic scattering. The position angle (PA) is kept constant at 356.5° which is obtained from Mazoyer et al. (2016); Perrot et al. (2016). To retrieve a best-fit model, each GRaTer model is first convolved and normalized to the instrumental PSF. Then this PSF convolved GRaTer model is injected into an empty cube and processed with KLIP-FM (details can be found in Sect. 2.3). The number of reduced models created in the grid are 5280. Finally, a χ^2 minimization is done by applying a half-elliptical mask (aperture) to the model and the science image. The mask is chosen such that it encompasses the southern part of R3. The half elliptical mask which is centered on the star has a width, semi-major axis and semi-minor axis of 0.074″, 0.36″ and 0.18″ respectively.

The reduced χ^2 is calculated between the science image ($S_{i,j}$) and the reduced models ($M_{i,j}$) at i, j^{th} pixel and added over the total number of pixels in the mask (N_{data}) as described in Chapter 2. Here, the set of five parameters are used to create one model. The parameter a is a scaling factor between the science image and the reduced model encompassed within the mask. The reduced model having a minimum value of χ^2 is taken as a reduced best-fit model. To compare the reduced model having 1% of the lowest value of χ^2 a histogram is plotted as seen in Fig. 4.5.

The inclination is found by fitting a Gaussian over its corresponding histogram plot and the peak of the Gaussian represents the inclination value and the 1σ deviation represents the error which is $55.38° \pm 1.25°$. The inclination, α_{in}, α_{out} and R_0 found here are within the error range of the values found by Perrot et al. (2016) which are $55.38° \pm 1.25°$, 22.11 ± 7.25, -22.11 ± 7.25 and 45 au (0.41″) respectively. The steep radial slopes α_{in} and α_{out} determines that the ringlet R3 is very thin. Most reduced models within 1% of the lowest value of χ^2 peak to R_0 = 45 au and g = 0.0 making it difficult to fit a Gaussian to their corresponding histogram. Therefore, errors are not measured on g and R_0. Whereas the histogram corresponding to the h parameter shows a very flat distribution so the mean and the dispersion is taken from the histogram as the best value h=0.025±0.015. This is because the parameter h measures the vertical profile or thickness of the disk which is difficult to constraint for a non-edge-on geometry. The parameters used to create the best-fit model and its χ^2 are provided in Table 4.2.

As seen from the contrast curve in Fig. 4.3, the H2H3 band observations are far superior in contrast than the K1K2 band observations. Therefore, the parameters of the best-fit model obtained for H2 band are used for all the spectral channels and epochs assuming that the wavelength dependent parameters have minimum spectral variation.

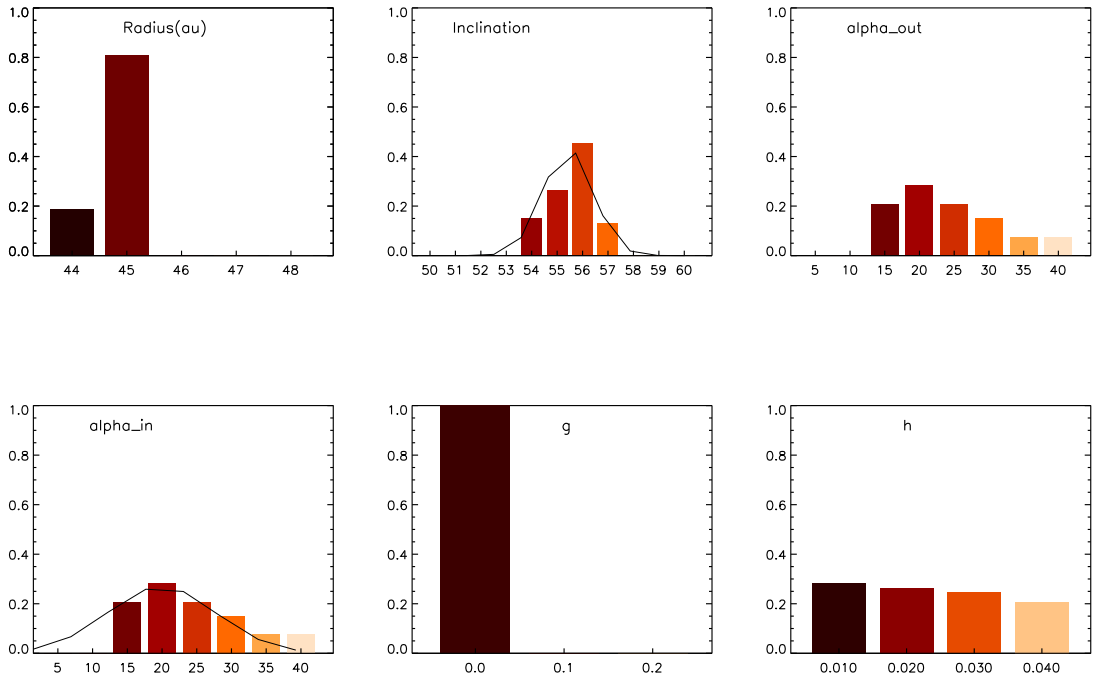

Figure 4.5 *– Histograms representing the 1% of reduced best-fit model for each parameter. Gaussians are overplotted for the histogram corresponding to the inclination and α_{in} parameters. The*

Table 4.2 *– Parameters of best-fit grain model for HD 141569*

Parameters	Best-fit model
r_0 (au)	45
α_{in}	20 (22.11±7.25)
α_{out}	-20 (22.11±7.25)
i (°)	56 (55.30±1.25)
g	0.0
h	0.01 (0.025±0.015)
χ^2	0.727

The parameters in bracket represent the value retrieved with Gaussian error analysis

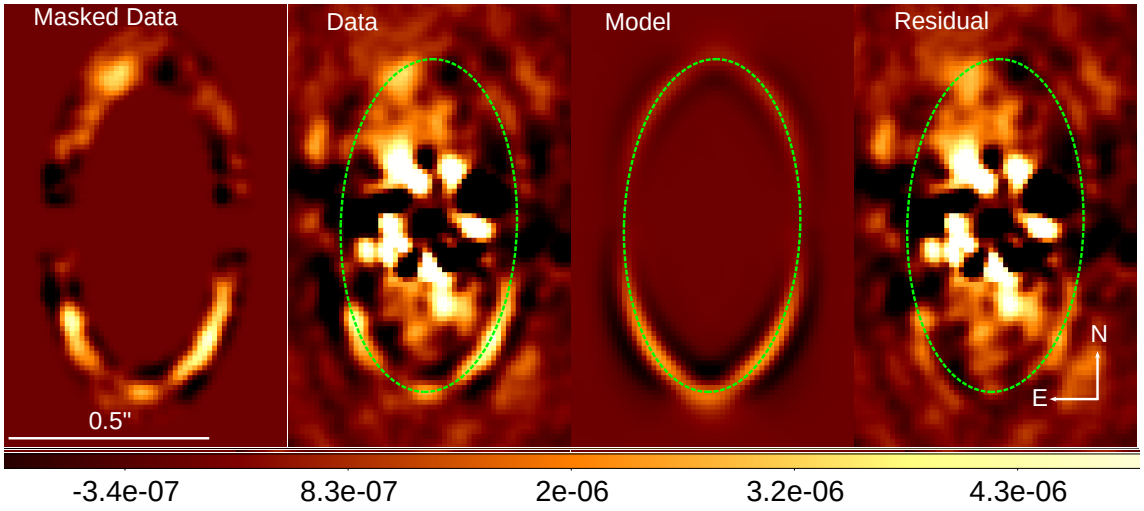

Figure 4.6 *– From Left to right: The images show the epoch1 masked KLIP processed data, the KLIP processed data without the mask, the scaled best-fit model and the residuals map. The green ellipse drawn shows the innermost ringlet R3. The FOV is* $0.7'' \times 0.98''$ *for all the images and smoothed to Gaussian kernel of radius of 2 pixels. Colorbar represents the intensity scale (in arbitrary units) for all the images.*

The masked data in Fig. 4.6 (Leftmost) is obtained by multiplying the half elliptical mask to the southern and northern part consecutively. The residual of (reduced best-fit model subtracted from the science image) is plotted in Fig. 4.6 (Rightmost). In this figure, the northern and the southern part of the best-fit model is scaled in flux separately to match the inherent North-South brightness asymmetry in the ringlet. The reduced best-fit model can be seen to have ADI artifacts especially in the ansae of the ringlet producing an intensity bump. This intensity bump could be due to enhancement caused by the negative lobes on each side of the position of the clump as seen in the reduced best-fit model. From the residual map, it can be said that the reduced model represents the science image fairly well especially at the position of the clump. However, there are still stronger residuals at certain positions of the disk compared to that of the position of the clump. This effect can either be because the reduced models do not account for azimuthal intensity variation which is seen in R3 or these can be stellar residuals. At this stage, it is difficult to conclude whether the fluctuations within the masked data are density fluctuations of the disk itself affected by ADI self-subtraction or noise.

4.1.4 Photometry of the ringlet R3

I investigated whether photometry can identify the presence of the clump as an artifact or a true disk density clump. To extract true photometry of the ringlet R3, the first step is taken by de-projecting the ringlet R3 in all the wavelengths using the geometry where inclination i=56° and PA = 356.5°. The de-projected images of the innermost ringlet observed in Epoch 1 with the IRDIS H2 filter and reduced by KLIP 3 along with the KLIP reduced best-fit model is shown in Fig. 4.7.

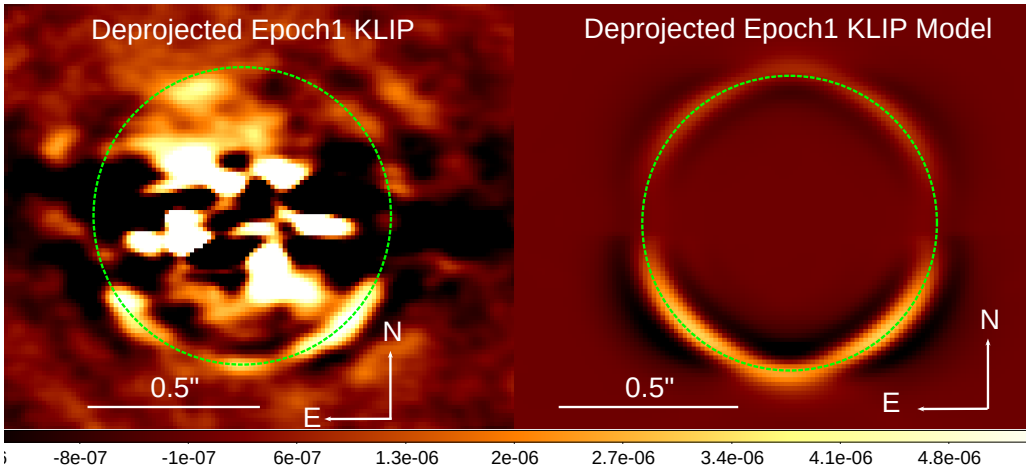

Figure 4.7 *– On left is the image representing the de-projected KLIP 3 modes reduced IRDIS H2 data. On right is the image representing the de-projected KLIP reduced best-fit model. The colorbar represent the intensity of both the images in arbitrary units. The image is cropped to* $2'' \times 1.36''$ *and smoothed to a Gaussian kernel of 2 pixels*

The surface brightness profile is calculated by taking an azimuthal average in concentric non-overlapping circles of width 4 pixels in the de-projected scaled best-fit model in the northern part and the southern part separately. The de-projected best-fit models are scaled by a factor a, which is retrieved by minimizing the masked science image to the masked reduced best-fit model using downhill simplex method (Powell, 1973). The mask used here is the same as used in χ^2 analysis. The profiles are then converted to magnitude/arcsec^2 taking the pixel scale into account and normalizing to the stellar PSF masked over a circular area of $0.4''$ radius for IRDIS and $0.3''$ radius for IFS. The instrumental PSFs are masked to certain radii such that 99% of their flux is retained. Error bars are a linear combination of the dispersion in the measurement of the de-projected data and extraction error of 2.2% for measurements in epoch 1 and 1.3 % in epoch 2. The extraction error is found by injecting a fake disk at 90° relative to the real disk in the data cube. The fake disk was scaled to a contrast of 5×10^{-3}, processed with KLIP 3 along with its corresponding GRaTer model (scaled to the contrast of 5×10^{-3}) and extracted the uncertainty in the scaling factor (should be ∼1). Unlike the inclined disk HD 32297 (explained in Sect. 5.2 Method 2 of Bhowmik et al. (2019)), the error corresponding to the stellar+background (without the disk) is not straightforward because the fragments of this disk signal are present throughout the field of view of the image. Since, the noise is different at every separation, extracting a background noise corresponding to the same separation as the measured photometry is not performed in this case.

The surface brightness profiles are plotted for all the images corresponding to wavelength channels in IFS and IRDIS for both epochs. The profiles corresponding to the H2 (epoch 1), H3 (epoch 1), K1 (epoch 2) and K2 (epoch 2) are plotted in Fig. 4.8 where the peak at $0.42''$ is present at the position of the ringlet R3. The northern part of the ringlet has a surface brightness peak to $14.91^{+0.41}_{-0.20}$ mag/arcsec^2 and the southern part to $13.64^{+0.24}_{-0.20}$ magnitude/arcsec^2. Therefore, the asymmetry in the contrast is visible in the IRDIS observations. The plots corresponding to the H2, H3, and K1 band has a similar trend of slow rise till the peak of the ringlet R3 and then a negative descent thereafter.

The overall profile in the K2 band is much steeper which could be because of the strong effects of background noise in this observation induced by the instrumental transmission of the K2 filter.

The process to obtain the spectral reflectance in the units of (arcsec^{-2}) in various parts of the ringlet R3 involves the same steps as for the extraction of surface brightness profile. First, an average azimuthal flux is calculated for the respective masked and scaled best-fit model. Then this flux is normalized to the PSF and converted to units of arcsec^{-2} from pixel^{-2} using respective pixel scale (12.25 mas for IRDIS and 7.46 mas for IFS). The same measures are taken while calculating the associated error bars. According to the need for aperture photometry, the geometry and position of the mask are changed and the scaling factor corresponding to the targeted region is extracted.

The mask used to retrieve the spectral reflectance for the northern and the southern part of the ringlet R3 is the same half elliptical mask as explained in the χ^2 analysis de-projected to the inclination $i = 56°$ and $PA = 356.5°$. Figure 4.9 shows the spectral reflectance in the northern and the southern parts in both epochs. The overall spectrum looks flat in both epochs. The measured flat spectrum could also be because of the low S/N of the disk and limitation in the error measurement, apart from an outcome of grains properties itself. The asymmetry between the north and the south parts of the ringlet is more consistently visible throughout the YJH band in epoch 2 of Fig. 4.9. However, in epoch 1 in the YJ band, the error bars are quite large to see any asymmetry between the two sides. This could be because of the presence of strong stellar residual in the northern part of the ringlet as seen in Fig 4.4. This puts a bias in obtaining the scaling parameter to finally calculate the photometry. The relatively large error bars at 1.4±0.5 μm is because of the water absorption feature which makes the data noisy and less reliable.

In Fig. 4.10, I plot the spectral reflectance of the southern part of the disk masking the clump and of the clump alone encompassed within a circular mask of radius 0.05″, which is at a stellocentric distance of 0.42″. The distinction between the clump and the rest of the southern part of the ringlet R3 is not compelling in the epoch 1 due to the larger error bars. However, globally the clump still seems fainter than the rest of the southern part of the ringlet. Whereas in epoch 2, this distinction is more visible where the rest of the southern ringlet is almost twice as bright as the clump, ignoring the water band. This test concludes that the clump does not posses an increased flux intensity feature compared to the rest of the disk.

As explained in Sect. 4.1.3, the negative lobes on each side of the position of the clump could be the result of the ADI self-subtraction. Extracting the photometry at the negative lobes along with the clump with the three non-overlapping circular masks each with radius 0.05″ and stellocentric distance of 0.42″ is performed. This test is to learn whether the clump is an ADI artifact. The masks are at three different azimuthal separations. One mask is around the clump, and the other two on either side of the clump as seen in Fig. 4.11 (Top). Plotting the spectral reflectance at these three positions for all the wavelength filters and both epochs, it is evident that the variations of flux between each aperture are minor when the corresponding errors are taken into account as seen in Fig. 4.11 (Bottom). With this analysis it can be concluded that the clump is more likely an ADI artifact rather than a physical clump of gas and dust indicating a possible planet-forming region.

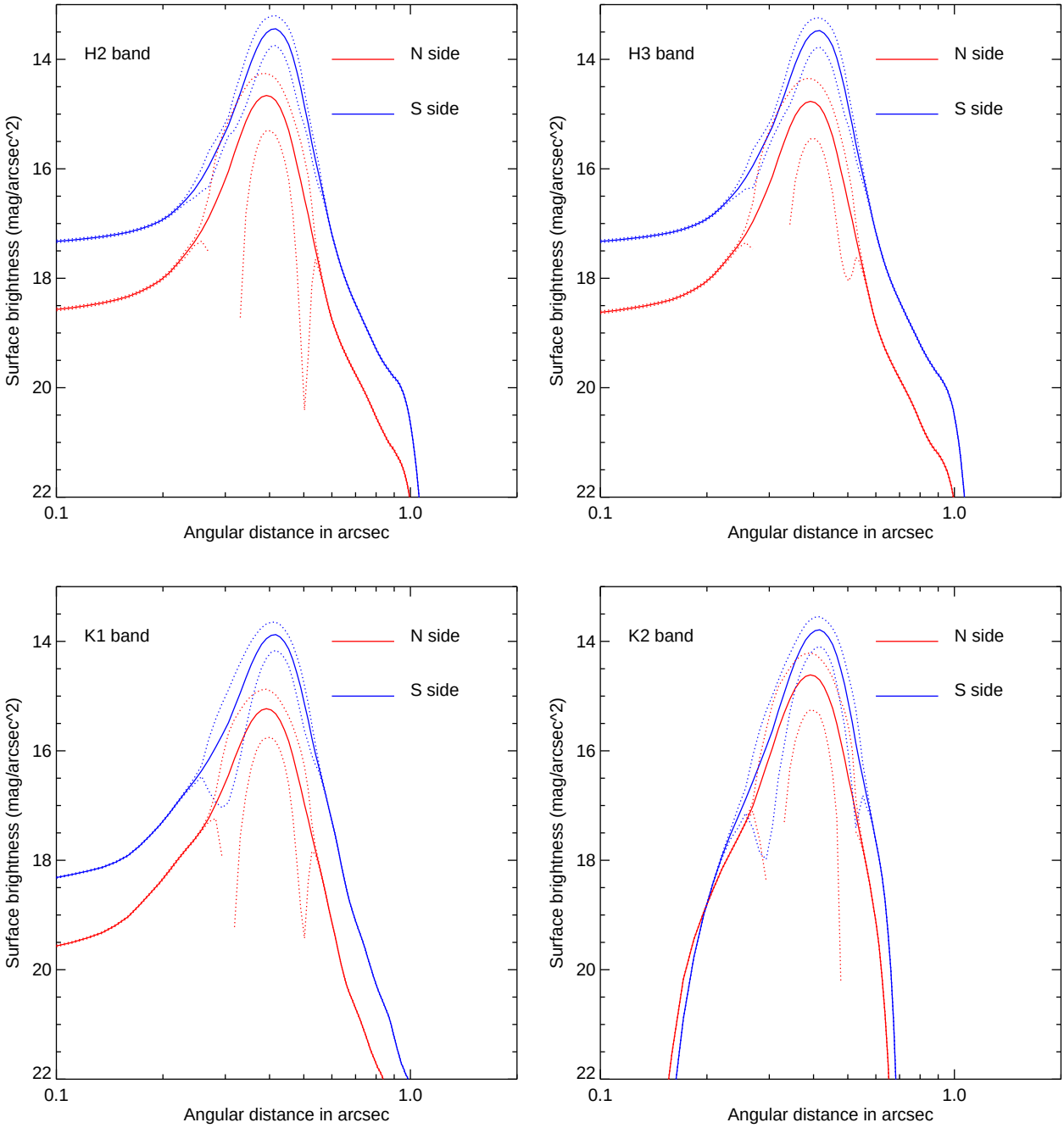

Figure 4.8 *– Surface brightness profiles corresponding to northern part (red) of the disk and southern part (blue) of the disk in H2,H3, K1 and K2 band of IRDIS.*

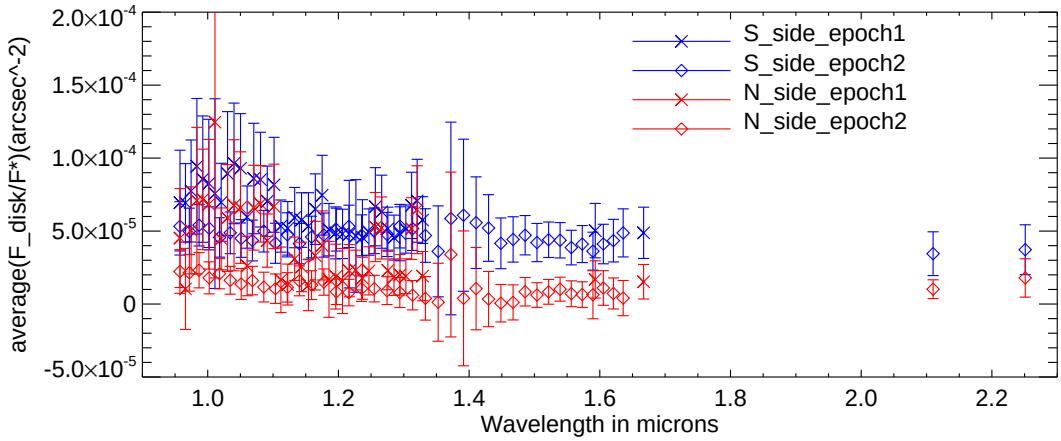

Figure 4.9 – *The figure represents spectral reflectance corresponding to the northern and southern part of the ringlet R3 in both epochs.*

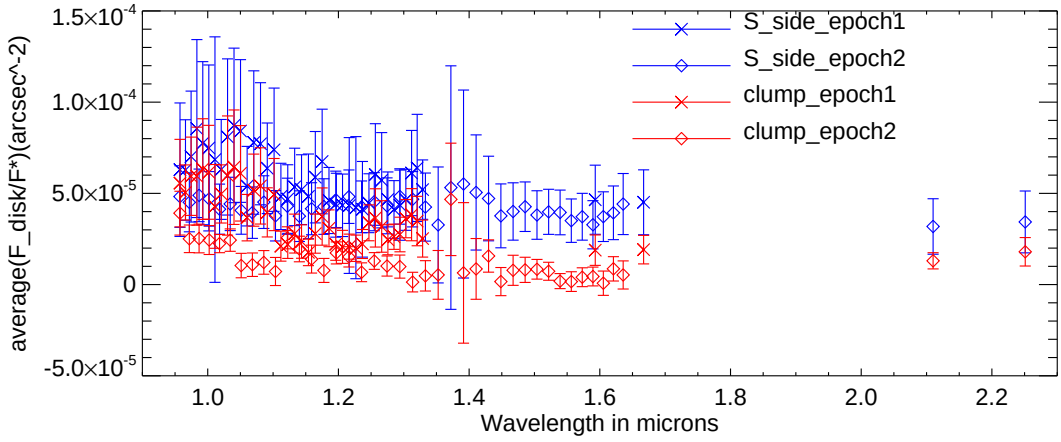

Figure 4.10 – *The figure represents spectral reflectance plot corresponding to the clump and the southern part of the ringlet R3 masking out the clump in both the epochs.*

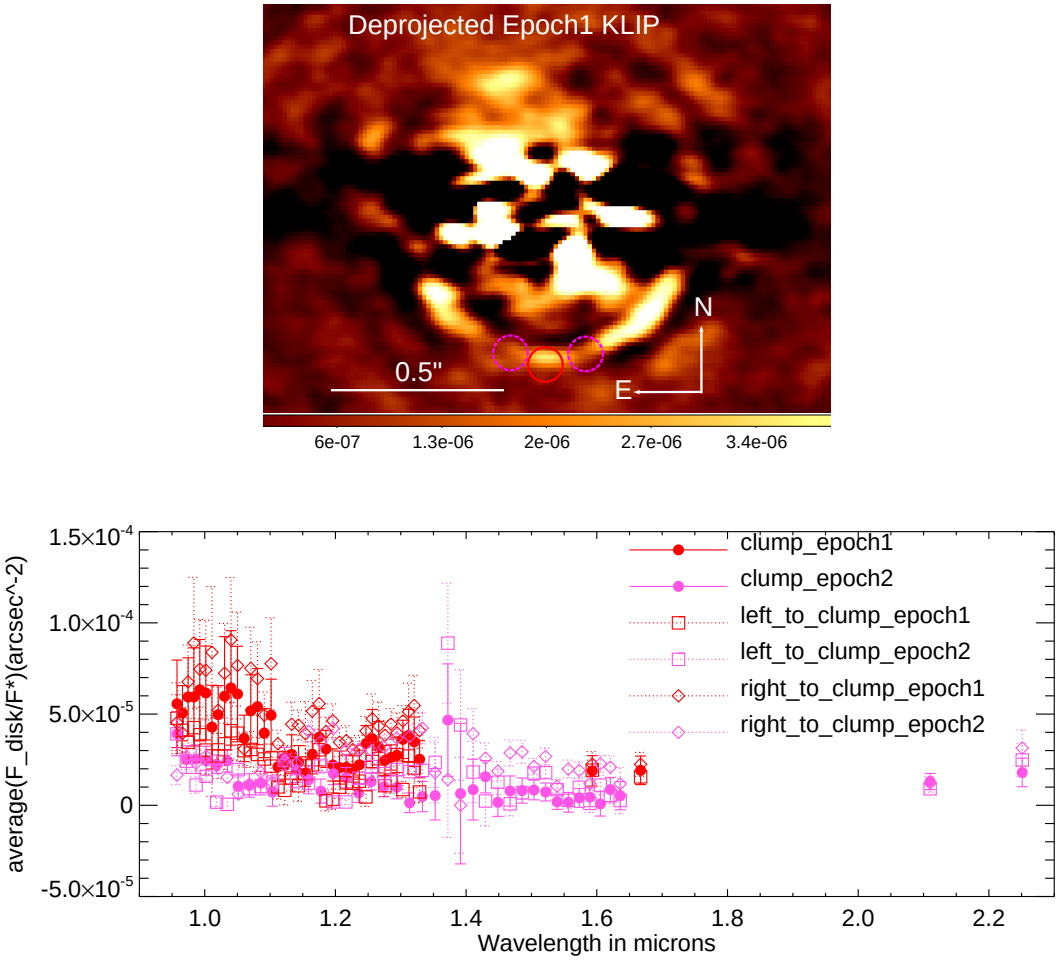

Figure 4.11 – *The figure (top) shows the three circular masks on the de-projected data where the red circular region is the clump and the pink dotted circular region encompasses the left and the right regions on each side of the clump.The figure (below) depicts the spectral reflectance at the clump and at circular masks adjacent to the clump (on each side) in both epochs. The dotted lines are the error-bars corresponding to the two other apertures other than that of the clump.*

4.1.5 Modeling the particle size distribution in the ringlet R3

To study the grain size distribution for ringlet R3 of HD 141569 similar to HD 32297 is performed. This study would help in constraining the minimum grain size within the ringlet. Using GRaTer, a geometry of $R_0 \pm dr$ is taken and the PSD assumes a distribution $dn(s) \propto s^{\kappa} ds$ where κ is the power-law index. The minimum grain size s_{min} and κ are taken as free parameters and $R_0 \pm dr$ is restricted to the value obtained for the best-fit model. For the preliminary test, only astro-silicate type grains are considered. The range of parameters explored for s_{min} are between 0.1 μm and 10.0 μm with an increment of 0.1 μm. Similarly, the parameter space explored for κ is between -5.0 and -3.0 with an increment of 0.1.

Each synthetic spectra is then interpolated on the 41 wavelength channels between 0.95 μm and 2.3 μm and scaled to the reflectance spectrum of epoch 2 using similar χ^2 minimization as detailed in Sect. 2.3. The analysis is done only for the second epoch spectrum because there are observations for a larger spectral range (Y,J H, and K), which provides a stronger constraint on the slope of the reflectance spectrum.

In order to calculate the blowout size of the astro-silicate grains for this stellar type, Eq. 8 of the Sect. 3.2 is used. The stellar luminosity and mass are taken to be $L_* = 24.2\, L_\odot$ (White & Boley, 2018) and $M_* = 3.1\, M_\odot$. Therefore, the s_{min} is 6.25μm. The best-fit values of κ and s_{min} are provided in Table 4.3. Traditionally, the distribution index κ is equal to -3.5 (Dohnanyi, 1969). Both the power-law index and minimum grain size are not well constrained. Several synthetic spectra fall within the $\sqrt{2\nu}$ χ^2 threshold possibly because the reflectance spectrum is flat and has significantly high error bars. Nevertheless, the best-fit spectra with least χ^2 value ($\chi^2 = 0.082$) has $s_{min} = 0.30$ μm and κ = -3.00. The fiducial spectra with κ = -3.5 and $s_{min} = s_{blow} = 6.25$ μm has a $\chi^2 = 0.14$. Both the fitted spectra are shown in Fig. 4.12. The value of χ^2 in this analysis is $\ll 1$ which is again because of the large error bars considered in the denominator of the calculation (refer Eq. 2.6). Therefore, I am interested in obtaining a best-fit specrum to the reflectance plot rather than the physical value of the least χ^2.

Fitting a straight line between 1 and 2.2 µm, the slope measured is however has a positive value of 1.95×10^{-5} µm. This measurement of the slope is also done by considering the high error bars. Therefore, the limitation of such analysis are both the low S/N data and the geometry of the system harbouring fragments of broken disk everywhere restricting in the error bar measurements as explained in Sect. 4.1.4.

Table 4.3 *– Parameters of the grains and their size distribution for astro-silicate, that generate the best-fit of the spectrum of HD 141569.*

κ	s_{min}	s_{blow}	s_{min}/s_{blow}	χ^2
-3.00 ($-5.05 \pm$ 4.95)	0.30 (4.00 ± 1.00)	6.25	0.048 ($0.64 \pm$ 0.16)	0.082 ($0.19 \pm$ 0.11)

The parameters of the spectrum falling within the χ^2 threshold is provided in brackets.

Considering the best-fit spectra, s_{min} is much less than s_{blow} which might have resulted from the massive concentration of gas found within the disk (Miley et al., 2019; Péricaud

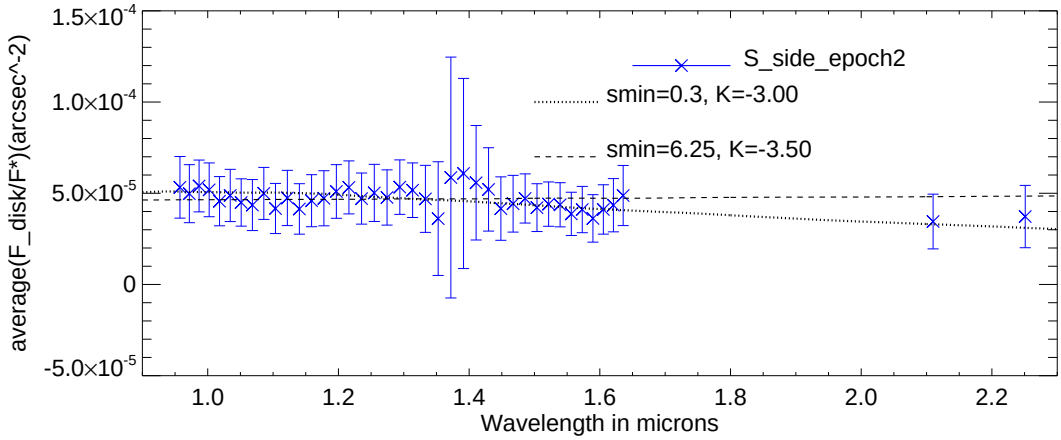

Figure 4.12 *– Fitted synthetic spectra to the reflectance spectrum of epoch2. The dotted line represents the best-fit spectra with s_{min} = 0.30 μm and κ = -3.00 and the dashed line represent the spectra for fiducial case where $s_{min} = s_{blow}$ and κ = -3.5.*

et al., 2017). The presence of gas can retain smaller grains for a longer time within the disk. However, this argument is valid only when there is concrete proof of grains following the condition where s_{min} is much less than s_{blow}. As seen from the spectrum Fig. 4.12 the ideal spectra with κ = -3.5 and $s_{min} = s_{blow}$ = 6.25 μm as well fits the reflectance spectrum within the error limits. Therefore at this stage, due to the limited accuracy of the s_{min} parameter the argument of very small grains' abundance within this ringlet can be questionable.

4.1.6 Discussion and Conclusion

The best-fit model to the ringlet R3 found has very steep power-law values (α_{in} and α_{out}) portraying an extremely thin ring. The steep edges are attributed to the thinness of the ring R3. In shaping such a ring, Lyra & Kuchner (2013) presented a possibility of dust-gas interactions. The presence of a significant amount of gas can encourage the formation of dust traps where small bound grains (grains bound to the host star) closer to the blowout limit can be present for a longer than usual period of time (e.g. Bhowmik et al., 2019; Kral et al., 2013).

The reflectance spectrum in Fig.4.9 has a characteristic trend of being flat, making the ringlet R3 "gray" in color in the YJH spectral channel. The ringlet looks brighter in the YJ band of epoch 1, however, the error bars suggest that these images are noisier than their epoch 2 counterpart. A limitation of the photometric analysis for this disk is its error estimation because the dominant error term is the dispersion (standard deviation) in the measurement of data itself. The stronger the variation between the true signal and the residuals around it, the larger is the error bar. Moreover, because the data is reduced with KLIP algorithm which naturally generates stronger positive to negative fluctuations

as also seen in the case of HD 32297 in Sect. 3.2, this kind of error estimation can be unreliable. Having said that, I am restricted by the morphology of this disk (non-edge-on inclination and fragmented throughout the FOV) as explained in Sect. 4.1.4 to extract an error bar which is completely independent of the true signal of the disk as done for HD 32297 (see Sect. 5.1 of Bhowmik et al. (2019)).

One of the incentives of this study was to identify the nature of the clump. From the aperture photometry performed I am still uncertain whether the clump is a physical component of the disk featuring a dust trap or an artifact. However, Fig. 4.11 shows that the azimuthal variations in the spectral reflectance are minor, therefore, hinting towards the "clump" to be an ADI artifact. The KLIP processing induces strong ADI artifacts, a modest amount of an azimuthal variation at the ansae of the KLIP reduced model is also seen in Fig. 4.6 making it a higher possibility of an ADI artifact.

With future observations of JWST and ELT, the slope of the reflectance spectrum can also be constrained giving better accuracy on the distribution of particle sizes.

4.1.7 Perspective and Outlook

In this work I have modeled only the disk with a uniform azimuthal and variable radial distribution. However, the intensity images as seen in Fig. 4.4 shows that the disk might have an azimuthally varying intensity. Apart from a north-south asymmetry in the luminosity, there are local density peaks seen in the images in the southern part of the ring R3. Since the photometric calculation performed here takes an azimuthal average of the ring, the information on the azimuthal variation within the ring is not studied. By modeling the ringlet R3 with an adequate azimuthally varying density function and then pursuing the photometric extraction based on the best-model can provide a global perspective.

A similar study of the azimuthally varying intensity in the ringlet R3 was pursued as an internship study by Ryan Boukrouche primarily using a Lorentzian density distribution to model the disk in DPI and DBI observations. The details of this study will be published in Singh et al. (in prep) which support a strong azimuthal density variation which is possibly related to a massive collision. The spectroscopy of the ringlet R3 of the disk HD 141569 presented in this thesis will also be a part of the article Singh et al. (in prep).

Another perspective would be to study the phase function of both the total intensity and the polarimetric observation and obtain an independent estimation on the grain size. This type of study has already been performed for disks such as HR 4796 (Milli et al., 2019, 2017; Olofsson et al., 2019).

4.2 Preliminary study of HD 106906

HD 106906AB is a binary system 15 Myr (Pecaut & Mamajek, 2016) old with both stars of stellar type F5V (Houk & Cowley, 1975) lying at a distance of 103 pc (Gaia Collaboration, 2018). This system is very interesting because it harbors an almost edge-on debris disk and a planet at 7″, orbiting the central star as seen in Fig 4.13 (Right). The planet was first imaged with Magellan Adaptive Optics (MagAO) system as presented in Bailey et al. (2014). While a debris disk was proposed by Chen et al. (2005) by studying the IR excess from the SED, it was first imaged with SPHERE and GPI as seen in Fig 4.13 (Kalas et al., 2015; Lagrange et al., 2016). Circumbinary planets at such high angular separation are rare (Lagrange et al., 2016) and such systems often bring us closer in constraining planet formation theory (Thalmann et al., 2014).

According to Kalas et al. (2015) the east side of the disk had larger radial extension and also was 20% brighter in H band. Kalas et al. (2015) also saw the backside of the disk and a warp feature on the western side of the disk as denoted in Fig. 4.13 (Left). The brightness asymmetry was also recognized by Lagrange et al. (2016) although a possibility of radial asymmetry was not explored. The origin of the confirmed brightness asymmetry was debated to be either dynamical interaction with the planet (Kalas et al., 2015; Nesvold et al., 2017) or a possibility of co-planer flybys perturbing the disk (De Rosa & Kalas, 2019). Therefore, a motivation to quantify the flux asymmetry was derived.

Performing spectral analysis similar to Sect 3.2 I investigated the minimum grain size present within the debris disk.

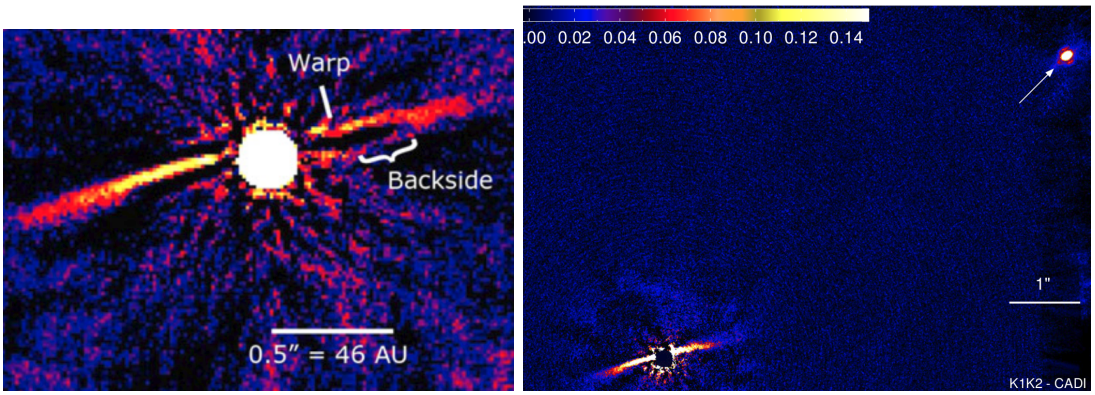

Figure 4.13 *– Debris disk around HD 106906 AB from Kalas et al. (2015) (Left) and an arrow pointing to the planet HD 106906 AB b at 7″ as seen in Lagrange et al. (2016) (Right). In both the images, north is up and east is left.*

4.2.1 Observation and Data Reduction

The total intensity observation of HD 106906 was done as a part of SPHERE open time observation on Feb. 6^{th}, 2017. In IRDIS, the broadband H (BB_H, $\lambda = 1.625\mu$m) filter was used. The target was simultaneously observed in IFS with YJ (λ = 0.95-1.35 μm)

narrow band filter. The conventional observation sequence as provided in Sect. 2.1.3 was followed. Observational details are provided in Table 4.4.

The sequence of data reduction for the intensity measurement in IRDIFS mode is done using the DRH pipeline (Pavlov et al., 2008) which includes flat field corrections, sky and dark subtractions, star-centering using waffle pattern, bad-pixel removal, anamorphism correction (Maire et al., 2016) and wavelength calibration. This data cube produced by the DRH pipeline is processed with SpeCal pipeline.

The data cube was also processed with the pipeline developed by Boccaletti et al. (2015) based on the algorithm KLIP truncated at 5 modes (Soummer et al., 2012). For this disk, I focus on KLIP reduced ADI images truncated at 5 modes even though the data set is tested with TLOCI providing relatively similar results.

HD 106906 was also observed with IRDIS-DPI mode in BB_J (λ=1.245 μm) filter in field-stabilized mode on Feb. 16^{th}, 2017 as a part of the open time program. The details of the observation sequence are given in Sect. 2.1.3. Q_ϕ and U_ϕ images are obtained as detailed in Sect. 2.2.2.

***Table 4.4** – SPHERE observation log of HD 106906.*

Data UT	prog. ID	Filter	PC	Field rotation	DIT	N_{exp}	T_{exp}	Seeing	τ_0	TN
2017-02-06	098.C-0686(C)	IRDIS-BB_H		25.68	64	18	8064	0.58	6.2	-1.75
2017-02-06	098.C-0686(A)	IFS-Y.J		25.87	64	18	8064	0.58	6.2	-1.71
2017-02-16	098.C-0686(D)	IRDIS-DPI-BB_J	11	stabilised	64		5632	0.74	9.0	-1.7

The following information is provided from left to right: The observation date, program ID, filter combination, the number of polarimetric cycles (PC), the total field rotation in degrees, the individual integration time of each frame (DIT) in second, the total number of exposure (N_{exp}), the total time in seconds (T_{exp}), the DIMM seeing in arcseconds, τ_0 the correlation time in ms, and the true north offset in degree (TN).

4.2.2 Morphology of the debris disk and photometry of the planet

The debris disk when observed in total intensity as presented in Fig 4.14 (Top and Middle) shows a smooth feature without any warp or clump. The brightness asymmetry is visible between the east and west side of the disk with the east side being brighter. A minute radial asymmetry of $\sim 0.1''$ between the two sides is observed. The front side being brighter than the backside can be attributed to forward scattering.

The disk in the Q_{phi} image as seen in Fig. 4.14 (Bottom) is much fainter and the signal is visible mostly closer to the star. This signal can either be stellar residual or a signature of a warm inner disk. However, with current resolving power, the confirmation on an inner warm component is not feasible and requires instruments and/or techniques that can achieve much deeper contrast presently achievable.

A total of thirteen point sources were identified in the IRDIS field of view however none of them were detected in IFS FOV. The associated planet is marked with an arrow in Fig 4.15 (Top). Using SpeCal, planet contrast is extracted by injecting a fake planet in the science cube at a roughly estimated position ($\sim 7''$) and by comparing the flux of the real planet to the fake planet. The contrast of the planet is $(8.564 \pm 0.687) \times 10^{-6}$ at the wavelength of 1.625±0.145 microns. The magnitude, separation, and PA of the planet is provided in Table 4.5. The values of angular separation and PA are 7114.0±8.0 mas and 307.15±0.06° respectively, which is similar to the values obtained in Lagrange et al. (2016). However, the planet contrast obtained in this study is 10.186±0.223 mag at BB_H filter. While in K1 and K2, Lagrange et al. (2016) obtained the contrast to be $9.4 \pm 0.1, 9.1 \pm 0.1$ mag respectively. Therefore, no significant angular variation is seen between the two epochs however according to the contrast variation the planet is red. This result is also consistent with Kalas et al. (2015).

Table 4.5 *– Planet around HD 106906AB*

	Δ Magnitude	Separation (mas)	PA (°)
Planet	10.186±0.223	7114.0±8.0	307.15±0.06

To constrain the geometry of the disk I next model the disk using GRaTer and then extract the surface brightness of the two sides of the disk to identify the asymmetry between them.

4.2.3 Modeling the debris disk

To account for the self-subtraction and constrain the geometry of the disk I model the disk with GRaTer and follow the forward modeling technique (Sect 2.3) for the total intensity images. Fitting an ellipse on the image in Fig. 4.14 (Top), the PA of the disk is measured to be 104.5 °. This value is kept constant throughout the modeling. A total of 5,120 total intensity models were created with the free parameters given below:

- ansae of the disk r_0 (au): 70, 75, 80, 85, 90

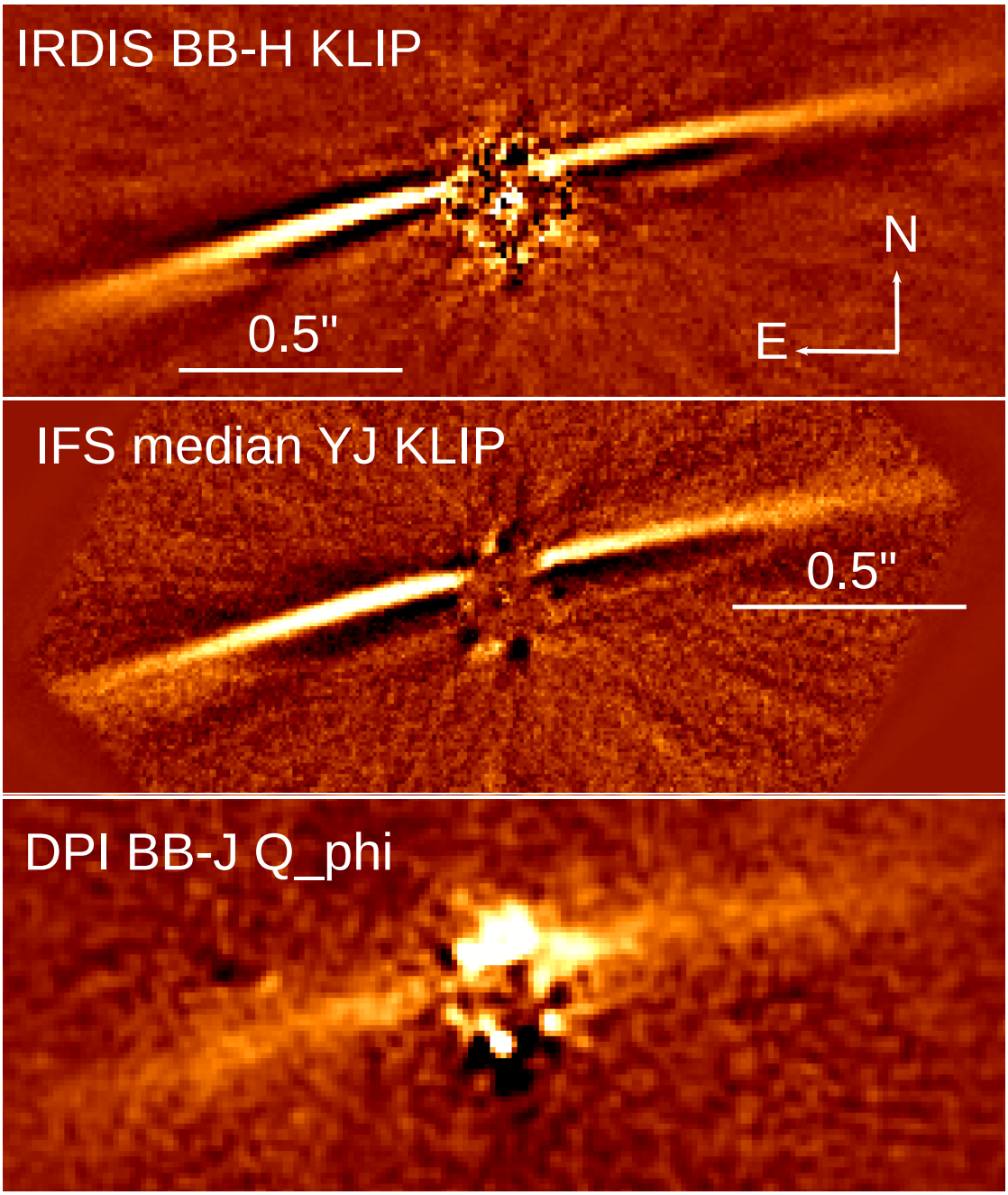

Figure 4.14 *– The topmost image is the KLIP-5 science image of HD 106906 as observed by IRDIS BB_H. The image in the middle row is the IFS median image of the debris disk and the polarimetric Q_ϕ image of the disk smoothed to a Gaussian kernel of radius of 2 pixel is in the third row.*

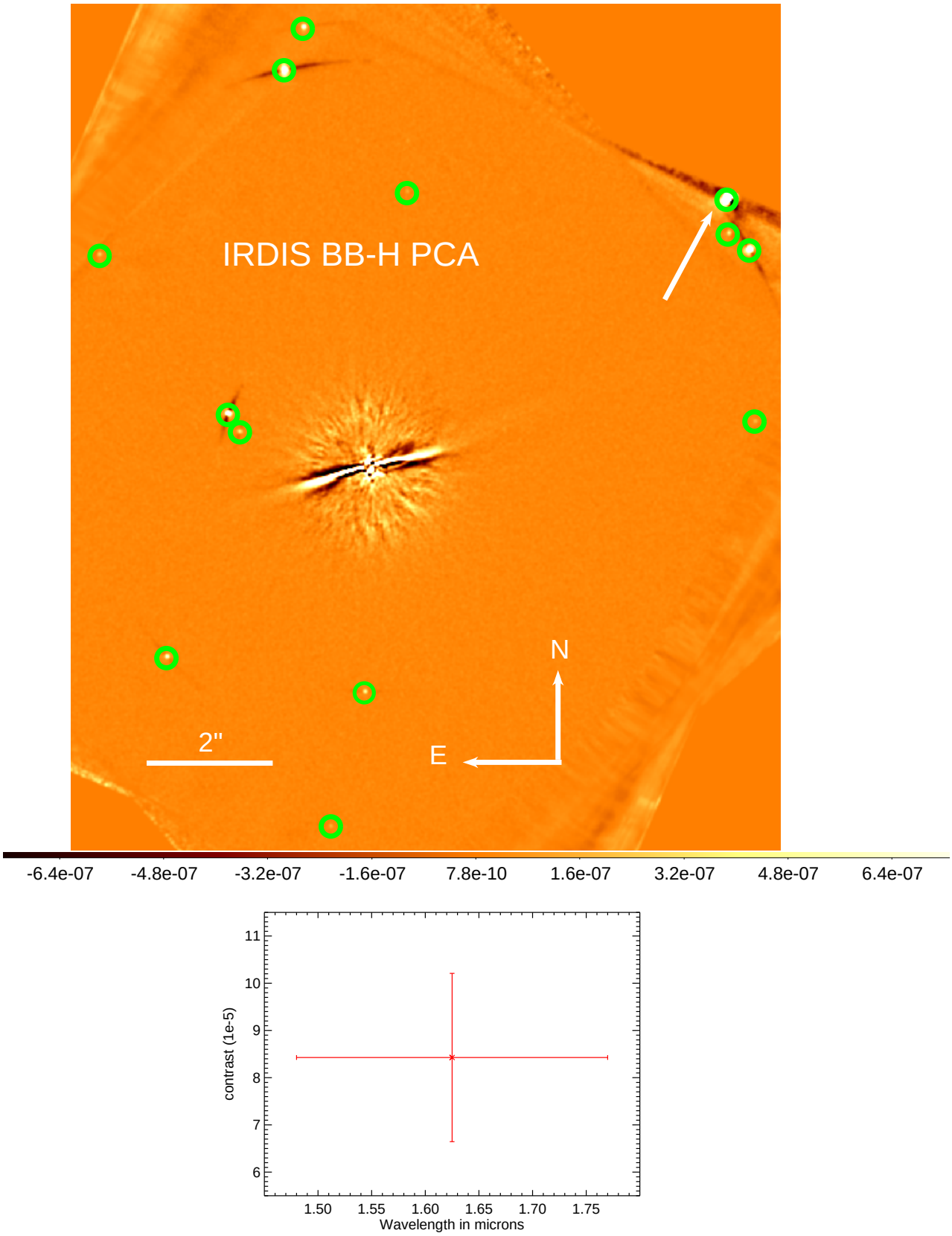

Figure 4.15 – *The disk and the thirteen point-sources encircled in green within the IRDIS FOV is presented in the top row. The white arrow indicates the already known planet. In the bottom row a plot of the contrast of the planet in IRDIS BB_H filter is presented.*

- α_{in}: 2, 5, 8, 10
- α_{out}: 4, 5, 6, 7
- scale height h: 0.01, 0.02, 0.03, 0.04
- inclination i (°): 85.0, 85.5, 86.0, 86.5
- HG parameter g: 0.4, 0.5, 0.6, 0.7

Each total intensity model is processed with the KLIP algorithm truncated at 5 modes (detailed in Sect 2.2.1.3) with the same eigenvalues which were calculated while processing the science images.

On the other hand, the grid of polarimetric models with 6,400 models had free parameters as:

- ansae of the disk r_0 (au): 70, 75, 80, 85, 90
- α_{in}: 2, 5, 8, 10
- α_{out}: 2, 3, 4, 5
- scale height h: 0.01, 0.02, 0.03, 0.04
- inclination i (°):85.0, 85.5, 86.0, 86.5
- HG parameter g: 0.6, 0.7, 0.8, 0.9

The parameter space of α_{out} and HG parameter in the grid of polarimetric models is different than its total intensity counterpart. This choice was made because the best models in polarimetry favoured a smaller α_{out} value and larger g value than that obtained for total intensity (also seen in the case of HD 32297 Bhowmik et al. (2019) detailed in Chapter 3).

Each reduced model $M_{i,j}$ and the science image $S_{i,j}$ are masked. The mask is an elliptical ring encompassing only the disk. The semi-major and semi-minor axis of the inner edge of the elliptical ring are 1.225″ and 0.098″. The width of this ring ,ΔR, is 0.527″. In the next step the χ^2 is obtained using equation Eq. 2.6. For polarimetric analysis alone, the science image is binned to 4 pixels and in the χ^2 calculation (Eq. 2.6) the degree of freedom ν is divided by 4. 1% of the models with lowest χ^2 values are plotted in the histogram as seen in Fig. 4.16 against each free parameter. Constrained values for each parameter is obtained from the histograms as detailed in Sect. 2.3. These constrained parametric values for total intensity and polarimetric best models are listed in Table. 4.6.

The inclination value is found to be $85.7 \pm 0.5°$ and $85.8 \pm 0.9°$ in total intensity and in polarimetry respectively. These inclination values are well constrained within the error limit of the value found in Lagrange et al. (2016). The ansae of the disk are 78.5 ± 7.7 au in total intensity and 80.0 ± 20.0 au in polarimetry. The R_0 value is better constrained

in total intensity than in polarimetric modeling as inferred from the errors. From the histogram, it is seen that the α_{in} values are extracted to better accuracy (more peaked distribution) than seen for the inclined disk HD 32297 in Fig. 3.5. The values of the inner slope are found to be 5.4 ± 2.3 and 3.5 ± 1.5 for total intensity and polarimetry respectively. The small deviation between the two values arises most possibly to replicate the strong signal observed at an angular separation closer to the star (Fig. 4.14 (Bottom)). The outer slope is found to be -5.7±1.5 and -3.4±0.8 for total intensity and polarimetry respectively. These values are within the error limit of the values found in Lagrange et al. (2016). The HG parameter converges to values of 0.55±0.08 and 0.94±0.05 in total intensity and polarimetry respectively. In polarimetry, the scattering angles probed are smaller than in total intensity giving rise to a higher g value. Additionally, the best model in polarimetry tries to mimic the strong signal seen at 0.1-0.15 $''$ attributing it to a forward scattering peak giving rise to higher g value than its total intensity counterpart. The constrained values of scale height show a discrepancy between the total intensity model and the polarimetric model since the values obtained are 0.015±0.0005 and 0.04 respectively. These discrepancies in the values of the best model of total intensity and polarimetric data can be a result of inherent grain properties: for example different grains being responsible for polarimetric and total intensity. However, because of low S/N of polarimetric data to quantitatively analyse the origin of these discrepancies is not done in this thesis.

For further analysis, the best-fit model is the reduced model corresponding to the least χ^2 value (for total intensity $\chi^2 = 6.18$ and for polarimetry $\chi^2 = 6.74$). Some disk signal is still visible in the total intensity residual image in Fig. 4.17 $Left$.This can be attributed to the limitation of our models which represents simple geometry. However examining the residual image Fig. 4.17 $Right$, the best-fit model seems to match the polarimetric data very well, irrespective of the high χ^2 value of 6.74.

Table 4.6 *– Parameters that provide the best GRaTer models fitting the IRDIS BB_H and DPI BB_J science image*

	Total Intensity			Polarimetry		
	E side	W side	Full disk	E side	W side	Full disk
i (°)	85.8±0.6	85.8±0.5	85.7±0.5 (85.5)	86.5±0.9	85.3±0.4	85.8±0.9 (85.5)
R_0 (au)	80.9±5.4	84.8±7.0	78.5±7.7 (75.0)	82.5±10.3	80.0±20.0	80.0±20.0 (90.0)
α_{in}	4.6±2.8	4.5±2.8	5.4±2.3 (5)	3.5±1.5	3.5±1.5	3.5±1.5 (2)
α_{out}	-6.0±0.1	-5.0±0.1	-5.7±1.5 (-5)	-4.2±1.1	-3.5±1.5	-3.4±0.8 (-4)
g	0.58±0.08	0.56±0.07	0.55±0.08 (0.5)	0.83±0.07	0.99	0.94±0.05 (0.90)
h	0.015±0.005	0.019±0.011	0.015±0.005 (0.010)	0.040	0.025±0.025	0.040 (0.040)

The model parameters corresponding to least χ^2 are provided in bracket in the fourth and seventh column

4.2.4 Photometry of the debris disk

To extract photometry, the best-fit model is first convolved and normalized to the instrumental PSF. Then, a flux is obtained by minimizing the science image and the reduced best-fit model as done in χ^2 analysis. This flux is then used to scale the PSF convolved best-fit model. This scaling is done for the east and west side separately to account for the brightness asymmetry.

Surface brightness profiles are obtained by calculating the contrast in the scaled best-fit model which is masked. The same mask as used for χ^2 analysis is used. This calculation is done by taking an azimuthal average of the contrast in concentric non-overlapping circles of 4 pixels. This contrast is then converted to magnitude/arcsec^2 by normalizing the contrast to the 99.99% of the instrumental PSF encircling a radial distance of 0.4″ for IRDIS and 0.3″ for IFS. In the polarimetric image, the surface brightness is calculated directly on the science image instead of the best-fit model because there is no self-subtraction.

The errors are a linear combination of the dispersion within the mask which is rotated 90 ° to the PA such that there is no disk signal. The extraction error is 1.3%. The extraction error follows the same process as detailed in Sect. 3.3.2 where the injected fake disk is scaled to a contrast of 5.6×10^{-5}.

The surface brightness profiles as observed in total intensity and polarimetry are shown in Fig 4.18. The profiles in Fig 4.18 (Left) indicate that the east side of the disk is 0.5 magnitude/arcsec^2 brighter than the west side in total intensity observation. As referred in the Sect. **??** a brightness asymmetry was also indicated by Kalas et al. (2015) of east side to be 1.8 times brighter than the west side by measuring the median value of the peak flux in the radial range of 0.2-0.4″. However, in the SPHERE's polarimetric observation, the west side is brighter than the east between 0.1-0.3″ which can be due to stellar residua or a warm component as explained in Sect. 4.2.2. Beyond 0.3″, there is no brightness asymmetry observed in the polarimetric observation as seen in Fig. 4.18 (Right).

To explain the reflectance plot in Fig. 4.19, the contrast as calculated during surface brightness calculation is averaged between 0.2-0.7″ in all the spectral channels. The east-west brightness asymmetry is seen throughout the spectrum in total intensity and is absent in polarimetry. The spectrum shows a positive slope of 1.2×10^{-3} from J to H band. Therefore, the disk appears to be red similar to HR 4796 (Milli et al., 2017). A rough estimate of polarisation fraction of 3-6% is made by taking the ratio of mean reflectances in J band of total intensity to that of the reflectance in BB_J band of polarimetry.

4.2.5 Modeling the particle size distribution in the debris disk

After analyzing the morphology and the photometry of the disk, I aim to constrain the PSD of the astro-silicate type grains. Similar approach is taken to constrain the grain distribution as presented in Sect. 3.2. The parameter space for $s_{\rm min}$ and κ is in between 0.1 to 10 μm and -5 to -1 respectively with increment of 0.1. Considering the measurement of blowout limit of grains in Wyatt (2008) $s_{\rm blow}$ is found to be 1.44μm for $L_* = 5.6\,L_\odot$ (Kalas, 2005) and $M_* = 1.5\,M_\odot$ (Bailey et al., 2014; Kalas, 2005).

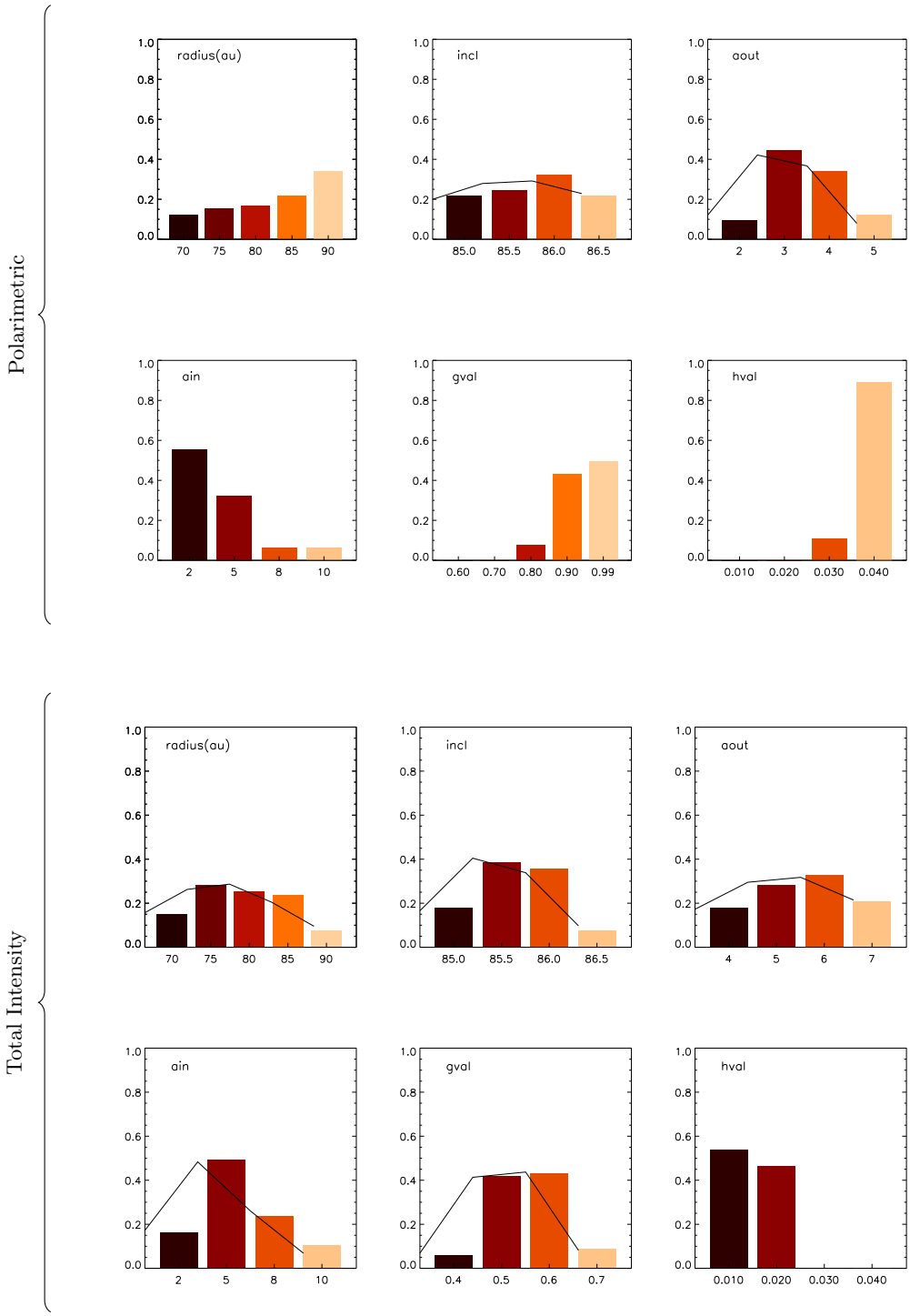

Figure 4.16 *– The histograms of total intensity models and polarimetric models are presented in the bottom two and top two rows respectively. Histograms are overlapped with Gaussian functions unless the distribution is continuously increasing or decreasing.*

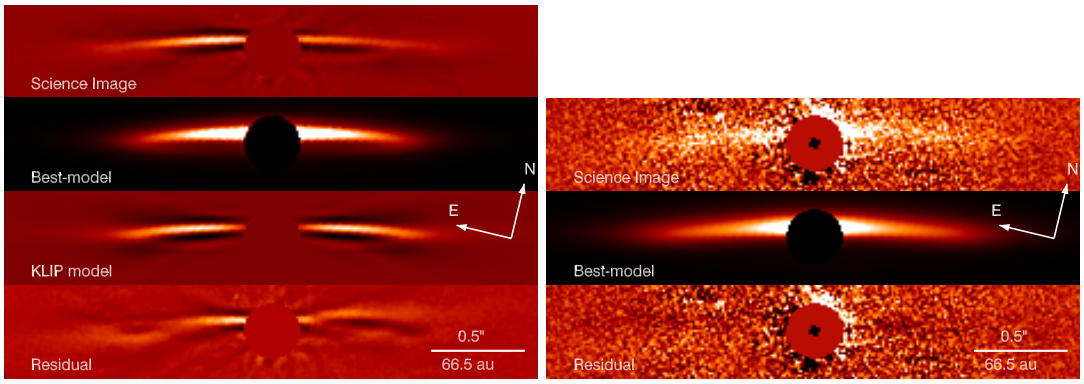

Figure 4.17 *– Left image from top to bottom presents the KLIP 5 IRDIS BB_H image, the total intensity best-fit model convolved with the instrumental PSF, the corresponding reduced best-fit model and the residual. The science image, reduced best-fit model and the residual image are scaled linearly between* $[-1\times10^{-5},1\times10^{-5}]$ *and the best-fit model convolved with the instrumental PSF is scaled linearly between [0.0,0.5].image from top to bottom presents the* Q_{phi} *image, the polarimetric best-fit model convolved with the instrumental PSF and the residual. All the three images are scaled linearly between* $[-4\times10^{-7},4\times10^{-7}]$ *. All the images are rotated to 90°-PA and cropped to* $2.85'' \times 0.5''$*.*

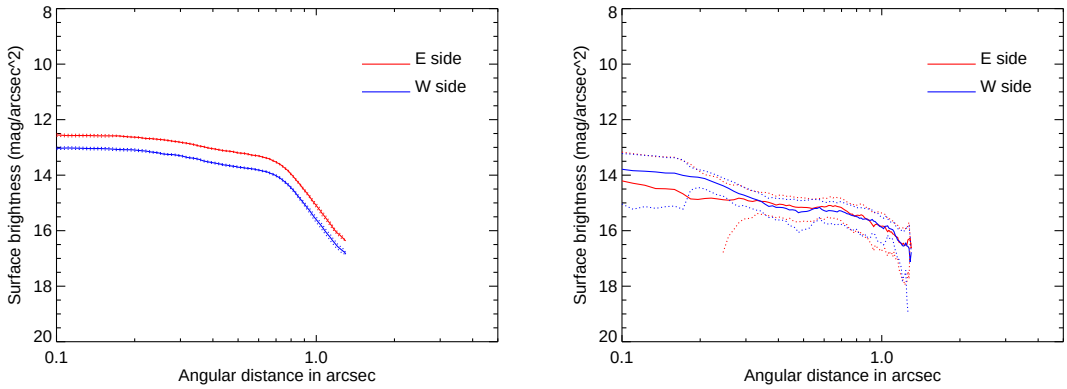

Figure 4.18 *– The surface brightness profile in total intensity (Left) in BB_H filter and polarimetry (Right) in BB_J filter.*

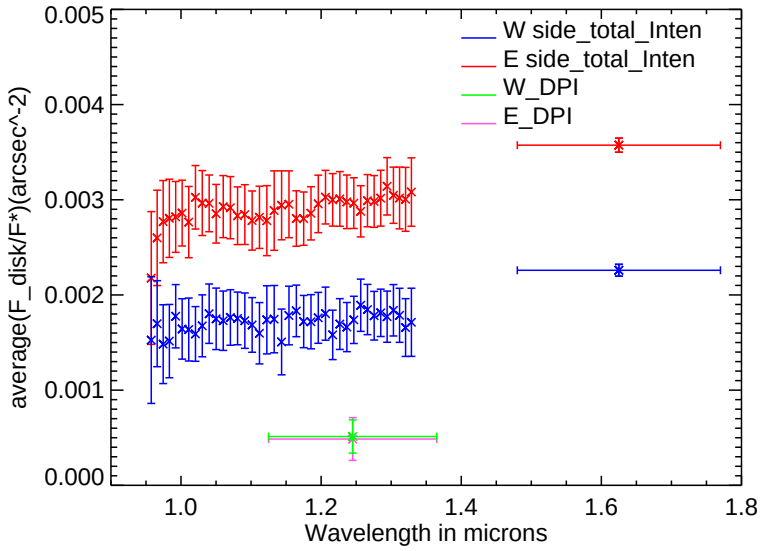

Figure 4.19 *– The spectral reflectance plot with a positive slope of 0.0012 contrast/arcsec^2 in NIR YJH bands*

I first fit the spectral reflectance with the synthetic spectra where I force $s_{min} = s_{blow}$ and κ = -3.5 (Dohnanyi, 1969). The spectra for these fiducial parameters do not match well the spectral reflectance as seen in Fig. 4.20 (Left). To find the best-fit spectra, I performed χ^2 analysis using Eq. 7 of Sect. 3.2. This analysis is done separately for the east side and the west side of the disk. The best fit found for κ is marginally different for the two sides of the disk however is close to the ideal value of -3.5 when the errors are considered. The best-fit spectra corresponds to $s_{min} = 0.70 \pm 0.20 \mu$m giving $s_{min}/s_{blow} = 0.50 \pm 0.13$. Even-though this ratio is not as small as found for HD 32297 it still tells us that there are smaller grains present in this disk. A redder spectrum is also measured for HR 4796 (Milli et al., 2017). However, studying the phase function Milli et al. (2017) does not suggest any presence of smaller grains than blowout size instead indicate presence of larger grains compared to observed wavelength within HR 4796. Further investigation based on phase function in the case of HD 106906 would be required for an independent assessment of grain size.

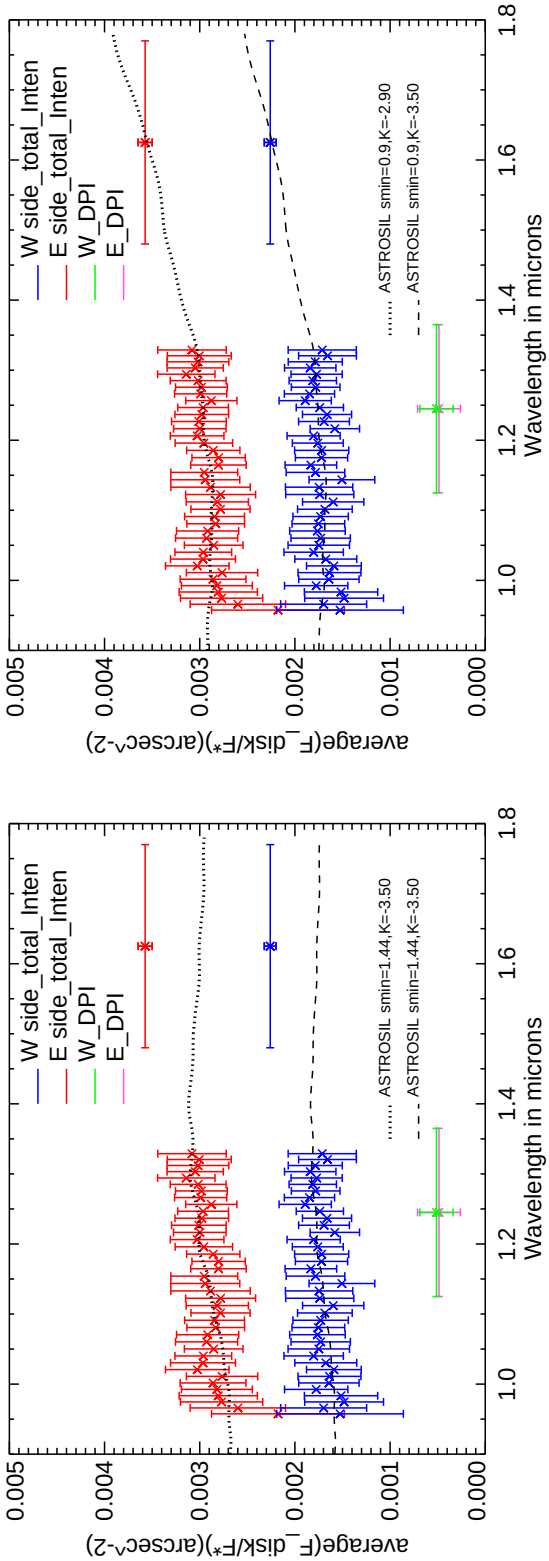

Figure 4.20 *– Best fits of the reflectance spectrum obtained for a fiducial case with* $s_{min} = s_{blow}$ *and* $\kappa = -3.5$ *(left), and for best-fit when* s_{min} *and* κ *are free parameters (right).*

Table 4.7 – *Parameters of the grains and their size distribution for astro-silicate, that generate the best-fit of the spectrum of HD 106906*

Side	κ	s_{min}	s_{blow}	s_{min}/s_{blow}	χ^2
East	-3.10 ± 0.90 (-2.90)	0.72 ± 0.15 (0.90)	1.44	0.50 ± 0.13 (0.63)	0.19 ± 0.11
West	-3.75 ± 1.25 (3.50)	0.71 ± 0.16 (0.90)	1.44	0.49 ± 0.13 (0.63)	0.20 ± 0.11

The parameters of the spectrum corresponding to least χ^2 value is provided in brackets.

4.2.6 Conclusion and Prospective

The binary stellar system HD 106906AB harbors a planet of 10 magnitude contrast at a very large separation 7114 mas being barely visible in the IRDIS FOV. Comparing to the earlier observation done by Lagrange et al. (2016) I conclude that the planet has red color but other photometric data points would be required for atmospheric modeling.

From the best-fit model, no significant radial asymmetry is seen between the two sides of the disk. The morphological parameters found in the total intensity best-fit model do concur with previous studies of Lagrange et al. (2016). Additionally, the value of anisotropic scattering factor $g = 0.99$ is found through modeling the polarimetric science data. As a result, this parameter's value found for the polarimetric model is much higher than its total intensity counterpart $g_{pol} >> g_{intn}$. This is a classic example of the presence of grains contributing to higher forward scattering in polarimetric observation than in total intensity.

A brightness asymmetry is seen in both total intensity and polarimetric science images. Surface brightness profiles suggest the same, quantifying a flux asymmetry of ∼0.5 magnitudes. The brightness asymmetry is seen throughout the reflectance plot and the disk also appears red in the NIR wavelengths. However, in surface brightness profile there is no significant brightness asymmetry seen in the polarimetric observation. This could be because the polarimetric images have high S/N and the background noise affects the photometric observation.

Fitting the reflectance plot to synthetic spectra retrieved by assuming a particle size distribution, the minimum grain size of possible astro-silicate grains within the disk was found to be 0.7 ± 0.2 μm. Similar, to HD 32297 and HD 141569 the minimum grain size is smaller than the blowout limit. In these prior analyses, the contradiction of finding grains smaller than their blowout limit was attributed to one of the two possibilities or both. First, being a dynamical avalanche collision giving rise to smaller grains with increasing collisions as suggested in Grigorieva et al. (2007); Thebault & Kral (2018). This effect is more prominent for double component debris disk with an inner warm luminous disk and an outer disk and/or a disk exhibiting bluer spectral profile. Second, is the presence of the massive amount of gas within the system to retain the smaller grains for longer timescale (Kral et al., 2013; Takeuchi & Artymowicz, 2001). However, unlike the disk of HD 32297, HD 106906 disk is red in color and no confirmation of a significant presence of gas has been found. The origin of the possible small dust grains in the disk is still to be

interpreted. Therefore, to constrain and further examine the effect of $s_{min} < s_{blow}$ K band observation of the disk along with the multiple composition grain modeling is impending.

CHAPTER 5

Conclusion and Perspectives

5.1 Conclusion 107
5.2 Perspective 109
5.2.1 Outlook on the characterization of morphological features 109
5.2.2 Future Telescopes 110

5.1 Conclusion

The primary motivation of this thesis was to take advantage of the integral field spectrograph of a high-contrast imager to identify spectral characteristics of circumstellar disks in NIR wavelengths. The thesis started with an objective to perform spectro-photometry of debris disks observed with SPHERE. The images obtained by high-contrast imagers such as SPHERE are polluted by speckles and therefore, the quality of the images is affected. In this thesis, I have used ADI and PDI post-processing techniques to correct for these speckles for total intensity and polarimetric images respectively. However, ADI techniques induce self-subtraction or an ADI bias. This bias affects the photometry of the disk. Hence, to correct for this bias I have used forward modeling. Primarily, I adopted the GraTer model to produce synthetic images of the disk depending on density and scattering parameters then process them with KLIP to obtain a post-processed model to be compared to the science image of the disk. Globally minimizing the intensity between the post-processed science image and the model of the disk allows to constrain the morphological parameters (such as semi-major axis, radial slopes, vertical profile, inclination, phase function, etc.) and provides the photometry of the disk.

This work allowed me to study three characteristics of debris disks. The first being the morphology of the disk, the second is the spectrum of the disk at NIR wavelengths and the third is the properties of grains present in the disk. During the three years of my thesis, I have analyzed these characteristics of three debris disks: HD 32297, HD 141569, and HD 106906. Hence, I am summarizing below the interpretation regarding these characteristics.

- **Morphology of the debris disks**: Obtaining the true morphology of a disk is often challenged by the limitations of our observation. The most important parameters to obtain disk morphology are its inclination i, position angle PA, the position of the ansae R_0, the inner and outer radial slopes of density function α_{in}, α_{out}, the anisotropic scattering factor g and the scale height h.

  In disks such as HD 32297 and HD 106906 which are highly inclined ($i \geq 85°$), the R_0 and α_{in} are not well constrained. In these disks, models produce errors up to 10% and 66% for R_0 and α_{in} respectively. This effect is seen in both total intensity and polarimetric images of HD 32297 and HD 106906 in Chapter 3 and 4. Additionally, for HD 106906 in polarimetry the disk ansae are not well resolved and have very high uncertainty ($R_0 = 80 \pm 20$ au) because of low signal to noise ratios in the images. The phase function is parameterized by g. In both the inclined disks, g_{pol} is greater than g_{intn} which shows that the grains scatter at a lower scattering angle in polarized light than in unpolarized light. However, in total intensity images, the disk is strongly affected by self-subtraction at smaller separations which would result in losing information on any forward scattering peak at small scattering angles.

  For disk such as HD 141569 which is inclined at 56°, the modeling provides a much better determination of $R_0 = 45$ au but on the contrary, the vertical scale height h is not well constrained. This is seen in the study of the innermost ringlet R3 of HD 141569 where $h = 0.025 \pm 0.015$.

  Therefore, with each unique morphology of debris disk the complexity of forward modeling increases. As a result, depending on the morphology of the disks some parameters are not well constrained than others.

- **The spectrum of the debris disks**: Using the forward model I extracted the spectro-photometry of the disks. The spectral reflectance plot of the disk of HD 32297, HD 106906 and the ringlet R3 of HD 141569 shows a gray to blueish, gray to reddish and a gray tendency respectively. These three disks have different intrinsic brightness features. For example, HD 32297 do not show any brightness asymmetry between the two sides of the disk, however, this is not true for HD 106906 and HD 141569. From the surface brightness and the spectral reflectance a brightness asymmetry of 0.5 magnitudes between the two sides of the disk of HD 106906 is measured. This brightness asymmetry probably implies dynamical events, possibly related to the presence of a giant planet at an angular separation of 7.1″ (∼730 au) at the northwest side of the disk which could have been ejected during the history of the system. However, this theory is not inspected in this study.

  For HD 141569, the surface brightness profile shows that the southern part of the ringlet R3 is brighter than the northern part by ∼1 magnitude. Apart from obtaining a spectro-photometry of the whole ringlet R3, aperture photometry is performed to extract the spectral reflectance of the clump. This spectral reflectance plot of the clump is compared to that of the rest of the southern ringlet. As seen in chapter 4 and, the unbiased photometries suggest that the reflectance is not significantly higher in the clump than the rest of the disk and does not have significant azimuthal variation near the southern ansa of R3. These analyses suggest that there is a higher probability of the clump being an ADI artifact than a physical dust trap.

  Comparing the three disk's spectral reflectance, the disk around HD 32297 is the brightest with a spectral reflectance of the order of 10^{-2}, HD 106906 and HD 141569

ascend with spectral reflectances of the order of 10^{-3} and 10^{-5} respectively.

- **The properties of grains in the debris disks**: The spectral reflectance plots of the debris disks are fitted with synthetic spectra to constrain the minimum size of the grains abundantly present in the disk. These synthetic spectra are obtained by modeling the particle size distribution (PSD) of grains within the disk. It is seen that even though the three disks have varied morphology and spectral characteristics, the possibility of the presence of an abundant amount of sub-micron grains smaller than the blowout size cannot be discarded. For HD 32297, the possible explanations of the presence of such small grains are provided to be a combination of a steady-state collisional cascade, collisional avalanche mechanism and/or gas drag. As there has not been any evidence of gas present in the disk of HD 106906 the possible explanation could be an avalanche mechanism for the presence of sub-micron grains. The reflectance plot of the southern ringlet R3 of HD 141569 is flat, has significant error-bars and also quite faint. Therefore, fitting synthetic spectra by modeling the PSD could not fully assert the presence of grains smaller than the blowout size. Also, this system is relatively young and has an abundance of gas which could certainly play a major role in the dynamics of harboring such grains for a longer time.

5.2 Perspective

In the last decade, the field of high-contrast imaging has exponentially increased the prospects of debris disks studies. Around 100 debris disks have been resolved as of today. This field has developed now to the extent where we are studying the grains, gas and possible planet interaction in such systems. A natural extension of the work presented in this thesis should be to study many other debris disks with detailed morphological, spectro-photometric, and PSD analysis. This kind of study can classify debris disks in terms of their relative brightness, color in NIR wavelengths, and venture on the number of disks which has sub-micron grains within them. Statistical analysis to correlate the number of disks with small grains to the presence of gas in such systems can assist in the theories related to planet formation.

In this thesis, the primary focus while analyzing the PSD was given to the astro-silicate type of grains. Extensive modeling of PSD in the NIR spectral range with carbonaceous, ices and porous grains could further constraint the grain sizes within the disks. Information on grain sizes and composition can also be derived by extracting the scattering phase function (SPF) of the disk and comparing it with theoretical SPFs of solar system type (asteroid, zodiacal, cometary) dust and/or synthetic SPFs obtained from modeling various grain properties (such as, minimum size, composition, etc.). This type of analysis has been carried out by Engler et al. (2019); Milli et al. (2019, 2017) for disks around HR 4796 and HD 15115. Measuring the phase function was not deemed very practical in the case of the three disks analyzed here, because of their geometry.

5.2.1 Outlook on the characterization of morphological features

Many circumstellar disks show morphological features such as clumps, spirals, warps, gaps, for instance, HD 100546 (Sissa et al., 2018), MWC758 (Benisty et al., 2015), HD 196142

(Gratton et al., 2019), LkCa15 (Thalmann et al., 2016), Au Mic (Boccaletti et al., 2018), TWA7 (Olofsson et al., 2016), etc.. Studying such features can result in anticipating the presence of planet-forming sites in such systems. Aperture photometry, similar to the study of HD 141569, could be performed to extract spectral information on these morphological features and then the grain properties can be studied at multi-wavelengths. For instance, Mouillet et al. (1997) discussed that a planet could be responsible for carving the warp in the debris disk β Pic. The warp feature was further observed and studied in mid-IR (Telesco et al., 2005) and scattered light (Golimowski et al., 2006), which paved the path to finally detect the β Pic b exoplanet (Lagrange et al., 2009).

While an outlook of studying various morphological features of a wide range of circumstellar disks is provided, it should be noted that modeling such intricate features to extract their morphological information and overcome the ADI bias can be challenging with the simplest form of radiative transfer models. An advancement in modeling the density and scattering parameters (e.g. using Lorentzian density function or Mie scattering) could mimic some of the morphologies of complex disks. To avoid ADI bias Reference Differential Imaging should be used for post-processing total intensity images which would help in spectral extraction without accounting for any self-subtraction. Currently, this technique for the ground-based telescopes such as GPI and SPHERE is not as efficient as it can be with HST because of stability reasons (Chauvin, 2018; Choquet et al., 2014), so more work in this direction is needed. A combined analysis of total intensity and polarimetric images with RDI and PDI would facilitate the study and characterization of grains from polarization fraction, and polarization and total intensity phase functions.

5.2.2 Future Telescopes

The upcoming space- and ground-based telescopes include JWST, ELT, and TMT. JWST which is expected to launch in early 2021 is a facility with 18 hexagonal segmented mirrors together forming a diameter of 6.5 m primary mirror. The Near InfraRed Camera (NIRCAM, Beichman et al., 2012; Rieke et al., 2005) and Mid-InfraRed Instrument (MIRI, Boccaletti et al., 2015; Rieke et al., 2015) could simultaneously resolve debris disks. One of the primary objectives of JWST is to resolve exo-Kuiper belts in IR. The overall interest is to bridge the gap between SPHERE/GPI and ALMA by providing high angular resolution in the mid-IR to probe the dust-grain population not much explored yet.

The ELT is a 39-meter class telescope which will be commissioned in ∼2025. The ELT would resolve warm dust in disks with a spatial resolution of 0.01″ at 1 au. The instruments of the ELT which would observe circumstellar environments are MICADO (Davies et al., 2016) which is a camera operating in NIR wavelengths and METIS (Brandl et al., 2016) which is a mid-IR spectrograph. The ELT would complement the JWST scientific results.

JWST and ELT both would resolve the morphological features such as gas traps and clumps of disks with great detail. The spectral resolution of MIRI and METIS would aid in resolving spectral features, such as water-ice features and also resolve features related to silicate grain crystallization. Grain composition would be better constrained from such

spectroscopy. The sizes of grains can be constrained by obtaining a spectral reflectance with NIRCAM's multiple filters and MICADO's J, H and K bands.

Both JWST/MIRI and ELT would be able to image young giant planets and characterize their atmospheres. In a system with planet and disk both present, the spectral features in the atmospheric characterization of a young planet and the disk would help in understanding planet-disk interaction. Therefore, in the next decade, these two instruments would provide observations that potentially would answer the questions, such as: What is the evolutionary process of planets? What is the evolutionary path of debris disks? How do the grains and gas interact? What mechanisms give rise to the morphological and spectral features in debris disk? How do planets and disk interact? Do all stellar systems go through the same evolutionary process?

"I believe alien life is quite common in the universe, although intelligent life is less so. Some say it has yet to appear on planet Earth. "
-Late Prof. Stephan Hawking

References

Bibliography

Absil, O., di Folco, E., Mérand, A., et al. 2006, A&A, 452, 237

Acke, B., Min, M., Dominik, C., et al. 2012, A&A, 540, A125

Alibert, Y., Mordasini, C., Benz, W., & Winisdoerffer, C. 2005, A&A, 434, 343

Apai, D., Schneider, G., Grady, C. A., et al. 2015, ApJ, 800, 136

Armitage, P. J. 2019, Saas-Fee Advanced Course, 45, 1

Asensio-Torres, R., Janson, M., Hashimoto, J., et al. 2016, A&A, 593, A73

Augereau, J. C., Lagrange, A. M., Mouillet, D., & Ménard, F. 1999a, A&A, 350, L51

Augereau, J. C., Lagrange, A. M., Mouillet, D., Papaloizou, J. C. B., & Grorod, P. A. 1999b, A&A, 348, 557

Augereau, J. C. & Papaloizou, J. C. B. 2004, A&A, 414, 1153

Aumann, H. H., Gillett, F. C., Beichman, C. A., et al. 1984, ApJ, 278, L23

Avenhaus, H., Quanz, S. P., Schmid, H. M., et al. 2014, ApJ, 781, 87

Babcock, H. W. 1953, PASP, 65, 229

Bailey, V., Meshkat, T., Reiter, M., et al. 2014, ApJ, 780, L4

Ballering, N. P., Rieke, G. H., Su, K. Y. L., & Montiel, E. 2013, The Astrophysical Journal, 775, 55

Ballering, N. P., Su, K. Y. L., Rieke, G. H., & Gáspár, A. 2016, ApJ, 823, 108

Baudoz, P., Boccaletti, A., Riaud, P., et al. 2006, PASP, 118, 765

Baudoz, P., Mazoyer, J., Mas, M., Galicher, R., & Rousset, G. 2012, in Society of Photo-Optical Instrumentation Engineers (SPIE) Conference Series, Vol. 8446, Proc. SPIE, 84468C

Beichman, C. A., Rieke, M., Eisenstein, D., et al. 2012, in Space Telescopes and Instrumentation 2012: Optical, Infrared, and Millimeter Wave, ed. M. C. Clampin, G. G. Fazio, H. A. MacEwen, & J. M. O. Jr., Vol. 8442, International Society for Optics and Photonics (SPIE), 973 – 983

Benisty, M., Juhasz, A., Boccaletti, A., et al. 2015, A&A, 578, L6

Bertini, I., La Forgia, F., Tubiana, C., et al. 2017, MNRAS, 469, S404

Beust, H., Rèche, R., & Augereau, J.-C. 2009, in American Institute of Physics Conference Series, Vol. 1094, 15th Cambridge Workshop on Cool Stars, Stellar Systems, and the Sun, ed. E. Stempels, 405–408

Beuzit, J.-L., Vigan, A., Mouillet, D., et al. 2019, arXiv e-prints

Bhowmik, T., Boccaletti, A., Thébault, P., et al. 2019, arXiv e-prints, arXiv:1908.08511

Biller, B. A., Liu, M. C., Rice, K., et al. 2015, MNRAS, 450, 4446

Blum, J. & Wurm, G. 2008, ARA&A, 46, 21

Boccaletti, A., Augereau, J.-C., Lagrange, A.-M., et al. 2012, A&A, 544, A85

Boccaletti, A., Augereau, J.-C., Marchis, F., & Hahn, J. 2003, ApJ, 585, 494

Boccaletti, A., Carbillet, M., Fusco, T., et al. 2008, in Society of Photo-Optical Instrumentation Engineers (SPIE) Conference Series, Vol. 7015, Proc. SPIE, 70156E

Boccaletti, A., Lagage, P.-O., Baudoz, P., et al. 2015, Publications of the Astronomical Society of the Pacific, 127, 633

Boccaletti, A., Sezestre, E., Lagrange, A.-M., et al. 2018, A&A, 614, A52

Boccaletti, A., Thalmann, C., Lagrange, A.-M., et al. 2015, Nature, 526, 230

Boley, A. C., Payne, M. J., Corder, S., et al. 2012, ApJ, 750, L21

Booth, M., Kennedy, G., Sibthorpe, B., et al. 2013, MNRAS, 428, 1263

Booth, R. A., Meru, F., Lee, M. H., & Clarke, C. J. 2018, MNRAS, 475, 167

Bordé, P. J. & Traub, W. A. 2006, ApJ, 638, 488

Boss, A. P. 2002, Earth and Planetary Science Letters, 202, 513

Bouwman, J., Meeus, G., de Koter, A., et al. 2001, A&A, 375, 950

Brandl, B. R., Agócs, T., Aitink-Kroes, G., et al. 2016, in Ground-based and Airborne Instrumentation for Astronomy VI, ed. C. J. Evans, L. Simard, & H. Takami, Vol. 9908, International Society for Optics and Photonics (SPIE), 633 – 647

Brittain, S. D., Simon, T., Najita, J. R., & Rettig, T. W. 2007, ApJ, 659, 685

Burns, J. A., Lamy, P. L., & Soter, S. 1979, Icarus, 40, 1

Cameron, A. G. W. 1978, Moon and Planets, 18, 5

Carbillet, M., Bendjoya, P., Abe, L., et al. 2011, Experimental Astronomy, 30, 39

Carbillet, M., Bendjoya, P., Abe, L., et al. 2010, in In the Spirit of Lyot 2010, E56

Carpenter, J. M., Bouwman, J., Mamajek, E. E., et al. 2009, ApJS, 181, 197

Chauvin, G. 2018, in Society of Photo-Optical Instrumentation Engineers (SPIE) Conference Series, Vol. 10703, Proc. SPIE, 1070305

Chauvin, G., Desidera, S., Lagrange, A. M., et al. 2017, in SF2A-2017: Proceedings of the Annual meeting of the French Society of Astronomy and Astrophysics, Di

Chauvin, G., Vigan, A., Bonnefoy, M., et al. 2015, A&A, 573, A127

Chen, C., Ballering, N., Duchene, G., et al. 2019, BAAS, 51, 342

Chen, C. H., Jura, M., Gordon, K. D., & Blaylock, M. 2005, ApJ, 623, 493

Chen, C. H., Sheehan, P., Watson, D. M., Manoj, P., & Najita, J. R. 2009, ApJ, 701, 1367

Choquet, É., Pueyo, L., Hagan, J. B., et al. 2014, in Society of Photo-Optical Instrumentation Engineers (SPIE) Conference Series, Vol. 9143, Proc. SPIE, 914357

Chun, M., Toomey, D., Wahhaj, Z., et al. 2008, in Society of Photo-Optical Instrumentation Engineers (SPIE) Conference Series, Vol. 7015, Proc. SPIE, 70151V

Clampin, M., Krist, J. E., Ardila, D. R., et al. 2003, AJ, 126, 385

Claudi, R. U., Turatto, M., Gratton, R. G., et al. 2008, in Proc. SPIE, Vol. 7014, Ground-based and Airborne Instrumentation for Astronomy II, 70143E

Currie, T., Grady, C. A., Cloutier, R., et al. 2016, ApJ, 819, L26

Currie, T., Rodigas, T. J., Debes, J., et al. 2012, ApJ, 757, 28

Davies, R., Schubert, J., Hartl, M., et al. 2016, in Ground-based and Airborne Instrumentation for Astronomy VI, ed. C. J. Evans, L. Simard, & H. Takami, Vol. 9908, International Society for Optics and Photonics (SPIE), 621 – 632

de Boer, J., Langlois, M., van Holstein, R. G., et al. 2019, arXiv e-prints, arXiv:1909.13107

De Rosa, R. J. & Kalas, P. 2019, AJ, 157, 125

Delorme, P., Meunier, N., Albert, D., et al. 2017, in SF2A-2017: Proceedings of the Annual meeting of the French Society of Astronomy and Astrophysics, ed. C. Reylé, P. Di Matteo, F. Herpin, E. Lagadec, A. Lançon, Z. Meliani, & F. Royer, 347–361

Dent, W. R. F., Greaves, J. S., & Coulson, I. M. 2005, MNRAS, 359, 663

Dent, W. R. F., Wyatt, M. C., Roberge, A., et al. 2014, Science, 343, 1490

Desidera, S., Gratton, R., Claudi, R., et al. 2008, in Society of Photo-Optical Instrumentation Engineers (SPIE) Conference Series, Vol. 7014, Proc. SPIE, 70143M

di Folco, E., Absil, O., Augereau, J. C., et al. 2007, A&A, 475, 243

Dohlen, K., Langlois, M., Saisse, M., et al. 2008, in Proc. SPIE, Vol. 7014, Ground-based and Airborne Instrumentation for Astronomy II, 70143L

Dohnanyi, J. S. 1969, J. Geophys. Res., 74, 2531

Donaldson, J. K., Lebreton, J., Roberge, A., Augereau, J.-C., & Krivov, A. V. 2013, ApJ, 772, 17

Draine, B. T. 2004, Astrophysics of Dust in Cold Clouds, Vol. 32, 213

Dullemond, C. P. & Dominik, C. 2008, A&A, 487, 205

Einstein, A. 1936, Science, 84, 506

Engler, N., Boccaletti, A., Schmid, H. M., et al. 2018a, arXiv e-prints

Engler, N., Boccaletti, A., Schmid, H. M., et al. 2019, A&A, 622, A192

Engler, N., Schmid, H. M., Quanz, S. P., Avenhaus, H., & Bazzon, A. 2018b, A&A, 618, A151

Feldt, M., Olofsson, J., Boccaletti, A., et al. 2017, A&A, 601, A7

Fitzgerald, M. P., Kalas, P. G., & Graham, J. R. 2007, ApJ, 670, 557

Foreman-Mackey, D., Hogg, D. W., Lang, D., & Goodman, J. 2013, PASP, 125, 306

Frattin, E., Muñoz, O., Moreno, F., et al. 2019, MNRAS, 484, 2198

Fusco, T., Sauvage, J.-F., Petit, C., et al. 2014, in Proc. SPIE, Vol. 9148, Adaptive Optics Systems IV, 91481U

Gaia Collaboration. 2018, VizieR Online Data Catalog, I/345

Galicher, R., Boccaletti, A., Mesa, D., et al. 2018, A&A, 615, A92

Give'on, A., Kern, B., Shaklan, S., Moody, D. C., & Pueyo, L. 2007, in Society of Photo-Optical Instrumentation Engineers (SPIE) Conference Series, Vol. 6691, Proc. SPIE, 66910A

Goldreich, P. & Ward, W. R. 1973, ApJ, 183, 1051

Golimowski, D. A., Ardila, D. R., Krist, J. E., et al. 2006, AJ, 131, 3109

Gonzalez, J. F., Laibe, G., & Maddison, S. T. 2017, MNRAS, 467, 1984

Goto, M., Usuda, T., Dullemond, C. P., et al. 2006, ApJ, 652, 758

Gratton, R., Ligi, R., Sissa, E., et al. 2019, A&A, 623, A140

Grigorieva, A., Artymowicz, P., & Thébault, P. 2007, A&A, 461, 537

Houk, N. & Cowley, A. P. 1975, University of Michigan Catalogue of two-dimensional spectral types for the HD stars. Volume I. Declinations -90_ to -53_f0.

Hueso, R. & Guillot, T. 2005, A&A, 442, 703

Hughes, A. M., Duchêne, G., & Matthews, B. C. 2018, ARA&A, 56, 541

Kalas, P. 2005, ApJ, 635, L169

Kalas, P., Graham, J. R., Fitzgerald, M. P., & Clampin, M. 2013, ApJ, 775, 56

Kalas, P. G., Rajan, A., Wang, J. J., et al. 2015, ApJ, 814, 32

Kennedy, G. M. & Wyatt, M. C. 2014, MNRAS, 444, 3164

Keppler, M., Benisty, M., Müller, A., et al. 2018, A&A, 617, A44

Kervella, P., Lagadec, E., Montargès, M., et al. 2016, A&A, 585, A28

Kobayashi, H., Watanabe, S.-i., Kimura, H., & Yamamoto, T. 2009, Icarus, 201, 395

Konishi, M., Grady, C. A., Schneider, G., et al. 2016, ApJ, 818, L23

Kral, Q., Marino, S., Wyatt, M. C., Kama, M., & Matra, L. 2018, arXiv e-prints

Kral, Q., Thébault, P., & Charnoz, S. 2013, A&A, 558, A121

Kral, Q., Wyatt, M., Carswell, R. F., et al. 2016, MNRAS, 461, 845

Krivov, A. V. 2010, Research in Astronomy and Astrophysics, 10, 383

Krivov, A. V., Löhne, T., & Sremčević, M. 2006, A&A, 455, 509

Krumholz, M. R. 2011, in American Institute of Physics Conference Series, Vol. 1386, American Institute of Physics Conference Series, ed. E. Telles, R. Dupke, & D. Lazzaro, 9–57

Kuhn, J. R., Potter, D., & Parise, B. 2001, ApJ, 553, L189

Lafrenière, D., Marois, C., Doyon, R., Nadeau, D., & Artigau, É. 2007, ApJ, 660, 770

Lagrange, A.-M., Boccaletti, A., Milli, J., et al. 2012, A&A, 542, A40

Lagrange, A.-M., Kasper, M., Boccaletti, A., et al. 2009, A&A, 506, 927

Lagrange, A. M., Keppler, M., Meunier, N., et al. 2018, A&A, 612, A108

Lagrange, A.-M., Langlois, M., Gratton, R., et al. 2016, A&A, 586, L8

Laibe, G., Gonzalez, J. F., & Maddison, S. T. 2012, A&A, 537, A61

Langlois, M., Dohlen, K., Augereau, J. C., et al. 2010, in Society of Photo-Optical Instrumentation Engineers (SPIE) Conference Series, Vol. 7735, Proc. SPIE, 77352U

Langlois, M., Dohlen, K., Vigan, A., et al. 2014, in Proc. SPIE, Vol. 9147, Ground-based and Airborne Instrumentation for Astronomy V, 91471R

Langlois, M., Vigan, A., Moutou, C., et al. 2013, in Proceedings of the Third AO4ELT Conference, ed. S. Esposito & L. Fini, 63

Lebreton, J., van Lieshout, R., Augereau, J. C., et al. 2013, A&A, 555, A146

Lenzen, R., Hartung, M., Brandner, W., et al. 2003, in Society of Photo-Optical Instrumentation Engineers (SPIE) Conference Series, Vol. 4841, Instrument Design and Performance for Optical/Infrared Ground-based Telescopes, ed. M. Iye & A. F. M. Moorwood, 944–952

Lisse, C. M., Beichman, C. A., Bryden, G., & Wyatt, M. C. 2007, The Astrophysical Journal, 658, 584

Lisse, C. M., Chen, C. H., Wyatt, M. C., et al. 2009, ApJ, 701, 2019

Lyot. 1930, Bulletin Astronomique, 6, 305

Lyra, W. & Kuchner, M. 2013, Nature, 499, 184

MacGregor, M. A., Matrà, L., Kalas, P., et al. 2017, ApJ, 842, 8

MacGregor, M. A., Weinberger, A. J., Hughes, A. M., et al. 2018, ApJ, 869, 75

MacGregor, M. A., Wilner, D. J., Andrews, S. M., & Hughes, A. M. 2015, ApJ, 801, 59

Macintosh, B. A., Graham, J. R., Palmer, D. W., et al. 2008, in Society of Photo-Optical Instrumentation Engineers (SPIE) Conference Series, Vol. 7015, Proc. SPIE, 701518

Madec, P. Y. 2012, in Society of Photo-Optical Instrumentation Engineers (SPIE) Conference Series, Vol. 8447, Proc. SPIE, 844705

Maire, A.-L., Boccaletti, A., Rameau, J., et al. 2014, in IAU Symposium, Vol. 299, Exploring the Formation and Evolution of Planetary Systems, ed. M. Booth, B. C. Matthews, & J. R. Graham, 21–25

Maire, A.-L., Langlois, M., Dohlen, K., et al. 2016, in Proc. SPIE, Vol. 9908, Ground-based and Airborne Instrumentation for Astronomy VI, 990834

Marois, C. 2015, IAU General Assembly, 22, 2254053

Marois, C., Correia, C., Galicher, R., et al. 2014, in Society of Photo-Optical Instrumentation Engineers (SPIE) Conference Series, Vol. 9148, Proc. SPIE, 91480U

Marois, C., Lafrenière, D., Doyon, R., Macintosh, B., & Nadeau, D. 2006a, ApJ, 641, 556

Marois, C., Macintosh, B., & Véran, J.-P. 2010, in Society of Photo-Optical Instrumentation Engineers (SPIE) Conference Series, Vol. 7736, Proc. SPIE, 77361J

Marois, C., Phillion, D. W., & Macintosh, B. 2006b, in Proc. SPIE, Vol. 6269, Society of Photo-Optical Instrumentation Engineers (SPIE) Conference Series, 62693M

Matthews, B., Kennedy, G., Sibthorpe, B., et al. 2014, ApJ, 780, 97

Matthews, B. C., Kennedy, G., Sibthorpe, B., et al. 2015, ApJ, 811, 100

Mawet, D., Riaud, P., Absil, O., & Surdej, J. 2005, ApJ, 633, 1191

Mazoyer, J., Baudoz, P., Galicher, R., & Rousset, G. 2014a, A&A, 564, L1

Mazoyer, J., Boccaletti, A., Augereau, J.-C., et al. 2014b, A&A, 569, A29

Mazoyer, J., Boccaletti, A., Choquet, É., et al. 2016, ApJ, 818, 150

Mesa, D., Gratton, R., Zurlo, A., et al. 2015, A&A, 576, A121

Miley, J. M., Panić, O., Haworth, T. J., et al. 2019, MNRAS, 485, 739

Milli, J., Engler, N., Schmid, H. M., et al. 2019, arXiv e-prints

Milli, J., Vigan, A., Mouillet, D., et al. 2017, A&A, 599, A108

Mittal, T., Chen, C. H., Jang-Condell, H., et al. 2015, ApJ, 798, 87

Moerchen, M. M., Churcher, L. J., Telesco, C. M., et al. 2011, A&A, 526, A34

Moór, A., Apai, D., Pascucci, I., et al. 2009, The Astrophysical Journal, 700, L25

Moór, A., Curé, M., Kóspál, Á., et al. 2017, ApJ, 849, 123

Morales, F. Y., Padgett, D. L., Bryden, G., Werner, M. W., & Furlan, E. 2012, The Astrophysical Journal, 757, 7

Morales, F. Y., Rieke, G. H., Werner, M. W., et al. 2011, ApJ, 730, L29

Mouillet, D., Lagrange, A. M., Augereau, J. C., & Ménard, F. 2001, A&A, 372, L61

Mouillet, D., Larwood, J. D., Papaloizou, J. C. B., & Lagrange, A. M. 1997, MNRAS, 292, 896

Müller, A., Keppler, M., Henning, T., et al. 2018, A&A, 617, L2

Nesvold, E. R., Naoz, S., & Fitzgerald, M. P. 2017, ApJ, 837, L6

Ollivier, M., Roques, F., Casoli, F., Encrenaz, T., & Selsis, F. 2009, Planetary Systems

Olofsson, J., Milli, J., Thébault, P., et al. 2019, arXiv e-prints, arXiv:1908.10378

Olofsson, J., Samland, M., Avenhaus, H., et al. 2016, A&A, 591, A108

Pavlov, A., Möller-Nilsson, O., Feldt, M., et al. 2008, in Proc. SPIE, Vol. 7019, Advanced Software and Control for Astronomy II, 701939

Pawellek, N., Krivov, A. V., Marshall, J. P., et al. 2014, ApJ, 792, 65

Pecaut, M. J. & Mamajek, E. E. 2016, MNRAS, 461, 794

Péricaud, J., Di Folco, E., Dutrey, A., Guilloteau, S., & Piétu, V. 2017, A&A, 600, A62

Perrin, M. D., Duchene, G., Millar-Blanchaer, M., et al. 2015, ApJ, 799, 182

Perrot, C. 2017, PhD thesis, thèse de doctorat dirigée par Rousset, Gérard et Boccaletti, Anthony Physique. Astronomie, Astrophysique Sorbonne Paris Cité 2017

Perrot, C., Boccaletti, A., Pantin, E., et al. 2016, A&A, 590, L7

Pollack, J. B., Hubickyj, O., Bodenheimer, P., et al. 1996, Icarus, 124, 62

Powell, M. J. D. 1973, 4, 193

Pueyo, L. 2016, ApJ, 824, 117

Pueyo, L., Soummer, R., Hoffmann, J., et al. 2015, ApJ, 803, 31

Quanz, S. P., Schmid, H. M., Birkmann, S. M., et al. 2011, The Messenger, 146, 25

Racine, R., Walker, G. A. H., Nadeau, D., Doyon, R., & Marois, C. 1999, PASP, 111, 587

Rice, W. K. M., Armitage, P. J., Bonnell, I. A., et al. 2003, MNRAS, 346, L36

Ricker, G. R., Winn, J. N., Vanderspek, R., et al. 2015, Journal of Astronomical Telescopes, Instruments, and Systems, 1, 014003

Rieke, G. H., Gáspár, A., & Ballering, N. P. 2016, ApJ, 816, 50

Rieke, G. H., Wright, G. S., Böker, T., et al. 2015, Publications of the Astronomical Society of the Pacific, 127, 584

Rieke, M. J., Kelly, D. M., & Horner, S. D. 2005, in Cryogenic Optical Systems and Instruments XI, ed. J. B. Heaney & L. G. Burriesci, Vol. 5904, International Society for Optics and Photonics (SPIE), 1 – 8

Rigaut, F. 2015, PASP, 127, 1197

Rodigas, T. J., Debes, J. H., Hinz, P. M., et al. 2014, ApJ, 783, 21

Rodigas, T. J., Stark, C. C., Weinberger, A., et al. 2015, ApJ, 798, 96

Rouan, D., Riaud, P., Boccaletti, A., Clénet, Y., & Labeyrie, A. 2000, PASP, 112, 1479

Sauvage, J.-F., Fusco, T., Petit, C., et al. 2016, Journal of Astronomical Telescopes, Instruments, and Systems, 2, 025003

Sauvage, J. F., Mugnier, L., Paul, B., & Villecroze, R. 2012, Optics Letters, 37, 4808

Schmid, H. M., Joos, F., & Tschan, D. 2006, A&A, 452, 657

Schneider, G., Grady, C. A., Hines, D. C., et al. 2014, AJ, 148, 59

Schneider, G., Silverstone, M. D., & Hines, D. C. 2005, ApJ, 629, L117

Schneider, G., Wood, K., Silverstone, M. D., et al. 2003, AJ, 125, 1467

Serabyn, E., Huby, E., Matthews, K., et al. 2017, AJ, 153, 43

Sissa, E., Gratton, R., Garufi, A., et al. 2018, A&A, 619, A160

Sivaramakrishnan, A., Koresko, C. D., Makidon, R. B., Berkefeld, T., & Kuchner, M. J. 2001, ApJ, 552, 397

Soummer, R. 2005, ApJ, 618, L161

Soummer, R., Pueyo, L., & Larkin, J. 2012, ApJ, 755, L28

Su, K. Y. L. & Rieke, G. H. 2014, in IAU Symposium, Vol. 299, Exploring the Formation and Evolution of Planetary Systems, ed. M. Booth, B. C. Matthews, & J. R. Graham, 318–321

Su, K. Y. L., Rieke, G. H., Defrére, D., et al. 2016, ApJ, 818, 45

Su, K. Y. L., Rieke, G. H., Misselt, K. A., et al. 2005, ApJ, 628, 487

Su, K. Y. L., Rieke, G. H., Stapelfeldt, K. R., et al. 2009, ApJ, 705, 314

Su, K. Y. L., Rieke, G. H., Stapelfeldt, K. R., et al. 2008, ApJ, 679, L125

Takeuchi, T. & Artymowicz, P. 2001, ApJ, 557, 990

Tamura, M., Suto, H., Itoh, Y., et al. 2000, in Society of Photo-Optical Instrumentation Engineers (SPIE) Conference Series, Vol. 4008, Proc. SPIE, ed. M. Iye & A. F. Moorwood, 1153–1161

Telesco, C. M., Fisher, R. S., Wyatt, M. C., et al. 2005, Nature, 433, 133

Thalmann, C., Janson, M., Buenzli, E., et al. 2011, ApJ, 743, L6

Thalmann, C., Janson, M., Garufi, A., et al. 2016, The Astrophysical Journal, 828, L17

Thalmann, C., Mulders, G. D., Hodapp, K., et al. 2014, A&A, 566, A51

Thalmann, C., Schmid, H. M., Boccaletti, A., et al. 2008, in Proc. SPIE, Vol. 7014, Ground-based and Airborne Instrumentation for Astronomy II, 70143F

Thébault, P. 2009, A&A, 505, 1269

Thebault, P. & Kral, Q. 2018, A&A, 609, A98

Thi, W.-F., Pinte, C., Pantin, E., et al. 2014, A&A, 561, A50

Tinbergen, J. 1996, Astronomical Polarimetry, 174

Traub, W. A. & Oppenheimer, B. R. 2010, Direct Imaging of Exoplanets, ed. S. Seager, 111–156

Trauger, J., Moody, D., Gordon, B., Krist, J., & Mawet, D. 2012, in Society of Photo-Optical Instrumentation Engineers (SPIE) Conference Series, Vol. 8442, Proc. SPIE, 84424Q

Vigan, A., Bonnefoy, M., Ginski, C., et al. 2016, A&A, 587, A55

Vigan, A., Langlois, M., Moutou, C., & Dohlen, K. 2008, A&A, 489, 1345

Vigan, A., N'Diaye, M., Dohlen, K., et al. 2019, A&A, 629, A11

Wagner, K., Apai, D., Kasper, M., et al. 2016, Science, 353, 673

Weinberger, A. J., Becklin, E. E., Schneider, G., et al. 1999, ApJ, 525, L53

White, J. A. & Boley, A. C. 2018, ApJ, 859, 103

Wilby, M. J., Keller, C. U., Snik, F., Korkiakoski, V., & Pietrow, A. G. M. 2017, A&A, 597, A112

Wilner, D. J., MacGregor, M. A., Andrews, S. M., et al. 2018, ApJ, 855, 56

Wyatt, M. C. 2005a, A&A, 440, 937

Wyatt, M. C. 2005b, A&A, 433, 1007

Wyatt, M. C. 2008, ARA&A, 46, 339

Wyatt, M. C., Dermott, S. F., Telesco, C. M., et al. 1999, ApJ, 527, 918

Yorke, H. W., Bodenheimer, P., & Laughlin, G. 1993, The Astrophysical Journal, 411, 274

Zsom, A., Ormel, C. W., Güttler, C., Blum, J., & Dullemond, C. P. 2010, A&A, 513, A57

Résumé

Les disques de débris sont caractérisés par un environnement poussiéreux, appauvri en gaz, composé de grains de poussière non primordiaux qui sont constamment générés par des collisions continues entre les planétésimaux. L'imagerie haut-contraste dans le proche infrarouge permet de mesurer la distribution d'intensité du disque, qui est dépendante des propriétés de ces grains. Mon objectif était d'étudier les images en lumière diffusée de disques de débris obtenues par l'instrument SPHERE/VLT installé au Chili. Les techniques de post-traitement utilisées pour réduire la contribution de l'étoile dans les images, comme l'imagerie différentielle angulaire, impliquent une auto-soustraction de l'image du disque qui doit être corrigée pour évaluer correctement la photométrie. Pour cela, j'utilise un modèle de transfert radiatif, GRaTer, pour modéliser la morphologie du disque et calculer ainsi l'effet de l'auto-soustraction. J'ai étudié les morphologies et la distribution spatiale des grains de trois disques de débris, HD 32297, HD 141569 et HD 106906 et développé des modèles reproduisant la distribution de densité et d'intensité de ces systèmes. En analysant les réflectances moyennes et les spectres obtenus en modélisation la distribution de taille des grains, on constate que ces disques contiennent des grains de taille inférieure à la taille d'éjection. Ce résultat peut être attribué à la présence de gaz et/ou à l'effet d'une avalanche collisionnelle. Cette étude apporte une contrainte sur notre compréhension actuelle de l'évolution des grains vers les planètes.

Mots Clés

disques debris, Imagerie haut contraste, SPHERE, exoplanète

Abstract

Debris disks are characterized by the dusty, gas-depleted environment bearing non-primordial dust grains which are constantly generated by continuous collisions between planetesimals. High-contrast imaging in the near infrared allows to measure the intensity distribution of the disk, which is dependent on the properties of these grains. My goal was to study the scattered light images of debris disks obtained by the SPHERE/VLT instrument installed in Chile. Post-processing techniques used to reduce the stellar contribution in images, such as angular differential imaging, involves self-subtraction of the disk image which must be corrected for to recover true photometry. For this, I use a model of radiative transfer, GRaTer, to model the morphology of the disk and so calculate the effect of self-subtraction. I studied the morphologies and the spatial distribution of the grains of three discs of debris, HD 32297, HD 141569 and HD 106906 and developed models reproducing the density and intensity distribution of these systems. By analyzing the average reflectances and the spectra obtained in modeling the grain size distribution, we see that these disks contain grains smaller than the blowout limit. This result can be attributed to the presence of gas and/or an effect of a collisional avalanche. This study puts a constraint on our current understanding of the evolution of grains towards the planets.

Keywords

debris disks, high-contrast imaging, SPHERE, exoplanet